



*A National Center of Excellence in Advanced Technology Applications*

ISSN 1520-295X

---

# Built-up Shear Links as Energy Dissipators for Seismic Protection of Bridges

by

Peter Dusicka, Ahmad M. Itani and Ian G. Buckle

University of Nevada-Reno  
Department of Civil Engineering  
Reno, Nevada 89557

Technical Report MCEER-06-0003

March 15, 2006

This research was conducted at the University of Nevada-Reno and was supported by the Federal Highway Administration under contract number DTFH61-98-C-00094.

## NOTICE

This report was prepared by the University of Nevada-Reno as a result of research sponsored by the Multidisciplinary Center for Earthquake Engineering Research (MCEER) through a contract from the Federal Highway Administration. Neither MCEER, associates of MCEER, its sponsors, the University of Nevada-Reno, nor any person acting on their behalf:

- a. makes any warranty, express or implied, with respect to the use of any information, apparatus, method, or process disclosed in this report or that such use may not infringe upon privately owned rights; or
- b. assumes any liabilities of whatsoever kind with respect to the use of, or the damage resulting from the use of, any information, apparatus, method, or process disclosed in this report.

Any opinions, findings, and conclusions or recommendations expressed in this publication are those of the author(s) and do not necessarily reflect the views of MCEER or the Federal Highway Administration.



---

## **Built-up Shear Links as Energy Dissipators for Seismic Protection of Bridges**

by

Peter Dusicka<sup>1</sup>, Ahmad M. Itani<sup>2</sup> and Ian G. Buckle<sup>3</sup>

Publication Date: March 15, 2006

Submittal Date: February 13, 2006

Technical Report MCEER-06-0003

Task Number 094-C-3.2

FHWA Contract Number DTFH61-98-C-00094

- 1 Assistant Professor, Department of Civil and Environmental Engineering, Portland State University; former Graduate Student, Department of Civil Engineering, University of Nevada-Reno
- 2 Associate Professor, Department of Civil Engineering, University of Nevada-Reno
- 3 Professor and Director of Center for Civil Engineering Earthquake Research, Department of Civil Engineering, University of Nevada-Reno

MULTIDISCIPLINARY CENTER FOR EARTHQUAKE ENGINEERING RESEARCH  
University at Buffalo, State University of New York  
Red Jacket Quadrangle, Buffalo, NY 14261

---



## Preface

The Multidisciplinary Center for Earthquake Engineering Research (MCEER) is a national center of excellence in advanced technology applications that is dedicated to the reduction of earthquake losses nationwide. Headquartered at the University at Buffalo, State University of New York, the Center was originally established by the National Science Foundation in 1986, as the National Center for Earthquake Engineering Research (NCEER).

Comprising a consortium of researchers from numerous disciplines and institutions throughout the United States, the Center's mission is to reduce earthquake losses through research and the application of advanced technologies that improve engineering, pre-earthquake planning and post-earthquake recovery strategies. Toward this end, the Center coordinates a nationwide program of multidisciplinary team research, education and outreach activities.

MCEER's research is conducted under the sponsorship of two major federal agencies, the National Science Foundation (NSF) and the Federal Highway Administration (FHWA), and the State of New York. Significant support is also derived from the Federal Emergency Management Agency (FEMA), other state governments, academic institutions, foreign governments and private industry.

The Center's Highway Project develops improved seismic design, evaluation, and retrofit methodologies and strategies for new and existing bridges and other highway structures, and for assessing the seismic performance of highway systems. The FHWA has sponsored three major contracts with MCEER under the Highway Project, two of which were initiated in 1992 and the third in 1998.

Of the two 1992 studies, one performed a series of tasks intended to improve seismic design practices for new highway bridges, tunnels, and retaining structures (MCEER Project 112). The other study focused on methodologies and approaches for assessing and improving the seismic performance of existing "typical" highway bridges and other highway system components including tunnels, retaining structures, slopes, culverts, and pavements (MCEER Project 106). These studies were conducted to:

- assess the seismic vulnerability of highway systems, structures, and components;
- develop concepts for retrofitting vulnerable highway structures and components;
- develop improved design and analysis methodologies for bridges, tunnels, and retaining structures, which include consideration of soil-structure interaction mechanisms and their influence on structural response; and
- develop, update, and recommend improved seismic design and performance criteria for new highway systems and structures.

The 1998 study, “Seismic Vulnerability of the Highway System” (FHWA Contract DTFH61-98-C-00094; known as MCEER Project 094), was initiated with the objective of performing studies to improve the seismic performance of bridge types not covered under Projects 106 or 112, and to provide extensions to system performance assessments for highway systems. Specific subjects covered under Project 094 include:

- development of formal loss estimation technologies and methodologies for highway systems;
- analysis, design, detailing, and retrofitting technologies for special bridges, including those with flexible superstructures (e.g., trusses), those supported by steel tower substructures, and cable-supported bridges (e.g., suspension and cable-stayed bridges);
- seismic response modification device technologies (e.g., hysteretic dampers, isolation bearings); and
- soil behavior, foundation behavior, and ground motion studies for large bridges.

In addition, Project 094 includes a series of special studies, addressing topics that range from non-destructive assessment of retrofitted bridge components to supporting studies intended to assist in educating the bridge engineering profession on the implementation of new seismic design and retrofitting strategies.

*This report presents the methods and results of experimental and numerical research conducted on built-up shear links intended for the earthquake protection of long span bridges. Large-scale experiments, material evaluations and numerical analyses were used to: (1) investigate the performance of built-up shear links fabricated from conventional plate steels, (2) develop design alternatives to improve the performance of the built-up shear links using HPS and LYP steels, (3) evaluate large-strain material properties of plate steels and their influence on the shear link performance, (4) develop a representative numerical model for built-up shear links, and (5) investigate the contributions to the overstrength of the shear links. Design recommendations for built-up shear links in bridges were developed on the basis of this experimental and analytical study.*

## ABSTRACT

A variety of applications of built-up shear links can be realized for the seismic protection of bridges. The objective of this research was to investigate the inelastic behavior of built-up shear links through the use of large-scale experiments and detailed numerical analyses. The purpose of the large-scale experiments was to determine the deformation capacity, maximum resistance and ultimate failure mode of built-up shear links by applying incrementally increasing cyclic plastic deformations. Two experiments utilizing conventional grade steel confirmed the viability of utilizing built-up sections. The use of high performance steel was then implemented to further extend the design options and illustrate the suitability of this grade for seismic applications. Low yield point steels were utilized to develop three types of shear links with low web compactness and without stiffeners. Two types of deformation history were used to evaluate these types of shear links; incremental cyclic and near-fault histories. The links exhibited ductile hysteretic behavior under both deformation histories, with the ultimate deformation capacity significantly exceeding the links where stiffeners were used. The improved performance was a direct result of excluding intermediate stiffeners which eliminated welds and reduced shear strain demand. However, the shear strength was found to vary among the different designs. The major shear strength contribution was found to relate to the grade of steel and minor shear strength contributions were found by parametric numerical studies to originate from the web and the flanges as well as the stiffeners. These results led to the development of a relationship for plastic shear strength of built-up shear links that reflected the trends obtained from the parametric studies. An expression was developed that effectively correlated with experimental results and conservatively estimated the shear link overstrength. Based on the results of the experimental and numerical research, built-up shear links were shown to be effective hysteretic energy dissipators. The importance of estimating the link overstrength was illustrated and design recommendations developed.



## ACKNOWLEDGEMENTS

The research was funded by the California Department of Transportation (Caltrans) via the toll bridge retrofit program through the University of California, San Diego and the Federal Highway Administration through the Highway Project at the Multidisciplinary Center for Earthquake Engineering Research (MCEER) at the State University of New York at Buffalo. Acknowledgement is also made of the constructive cooperation of T.Y. Lin International.

High performance steel was provided by Oregon Steel Mills (Portland, OR) and low yield point steel shear links by Nippon Steel (Japan). The generous assistance of Dr. Ian Aiken and Dr. Isao Kimura is also gratefully acknowledged.

The successful completion of the laboratory experiments would not be possible without the hard work of Dr. Patrick Laplace and helpful assistance of Paul Lucas, Charles Safford and Ersan Eldeleklioglu.



## TABLE OF CONTENTS

SECTION	TITLE	PAGE
<b>1</b>	<b>SHEAR LINK HYSTERETIC DEVICES FOR HIGHWAY BRIDGES</b>	
1.1	Shear Links in Seismic Design	1
1.1.1	Background to Eccentrically Braced Frames	1
1.1.2	Review of EBF Shear Link Design Provisions	2
1.1.2.1	Nominal Strength and Effective Length of Shear Links	2
1.1.2.2	Shear Deformation Limit and Stiffener Spacing	3
1.1.2.3	Strength of Components Outside the Link	4
1.1.3	Global Geometry and Shear Link Demands	4
1.1.4	Need for Built-up Shear Links	4
1.1.5	Design Strength of Built-up Shapes	5
1.2	Desirable Shear Link Performance Characteristics	6
1.2.1	Deformation Capacity	6
1.2.2	Overstrength	7
1.2.3	Failure Mode	7
1.3	Observed Earthquake Performance of EBFs	8
1.4	Applications of Built-up Shear Links to Bridges	8
1.4.1	Richmond San Rafael Bridge EBF Retrofit	9
1.4.2	Shear Links in New SFOBB Bridge Tower	10
1.5	Potential Uses of Shear Links in Bridges	12
1.5.1	Shear Links in Bridge Support Structures	13
1.5.2	Shear Links as Hysteretic Dissipators in Pier Rocking	14
1.5.3	Shear Links in Truss Bridges	15
1.5.4	Shear Links in Steel Girder Bridge Diaphragms	16
1.6	Research Purpose	17
1.7	Report Organization	18
<b>2</b>	<b>CYCLIC PERFORMANCE OF SHEAR LINKS DESIGNED USING CONVENTIONAL PLATE STEEL</b>	
2.1	Shear Link Properties and Test Setup	19
2.1.1	Shear Link Design	19
2.1.2	Shear Link Fabrication	21
2.1.3	Test Setup	22
2.2	Load History and Instrumentation	22
2.2.1	Applied Cyclic Deformation History	22
2.2.2	Instruments and Data Acquisition	24
2.3	Experimental Results	25
2.3.1	Visual Observations and General Comments	25
2.3.2	Failure Mode	28
2.3.2.1	Failure of Link C345a	28
2.3.2.2	Failure Link C345b	29

## TABLE OF CONTENTS (CONT'D)

SECTION	TITLE	PAGE
2.3.3	Shear Deformation Capacity	29
2.3.3.1	Deformation of Link C345a	30
2.3.3.2	Deformation of Link C345b	32
2.3.4	Link Resistance	35
2.3.5	Strains in Shear Link	37
2.3.5.1	Web Strains	37
2.3.5.2	Flange Strains	37
2.3.5.3	Intermediate Stiffener Strains	41
2.3.6	Performance Comparison to Larger Scale Tests	41
2.3.6.1	Overmatching of Welds	42
2.3.6.2	Stiffener Weld Grinding	42
2.3.6.3	Stiffener Chamfer Size	43
2.4	Summary	43
<b>3</b>	<b>CYCLIC PERFORMANCE OF SHEAR LINK DESIGNED USING HIGH PERFORMANCE STEEL</b>	
3.1	Shear Link Properties and Test Setup	45
3.1.1	Potential Suitability of High Performance Steel	45
3.1.2	Shear Link Design	46
3.1.3	Shear Link Fabrication	47
3.1.4	Test Setup	48
3.2	Load History and Instrumentation	48
3.2.1	Cyclic Load History	48
3.2.2	Instruments and Data Acquisition	49
3.3	Experimental Results	49
3.3.1	Visual Observations and General Comments	49
3.3.2	Failure Mode	49
3.3.3	Shear Deformation Capacity	50
3.3.4	Shear and Moment Resistance	53
3.3.5	Strains	53
3.3.5.1	Web Strains	55
3.3.5.2	Flange Strains	55
3.3.5.3	Stiffener Strains	58
3.4	Summary	58
<b>4</b>	<b>CYCLIC PERFORMANCE OF SHEAR LINKS DESIGNED USING LOW YIELD POINT STEELS</b>	
4.1	Evolution of Shear Link Design Philosophy	63
4.1.1	Need for Low Yield Point Steels	63
4.1.2	Objectives	64

## TABLE OF CONTENTS (CONT'D)

<b>SECTION</b>	<b>TITLE</b>	<b>PAGE</b>
4.1.3	Shear Link Designs	64
4.1.4	Fabrication and Test Setup	67
4.2	Deformation History and Instrumentation	69
4.2.1	Deformation Histories	69
4.2.2	Instrumentation and Data Acquisition	70
4.3	Results from Incremental Cyclic Experiments	70
4.3.1	Visual Observations and General Comments	70
4.3.2	Cyclic Response of Link L100	72
4.3.2.1	Failure Mode	72
4.3.2.2	Shear Deformation Capacity	72
4.3.2.3	Shear and Moment Resistance	75
4.3.3	Cyclic Response of Link L225	75
4.3.3.1	Failure Mode	75
4.3.3.2	Shear Deformation Capacity	76
4.3.3.3	Shear and Moment Resistance	78
4.3.4	Cyclic Response of Link X100	78
4.3.4.1	Failure Mode	78
4.3.4.2	Shear Deformation Capacity	81
4.3.4.3	Shear and Moment Resistance	81
4.3.5	Flange Cracking	83
4.3.6	Web Shear Strains	85
4.3.7	Web Length Without Stiffeners	85
4.4	Results from Near-Fault Deformation History Experiments	89
4.4.1	Response of Link L100	89
4.4.1.1	Shear Deformation Capacity	89
4.4.1.2	Shear Resistance	89
4.4.2	Response of Link L225	89
4.4.2.1	Shear Deformation Capacity	91
4.4.2.2	Shear Resistance	91
4.4.3	Response of Link X100	92
4.4.3.1	Shear Deformation Capacity	92
4.4.3.2	Shear Resistance	92
4.4.4	Response to Additional Cyclic Deformations	95
4.5	Summary	98
<b>5</b>	<b>BUILT-UP SHEAR LINK CYCLIC PERFORMANCE COMPARISONS</b>	
5.1	Overview	99
5.1.1	Experimental Program	99
5.2	Energy Dissipation	99
5.3	Cyclic Shear Behavior and Overstrength	103
5.3.1	Cyclic Shear Strength	103

## TABLE OF CONTENTS (CONT'D)

SECTION	TITLE	PAGE
5.3.2	Influence of Material Behavior	106
5.3.3	Influence of Deformation History	107
5.4	Deformation Capacity and Failure Mode	111
5.4.1	Effectiveness of eliminating stiffeners	111
5.4.2	Cumulative Plastic Shear Deformation	113
5.4.3	Influence of Deformation History	113
5.5	Implications on Built-up Shear Link Design	116
5.6	Summary	116
<b>6</b>	<b>NUMERICAL INVESTIGATION OF BUILT-UP SHEAR LINKS</b>	
6.1	Finite Element Modeling	119
6.2	Model Description	119
6.2.1	Element Type	119
6.2.2	Boundary Conditions	120
6.2.3	Material Models	120
6.2.4	Discretization	121
6.3	Results of Shear Link Analyses	122
6.3.1	Element Type and Size	122
6.3.2	Correlation to Cyclic Response	127
6.3.3	Influence of Axial Force on Shear Resistance	127
6.4	Plastic Strain Demand	131
6.4.1	Influence of Stiffeners on Web Strains	131
6.4.2	Stiffener Bending	133
6.4.3	Plastic Strains in Flanges	137
6.4.4	Strain Demand in Link L100	137
6.5	Implications for Built-up Shear Link Design	138
6.6	Summary	139
<b>7</b>	<b>PLASTIC SHEAR STRENGTH OF BUILT-UP SHEAR LINKS</b>	
7.1	Parametric Study	141
7.2	Model Description	141
7.3	Flange Contribution to Shear Strength	143
7.3.1	Influence of Flange Steel Yield Strength	143
7.3.2	Flange Thickness	145
7.4	Stiffener Contribution to Shear Resistance	145
7.4.1	Web Stiffening	145
7.4.2	Stiffener Bending	145
7.5	Influence of Effective Length on Shear Resistance	148
7.6	Shear Strength of Built-Up Shear Links	148
7.6.1	Development of Equation	148

## TABLE OF CONTENTS (CONT'D)

<b>SECTION</b>	<b>TITLE</b>	<b>PAGE</b>
7.6.2	Equation Comparison to FEM Analyses	152
7.6.3	Incorporating Material Stress-Strain Behavior	154
7.7	Accounting for Overstrength	159
7.7.1	Nominal Shear Strength	160
7.7.2	Tolerances	160
7.7.3	Material Characteristics	160
7.8	Summary	160
<b>8</b>	<b>BUILT-UP SHEAR LINK DESIGN RECOMMENDATIONS</b>	
8.1	General Requirements	163
8.1.1	Design Philosophy	163
8.1.2	Steel Grades	163
8.1.3	Section Compactness	163
8.2	Shear Link Effective Length	164
8.3	Stiffener Requirements	165
8.4	Connections and Members Outside the Effective Length	166
<b>9</b>	<b>CONCLUSIONS</b>	
9.1	Conclusions	167
9.1.1	General Conclusions	167
9.1.2	Conclusions for Design	167
9.1.3	Conclusions for Construction	168
<b>10</b>	<b>REFERENCES</b>	169
<b>Appendix A</b>	<b>TEST SET UP DETAILS</b>	173
<b>Appendix B</b>	<b>SUPPORT DOCUMENTS</b>	187



## LIST OF ILLUSTRATIONS

FIGURE	TITLE	PAGE
1-1	Typical Layout of Shear Link in Eccentrically Braced Frame	2
1-2	Global Geometry and Shear Link Deformation in EBF	3
1-3	Shear Link Effective Length Options for Rolled Wide Flanges	5
1-4	Retrofitted Building After Nisqually Earthquake (Filiatrault et al 2001)	8
1-5	Richmond San Rafael Bridge Retrofit Under Construction	9
1-6	EBF Proof Test of Richmond San Rafael EBF Retrofit (Itani 1997)	10
1-7	Rendering of the New SFOBB Suspension Signature Span	11
1-8	Full-scale Proof Test for SFOBB Shear Links at UCSD	11
1-9	Rendering of the SFOBB Signature Span Cable Stay Alternative	12
1-10	Example of Lateral Bracing for EBFs (Vincent 1996)	14
1-11	Hysteretic Dissipators for Pier Rocking	15
1-13	Shear Links in Through-Truss Bridges	16
1-12	Shear Links in Deck-Truss Bridges (Saraf & Bruneau 1998)	16
1-14	Shear Links in Steel Girder Diaphragms (Seyed & Bruneau 1999a,b)	17
2-1	Built-up Shear Links C345a and C345b Details	20
2-2	Fillet Weld Detail for Stiffener to Web Connection	22
2-3	Photograph of Installed Dual Shear Links C345a	23
2-4	Photograph of Installed Shear Link C345b	23
2-5	Incremental Amplitude Cyclic Deformation History	24
2-6	Instrumentation for Links C345a	26
2-7	Instrumentation for Links C345b	27
2-8	Flange Localized Deformation at Ends of Effective Length	28
2-9	Bolt Slippage Between Flange and Splice Plates	29
2-10	Initial Crack Location in Link C345a	30
2-11	Ultimate Failure of Link C345a	30
2-12	Stiffener Cracking at Flange Fillet Welds	31
2-13	Initial Crack Location in Link C345b	32
2-14	Ultimate Failure of Link C345b	32
2-15	Deformation Comparison of Two Parallel Links C345a	33
2-16	Cyclic Behavior of Link C345a	33
2-17	Cyclic Plastic Behavior of Link C345a	34
2-18	Panel Deformation Along the Length of Link C345a	34
2-19	Cyclic Behavior of Link C345b	35
2-20	Cyclic Plastic Behavior of Link C345b	36
2-21	Shear Strain in Web in Mid-Length of Link C345a	38
2-22	Shear Strain in Web at End of Effective Length for Link C345a	38
2-23	Shear Strain in Web at Link Center of Link C345a	39
2-24	Shear Strain in Web near Bottom Flange of Link C345a	39
2-25	Strains in Outside Face of Flange for Link C345a	40
2-26	Strains on Inside Face of Flange for Link C345a	40

## LIST OF ILLUSTRATIONS (CONT'D)

FIGURE	TITLE	PAGE
2-27	Strains in Outside Face of Flange Fibers for Link C345b	41
2-28	Strains in Intermediate Stiffener of Link C345a	42
3-1	Built-up Shear Link H485 Details	46
3-2	Photograph of Installed Link H485	48
3-3	Instrumentation of Link H485	50
3-4	Initial Crack Locations in Link H485	51
3-5	Close-up View of Crack Initiation and Propagation	51
3-6	Deformed Link H485	52
3-7	Ultimate Failure of Link H485	52
3-8	Cyclic Behavior of Link H485	53
3-9	Plastic Cyclic Behavior of Link H485	54
3-10	Panel Shear Deformation Along the Length of Link H485	54
3-11	Shear Strain at Mid-length of Link H485	56
3-12	Shear Strain Next to Stiffener in Web Panel 00 of Link H485	56
3-13	Shear Strain at Mid-length of Link H485	57
3-14	Shear Strain in Web at End of Effective Length of Link H485	57
3-15	Shear Strain in Web at Mid-depth of Link H485	58
3-16	Strains in Outside Face of Flange for Link H485	59
3-17	Strains in Inside Face of Flange for Link H485	59
3-18	Strains in Intermediate Stiffener of Panel E2	60
3-19	Strains in End Stiffener of Panel E2	60
4-1	Details of Shear Links without Stiffeners	65
4-2	Web Compactness Comparison to Available Rolled Sections	66
4-3	Photograph of Shear Links without Stiffeners	68
4-4	Splice Plate Connection for Links L100 and L225	68
4-5	Near-Fault Deformation History Set	70
4-6	Typical Instrumentation of Link without Stiffeners	71
4-7	Location of Initial Cracks in Link L100	73
4-8	Flange Tearing Next to Web Weld in Link L100	73
4-9	Bolt Fracture in Connection Zone of Link L100	74
4-10	Fracture of Connection in Link L100	74
4-11	Cyclic Behavior of Link L100	75
4-12	Normalized Cyclic Plastic Behavior of Link L100	76
4-13	Location of Initial Cracks in Link L225	77
4-14	Web Out of Plane Web Deformation of Link L225	77
4-15	Ultimate Failure of Link L225	78
4-16	Cyclic Behavior of Link L225	79
4-17	Normalized Cyclic Plastic Behavior of Link L225	79
4-18	Location of Initial Crack in Link X100	80
4-19	Web Out of Plane Web Deformation in Link X100	80

## LIST OF ILLUSTRATIONS (CONT'D)

FIGURE	TITLE	PAGE
4-20	Ultimate Failure of Link X100	81
4-21	Cyclic Behavior of Link X100	82
4-22	Normalized Cyclic Plastic Behavior of Link X100	82
4-23	Flange Crack Next At Connection Zone Weld in Link L100	84
4-24	Flange Cracks in Link X100	84
4-25	Flange Crack at Location of Attachment Hook in Link L225	85
4-26	Flange Strains at Ends of Effective Length for Link L100	86
4-27	Flange Strains at Ends of Effective Length for Link L225	86
4-28	Flange Strains at Ends of Effective Length for Link X100	87
4-29	Typical Web Shear Strain at Mid-Length (Link L100 Shown)	87
4-30	Typical Web Shear Strain at End of Effective Length (Link L100 Shown)	88
4-31	Typical Web Shear Strain Along Link at Mid-Depth (Link L100 Shown)	88
4-32	Response of Link L100 to Near-Fault History Set 1	90
4-33	Response of Link L100 to Near-Fault History Set 2	90
4-34	Response of Link L225 to Near-Fault History Set 1	91
4-35	Response of Link L225 to Near-Fault History Set 2	92
4-36	Weld Crack in Link X100	93
4-37	Web Distortion in Link X100 at End of Second Set	93
4-38	Response of Link X100 to Near-Fault History Set 1	94
4-39	Response of Link X100 to Near-Fault History Set 2	94
4-40	Additional Cyclic Deformations for Link L225	96
4-41	Additional Cyclic Deformations for Link X100	96
4-42	Ultimate Failure of Link L225 After Additional Cyclic Deformations	97
4-43	Ultimate Failure of Link X100 After Additional Cyclic Deformations	97
5-1	Shear Force-Displacement Cyclic Response	101
5-2	Hysteretic Energy Dissipated per Cycle of Average Shear Deformation	102
5-3	Hysteretic Efficiency Factor	102
5-4	Cyclic Backbone Curve from IC History Response	104
5-5	Cyclic Backbone Curve Comparison for All Link Types	105
5-6	Cyclic Backbone Curve Comparison without Link L100 and X100	105
5-7	Overstrength Comparison from IC History	106
5-8	Normalized Overstrength Comparison from IC History	106
5-9	Initial Deformations of Link L100 Subjected to NF Deformation History	108
5-10	Initial Deformations of Link L225 Subjected to NF Deformation History	108
5-11	Monotonic and Cyclic Response Comparison for Link L100	109
5-12	Monotonic and Cyclic Response Comparison for Link L225	109
5-13	Envelope and Backbone Comparison for Link L100	110
5-14	Envelope and Backbone Comparison for Link L225	111
5-15	Shear Link Maximum Cyclic Deformation Capacity	112
5-16	CPSD at Failure from Incremental Deformation Tests	112
5-17	CPSD in Link L225 Under Different Deformation Histories	115

## LIST OF ILLUSTRATIONS (CONT'D)

FIGURE	TITLE	PAGE
5-18	CPSD in Link X100 Under Different Deformation Histories	115
6-1	Typical Model Layout Including Boundary Conditions	120
6-2	Details of Model Discretization	122
6-3	Global Response Comparison of Considered Models of Link C345a	123
6-4	Strain Comparison of Link C345a Models at $\gamma_{\text{eff}} = 0.10$ rad	124
6-5	Models of Shear Links with Stiffeners	125
6-6	Models of Shear Links without Stiffeners	126
6-7	Model and Experimental Response Comparison of Link C345a	128
6-8	Model and Experimental Response Comparison of Link C345b	128
6-9	Model and Experimental Response Comparison of Link H485	129
6-10	Model and Experimental Response Comparison of Link L225	129
6-11	Model and Experimental Response Comparison of Link L100	130
6-12	Model and Experimental Response Comparison of Link X100	130
6-13	Influence of Axial Force on Shear Resistance	132
6-14	Equilibrium of Shear Link With Axial Force	133
6-15	Plastic Shear Strain Distribution in Web of Links with Stiffeners	134
6-16	Plastic Shear Strain Distribution in Web of Links without Stiffeners	135
6-17	Maximum Principal Plastic Strains in Stiffeners	136
6-18	Plastic Shear Strain with Stiffeners Detached from Flanges	136
6-19	Maximum Principal Plastic Strains in Shear Link Flanges	138
7-1	General Layout of Shear Link Model	142
7-2	Influence of Flange Steel Yield Strength	144
7-3	Influence of Flange Thickness	144
7-4	Influence of Web Stiffening	146
7-5	Influence of Stiffener Bending	146
7-6	Influence of Stiffener Thickness ( $n_s = 3$ )	147
7-7	Influence of Effective Length	147
7-8	Flange Plastic Zone at End of Effective Length	150
7-9	Illustration of Flange Contribution to Link Shear Resistance	151
7-10	Illustration of Stiffener Contribution to Link Shear Resistance	152
7-11	Comparison of Shear Formula to Numerical Analyses Results	153
7-12	Comparison of Equation and FEM analyses at $\gamma_{\text{eff}} = 0.08$ rad	155
7-13	Comparison of Equation and Experimental Results at $\gamma_{\text{eff}} = 0.08$ rad	158
7-14	Comparison of Equation and Experimental Results at $\gamma_{\text{max}}$	158

## LIST OF TABLES

<b>TABLE</b>	<b>TITLE</b>	<b>PAGE</b>
1-1	Summary of Previous Tests on Built-up Shear Links for Bridges	13
2-1	Nominal Design Properties of Built-up Shear Link from Conventional Grade Steel	19
2-2	Capacity of Built-up Steel Shear Link from Conventional Grade Steel	21
2-3	Incremental Cyclic Deformation Protocol	24
2-4	Instrumentation Description	28
2-5	Shear Links C345a and C345b Performance Summary	36
3-1	Nominal Design Properties of Built-up Shear Link from HPS	47
3-2	Capacity of Built-up Steel Shear Link from HPS	47
3-3	Shear Link H485 Performance Summary	55
4-1	Nominal Design Properties of Built-up Shear Links Designed Without Stiffeners	66
4-2	Capacity of Built-up Steel Shear Links Designed Without Stiffeners	67
4-3	Nominal Design Properties of Built-up Shear Links without Stiffeners	72
4-4	Cyclic Performance Summary of Shear Links without Stiffeners	83
4-5	Performance Summary of Shear Links without Stiffeners under Near-fault History	95
5-1	Summary of Tested Built-up Shear Links	100
5-2	Summary of Maximum Overstrengths	107
5-3	Summary of Deformation Characteristics from Built-up Shear Link Experiments	114
6-1	Stress-Strain Power Function Coefficients (Dusicka et al 2004)	121
7-1	Summary of Base Model and Considered Variations	143
7-2	Cyclic Stress Factors at Specific Shear Deformation Levels for Tested Shear Links	154
7-3	Plastic Shear Strength of Tested Built-up Shear Links	156
7-4	Comparison of Plastic Shear Resistance to Finite Element Analyses Results	156
7-5	Comparison of Plastic Shear Resistance to Experimental Results	157
7-6	Comparison of Maximum Shear Resistance to Built-up Shear Links Tested by Others	159
8-1	Steel Grades	164



# SECTION 1

## SHEAR LINK HYSTERETIC DEVICES FOR HIGHWAY BRIDGES

### 1.1 Shear Links in Seismic Design

Earthquakes can be devastating to a society's infrastructure by inducing significant damage in structures that may cause collapse and loss of life. The ability of a structure to deform inelastically without significant loss of strength generally improves the seismic response by limiting forces in the structural members, lengthening the effective period and providing hysteretic energy dissipation. Structural components can yield under axial force, shear force, moment or torsional demands and can be designed to do so at predetermined locations in the structure. The concept of designing specific members of a structure to yield while preserving the integrity of other components is a common approach in capacity design.

The use of shear plastic deformations in steel beams is one example which has been adopted primarily for special cases of braced frame buildings referred to as eccentrically braced frames. The beam sections in which shear dominates the inelastic response are called shear links and are the subject of this research. In effect, shear links are response modification devices that dissipate energy through hysteretic action of steel yielding and deformation under plastic strains. The hysteretic attributes, such as deformation capacity, shear strength and failure mode, are therefore primary characteristics of the device. Examples of applying shear links for bridges are illustrated later in this section.

#### 1.1.1 Background to Eccentrically Braced Frames

Buildings with eccentrically braced frame (EBF) lateral load resisting systems have become popular in regions of high seismicity because they combine high lateral stiffness with excellent ductility. In EBFs, braces connect to beams at short distance offsets from a column-to-beam or from another brace-to-beam connection as illustrated in a typical layout in Figure 1-1. The beams are typically located at building floor levels.

EBF development and associated research was primarily conducted during the 1980s (Roeder & Popov 1978, Hjelmstad & Popov 1983, Popov & Malley 1983, Kasai & Popov 1986, Ricles & Popov 1987, Englehardt & Popov 1989). Experimental research involved tests of rolled steel shapes ranging in depths from 305 mm (12 in) to 457 mm (18 in) and fabricated from A36 250 MPa (36 ksi) nominal yield steel. The links were primarily divided into short shear links where shear deformations dominate the behavior, long links where moment deformations dominate the inelastic behavior and intermediate links for regions in between. Analytical studies were conducted on local link behavior as well as global EBF models. The results of this research form the basis of the design guidelines for shear links.

The ductility of the EBF system depends on the plastic deformation capacity of the eccentric length of a beam called a link. The plastic deformations are caused by the shear forces and bending moments induced by the connection eccentricity. The link shear  $V$  and the moment  $M$  at the ends of the effective length  $e$  can be related through equilibrium when assuming equal end moments as expressed in Equation 1-1.

$$2M = Ve \tag{1-1}$$

This expression allows structural elements such as columns, braces and beams outside of the effective length to be designed to remain elastic and thereby confine yield to the link alone.

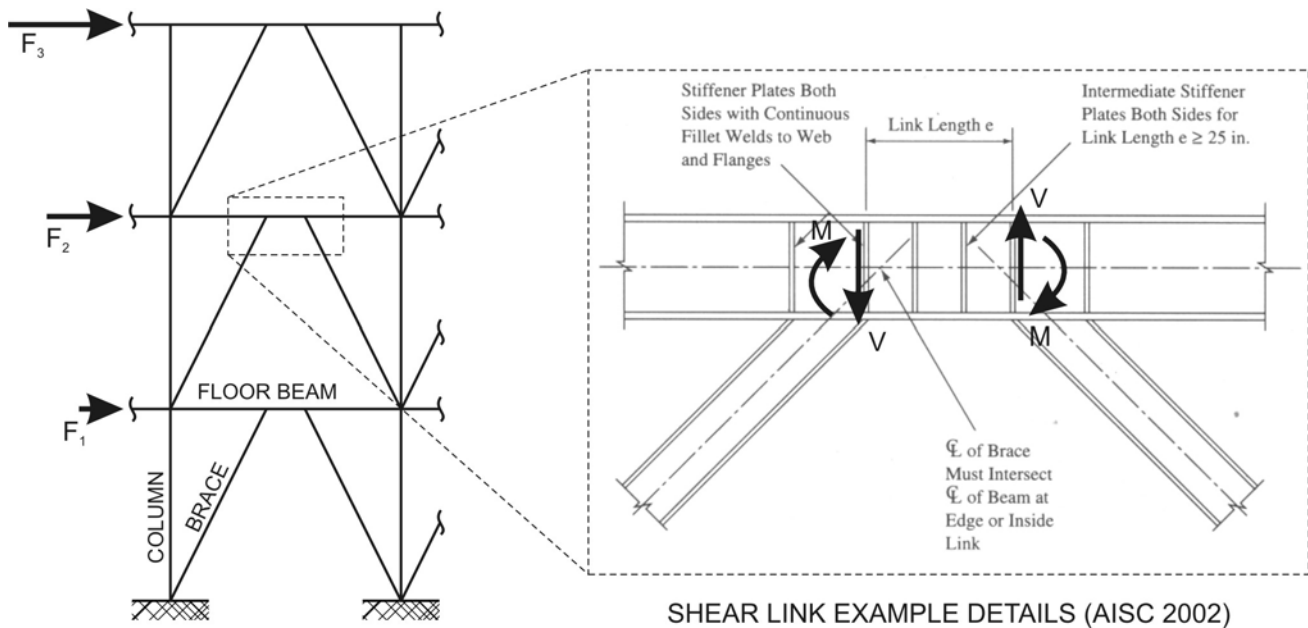


**Figure 1-1: Typical Layout of Shear Link in Eccentrically Braced Frame**

### 1.1.2 Review of EBF Shear Link Design Provisions

The results of the above research formed the basis of design provisions published as part of the Seismic Provisions for Structural Steel Buildings by the American Institute for Steel Construction (AISC 2002). These provisions provide general guidelines for the designs of eccentrically braced frames and detailing of the shear links. The specifications include equations for nominal strength of the link, effective link length, spacing of stiffeners and the required strength of components outside of the link.

#### 1.1.2.1 Nominal Strength and Effective Length of Shear Links

Nominal design shear strength  $V_p$  is based on the plastic shear strength of the web according to Equation 1-2, where  $f_y$  is the nominal yield strength,  $d$  is the depth of the section,  $t_f$  and  $t_w$  are the flange and web thicknesses respectively. The shear strength is based on von Mises yield criteria for shear, where the shear yield stress  $\tau_y$  is approximated as  $\tau_y = f_y / (\sqrt{3}) \approx 0.6f_y$  (Maley & Popov 1983).

$$V_p = 0.6f_y t_w (d - 2t_f) \quad (1-2)$$

The plastic moment strength  $M_p$  is calculated assuming full section plasticity according to Equation 1-3, where  $Z$  is the plastic section modulus.

$$M_p = f_y \cdot Z \quad (1-3)$$

The eccentric link length is an important characteristic relative to the plastic moment and the plastic shear capacity as it determines if the shear force, flexural moment or their combination dominate the inelastic response. Based on equilibrium (Equation 1-1), a balanced condition exists when the link length equals to  $2M_p/V_p$ . The AISC Seismic Provisions restrict link length to ensure shear dominated behavior by maintaining end moments  $M < 0.8M_p$ . Hence, the effective length of shear links must satisfy Equation 1-4.

$$e \leq 1.6 \frac{M_p}{V_p} \quad (1-4)$$

The response of links with lengths greater than  $2.6M_p/V_p$ , were determined to be dominated by inelastic flexure deformations and lengths between  $1.6M_p/V_p$  and  $2.6M_p/V_p$  by a combination of shear and flexural deformations (Engelhardt & Popov 1989).

### 1.1.2.2 Shear Deformation Limit and Stiffener Spacing

The provisions limit the maximum expected demand on the shear link based on the intermediate web stiffeners spacing. The use of stiffeners was found to influence the shear deformation capacity, with improved hysteretic performance caused by the delaying of web buckling. The stiffener spacing  $a$  is expressed using Equation 1-5 and Equation 1-6 for two maximum demand levels, which are measured by the plastic shear deformation  $\gamma_p$  illustrated in Figure 1-2.

$$a \leq (52t_w - d/5) \text{ for } \gamma_p \leq 0.02 \text{ rad} \quad (1-5)$$

$$a \leq (30t_w - d/5) \text{ for } \gamma_p \geq 0.08 \text{ rad} \quad (1-6)$$

Linear interpolation can be used for the expected demands between the two values. The implied minimum rotation that should be achieved by a shear link satisfying Equation 1-6 is  $\gamma_p = 0.08 \text{ rad}$ .

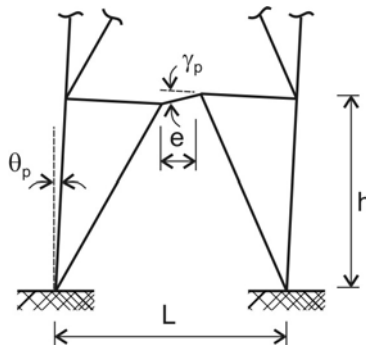


**Figure 1-2: Global Geometry and Shear Link Deformation in EBF**

### 1.1.2.3 Strength of Components Outside the Link

The AISC Seismic Provisions stipulate the design strength of components outside of the link to exceed the forces generated by the nominal shear strength of the link, multiplied by  $R_y$  and further increased by 25% to account for strain hardening. The  $R_y$  factor accounts for the variability in the material yield strength, which ranges from 1.1 to 1.5 depending on the steel grade.

### 1.1.3 Global Geometry and Shear Link Demands

At the early design stage, significant leeway exists regarding global geometry of the system being designed. The global geometry can have significant impact on the demands imposed on a shear link and variations in global geometric parameters can be used to optimize the design. Considering the EBF rigid-plastic mechanisms shown in Figure 1-2, the link rotation angle  $\gamma_p$  can be shown to be directly proportional to the bay width  $L$  and plastic inter-storey drift  $\theta_p$ , but inversely proportional to the link effective length  $e$  as shown in Equation 1-7 (AISC 2002). By altering the relative dimensions of the link effective length and bay width, a reduced link rotation angle can be achieved.

$$\gamma_p = \frac{L}{e} \cdot \theta_p \quad (1-7)$$

At the same time high stiffness is often desired from the serviceability point of view, which requires shorter link lengths. The shorter the link, the greater the plastic demand on the link at a constant value of inter-storey drift and bay length. Using Equation 1-7, the global geometry of the structural system can therefore be adjusted to optimize the system stiffness and plastic demands on the link based on the specific requirements of each application.

### 1.1.4 Need for Built-up Shear Links

The focus of previous research was on the use of rolled wide flange beams for shear links in eccentrically braced frame buildings. However, rolled sections are not suitable for applications where large strengths are required, such as in major long span bridges. Additional design freedom of geometry and material selection can be realized through the use of steel plates to assemble the link section.

The use of built-up shear links allows for the optimization of stiffness and strength through greater choice of plate size and link geometry. Deep rolled wide flange sections typically have web thicknesses that result in undesirably high shear strengths as compared to their moment capacities. The maximum design length in Equation 1-4 can be normalized to the section depth  $d$  in order to obtain a relative sense for different link sizes. Based on this relation, Figure 1-3 summarizes the maximum possible effective lengths of all available wide flange shapes obtained from the Manual of Steel Construction (AISC 2001). As shown, some sections do not meet the limiting compactness ratios when considering 345 MPa (50 ksi) nominal yield strengths according to Equation 1-8 and Equation 1-9 for the flange and web respectively, where  $E$  is the elastic modulus,  $b$  is the flange width and  $h$  is the web height. For shear links deeper than 400 mm (16 in), the options greatly decrease, eventually leading to maximum effective lengths that are well below 3 times the link depth for sections deeper than 600 mm (24 in).

$$\frac{b}{2t_f} \leq 0.3 \sqrt{E/f_y} \text{ for the flanges} \quad (1-8)$$

$$\frac{h_w}{t_w} \leq 3.14 \sqrt{E/f_y} \text{ for the web} \quad (1-9)$$

The use of built-up sections removes the predetermined geometry design limits associated with rolled sections and also permits the use of alternative steels in an effort to improve the performance. Typically, new product lines are initially only produced as plates, meaning that the inclusion of such materials in shear link design must be through the use of built-up sections.

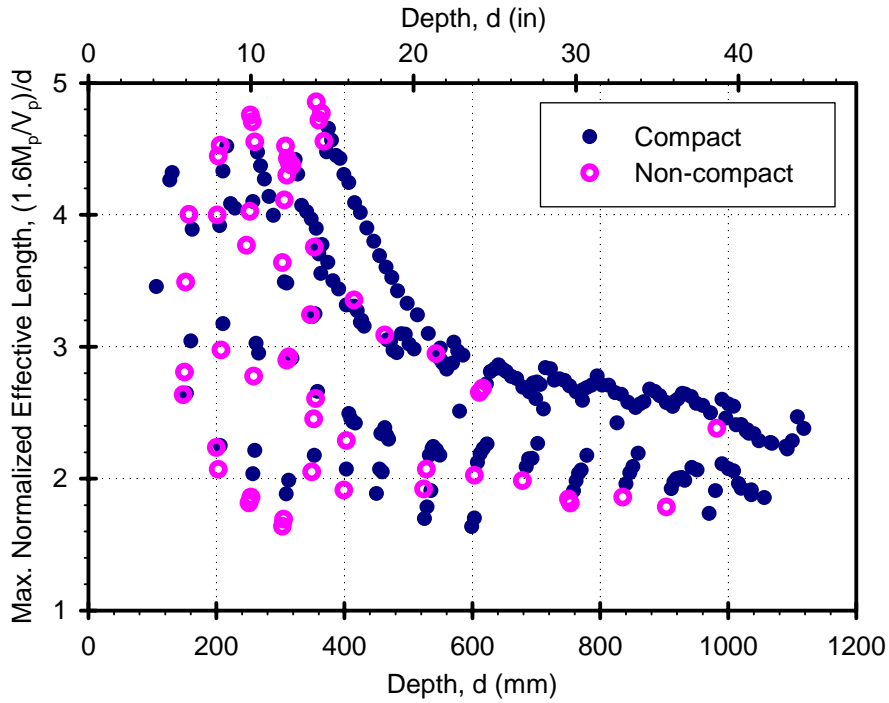


**Figure 1-3: Shear Link Effective Length Options for Rolled Wide Flanges**

### 1.1.5 Design Strength of Built-up Shapes

Built-up shear link actual design strength can be determined using the shear link design equations along with the actual yield strength  $f_{ya}$  obtained from tests on coupons from the same plate as that used to fabricate the link. For built-up shear links, the measured web yield strength  $f_{yaw}$  and flange yield strength  $f_{yaf}$  can vary. The ratio of the measured yield strength to the nominal accounts for the yield strength variability and can be compared to the  $R_y$  value in the design provisions. The actual shear strength  $V_{pa}$  can therefore be calculated from Equation 1-2 as follows.

$$V_{pa} = 0.6f_{yaw}t_w(d - 2t_f) \quad (1-10)$$

The plastic moment strength of built-up shapes needs to incorporate the potential variability in material between the flange and web. The plastic section modulus is therefore insufficient. Based on a symmetric wide flange built-up section, the actual moment capacity  $M_{pa}$  can be expressed as in Equation 1-11.

$$M_{pa} = f_{yaf}[bt_f(d - t_f)] + f_{yaw}\left[t_w\left(\frac{d - 2t_f}{2}\right)^2\right] \quad (1-11)$$

Shear link deformation is expected to be dominated by shear. In order to obtain a sense of the relative shear and moment capacities, a non-dimensional ratio can be introduced based on the equilibrium relationship in Equation 1-1 and the above capacities. The link capacity ratio defined in Equation 1-12 is unity when the plastic shear and moment capacities are simultaneously reached. Ratios greater than 1.0, indicate a shear link section that will first yield in shear.

$$\text{link capacity ratio} = \frac{2M_{pa}}{eV_{pa}} \quad (1-12)$$

For example, the AISC provisions length restriction of Equation 1-4 for shear links results in link capacity ratio of 1.25.

## 1.2 Desirable Shear Link Performance Characteristics

Possible failure modes of shear links include the plastic buckling of the web, fracture of the web, fracture of the tension flange, cracking of the compression flange caused by low cycle fatigue and connection failure. The underlying philosophy of the shear link design is to delay the aforementioned failure modes until the required performance criterion is achieved. The performance is mainly defined by the deformation capacity, but other important considerations must be made.

### 1.2.1 Deformation Capacity

The shear link must be capable of sustaining the deformation demands imposed during an earthquake without reaching failure. For ductile capacity design, it is the plastic deformations that define the deformation capacity. The plastic rotation angle of Figure 1-2 can be obtained from the total link rotation  $\gamma_{eff}$ , by subtracting the elastic contribution using Equation 1-13 where  $V$  is the shear and  $k_{ve}$  is the stiffness obtained from the elastic shear rotation response. The AISC Seismic Provisions imply a minimum plastic deformation capacity of a shear link by restricting the demand to below  $\gamma_p = 0.08 \text{ rad}$  at the design storey drift. The implication is that any link that is designed according to the provisions can endure at least  $0.08 \text{ rad}$  of plastic rotation.

$$\gamma_p = \gamma_{eff} - \frac{V}{k_{ve}} \quad (1-13)$$

As explained in Section 1.1.3, link deformation demand can vary for the same drift values based on the global geometry. If it can be shown that links can endure significantly higher levels of deformation, stiffer frames can be designed with improved ductility. The higher the link deformation capacity the better the performance characteristics.

## 1.2.2 Overstrength

The maximum shear strength  $V_{max}$  that develops in the link can be different to the plastic shear capacity. The ratio of the maximum shear strength to the plastic shear capacity is referred to as overstrength and encompasses all factors that can contribute to the increased resistance, including material strain hardening and composite floor action in building frames. Two plastic shear capacities were defined as the nominal (Equation 1-2) and the actual (Equation 1-10), resulting in two definitions of overstrength expressed in Equation 1-14 and Equation 1-15.

$$\Omega_s = \frac{V_{max}}{V_p} \quad (1-14)$$

$$\Omega = \frac{V_{max}}{V_{pa}} \quad (1-15)$$

The relationship between the two overstrength ratios is based on the variability in the steel yield strength between the nominal and the measured and can be expressed as  $\Omega = f_{y\alpha}/f_y \Omega_s$ . For cases where the measured yield strength is not known,  $R_y$  factor can be used in place of  $f_{y\alpha}/f_y$  ratio.

The design of components outside of the link must account for the maximum force that can be developed in the shear link, placing significant importance on quantifying the overstrength. As explained in the AISC Seismic Provision's (2002) commentary, the chosen increase of 25% in shear link capacity is only slightly below the measured overstrength from links constructed from A922 rolled shapes (Arce 2002). The AISC Seismic Provisions encourage conservative designs because tests on links from A36 steel were shown to have hardening of approximately 1.5. Earlier versions of the AISC Seismic Provisions (1997) commentary explained that when the 25% increase is combined with design resistance factor  $\phi$ , which can be 0.5 or 0.9 for axial compression or flexure design respectively, the overstrength being designed for corresponds to the observed overstrength of 1.5 as  $1.25/\phi \approx 1.5$ . It was noted that results of large strain hardening were recorded from tests on shear links with proportions that are significantly different than rolled sections. These tests are discussed in greater detail in Section 1.4.

Underestimating the overstrength developed in a shear link can lead to deficient designs and undesirable failure modes. The link itself is also affected by the overstrength since statics dictate that the increased shear leads to proportionately larger end moments in the link. High values of overstrength can be designed for as long as they can be quantified. However, little is known about the cause and variability of overstrength, especially in built-up sections.

## 1.2.3 Failure Mode

Desirable failure limit state of a shear link is plastic deformation that is contained to within the effective length in the webs that deform without buckling. Web buckling was found to gradually degrade the cyclic hysteretic behavior and is acceptable if the degradation can be delayed until the performance criteria of the shear links are met. From past research on shear links from rolled sections, failures of the flange or connections can result in sudden decrease in resistance and should be avoided.

### 1.3 Observed Earthquake Performance of EBFs

A number of cyclic experiments have been conducted to investigate shear link performance (Popov et al) and a simulated earthquake excitation of EBF building has also been performed in the laboratory (Foutch 1989). However, observations of EBF performance after major earthquakes is scarce. As a relatively new structural system, EBFs do not had the history of other systems such as wood frame, masonry walls, concrete and ordinary steel frames and shear walls. Structural steel construction is common in more developed countries limiting the observations to only a few significant seismic events within the last couple decades.

During the Loma Prieta earthquake of 1989, building damage was mainly in structures with known vulnerabilities and damage to the transportation system was significantly more notable (Astaneh-Asl et al 1989). The Northridge earthquake in 1994 illustrated a particular vulnerability in steel moment framed structures, but no observations of damage to EBFs have been reported (Bertero et al 1994). Similarly, the city of Kobe experienced widespread damage throughout the region after the Hanshin-Awaji earthquake of 1995, but no evidence of damage to EBFs has been found (Bertero et al 1995).

The only documented example of EBF field performance was after the Nisqually earthquake in Washington State in February 2001 (Filiatrault et al 2001). The Starbucks Headquarters Building had been retrofitted with EBFs in both principal directions in 1995. Comprising of masonry walls and flat floor slab, the building escaped major damage. The performance was mainly attributed to the EBFs that were observed to have significant yielding in the shear links as shown by the peeling paint on the sixth floor in Figure 1-4. The EBF retrofit performed well and successfully protected the building from brittle failure.

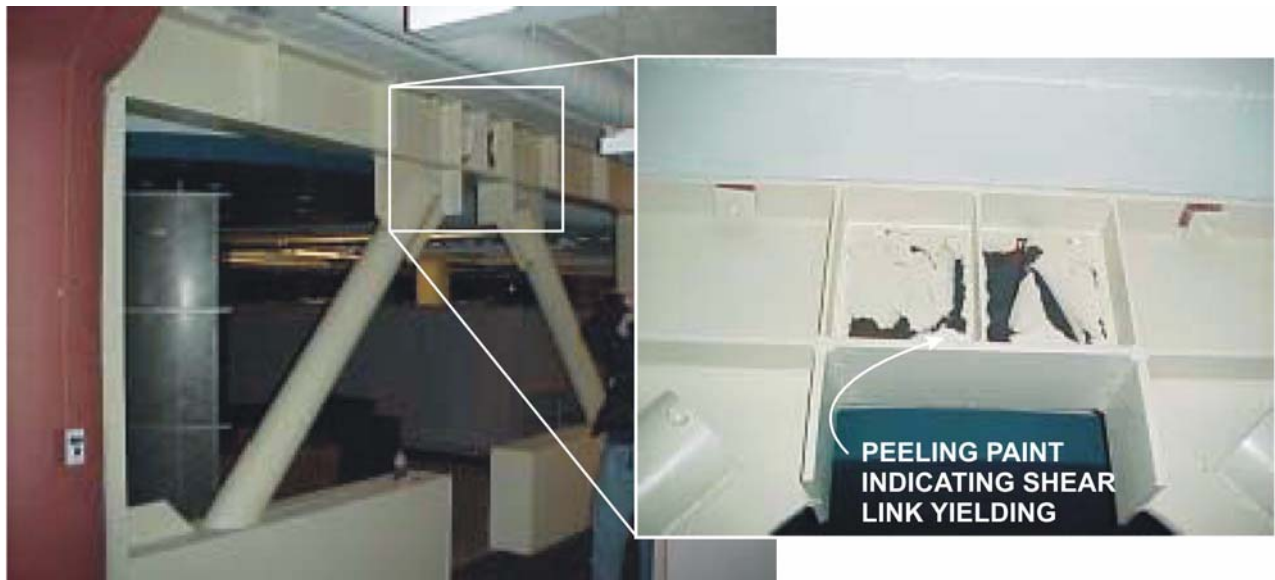


**Figure 1-4: Retrofitted Building After Nisqually Earthquake (Filiatrault et al 2001)**

### 1.4 Applications of Built-up Shear Links to Bridges

Built-up shear links become especially attractive in the design and retrofit of bridges where the large capacity requirements exclude the use of rolled shapes. Two such examples of bridges located in high seismic areas are the retrofit of the Richmond-San Rafael Bridge and the tower of the new replacement span of

the San Francisco-Oakland Bay Bridge (SFOBB). Both of these bridge projects involved large-scale proof testing to verify the design. These tests provided some of the only experimental data for large-capacity built-up shear links.

#### 1.4.1 Richmond San Rafael Bridge EBF Retrofit

The eccentrically braced frame approach was applied as part of the retrofit by Gerwick/Sverdrup/DMJM Joint Venture for the Richmond-San Rafael Bridge (RSRB) near San Francisco, California (Vincent 1996). The EBF retrofit involved the complete replacement of the laced chevron braces of the support towers with dual eccentrically braced frames. These are as shown under construction in August 2003 in Figure 1-5. The gravity load carrying columns were strengthened, but otherwise left in place.

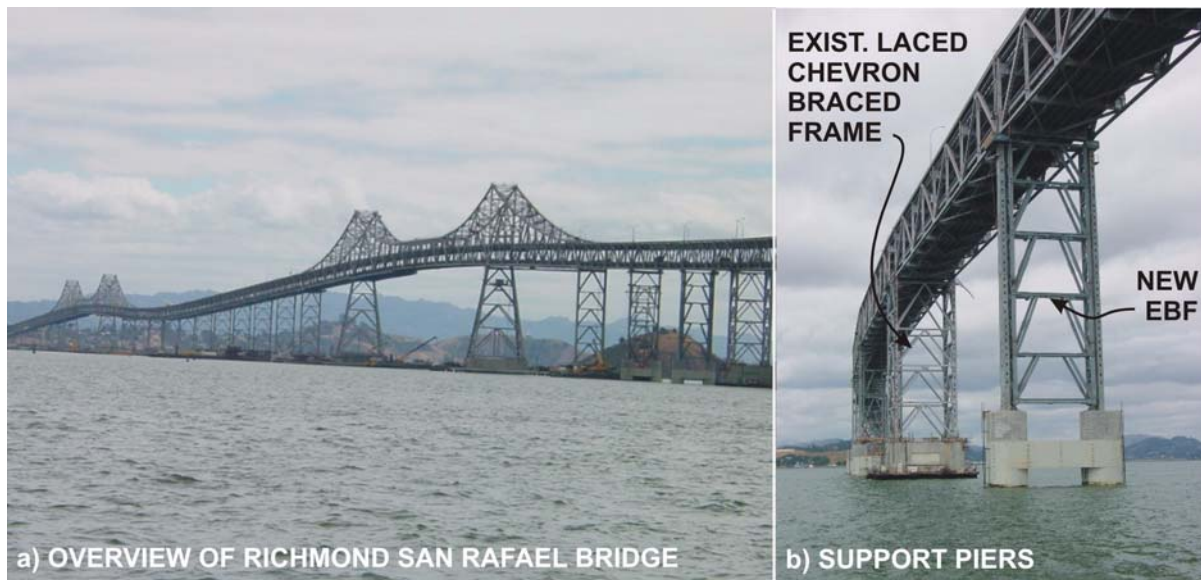


**Figure 1-5: Richmond San Rafael Bridge Retrofit Under Construction**

The cyclic behavior of the built-up shear links was investigated using full-scale EBF specimens at the University of Nevada, Reno (Itani 1997). The test setup used symmetry and boundary conditions such that only one half of the EBF was tested as illustrated in Figure 1-6(a). The effective length of a typical shear link was  $3660\text{ mm}$  ( $12\text{ ft}$ ) and section depths ranged from  $410\text{ mm}$  ( $16\text{ in}$ ) to  $760\text{ mm}$  ( $30\text{ in}$ ). The length to depth proportions are unusually high for shear links so thin web plates were used to ensure that shear dominated the inelastic behavior.

Two test specimens, designated BU30 and BU16 for the deepest and the shallowest EBF beam section, were cyclically tested. The characteristics and achieved capacities are summarized in Table 1-1. The maximum achieved deformation  $(\gamma_p)_{max}$  found to exceed the expected demands on the bridge, but cracking of the flange was observed in the experiments and was found to cause brittle failure in the deeper link as shown in Figure 1-6(b). The overstrength was significantly higher than the AISC Provisions stipulate.

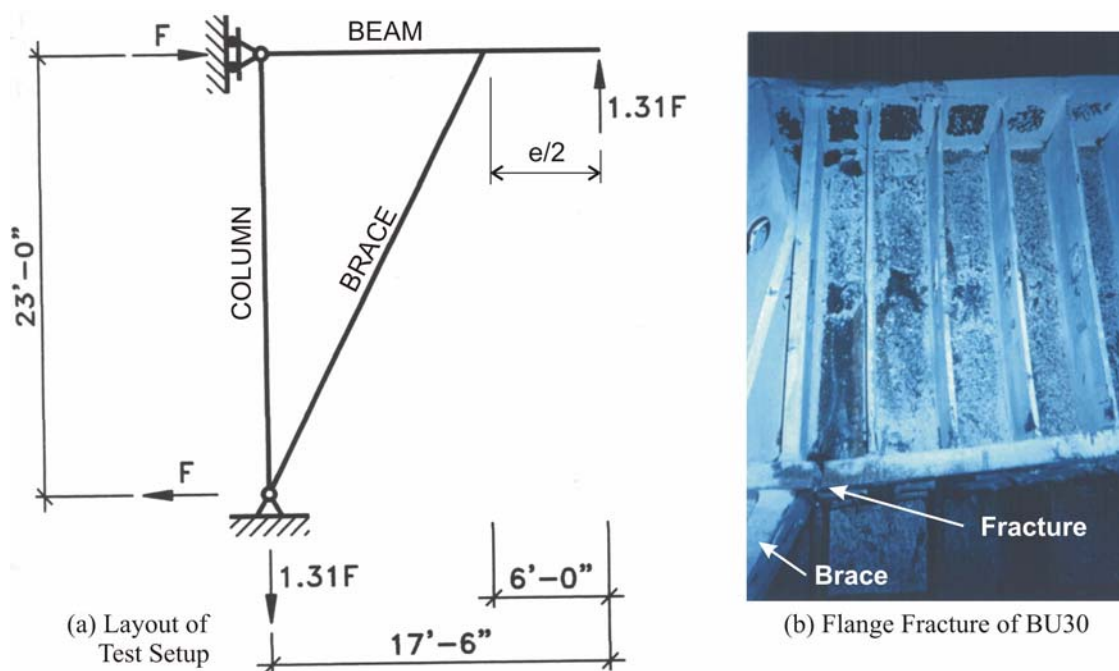


**Figure 1-6: EBF Proof Test of Richmond San Rafael EBF Retrofit (Itani 1997)**

### 1.4.2 Shear Links in New SFOBB Bridge Tower

The new replacement span of the San Francisco-Oakland Bay Bridge was designed by the joint venture of T.Y. Lin International and Moffatt & Nichol Engineers to include a self-anchored, single tower suspension span, scheduled for completion in 2010 (Nader et al 2004 and 2002, Tang et al 2000). The main tower consists of four pentagonal steel shafts that are tied together by shear links in the longitudinal as well as the transverse directions. A total of 120 shear links are distributed at various heights. A computer generated rendering of the bridge and a typical tower cross-section at one of the levels is shown in Figure 1-7. The shear links are designed to yield under large lateral demands and limit the forces transferred to the gravity load carrying shafts. Two shear links connect the adjacent shafts in the longitudinal direction at each level and two links join the adjacent shafts in the transverse direction at each level. Detailed description of the link-to-tower assembly is described in Appendix A. The shear links are stiffened steel beams built-up from plates and are bolted to the shafts to facilitate post-earthquake replacement. The width of the shafts and the distance between the shafts eliminate the need for braces in engaging the shear links.

Full-scale proof tests of two types of shear links were conducted at the University of California, San Diego (McDaniel 2002). The links (Type 1 and Type 3) corresponded to typical links used for the transverse and longitudinal direction of the bridge. Each link was mounted between two columns shown in Figure 1-8 and cyclically loaded by increasing the top tower displacement. The details of the link characteristics and performance values are summarized in Table 1-1. The deformation capacity exceeded the expected design demand on the bridge, but underachieved the implied minimum of the AISC Seismic Provisions of  $0.08 \text{ rad}$  for both cases. A brittle failure mode was initiated in the web next to the stiffener and web welds. The overstrength was significantly higher than the AISC Provisions stipulate, but of similar levels as those

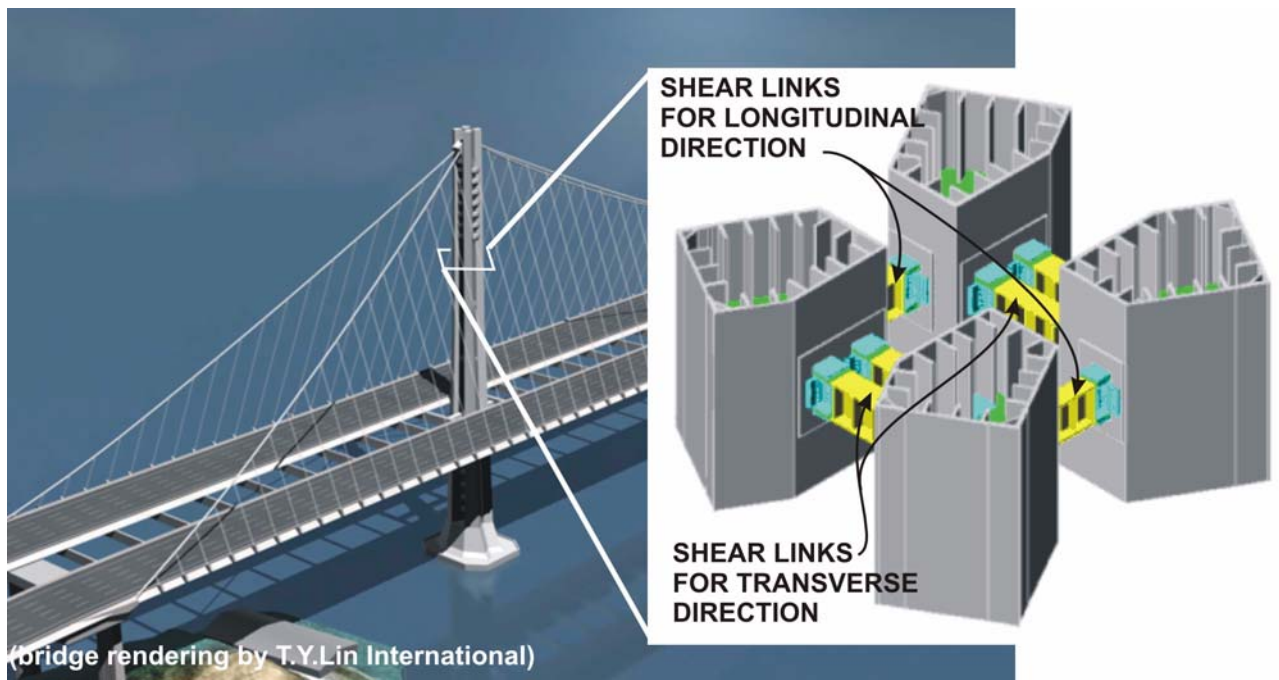


**Figure 1-7: Rendering of the New SFOBB Suspension Signature Span**

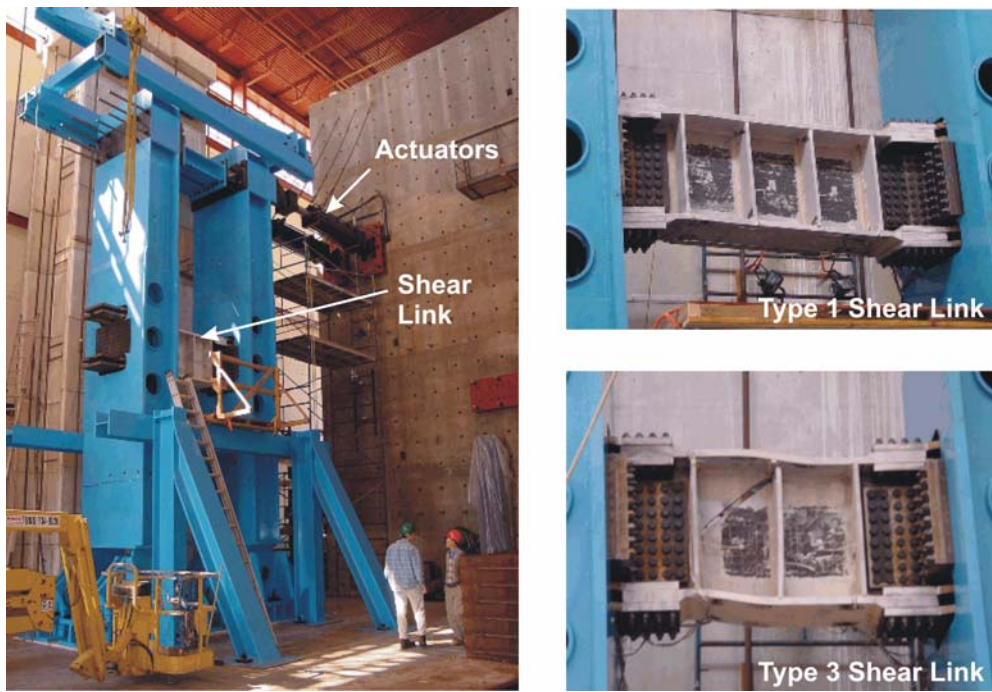


**Figure 1-8: Full-scale Proof Test for SFOBB Shear Links at UCSD**

recorded during the Richmond-San Rafael shear link tests (McDaniel 2002, Itani 1997). The overstrength based on Equation 1-15 is included in Table 1-1.

A similar concept of shear links had also been proposed for the cable stay alternative for the same crossing, also designed by T.Y. Lin International (Goodyear & Sun 2003) and illustrated in Figure 1-9. The tower itself was proposed as two hollow concrete semi-circular shafts connected by shear link fuses in the transverse direction only. The principal difference in the design of the shear links as compared to the suspension cable links was the use of a box cross section instead of a I-shaped girder and the utilization of the shear links in the transverse direction only. The cable stay design was not selected for construction and was these particular links were not designed in detail or proof-tested (Vincent 1996).

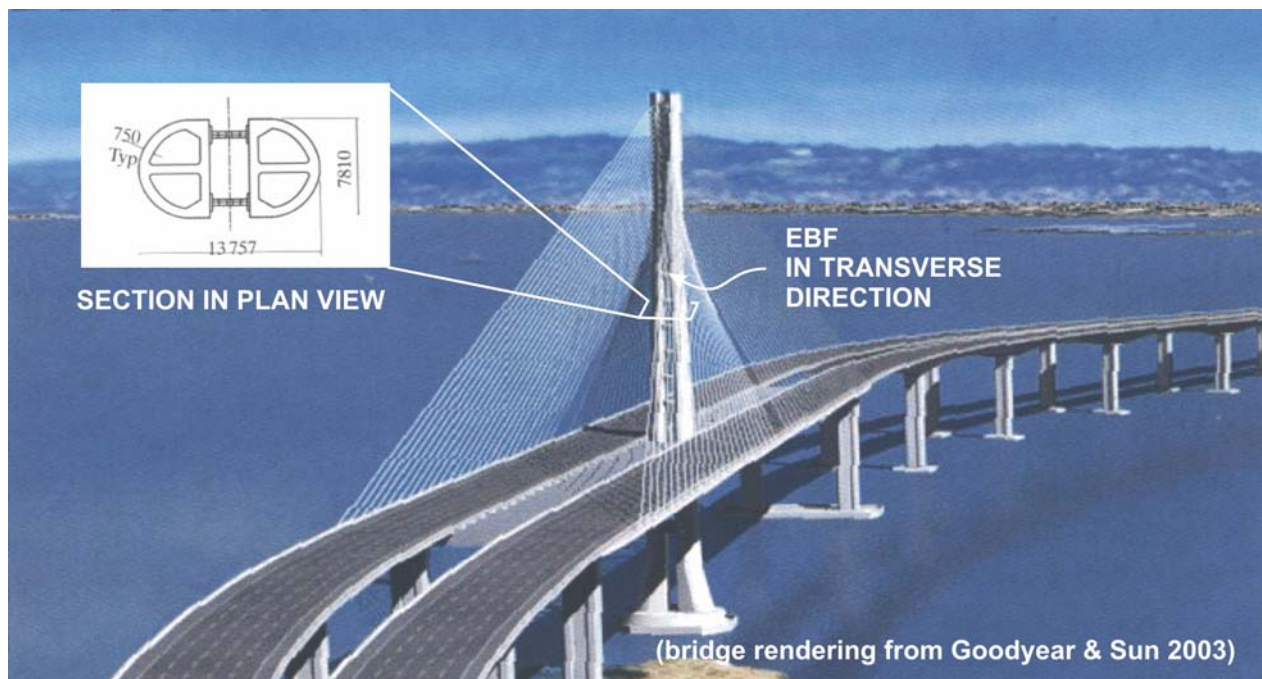


**Figure 1-9: Rendering of the SFOBB Signature Span Cable Stay Alternative**

## 1.5 Potential Uses of Shear Links in Bridges

In addition to the systems discussed in the previous section, a number of other applications of built-up shear links can be realized to enhance the seismic performance of different types of bridges in high seismic areas. Some of these are generalizations of the aforementioned systems, while others are extensions of previously proposed concepts and suggestions for new potential uses.

**Table 1-1: Summary of Previous Tests on Built-up Shear Links for Bridges**

Parameter	Link Type			
	Richmond-San Rafael Bridge (Itani 1997)		San Francisco-Oakland Bay Bridge (McDaniel 2002)	
	BU30	BU16	Type 1	Type 3
$e, mm (in)$	3658 (144)	3658 (144)	1680 (66)	1000 (39)
$d, mm (in)$	762 (30)	406 (16)	950 (37)	950 (37)
$b_f, mm (in)$	356 (14)	356 (14)	600 (26.6)	475 (18.7)
$t_f, mm (in)$	38 (1.5)	38 (1.5)	45 (1.8)	45 (1.8)
$t_w, mm (in)$	10 (0.4)	10 (0.4)	28 (1.1)	28 (1.1)
Steel Grade	A572 345 MPa (50 ksi)		A709 345 MPa (50 ksi)	
Maximum Achieved Shear Deformation $(\gamma_p)_{max}, rad$	0.080	0.097	0.060	0.066
Maximum Measured Shear $V_{max}, kN (kip)$	2780 (625)	1446 (325)	9363 (2105)	9919 (2230)
Measured Overstrength $\Omega = V_{max}/V_{pa}$	1.89	1.93	1.84	1.94

### 1.5.1 Shear Links in Bridge Support Structures

The extension of the EBF concept can be made for any bridge support structure for which braced frames would normally be considered. These can include simple bridge bents with a single EBF or tall piers containing multiple levels of EBFs, such as the Richmond-San Rafael Bridge piers. The main difficulty in implementing the EBF concept for the latter case relates to the lateral stability of the steel frames.

Compression can occur in both the top as well as the bottom flange of the shear link and lateral bracing is therefore required at the ends of each link effective length to prevent lateral torsional buckling. Floor slabs or transfer beams of buildings can provide sufficient lateral support, but bridges typically lack those secondary structural systems and alternate framing must therefore be implemented. In the case of the Richmond-San Rafael Bridge, dual EBFs that laterally brace each other were built (Vincent 1996). Illustrations are shown in Figure 1-10 for two leg as well as four leg pier arrangements.

As shown by the new SFOBB designs for both the suspension as well as the cable stay alternatives, shear links can be effective fuses in tall slender support towers. For SFOBB, the close spacing of the towers eliminated the need for the eccentric bracing and the torsional rigidity of the towers eliminated the need for lateral bracing. These design schemes also allow for post-earthquake replacement of the links via bolted connections between the shear links and the towers.

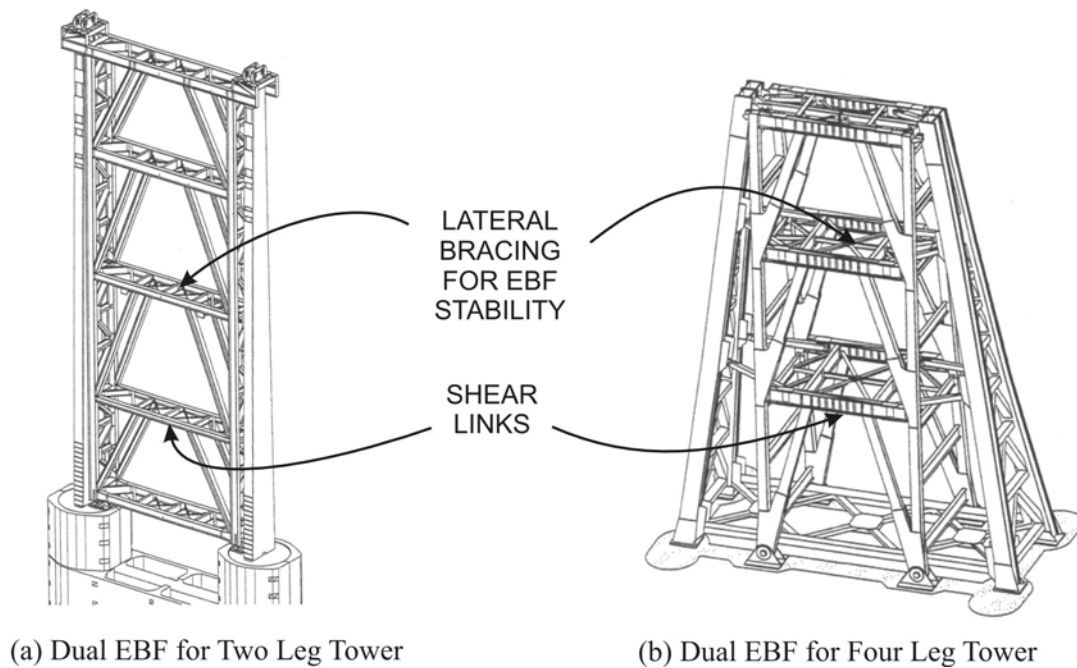


**Figure 1-10: Example of Lateral Bracing for EBFs (Vincent 1996)**

### 1.5.2 Shear Links as Hysteretic Dissipators in Pier Rocking

Back-and-forth rocking of bridge piers was implemented in the design of the South Rangitikei rail bridge in New Zealand in the 1970's as a form of base isolation to reduce the seismic demands by increasing the period of the bridge. A number of retrofit schemes of long span bridges have also involved pier rocking, which reduces the overall cost of the strengthening. For example, the retrofit of the partially collapsed pier E9 of the SFOBB truss spans involved the ability of the pier to rock in the longitudinal direction on top of the concrete footing (Astaneh-Asl & Shen 1993). Similarly, rocking of the main towers of Golden Gate Bridge near San Francisco, California, as well as the approaches to Lions Gate bridge in Vancouver, British Columbia, have shown to improve the global seismic performance (Seim & Rodriguez 1993, Dowdell & Hamersley 2001).

Gravity is relied upon to produce the restoring force, but energy dissipation is often needed to limit the displacement demand and dampen the rocking response. Hysteretic devices such as torsion yielding of mild steel rods and triangular flexural yielding devices have been incorporated at the anchorage of the South Rangitikei and Lions Gate Bridges respectively. More recently, adding unbonded braces has been proposed (Pollino & Bruneau 2004). Shear links could also be candidates given their potential for high capacity and ductile hysteretic behavior.

Shear links can be incorporated at the anchorage of piers as shown in Figure 1-11(b), but special attention is required to resist the link end moments at the piers as well as the foundation. The end moments can be self-reacted at the pier by providing dual facing links. The dual links would provide restraint without inducing moments into the piers. A pin connection can be used at the foundations to completely eliminate moment reactions. In this arrangement, the equilibrium changes the effective length for design by half.

Built-up shear links can be utilized to provide section geometries with sufficient length and resistance to counteract the shortening of the effective length caused by the pin connection and yet continue to plastically deform in shear.

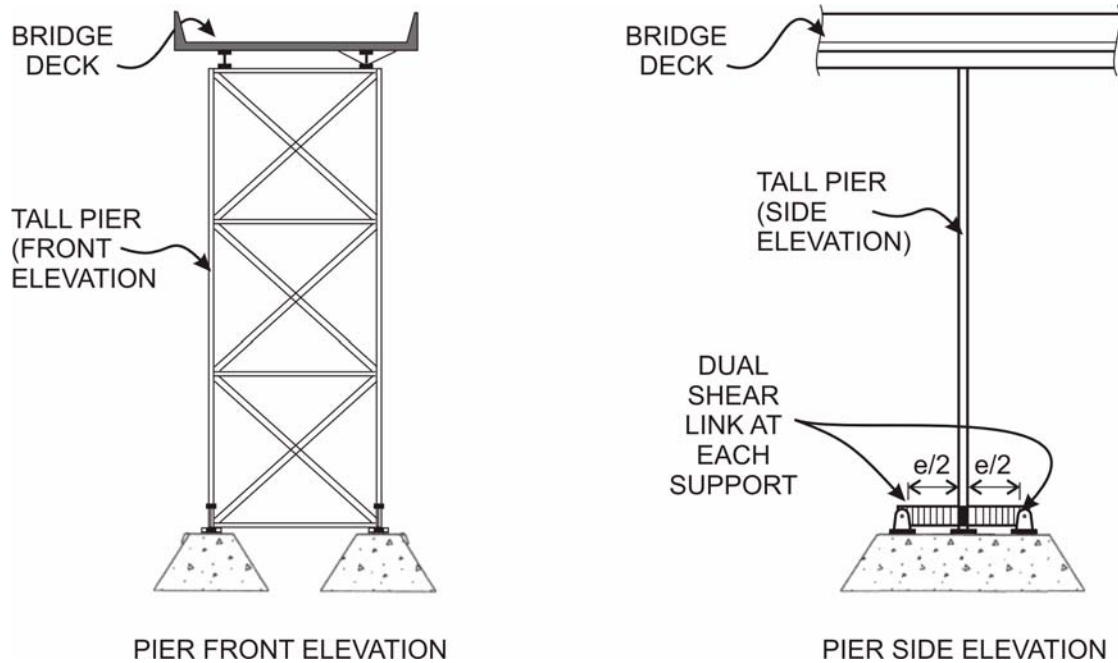


**Figure 1-11: Hysteretic Dissipators for Pier Rocking**

### 1.5.3 Shear Links in Truss Bridges

A ductile design solution utilizing EBFs has been proposed as a retrofit scheme for enhancing seismic performance of steel deck-truss bridges (Sarraf & Bruneau 1999a, b). After making the deck composite with the top chord of the truss to efficiently transfer the inertia loads, the end cross-frames and the lower lateral brace panels of the truss can be replaced by EBFs as illustrated in Figure 1-12. The shear links in the EBFs act as fuses, limiting the force in the transverse direction on both the superstructure as well as the substructure. Other types of ductile end frames were also suggested, such as vertical shear link and triangular plate added damping and stiffness device. The validity of this retrofit scheme was shown by numerical analysis and design recommendations were proposed.

A similar concept can also be extended for through-truss bridges. In this case, the inertia loading from the deck would be transferred at the elevation of the lower chords of the truss. The lower horizontal end panel EBF illustrated in Figure 1-13 can be used to protect the bottom truss chords. Special attention would have to be placed on ensuring that the deck is not made composite for the entire length of the bridge. Since ductile deformation of the end panels is required, the deck would need to be uncoupled in those locations so that it does not act as a stiff diaphragm. To protect the top chords, portal frames could be designed as special moment frames at the ends of the bridge, or as EBFs for bridges with sufficient height.

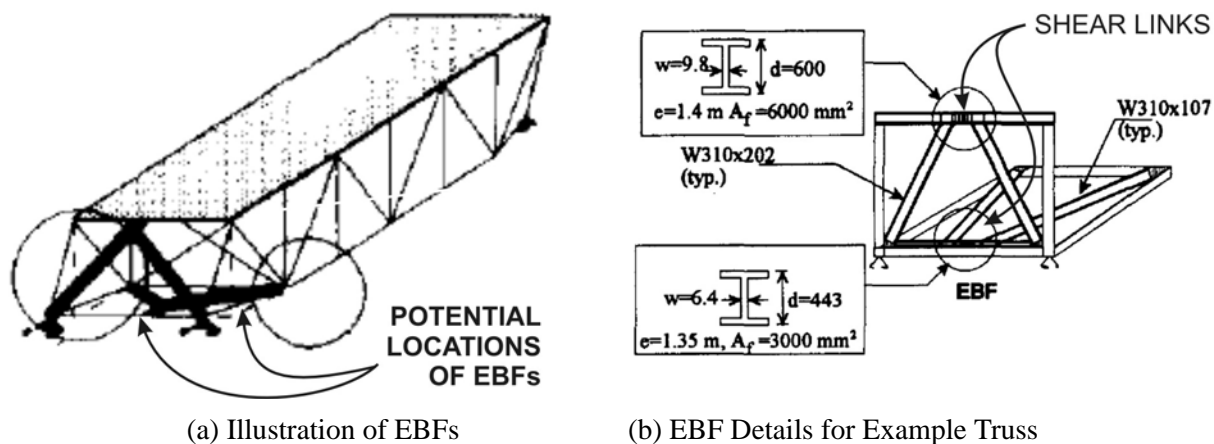


**Figure 1-12: Shear Links in Deck-Truss Bridges (Saraf & Bruneau 1998)**

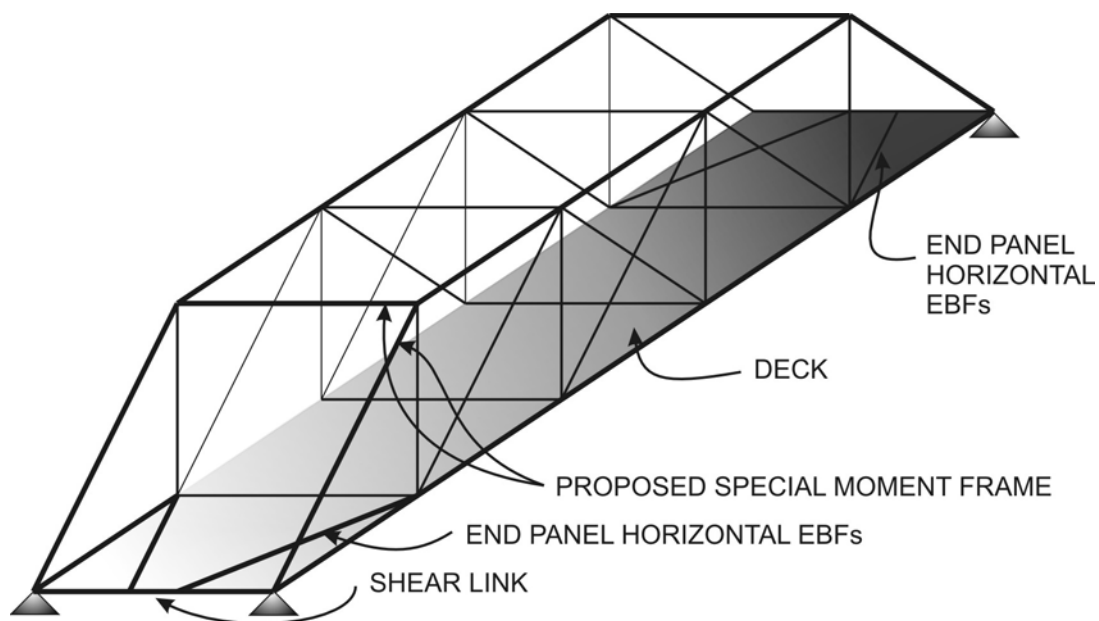


**Figure 1-13: Shear Links in Through-Truss Bridges**

### 1.5.4 Shear Links in Steel Girder Bridge Diaphragms

The potential use of shear links is not restricted to long span bridges and has been suggested for the end diaphragms of slab-on-girder bridges. Bridge diaphragms are typically considered secondary members, but seismic inertia forces are transferred through the end diaphragms to the substructure making them an inte-

gral part of the seismic load path. The demands on the superstructure or substructure can be reduced if the end diaphragms are designed to yield under large seismic forces (Astaneh-Asl 1996) and EBFs can be incorporated as illustrated in Figure 1-14 (Seyed & Bruneau 1999a,b). Cyclic tests of full-scale specimens utilizing rolled wide flange shear links demonstrated the capacity of the assembly to dissipate energy (Zahrai & Bruneau 1999a, b).

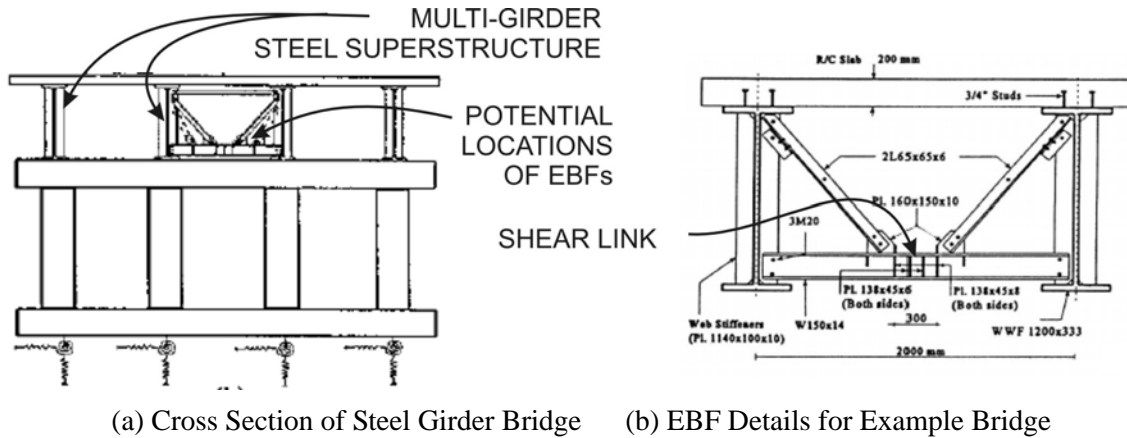


**Figure 1-14: Shear Links in Steel Girder Diaphragms (Seyed & Bruneau 1999a,b)**

## 1.6 Research Purpose

Eccentrically braced frames use shear yielding elements called shear links to protect structures from earthquake induced loads. The use of sections that are built-up from plates instead of rolled shapes becomes necessary for applications requiring large capacities, such as when used in major bridges. Little is known about the performance of built-up shear links and consequently the design requirements for such components. Isolated cases of built-up shear links have been implemented for seismic retrofit and design of major long span bridges in high seismic areas and a variety of other potential applications for bridges are also possible. The overall effectiveness of these structural systems during an earthquake depends on the performance of the shear links components, demanding an improved understanding of the behavior of built-up shear links.

The primary goal of the research was to investigate the performance of built-up shear links subjected to cyclic inelastic deformations. The objectives were to use large-scale experiments, material evaluations and numerical analyses to:

- investigate the performance of built-up shear links fabricated from conventional plate steels, which are commonly used in steel bridge construction
- develop design alternatives to improve the performance of the built-up shear links using alternative steels such as HPS and LYP steels
- evaluate large-strain material properties of plate steels and their influence on the shear link performance
- develop a representative numerical model for built-up shear links.
- investigate the contributions to the overstrength of the shear links.
- develop design recommendations for built-up shear links in bridges.

## 1.7 Report Organization

This report contains the methods and results of experimental and numerical research conducted on built-up shear links intended for the earthquake protection of long span bridges. The general organization follows a chronological sequence of the experimental phases in order to reflect the evolution of ideas and concepts. The sections are outlined as follows:

- Section 1 serves as an introduction by reviewing past literature and outlining the applications of built-up shear links for the earthquake protection of long span bridges.
- Section 2 discusses the results from experiments on built-up shear links utilizing conventional plate steel. The load history and test setup in these tests became the experimental platform for subsequent link designs.
- Section 3 presents the design and results from testing a shear link utilizing high performance steel.
- Section 4 discusses the evolution of the shear link design philosophy to links without stiffeners and utilizing low yield point steels. Two different loading histories were used to experimentally evaluate the performance of these innovative designs.
- Section 5 compares the performance of the different shear links and outlines the relative advantages and disadvantages.
- Section 6 discusses the results from detailed numerical analyses of the built-up shear links that were experimentally tested.
- Section 7 discusses the results of parametric studies used to investigate the different contributions to built-up shear link geometry on the shear resistance. The results from the experiments and numerical analyses are used to develop an expression for evaluating the shear resistance of built-up shear links that incorporates the link geometry as well as the material stress-strain characteristics.
- Section 8 provides recommendations for the design of built-up shear links based on the research findings.
- Section 9 contains the conclusions from the experimental and analytical phases of the research and outlines recommendations for future research.
- Appendix A provides detailed description of the experimental test setup that was utilized for the large scale shear link experiments.
- Appendix B contains support documents such as mill certificates from the materials used and welding procedures from fabrication.

**SECTION 2**  
**CYCLIC PERFORMANCE OF SHEAR LINKS DESIGNED USING**  
**CONVENTIONAL PLATE STEEL**

**2.1 Shear Link Properties and Test Setup**

Built-up shear links were designed from steel that would typically be used for construction of steel bridges. Typical construction grade steels are composed of mainly iron with carbon, manganese, sulphur, silicon and aluminum as primary additives that are mixed to control the properties of the steel. Of particular interest is the high content of carbon and manganese elements, which generally increase the yield strength but have adverse effects on ductility and weldability. The steel bridge industry commonly specifies A709 Grade 345 MPa (50 ksi) weathering steel for fabrication of plate girders for its ductility and weldability. The A709 grade steel represents the conventional steels that is available from mills in the United States in wide range of plate thicknesses.

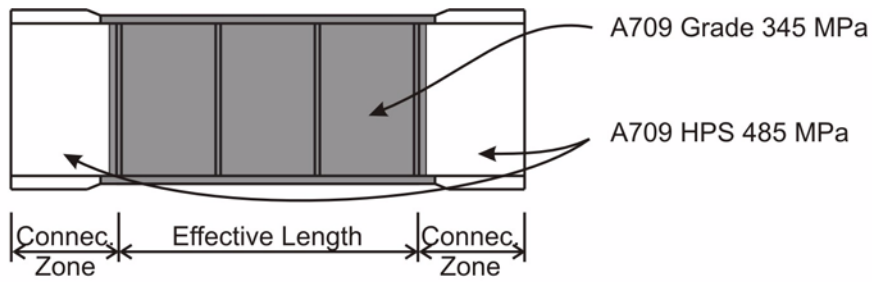
The experiments on these links were aimed to demonstrate the feasibility of using built-up sections for hysteretic shear links. The objectives of the tests were to experimentally investigate the performance of built-up shear links designed from conventional plate steel and subjected to cyclic loading. Of specific interest was the deformation capacity, ultimate resistance and failure mode.

**2.1.1 Shear Link Design**

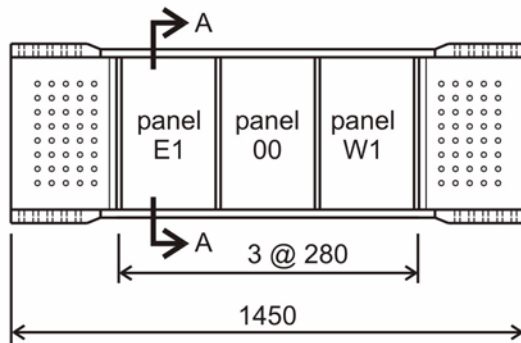
Two different shear link geometries were designed using the conventional grade steel. These are referred to as Link C345a and Link C345b and were half-scale replicas of typical shear links in the transverse and longitudinal orientations of the new SFOBB tower. As shown in Figure 2-1, each link consisted of an effective length in the middle and connection regions at the ends of each link, which allowed bolted connections to the test setup. The effective length was designed using A709 Grade 345 MPa (50 ksi) steel and was intended to deform inelastically, while the connection regions were designed from higher strength A709 High Performance Steel HPS 485 MPa (70 ksi) and were intended to remain elastic. Thicker plates were incorporated into the connection zone to compensate for the net section reduction caused by the bolt holes. Typical connection details of the links to the rest of the test setup is described as part of Appendix A.

**Table 2-1: Nominal Design Properties of Built-up Shear Link from Conventional Grade Steel**

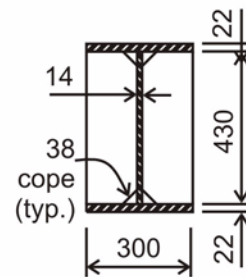
Design Property	Link Type	
	C345a	C345b
$e, mm (in)$	840 (33.1)	500 (19.7)
$V_p, kN (kip)$	1245 (280)	1245 (280)
$M_p, kNm (kip ft)$	1252 (923)	1043 (769)
Stiffener Spacing, $mm (in)$	280 (11.0)	250 (9.8)
$h_w/t_w$	31	31
$b_f/2t_f$	6.8	5.4



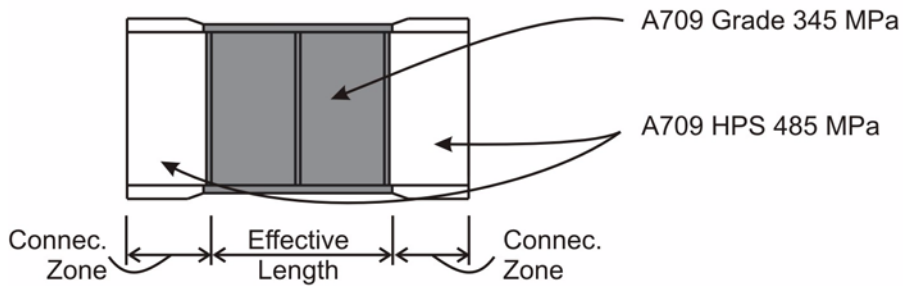
(a) Steel Grades in Link C345a



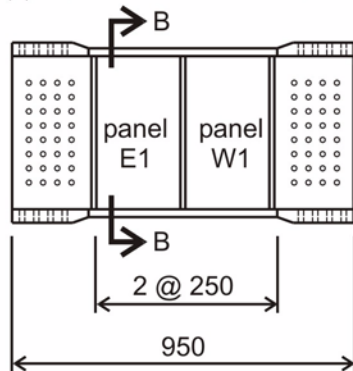
(b) Link C345a Elevation



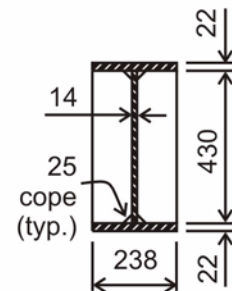
(c) Section A-A



(d) Steel Grades in Link C345b



(e) Link C345b Elevation



(f) Section B-B

**Figure 2-1: Built-up Shear Links C345a and C345b Details**

The two different shear link geometries were based on the SFOBB design by T.Y. Lin International and are shown in Figure 2-1. The link design properties were calculated based on the recommendations of the AISC Seismic Provisions for EBF shear links reviewed in Section 1.1.2. The resulting design properties that are based on the nominal yield strengths only are summarized in Table 2-1. The shear capacity was the same for both links and the effective lengths were within the recommended maxima for shear links. The web and flange compactness satisfied the specified ratios for compact sections. Full depth web stiffeners were provided at the ends of the effective length, with intermediate stiffener spacing at less than the minimum specified for shear links. The stiffeners divided the shear link into panels that were identified starting from middle panel 00, the East panel as E1 and West panel as W1. Stiffener chamfers of 38 mm (1.5 in) and 25 mm (1.0 in) were incorporated at each flange to web intersection for links C345a and C345b respectively. The stiffeners formed panels within the effective length as identified in Figure 2-1.

Tensile coupon tests were performed based on ASTM A370 Standard to obtain the actual yield strength  $f_{ya}$  for plates used for the flange as well as the web in the effective length of the link. The tests were conducted by Testing Engineers Inc. and stress-strain traces are included as part of the support documents in Appendix B. The results of these tests along with the shear and moment capacities based on the those values are summarized in Table 2-2. Shear was expected to dominate the behavior as indicated by the shear capacity ratios  $2M_{pa}/(eV_{pa})$  for both links.

**Table 2-2: Capacity of Built-up Steel Shear Link from Conventional Grade Steel**

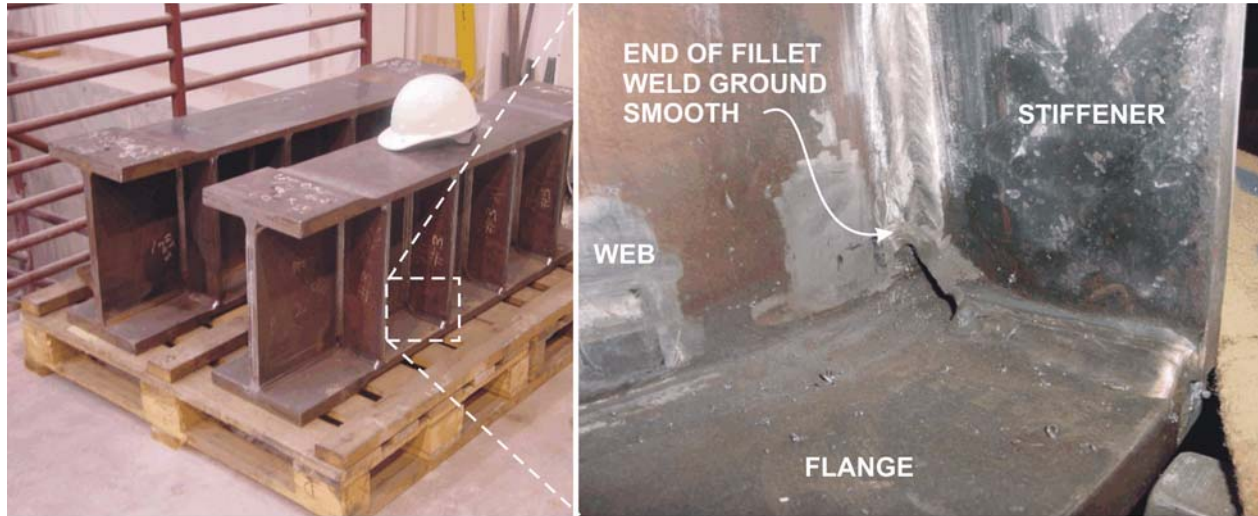
Capacity Characteristic	Link Type	
	C345a	C345b
$f_{yaw}, MPa (ksi)$	372 (54.0)	372 (54.0)
$f_{yaf}, MPa (ksi)$	390 (56.6)	390 (56.6)
$V_{pa}, kN (kip)$	1344 (302)	1344 (302)
$M_{pa}, kNm (kip ft)$	1404 (1036)	1164 (858)
$2M_{pa}/(eV_{pa})$	2.49	3.46

### 2.1.2 Shear Link Fabrication

Both types of shear links were fabricated by Christie Constructors Inc. in Richmond, CA. Because different plate thicknesses and different grades of steel made up each shear link, the individual plates were welded together. Complete joint penetration welds were used to form the flanges and webs separately. The flanges and webs were then joined together using full penetration welds with an additional reinforcing fillet weld at the flange toe. All welds were specified to match the higher grade of steel, even where two lower grade plates connected. The welding procedure is included as part of the support documents in Appendix B. For quality assurance, the welds were inspected according to the Bridge Welding Code D1.5 (AWS 2004).

The stiffeners were connected to the flanges and web using fillet welds, the ends of which were ground to smooth the transition onto the web. This weld finish detail shown in Figure 2-2 was implemented based on

the SFOBB design team recommendation, which was made to try to alleviate cracking at that location. The link bolted connection zone was drilled on site to ensure proper fit into the test setup. The connection regions consisted of 232 A490 - M16 (5/8 in) diameter bolts for Link C345a and 160 A490 - M16 (5/8 in) diameter bolts for Link C345b.



(a) Links C345 Prior to Installation

(b) Fillet Weld Finish Detail

**Figure 2-2: Fillet Weld Detail for Stiffener to Web Connection**

### 2.1.3 Test Setup

The fabrication and erection details of the test setup are included in Appendix A. Two links of type C345a were used in parallel in the transverse test setup and one link C345b was used in the longitudinal test setup to reflect the unique configurations of the SFOBB tower assembly. The installed links are shown prior to testing in Figure 2-3 and Figure 2-4.

## 2.2 Load History and Instrumentation

Incremental cyclic deformation was applied to each shear link. The response was measured by electronic instruments and the data was recorded and stored on personal computers in tab delimited text format at 1 Hz sampling frequency.

### 2.2.1 Applied Cyclic Deformation History

Each specimen was subjected to incrementally increasing cyclic deformations. The deformation history was developed from the AISC Seismic Provisions (AISC 1997, Supplement 2) for links in eccentrically braced frames. Based on a decision made by the SFOBB design team and in deviation from the Seismic Provisions, a greater number of cycles were included prior to  $\gamma_{eff} = 0.0025 \text{ rad}$  and cycles greater than  $\gamma_{eff} = 0.03 \text{ rad}$  were incrementally increased by  $0.01 \text{ rad}$  after just one cycle. The incremental amplitude

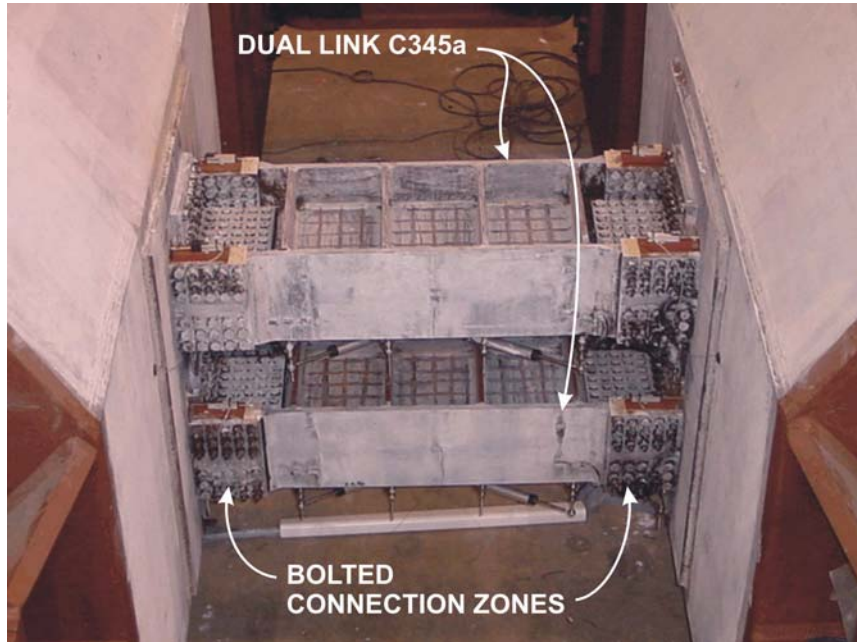


**Figure 2-3: Photograph of Installed Dual Shear Links C345a**

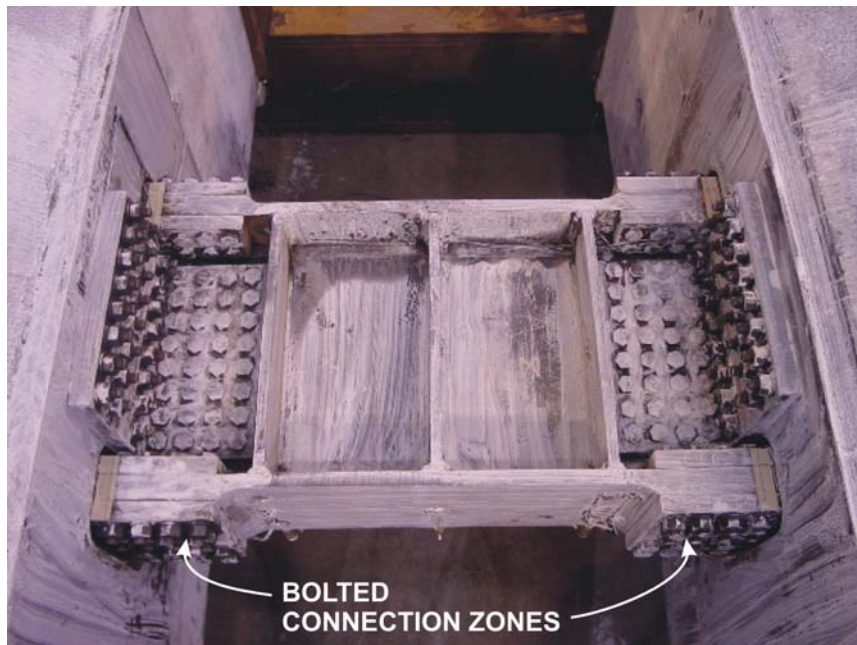


**Figure 2-4: Photograph of Installed Shear Link C345b**

cyclic history is illustrated in Figure 2-5, with specific amplitude target shear deformations listed in Table 2-3.

The actuator was controlled based on the link shear rotation angle  $\gamma_{eff}$  calculated using displacement transducers installed across the effective length as described in Appendix A. By having the actuator controlled by the link deformation and not by the actuator displacement, the load history was followed without deviations resulting from the test setup flexibility or slippage in the link connections.

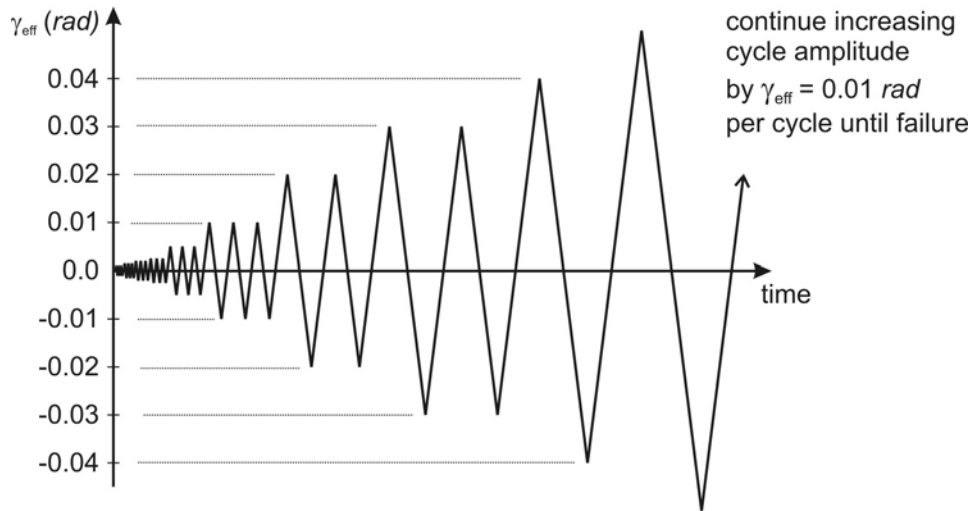


**Figure 2-5: Incremental Amplitude Cyclic Deformation History**

### 2.2.2 Instruments and Data Acquisition

A combination of displacement transducers and strain gauges were used to monitor the deformation of the shear links. Two data acquisition systems were utilized; Lab View by National Instruments Inc. for the displacement transducers and Megadac 3416 Series by Optim Inc. for the strain gauges. Locations and reference numbers of each instrument are shown in Figure 2-6 and Figure 2-7 for links C345a and C345b respectively. Description of the different types of instruments is contained in Table 2-4.

**Table 2-3: Incremental Cyclic Deformation Protocol**

No. of Cycles	Effective Length Shear Deformation, $\gamma_{eff}$ (rad)
3	0.001
3	0.0015
3	0.002
3	0.0025
3	0.005

**Table 2-3: Incremental Cyclic Deformation Protocol**

No. of Cycles	Effective Length Shear Deformation, $\gamma_{eff}$ (rad)
3	0.01
2	0.02
2	0.03
1	0.04
1	continue increasing by 0.01 rad increments

Displacement transducers were installed diagonally across the effective length as well as across each panel to monitor the average shear deformation at those locations. Link C345a was more extensively monitored because of its longer length. Rosette gauges were used for the web such that the maximum shear strains could be calculated. The locations of the rosettes were chosen to capture the shear strain along the link length as well as the depth. The locations of flange strain gauges were concentrated at the ends of the link due to the highest moment demands at those locations.

In addition to electronic monitoring, the specimen was coated with whitewash, which was applied as a mixture of water and lime. The brittle layer of whitewash, which flaked and peeled away from the steel under large strains, provided for a visual indication of the relative level of surface strain in the specimen.

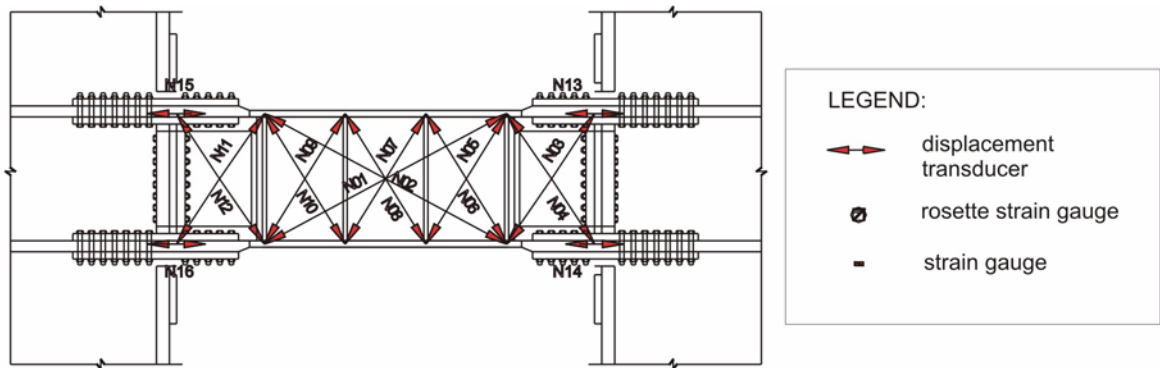
## 2.3 Experimental Results

Experiments on built-up shear links C345a and C345b were conducted on March 29<sup>th</sup>, 2002, and November 30<sup>th</sup>, 2001 respectively. The investigation concentrated on the behavior of the effective length of the link. This section reviews the observed and recorded experimental results.

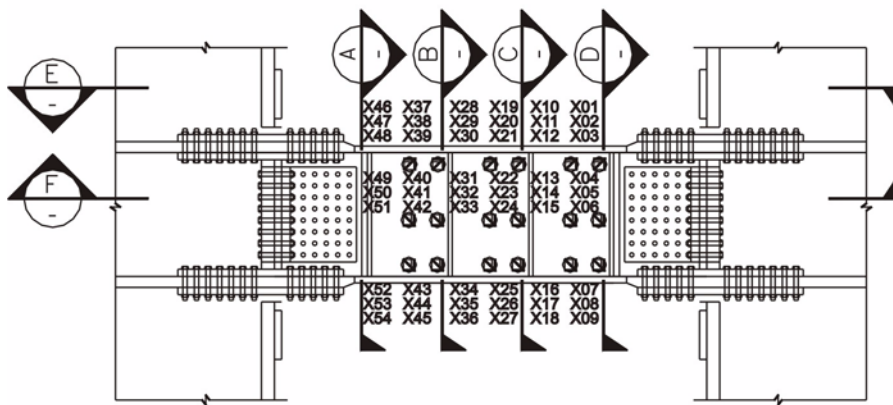
### 2.3.1 Visual Observations and General Comments

Visual observations during testing followed the same trends for both types of built-up shear links. The whitewash flaked away from the web near the middle of the link first. As the deformation of the link increased, the flaking progressed throughout the entire web area up to the end stiffeners next to the connection zone. Further observations using whitewash within the web area became less effective after deformations exceeding  $\gamma_{eff} = \pm 0.005$  rad as most of the coating had flaked away. Localized whitewash flaking was noticed in the link flanges at the ends of the effective length as shown in Figure 2-8. No web or flange buckling was observed at any point during the experiment.

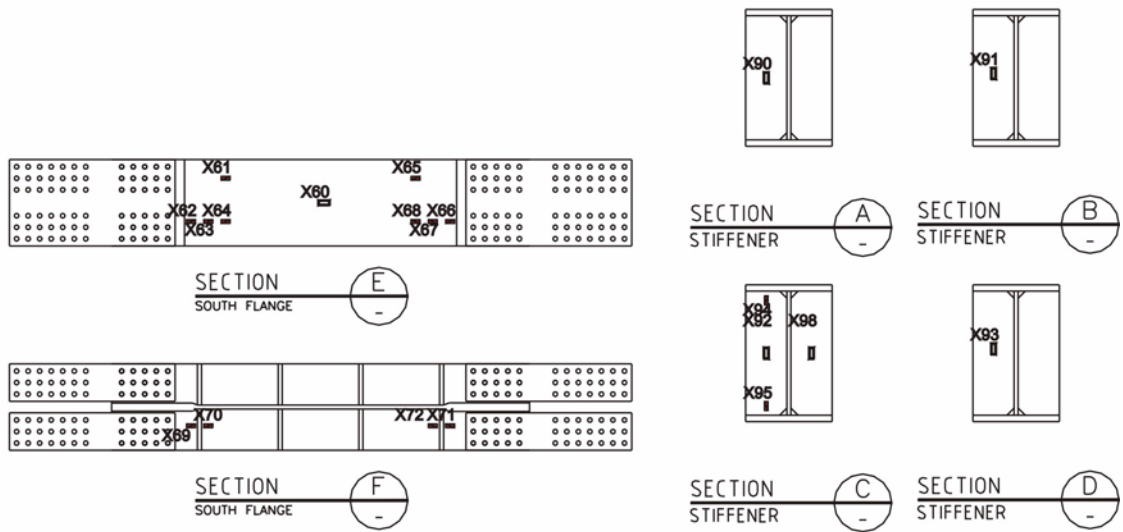
Bolt slippage in the connection of the link was first recorded at the push cycle towards  $\gamma_{eff} = 0.04$  rad for Link C345a and at the push cycle towards  $\gamma_{eff} = 0.005$  rad for Link C345b. The slippage became increasingly frequent with larger deformation values and was signified by an abrupt reductions in resistance accompanied by a loud impact noise. Figure 2-9 shows examples of the relative slip of the link flange with



(a) Displacement Transducers

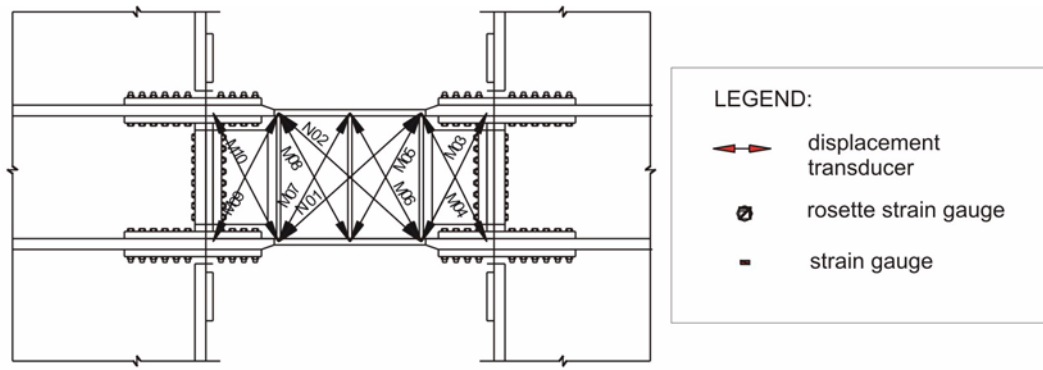


(b) Web Strain Gauges

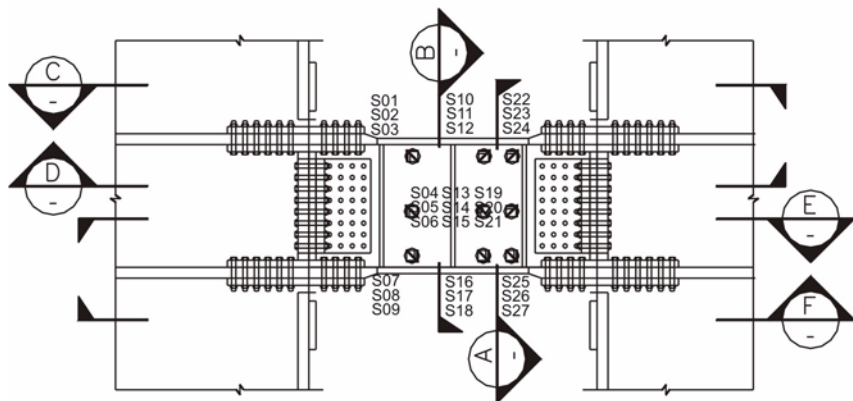


(c) Sections with Flange and Stiffener Gauges

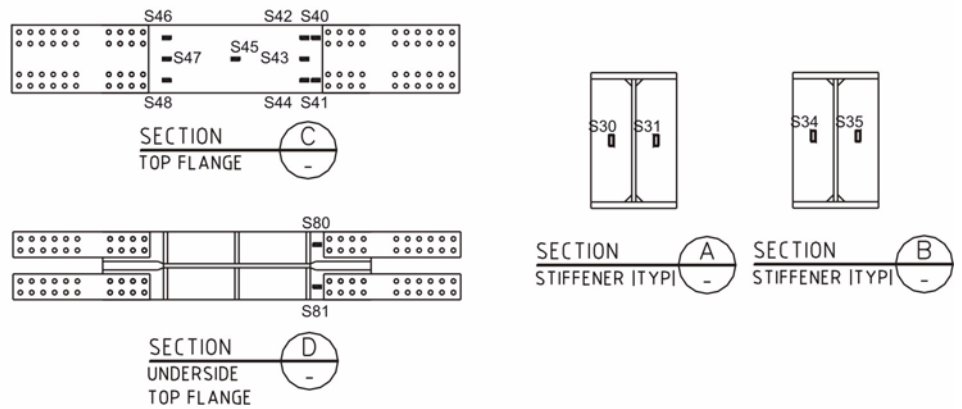
Figure 2-6: Instrumentation for Links C345a



(a) Displacement Transducers



(b) Web Strain Gauges

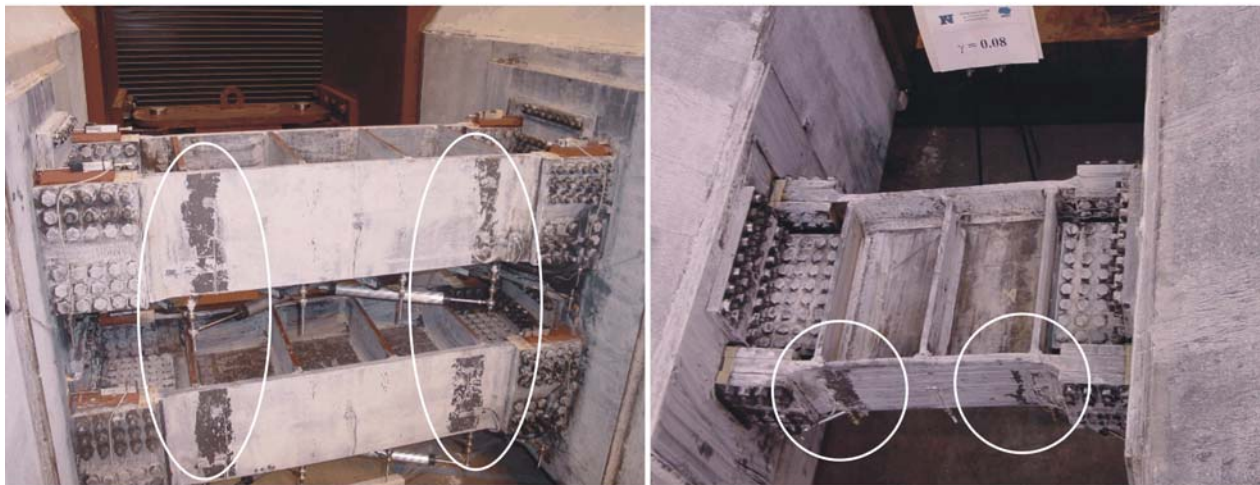


(c) Sections with Flange and Stiffener Gauges

Figure 2-7: Instrumentation for Links C345b

**Table 2-4: Instrumentation Description**

Manufacturer	Model No.	Description
Novotechnic	TR50	50 mm Stroke Displacement Transducers
	TR100	100 mm Stroke Displacement Transducers
Tokyo Sokki Kenkyujo Co.	FLA-5	Elastic Strain Gauges
	YFLA-5	Post-yield Strain Gauges
	YEFRA-5	Post-yield Rosette Gauges



(a) Links C345a at  $\gamma_{eff} = 0.08 \text{ rad}$

(b) Link C345b at  $\gamma_{eff} = 0.08 \text{ rad}$

**Figure 2-8: Flange Localized Deformation at Ends of Effective Length**

respect to the splice plates, which commonly exceeded 2 mm (1/16 in). At the end of the tests, loosened bolts were noticed in the web angles to the tower shafts connections.

### 2.3.2 Failure Mode

The failure modes occurred within the deformable length in both types of shear links. Due to safety concerns, observations were made between cycles when the actuator load was at approximately zero load.

#### 2.3.2.1 Failure of Link C345a

The failure mode of Link C345a was ductile and characterized by web tearing. Cracks initially formed in the middle web panel, next to the stiffener weld as shown in Figure 2-10. The first was recorded after  $\gamma_{eff} = \pm 0.04 \text{ rad}$  cycle and was located in the web metal, next to the toe of the fillet weld connecting the stiffener to the web. The second formed after  $\gamma_{eff} = \pm 0.06 \text{ rad}$  cycle in a location diagonally across from the first. With increasing deformations, these cracks did not immediately propagate. At ultimate failure, the

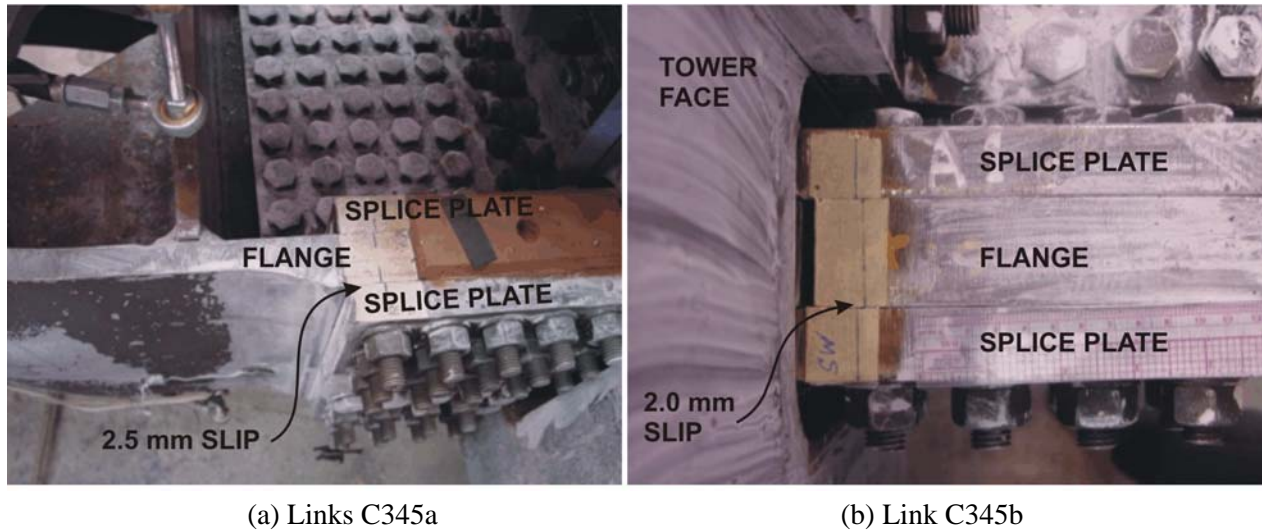


**Figure 2-9: Bolt Slippage Between Flange and Splice Plates**

cracks tore through the entire depth of the web along the stiffener-to-web welds as shown in Figure 2-11. Following the crack propagation, one of the stiffeners fractured and the web crack continued parallel to the flange next to the weld. After significant additional deformation, one of the flanges fractured at the end of the effective length.

Cracking was also observed in the intermediate stiffeners near the flange fillet welds as shown in Figure 2-12(a). These were caused by the repeated bending of the stiffener that was forced to remain perpendicular to the flanges despite their relative deformations, forming a double curvature shape as shown in Figure 2-12(c). The stiffeners at the ends of the effective length were not affected since they were located next to the connection zone, which remained primarily elastic.

### 2.3.2.2 Failure Link C345b

Ductile failure mode of Link C345b also initiated with the formation of cracks in the web. The first cracks occurred during  $\gamma_{eff} = \pm 0.07 \text{ rad}$  cycle and were located in the web steel, next to the end of the middle stiffener weld as shown in Figure 2-13. After the completion of  $\gamma_{eff} = \pm 0.07 \text{ rad}$  cycle, the two cracks grew around the toe of the welds, but remained relatively unchanged until the excursion toward  $\gamma_{eff} = -0.11 \text{ rad}$ . The crack propagated along the flange as well as the web and led to the tensile fracture of the middle stiffener shown in Figure 2-14. Similar to Link C345a, the middle stiffener showed signs of cracking prior to failure as shown in Figure 2-12(b).

### 2.3.3 Shear Deformation Capacity

The link shear deformation was calculated using diagonal measurements across the effective length as described in Appendix A.

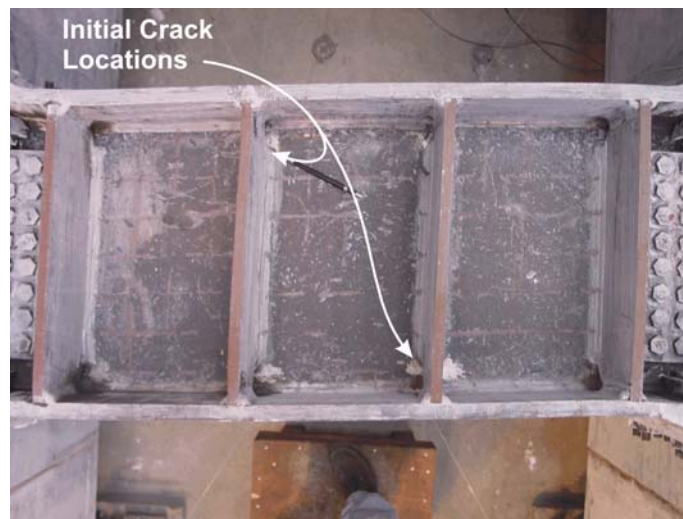


**Figure 2-10: Initial Crack Location in Link C345a**

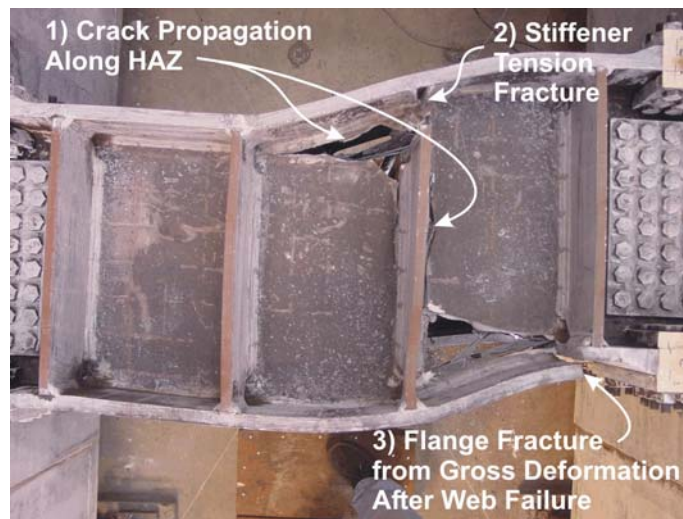


**Figure 2-11: Ultimate Failure of Link C345a**

### 2.3.3.1 Deformation of Link C345a

For testing of link C345a, two links were used in parallel within one test setup. This simulated the layout of the SFOBB design. The specimens exhibited the same shear deformation as shown by the linear one-to-one relationship in Figure 2-15. Hence, the links were assumed to have the same behavior and were assumed to share the resistance equally up to failure. Representative cyclic behavior is presented for one of these links in Figure 2-16. During the experiment, the actuator force capacity was reached in the pull direction after the completion of  $\pm 0.07$  rad cycle. Since additional actuator force capacity remained in the push



**Figure 2-12: Stiffener Cracking at Flange Fillet Welds**

direction, the actuator underachieved the target in subsequent cycles in the pull direction only. This resulted in a positive shear deformation bias in the applied load history.

The cyclic response was ductile and did not exhibit any pinching or degradation. The plastic shear rotation was separated from the elastic using Equation 1-13 and the resulting response is shown in Figure 2-17. The maximum recorded shear rotation, denoted by  $(\gamma_{eff})_{max}$ , as well as the maximum plastic shear rotation, denoted by  $(\gamma_p)_{max}$ , are summarized in Table 2-5. Given the high elastic stiffness of the shear link, the total and plastic capacities were nearly the same. The plastic rotation capacity surpassed the AISC implied minimum of 0.08 *rad* for EBF shear links by 56%.

The measured shear link deformation was representative of the average deformation across the effective length. The effective length of C345a consisted of three panels that were separated by stiffeners. The shear rotation of an individual panel was found to be proportional to the overall average link rotation, but varied along the length of the link. Figure 2-18 shows the relative panel rotation expressed by the ratio  $\gamma_{pan}/\gamma_{eff}$ , where  $\gamma_{pan}$  is the panel rotation calculated by diagonal displacement transducers across the panels. Con-

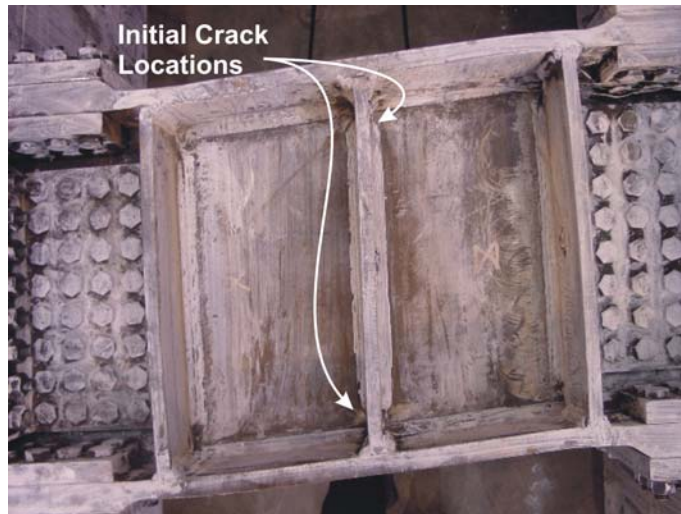


**Figure 2-13: Initial Crack Location in Link C345b**

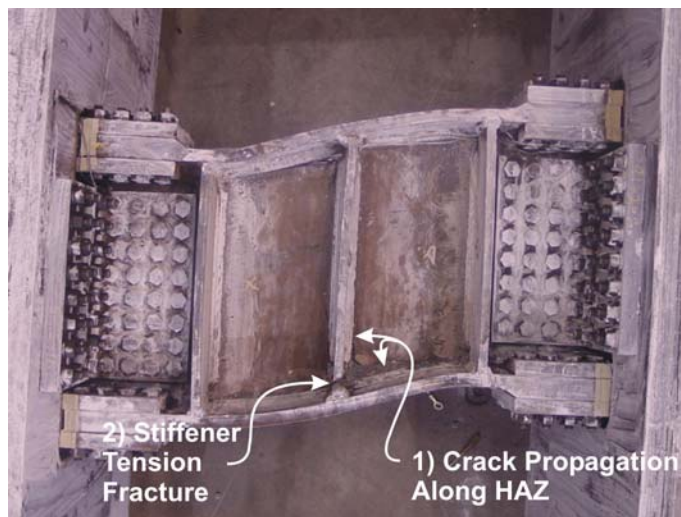


**Figure 2-14: Ultimate Failure of Link C345b**

firming visual observations, the center panel was found to have the greatest demand and exceeded the average by 13%.

### 2.3.3.2 Deformation of Link C345b

The cyclic behavior of Link C345b is shown in Figure 2-19. The behavior was ductile and did not exhibit any pinching or degradation. The load history was followed until a gradual resistance decrease started to occur while approaching  $\gamma_{eff} = -0.11 \text{ rad}$ . Anticipating failure, the actuator displacement was not reversed and the specimen was pushed to ultimate failure, which did not occur until  $\gamma_{eff} = -0.15 \text{ rad}$ .

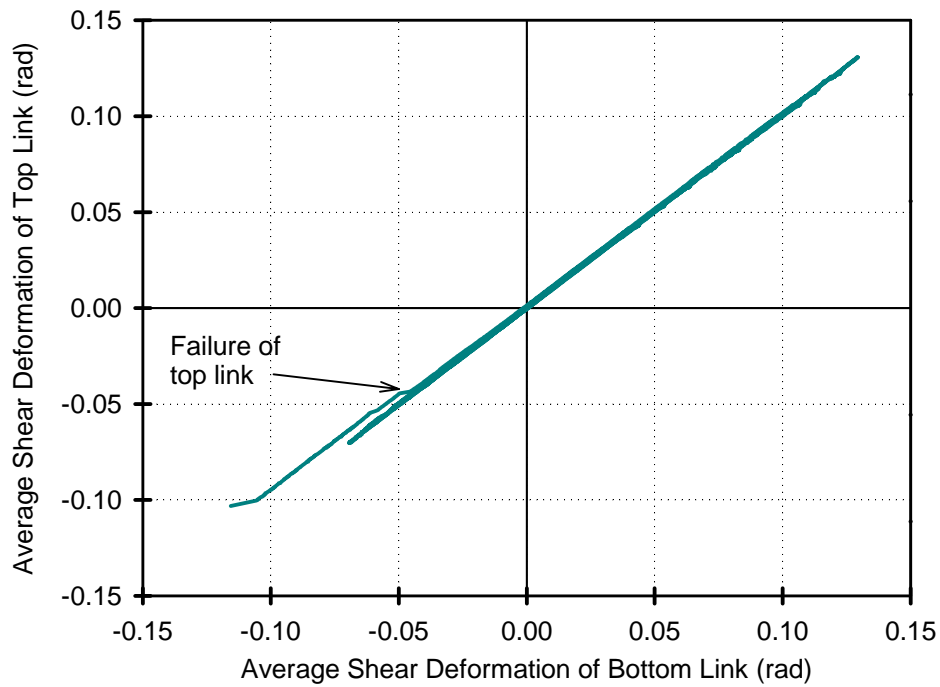


**Figure 2-15: Deformation Comparison of Two Parallel Links C345a**

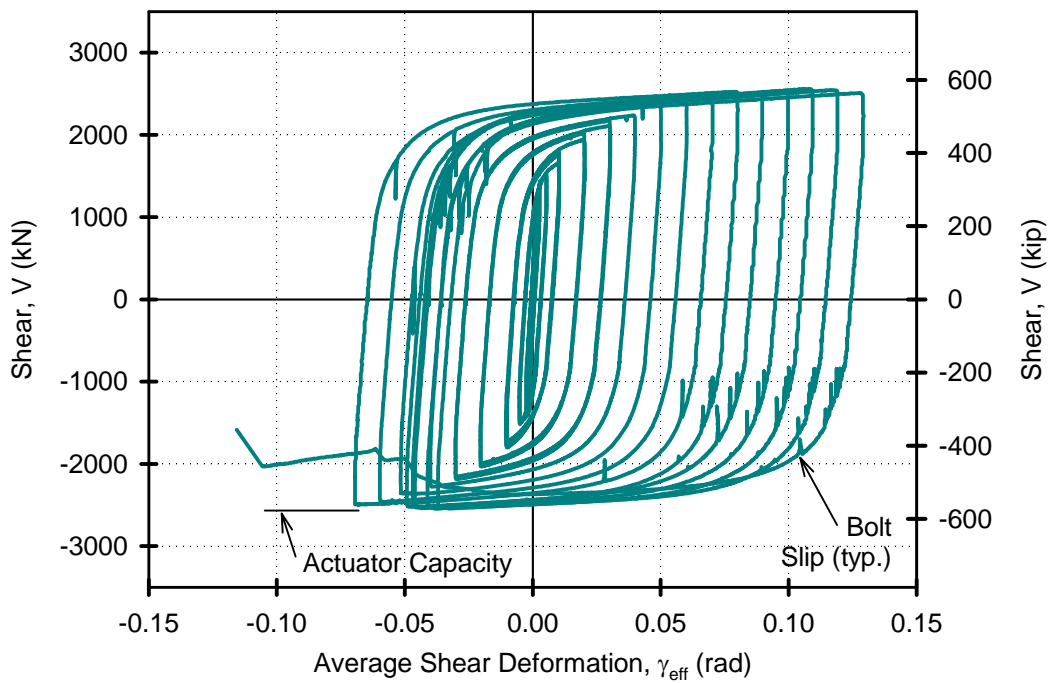


**Figure 2-16: Cyclic Behavior of Link C345a**

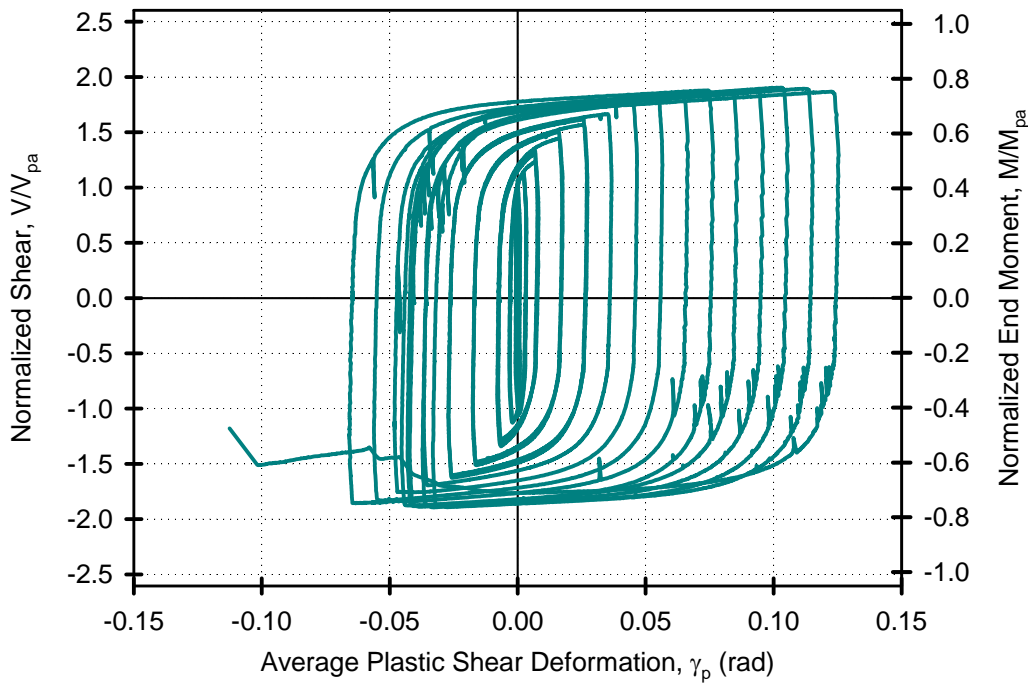


**Figure 2-17: Cyclic Plastic Behavior of Link C345a**

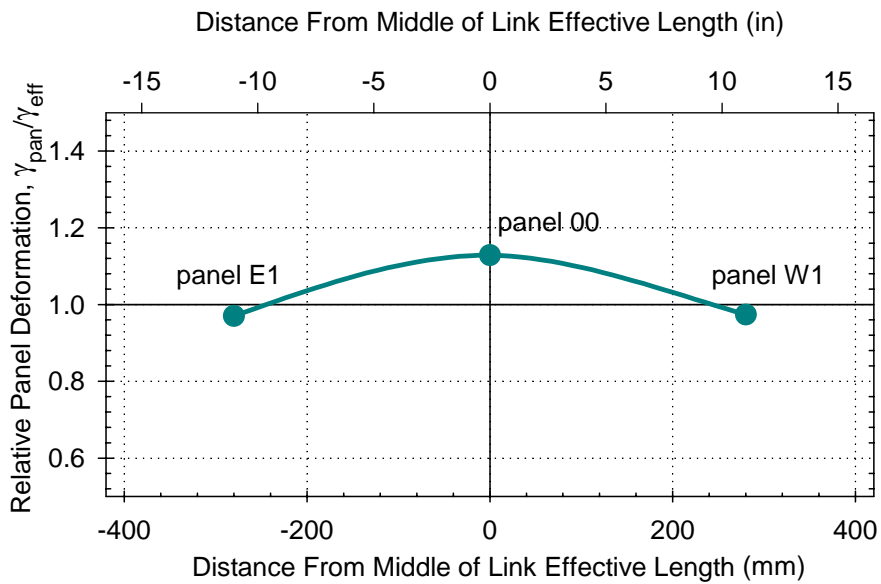


**Figure 2-18: Panel Deformation Along the Length of Link C345a**

The plastic cyclic behavior is shown in Figure 2-20. The shear deformation maxima summarized in Table 2-5 considered only values of completed reversals and discounted the last push to failure. The plastic

rotation capacity exceeded the AISC implied minima by 34%. Since the link contained only two panels, the average distribution was not separated into the individual panel contributions as symmetry was assumed.

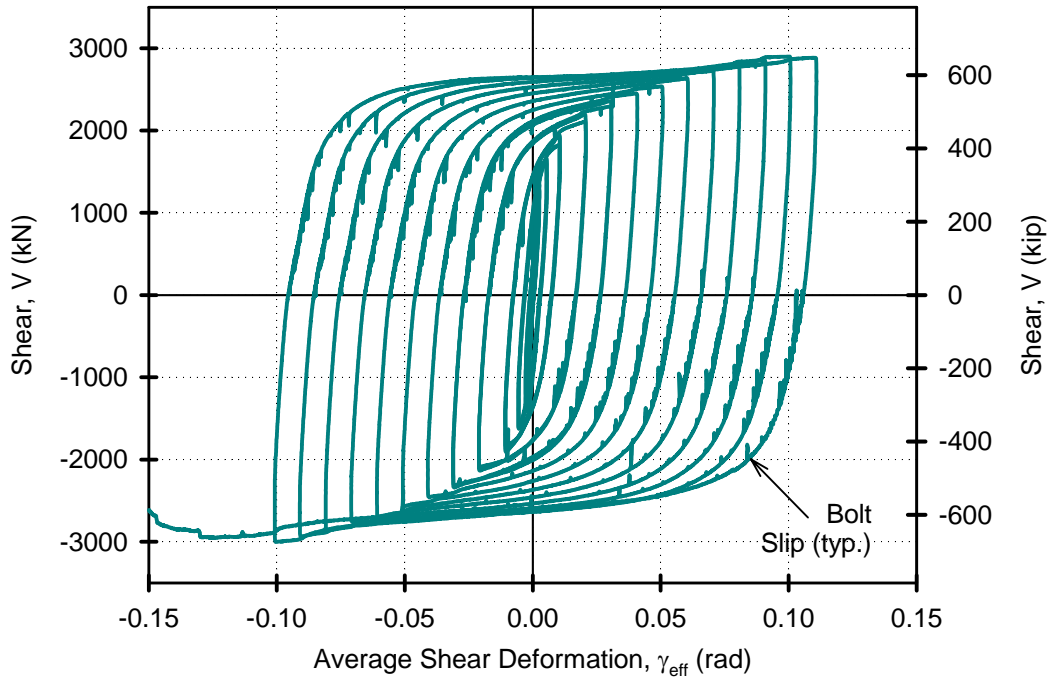


**Figure 2-19: Cyclic Behavior of Link C345b**

### 2.3.4 Link Resistance

The link shear resistance was calculated from the actuator load and geometry of the test setup as described in Appendix A, resulting in the shear resistance values shown in Figure 2-16 and Figure 2-19 for Link C345a and C345b respectively. For comparison with the calculated capacity, the link shear was normalized to the plastic shear capacity as shown in Figure 2-17 and Figure 2-20. The onset of non-linear behavior corresponded well with the plastic shear strengths in both cases.

The maximum recorded forces and the resulting overstrength ratios, calculated using Equation 1-14, are summarized in Table 2-5 for both types of links. Overstrength values exceeded the maximum expected by the AISC Seismic Provisions for shear links in EBFs, which is approximately 1.5. The recorded overstrengths were in good agreement with the findings from tests on other built-up shear links discussed in Section 1.4.

The design shear capacities of the two link types were the same, but the moment capacities and the effective lengths were not. The moment demand  $M_{max}$  at the ends of the effective length was calculated based on statics in Equation 1-1 and normalized to the moment capacity as shown on the secondary axis in Figure 2-17 and Figure 2-20. The end moments were well below the plastic capacity, with the maxima summarized in Table 2-5. Based on these values, it was assumed that the link deformations were dominated by shear.

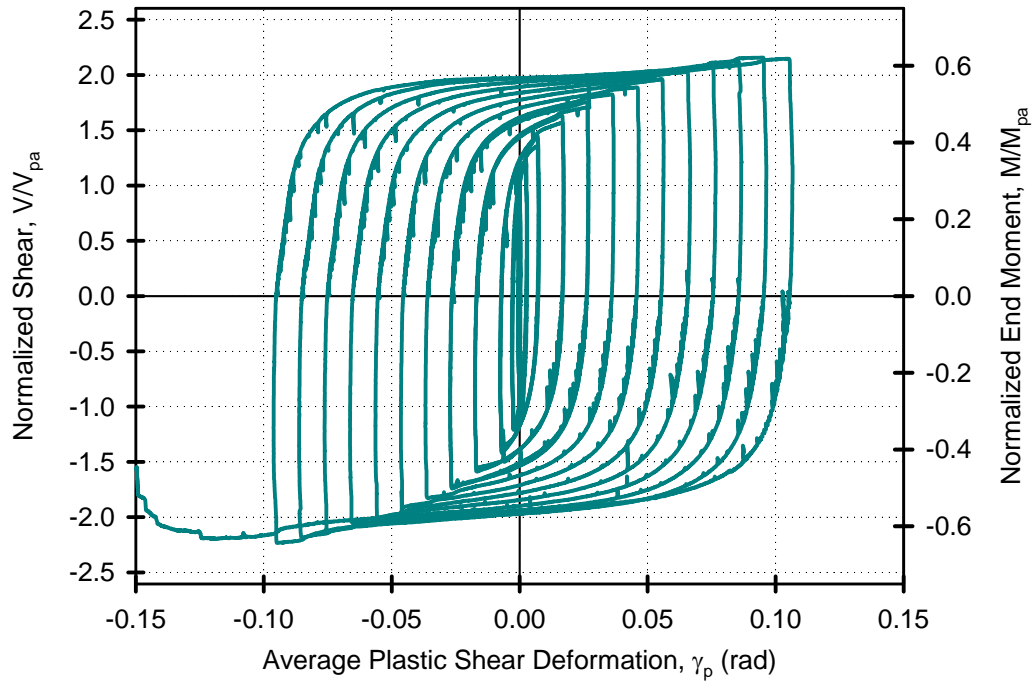


**Figure 2-20: Cyclic Plastic Behavior of Link C345b**

**Table 2-5: Shear Links C345a and C345b Performance Summary**

Parameter	Link Type	
	C345a	C345b
$(\gamma_{eff})_{max}, rad$	0.129	0.111
$(\gamma_p)_{max}, rad$	0.125	0.107
$V_{max}, kN (kip)$	2560 (575)	3025 (680)
$\Omega$	1.9	2.2
$M_{max}, kNm (kip ft)$	1075 (793)	756 (557)
$M_{max}/M_{pa}$	0.77	0.65

### 2.3.5 Strains in Shear Link

Strains were continuously recorded in the web as well as the flange for both shear links types. Data was extracted from the recordings at each reversal of load, which allowed for analysis at different milestones within the response. The following reversal points were chosen to demonstrate the strain distribution in the built-up shear links:

- $\gamma_{eff} = \pm 0.02 \text{ rad}$  for moderate inelastic link deformations;
- $\gamma_{eff} = \pm 0.08 \text{ rad}$  to represent the AISC Seismic Provisions implied minimum shear link deformation (note maximum negative rotation achieved for Link C345a was  $-0.07 \text{ rad}$ );
- $\gamma_{eff} = \pm 0.10 \text{ rad}$  for the maximum strain gauge values.

#### 2.3.5.1 Web Strains

The measurements taken from gauges in the webs of the effective length showed significant inelasticity. More gauges were included in Link C345a to gain better understanding of the strain distribution because the link had longer length and more web panels. Maximum shear strains were calculated from the three strain components of each rosette. The recorded strains through the depth of the web of Link C345a are shown in Figure 2-21 for the mid-length and in Figure 2-22 for end of the effective length. As expected, web shear strain increased with increased link deformation. In general the strains were higher at mid-depth, but the strain distribution did not significantly vary throughout the height. The top strain gauges at the end of the effective length reached their limit after the link  $\gamma_{eff}$  exceeded  $0.07 \text{ rad}$ .

The shear strain distribution at mid-depth along the link length is shown in Figure 2-23 and near the bottom flange is shown in Figure 2-24. The shear strains were not distributed uniformly throughout the link effective length. At mid-depth, a clear difference can be seen among gauges at the center of the link panel and those located near the stiffeners, especially at higher link rotations. The web shear strains were consistently higher near the locations of stiffeners. The shear strains near the bottom flange were more uniform. This is likely caused by the fact that the stiffeners are attached to the web at a higher point than where the gauges were located, resulting in lesser influence on the web strains.

#### 2.3.5.2 Flange Strains

Confirming visual observations, large plastic strains were recorded in the flanges at the ends of the effective length as shown in Figure 2-25 and Figure 2-27 for Link C345a and C345b respectively. The strains are shown for selected values of  $\gamma_{eff}$  at specific load reversal points and were shown to increase with increasing link deformations. For the locations where the gauges were installed, the strains were found to increase towards the mid-length. However these were only localized deformations at the ends of the link effective length. The plastic strains extended into the link connection zone in both cases.

Since the moment demand was found to be significantly less than the plastic capacity of the section, it is inferred that the moment demand did not cause the large plastic strains at the ends of the effective length. Furthermore, the high strains did not occur throughout the entire flange depth. As shown in Figure 2-26 for Link C345a, the strains at the inside face of the flange were significantly less than those on the outside face. The inside face strains were not recorded for link C345b because stiffeners and flange splice plates prevented installation of gauges at the ends of the effective length. The flange strains were caused by the imposed deformation that occurred in the transition from the elastic connection zone to the deformed effective length of the link and were therefore localized in the outside fibres of the section.

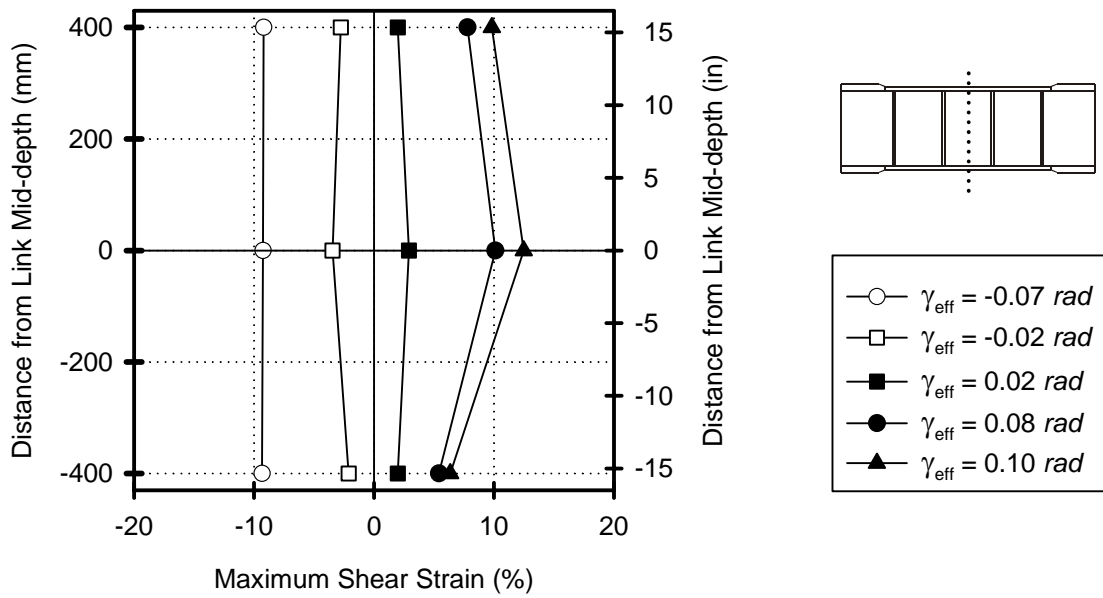


Figure 2-21: Shear Strain in Web in Mid-Length of Link C345a

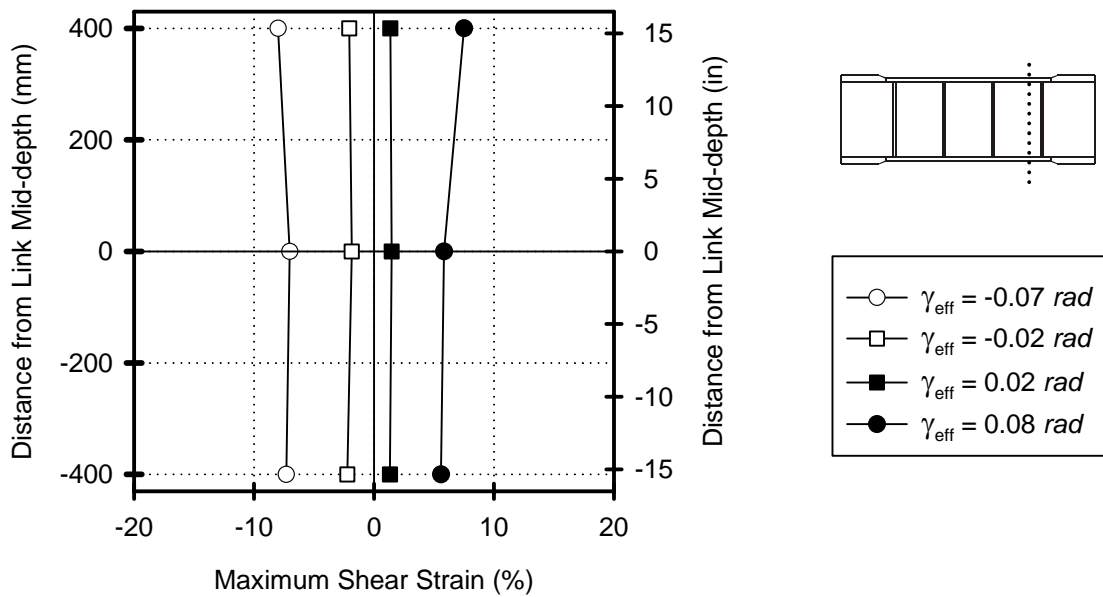


Figure 2-22: Shear Strain in Web at End of Effective Length for Link C345a

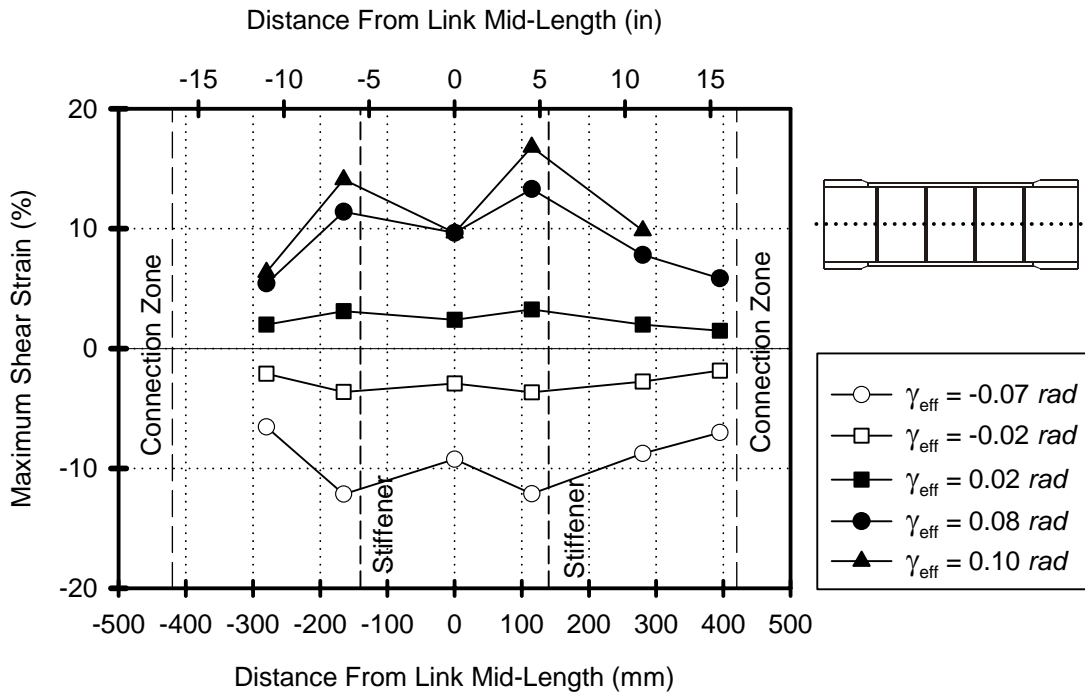


Figure 2-23: Shear Strain in Web at Link Center of Link C345a

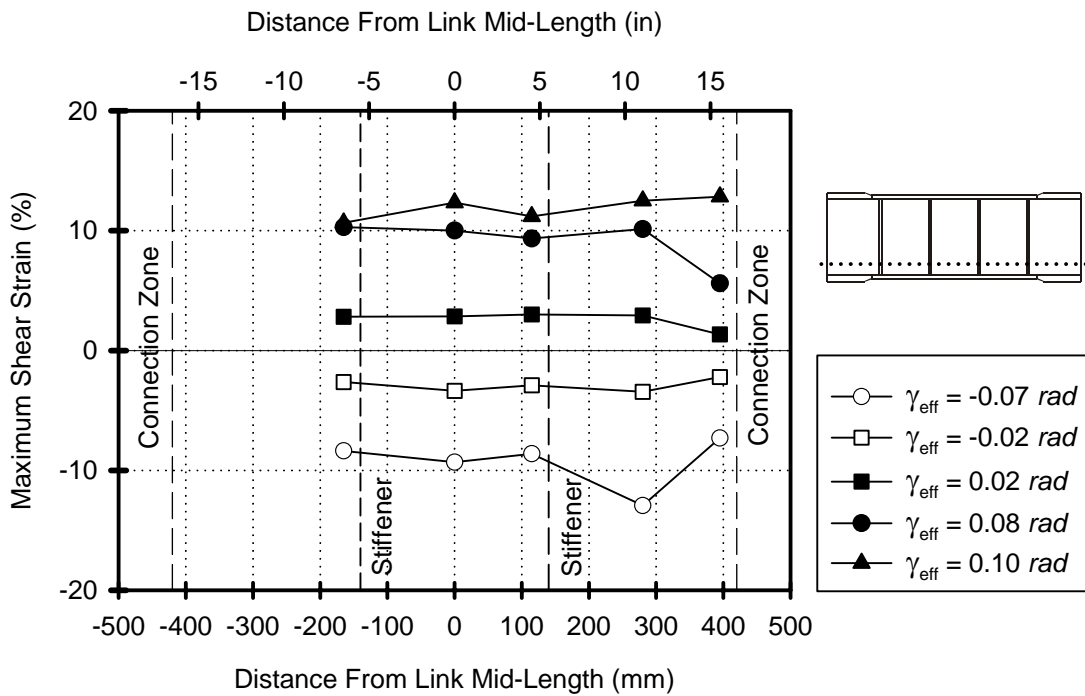
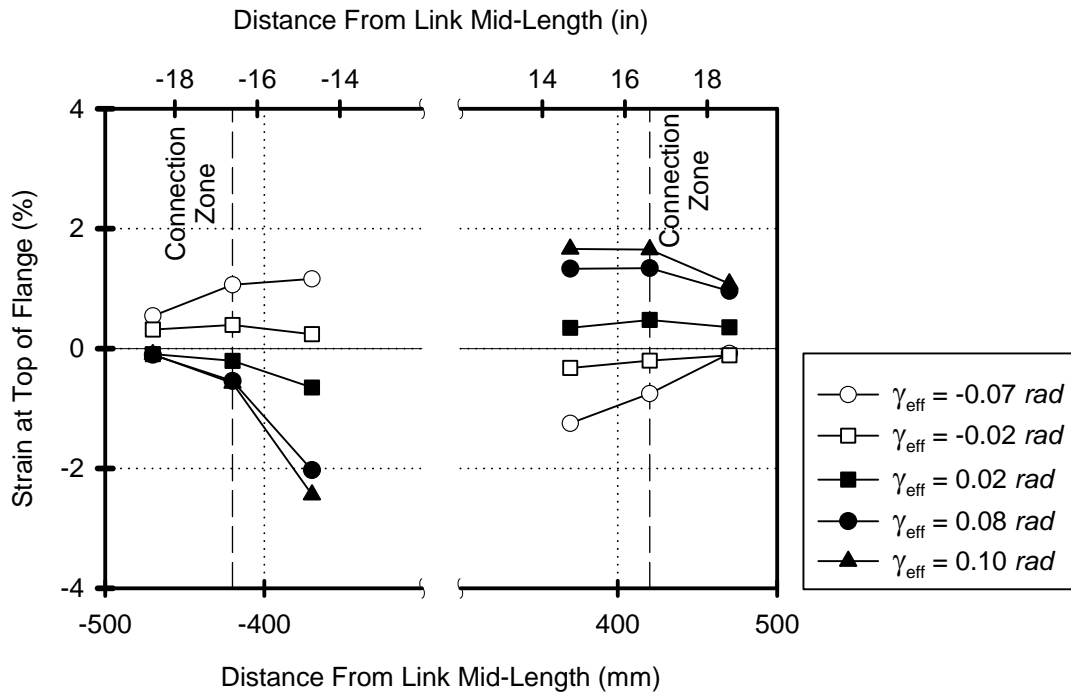
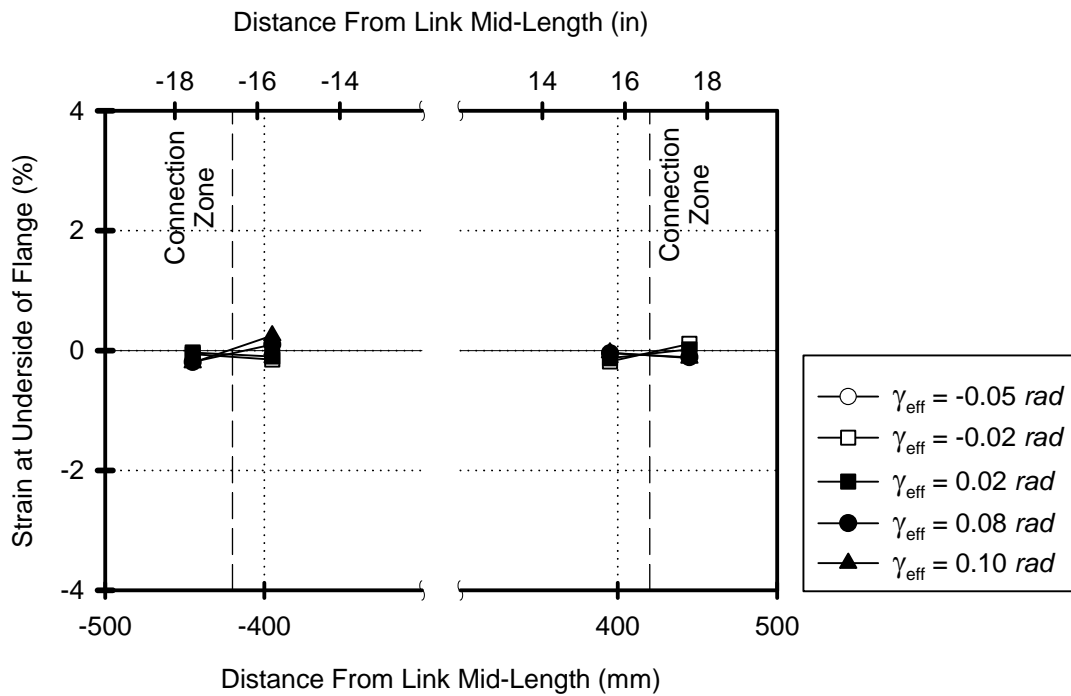


Figure 2-24: Shear Strain in Web near Bottom Flange of Link C345a



**Figure 2-25: Strains in Outside Face of Flange for Link C345a**



**Figure 2-26: Strains on Inside Face of Flange for Link C345a**

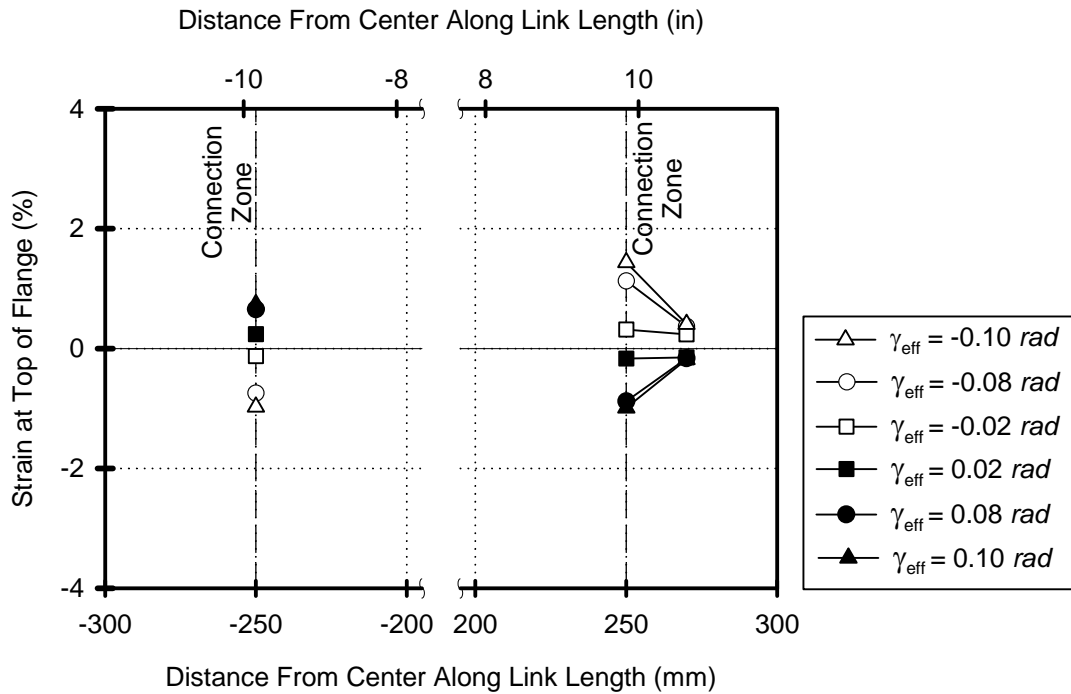


**Figure 2-27: Strains in Outside Face of Flange Fibers for Link C345b**

### 2.3.5.3 Intermediate Stiffener Strains

Large plastic strains were also recorded in the intermediate stiffeners of Link C345a near the fillet welds to the flanges as shown in Figure 2-28. The stiffeners of Link C345b were not instrumented at those locations. The measurements confirmed the visual observations of deformation in the intermediate stiffeners and the consequent cracks that developed next to the welds. Although only three gauges were used, the stiffener deformed shape suggested that large strains were localized next to the proximity of the flange connection.

### 2.3.6 Performance Comparison to Larger Scale Tests

Built-up shear links based on the SFOBB design were also tested at the University of California, San Diego (UCSD) as discussed in Section 1.4.2. The specimens Type 1 and Type 3 corresponded to Links C345a and C345b and were full-scale replicas of the bridge links. Based on the recommendations made by the SFOBB design team in light of the UCSD tests, a number of modifications were made for shear links C345a and C345b. The changes that were adopted were:

- Over-matching of weld strengths.
- Grinding smooth the ends of the stiffener to web fillet welds.
- Increasing the stiffener chamfer size.

Although all of these factors prevented conclusive comparisons to study scale effects, the tests did provide an indication of the effectiveness of these changes. The overstrength values were comparable, but the plastic deformation capacity was 108% and 62% larger for Link C345a and C345b when compared to Type 1

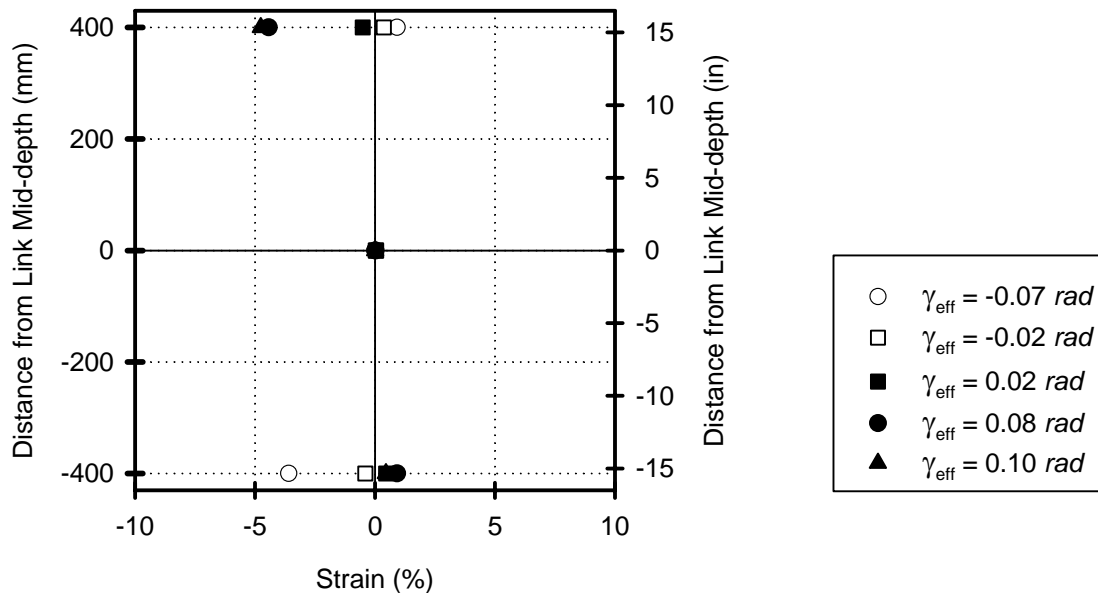


**Figure 2-28: Strains in Intermediate Stiffener of Link C345a**

and Type 3 in the UCSD tests. The influence of each change on the links deformation capacity improvement are discussed below.

### 2.3.6.1 Overmatching of Welds

Unlike Links C345a and C345b, the welds in the UCSD tested shear links were welded using electrodes matching the lower grade steel, i.e. matching grade 345 MPa (50 ksi). Failure in the welds was not observed during any of the tests and hence does not account for the difference in the deformation performance.

### 2.3.6.2 Stiffener Weld Grinding

The initial cracks in Type 1 and Type 3 links occurred at the weld toe near the end of the stiffener to flange fillet weld, which was the same location as observed in Links C345a and C345b. It is therefore unlikely that grinding the ends of the stiffener welds had any effect on the location of crack initiation. The initial cracks did not form in the weld itself, but occurred in the web metal next to the stiffener welds in what is referred to as the heat affected zone (HAZ).

HAZ is the portion of the weld metal which has not been melted, but whose mechanical properties or microstructure have been altered by the heat generated from welding (AWS 2002). The extent of HAZ varies and depends on number of parameters, such as weld size, preheat and metal characteristics, but is generally regarded to be up to approximately 3 mm (1/8 in) for low carbon weldable steels. Start and stop locations of welds are especially vulnerable and the use of runoff tabs, which are often provided to reduce these effects, are not possible for fillet welds of stiffeners to web in the built-up shear links.

### 2.3.6.3 Stiffener Chamfer Size

The most significant factor influencing the improved deformation capacity in Link C345a and C345b was attributed to the larger stiffener chamfer size. The chamfer was increased from approximately  $0.5t_w$  in Type 1 and Type 3 links to  $2.7t_w$ , and  $1.8t_w$  for Links C345a and C345b, where  $t_w$  is the web thickness. The initial crack formation was observed at approximately the same deformation levels in Link C345a and C345b as in Links Type 1 and Type 3. The actual link deformation is difficult to ascertain from the UCSD tests because the crack initiation was reported as a function of the actuator displacements without being related back to the deformation of the link. Nonetheless, the actuator displacements corresponded to shear deformations of approximately 0.04-0.06 *rad*. Despite the similarities in crack initiation, the cracks did not immediately propagate in Links C345a and C345b until significantly later. These observations support the results from finite element analyses, which indicate lower stresses and lower equivalent plastic strains for larger stiffener chamfer sizes (McDaniel 2002).

## 2.4 Summary

Cyclic experiments were conducted on two types of built-up shear links designed and fabricated from conventional A709 grade 345 *MPa* (50 *ksi*) steel. Cracking was consistently initiated in the web, next to the ends of the stiffener to web fillet welds. The ultimate failure mode of both link types was ductile and characterized by web tearing, which initiated with cracks at the ends of the stiffener to web fillet welds.

Both shear links exhibited ductile cyclic behavior without pinching or strength degradation of the hysteretic shear deformation curve. The maximum shear deformation of approximately 0.12 *rad* exceeded the AISC Seismic Provisions implied minimum for EBF shear links of 0.08 *rad* illustrating the suitability of utilizing built-up sections for hysteretic shear links. However, higher than expected overstrengths of approximately 2.0 were recorded. Current AISC Seismic Provisions underestimate the required strength for members outside the effective length, potentially resulting in deficient design.

The web shear strain distribution varied throughout the length of the shear link, with higher values recorded near the stiffeners at mid-depth. Localized plastic strains were recorded in the flanges at the ends of the effective length and extended into the connection zone. These strains were not caused by the moment demand alone, but primarily by the local deformations imposed by the change in geometry from the elastic connection zone to the plastically deformed effective length. Localized plastic strains were also recorded in the intermediate stiffeners near the flange connection and led to development of cracks next to the fillet welds.

The longer stiffener chamfer length likely contributed to the improved deformation capacity of Link C345a and C345b over the shear links tested at UCSD. Overmatching of welds and grinding details at the end of the stiffener welds had lower effect on the overall response based on the type of failure mode.



## SECTION 3

### CYCLIC PERFORMANCE OF SHEAR LINK DESIGNED USING HIGH PERFORMANCE STEEL

#### 3.1 Shear Link Properties and Test Setup

The AISC Seismic Provisions limit the nominal yield strength of the steel used for design to  $345\text{ MPa}$  ( $50\text{ ksi}$ ) or less for shear links in eccentrically braced frames and any other earthquake load resisting component designed for inelastic action. As explained in the commentary (AISC 2002), this limitation is mainly in place because higher grades of steel typically have less inelastic strain capability and special procedures are required during welding. However, higher strength steels are often used to reduce the weight of structures and specially bridges by decreasing the required sectional geometric properties. The incorporation of high strength structural grade steel to a built-up shear link was made by utilizing the recently developed high performance steel, which is gaining acceptance in steel bridges.

The objective of this research was to experimentally investigate the suitability of high performance steel for built-up shear links, which are specifically intended to undergo large inelastic strains. Large-scale cyclic testing was implemented to determine the deformation capacity, ultimate resistance and failure mode of a built-up shear link that was designed using high performance steel.

##### 3.1.1 Potential Suitability of High Performance Steel

High performance steel (HPS) was developed by the joint effort of the American Iron and Steel Institute, the Office of Naval Research and the Federal Highway Administration (Wright 1997). This new grade of steel is available in  $485\text{ MPa}$  ( $70\text{ ksi}$ ) and  $690\text{ MPa}$  ( $100\text{ ksi}$ ) nominal yield strengths, designated A709 HPS 485W (A709 HPS 70W) and A709 HPS 690W (A709 HPS 100W) respectively. It was developed to combine high strength, improved toughness and improved welding characteristics (Barsom 1996). HPS grades also have controlled rusting characteristics and have been used for a number of steel girder bridges in the United States, mainly for resisting gravity loads (Yost & Funderburk 2001). Prior to this study HPS was not implemented or tested in structural components that are expected to perform under repeated inelastic deformations.

The observed failure mode of built-up shear links designed from conventional grade steel initiated with cracking in the heat affected zone (HAZ) next to the stiffener welds. Because welding is necessary during the fabrication, improved weldability was an important consideration for selecting this higher strength material. HPS has less than 60% of the carbon and about 15% of the sulfur of conventional  $485\text{ MPa}$  ( $70\text{ ksi}$ ) steels, resulting in a low carbon equivalent number. Low carbon equivalent numbers typically result in improved resistance to cracking and hardening in the heat affected zone after welding (Wright 1997).

An additional appeal of adopting HPS grade in shear links was the high toughness characteristics of the material, typically reported using Charpy V-notch values. Toughness values can reach  $200\text{ J}$  ( $147\text{ ft-lb}$ ), compared with  $30\text{--}70\text{ J}$  ( $22\text{--}37\text{ ft-lb}$ ) for conventional grades (Yost & Funderburk 2002). Although not directly linked to seismic performance, the higher toughness of HPS provides for higher impact energy absorption capacity, which is desirable during the inelastic performance of a shear link.

### 3.1.2 Shear Link Design

Despite the exclusion of high strength steels from the AISC Seismic Provisions (AISC 2002), the design recommendations for EBF shear links in those provisions were used for designing a single built-up shear link with A709 HPS 485W (A709 HPS 70W) steel. This link type is referred to in this report as Link H485. The design approach was to obtain a shear link that had the same nominal capacity as one of the conventional grade links, thereby allowing for a comparable performance evaluation. The plastic shear strength as well as the plastic moment strength were designed to match Link C345a, which was chosen for its longer length and more accessible test setup installation.

The connection details of the test setup restricted the web height to 430 mm (16.9 in). The web thickness was calculated based on Equation 1-2 and the nominal shear capacity of 1245 kN (280 kip). Numerous flange dimension combinations are possible to achieve the required plastic moment capacity. To achieve a unique solution, the flange compactness ratio was also chosen to match Link C345a. By simultaneously solving Equation 1-3 with the flange compactness constraints, the flange thickness and width was determined. The dimensions, which were rounded to the nearest millimeter, for Link H485 are shown in Figure 3-1 and the resulting nominal design properties are summarized in Table 3-1.

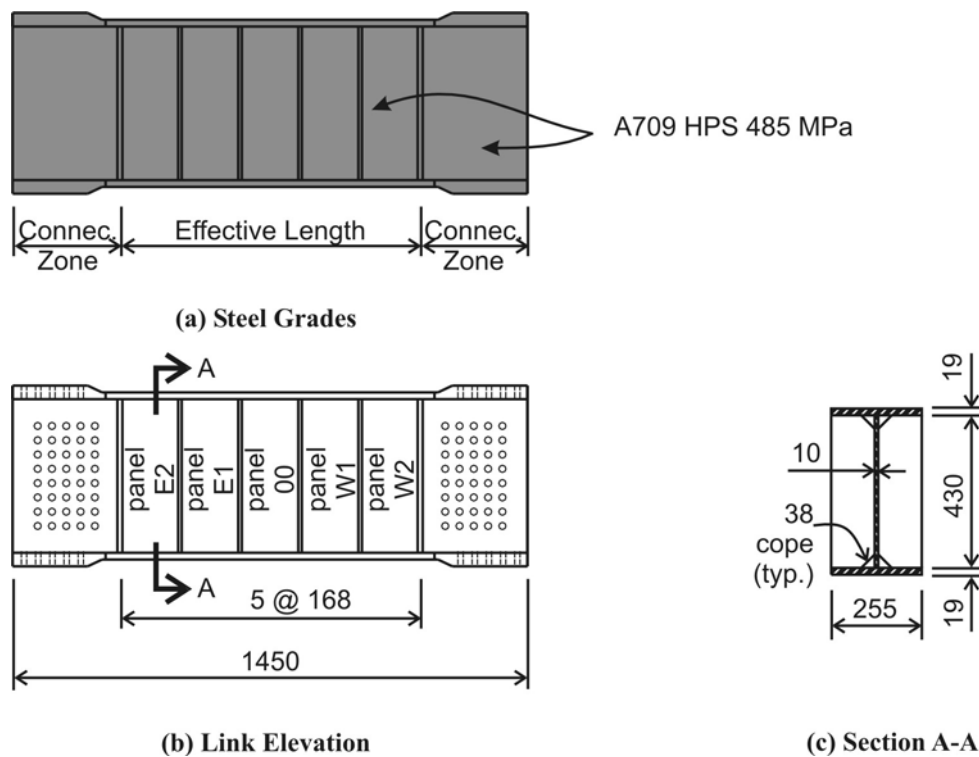


**Figure 3-1: Built-up Shear Link H485 Details**

Full depth web stiffeners were provided at the ends of the effective length and intermediate stiffeners were provided at spacing satisfying the AISC recommendations for EBF shear links. The stiffeners divided the effective length into five equal panels, which are referred to starting from the middle panel 00 and counting East for panels E1 and E2 and counting West for panels W1 and W2. Stiffener chamfers of 38 mm (1.5 in)

were incorporated at each flange to web intersections to match the chamfer size of Link C345a. The actual yield strength was determined from a series of experiments conducted on coupons from the same heat as that used for the link (Dusicka et al 2004). The yield values from the coupon tests and the shear and moment capacities based on those values are summarized in Table 3-2.

**Table 3-1: Nominal Design Properties of Built-up Shear Link from HPS**

Design Property	Link Type H485
$e, mm (in)$	840 (33.1)
$V_p, kN (kip)$	1250 (281)
$M_p, kNm (kip ft)$	1279 (943)
Stiffener Spacing, $mm (in)$	168 (6.6)
Web Compactness Ratio, $h_w/t_w$	43
Flange Compactness Ratio, $b_f/2t_f$	6.7

**Table 3-2: Capacity of Built-up Steel Shear Link from HPS**

Capacity Characteristic	Link Type H485
Web Yield Strength $f_{yaw}, MPa (ksi)$	503 (73.0)
Flange Yield Strength $f_{yaf}, MPa (ksi)$	503 (73.0)
$V_{pa}, kN (kip)$	1298 (291)
$M_{pa}, kNm (kip ft)$	1327 (979)
$2M_{pa}/(eV_{pa})$	2.43

### 3.1.3 Shear Link Fabrication

Due to the recent introduction and limited usage of HPS, plates are available from mills in the United States per order basis and are not stock piled. Obtaining the small quantities required for fabrication of the shear link specimen was made financially feasible through donation from Oregon Steel Mills. This donation was made by a single plate measuring 8636x2133x35 mm (340x84x1.378 in). The flange and web plates were milled down to the required thicknesses prior to fabrication.

The built-up shear link was fabricated by McBride Machine Inc. in Sparks, NV. The flanges and webs were made separately by welding different thickness plates together using full penetration welds. The web and flanges were also welded together using full penetration welds, but the stiffeners were fillet welded. The welding procedure is included as part of the support documents in Appendix B. For quality assurance, the welds were inspected according to the Bridge Welding Code D1.5 (AWS 2004).

### 3.1.4 Test Setup

The test setup is described in detail in Appendix A. The transverse orientation of the shafts was used with one Link H485 installed between the tower shafts. The link connection zones were drilled on site to ensure proper fit into the connections of the test setup. The installed link is shown prior to testing in Figure 3-2. Each connection region consisted of 232 - A490 M16 (5/8 in) diameter bolts connecting the flange splice plates and web angles, which were re-used from previous experiments on Link C345a.

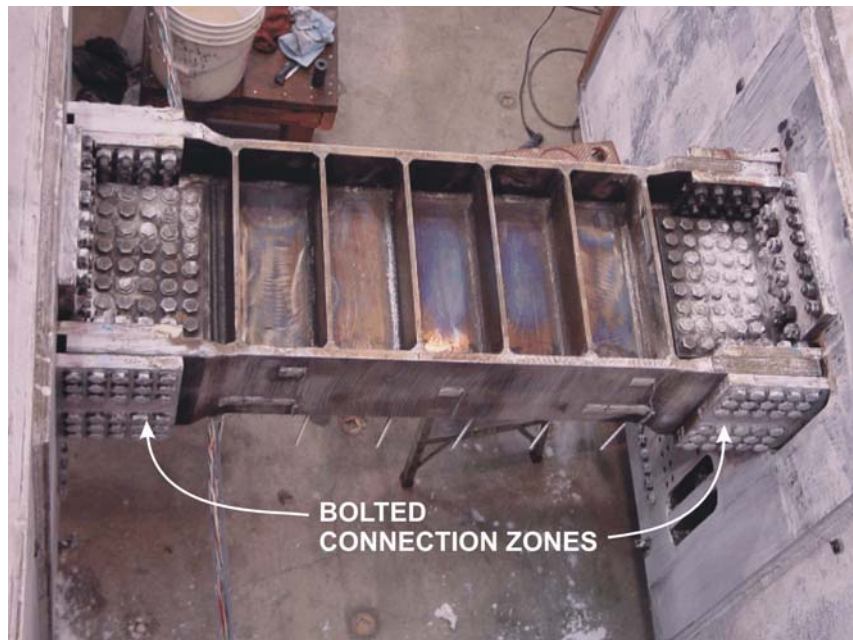


**Figure 3-2: Photograph of Installed Link H485**

## 3.2 Load History and Instrumentation

Incremental cyclic deformation was applied to the shear link. The link response was measured by electronic instruments and the data recorded and stored on personal computers in tab delimited text format at 1 Hz sampling frequency.

### 3.2.1 Cyclic Load History

The imposed deformation history was the same as that used for the conventional steel links and is described in Section 2.2.1. The actuator was controlled based on the link shear rotation angle  $\gamma_{eff}$ , calculated using displacement transducers installed across the effective length as described in Appendix A.

### 3.2.2 Instruments and Data Acquisition

The same data acquisition systems and instrument types were used as those described in Section 2.2.2. Locations and reference numbers of each instrument are shown in Figure 3-3. Displacement transducers were installed to measure the shear deformation across the effective length as well as each individual panel.

The shear strain in the web was measured by rosette strain gauges, which were distributed primarily in the middle panel 00 and the end panel E2. The rosettes were installed in the center of the panel as well as next to the stiffeners in an effort to capture the influence of the stiffeners on plastic strain in the web. Additional gauges were also installed in the middle panel 00 to provide intermediate data points between the center of the link and the flanges. Flange strains were primarily measured at the ends of the effective length to capture any localized yielding that may occur. The specimen was also coated with whitewash to aid visual observations.

### 3.3 Experimental Results

This section reviews the observations and test results from the experiment on built-up shear link H485, conducted during February 19-20, 2004. Comparison to results from experiments on other types of built-up shear links is discussed in Section 5.

#### 3.3.1 Visual Observations and General Comments

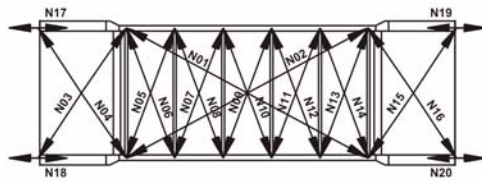
Because mill scale was not present on the link surfaces, photographs did not capture well any of the whitewash flaking. Nonetheless, whitewash flaking did occur to a greater extent in the web within the middle panel and spread quickly with increasing deformation to the remainder of the web up to the end stiffeners. Localized deformations were also observed in the flanges at the ends of the effective length. No web or flange buckling was observed during the experiment.

The first bolt slip was recorded near the completion of the first cycle at  $\gamma_{eff} = 0.03 \text{ rad}$ . The slippage became more frequent after approximately  $0.05 \text{ rad}$  deformation and occurred primarily after the reversal of load. Each bolt slip resulted in sudden but immediately recoverable decrease in resistance.

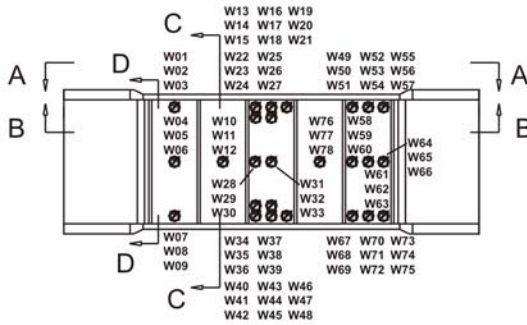
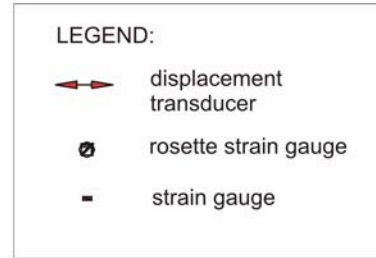
#### 3.3.2 Failure Mode

The failure mode of Link H485 was ductile and characterized by web tearing. The first cracks occurred during the cycle to  $\pm 0.07 \text{ rad}$  and were located in the middle panel as shown in Figure 3-4. The cracks initiated in the heat affected zone at the ends of the stiffener to web fillet weld as shown in Figure 3-5(a). During the next few cycles, similar cracks were observed at the other internal stiffeners. The cracks slowly propagated around the weld, forming a U-shape crack around the stiffener as shown in Figure 3-5(b) at  $\gamma_{eff} = 0.11 \text{ rad}$ . The shear link sustained significant deformation as shown in Figure 3-6 and despite the development of the web cracks, the resistance did not degrade.

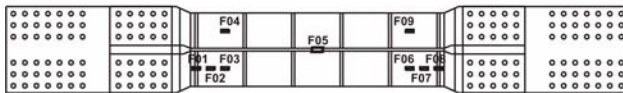
Ultimate failure occurred near the completion of  $\gamma_{eff} = 0.12 \text{ rad}$  cycle. The resistance gradually decreased while the crack in the middle panel tore through the depth of the web. The shear remained at approximately 75% of the maximum. The unexpected residual resistance was caused by the torn web panel bearing against the flange. With additional imposed deformation, the flange deformed and pulled on the stiffener that ultimately ruptured as shown in Figure 3-7. When the stiffener failed, the crack propagated in the web next to the flange. The resistance dropped and the test was terminated.



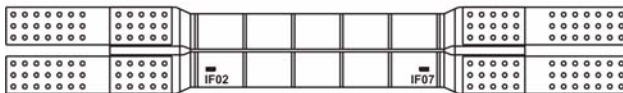
(a) Displacement Transducers



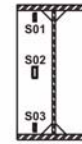
(b) Web Stain Gauges



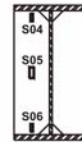
Section A-A



Section B-B



Section C-C



Section D-D

(c) Sections with Flange and Stiffener Gauges

Figure 3-3: Instrumentation of Link H485

### 3.3.3 Shear Deformation Capacity

The link shear deformation capacity was calculated using diagonal measurements across the effective length as described in Appendix A. The cyclic behavior of Link H485 is shown in Figure 3-8. The hysteretic response was ductile and did not exhibit any pinching or strength degradation in the hysteretic loop. After finishing the cycle to  $\pm 0.05$  rad, one of the displacement transducers measuring the average deformation across the effective length malfunctioned. One cycle was completed before the instrument was replaced. This cycle reached deformations of  $0.073$  rad and  $-0.046$  rad, instead of  $\pm 0.06$  rad because the

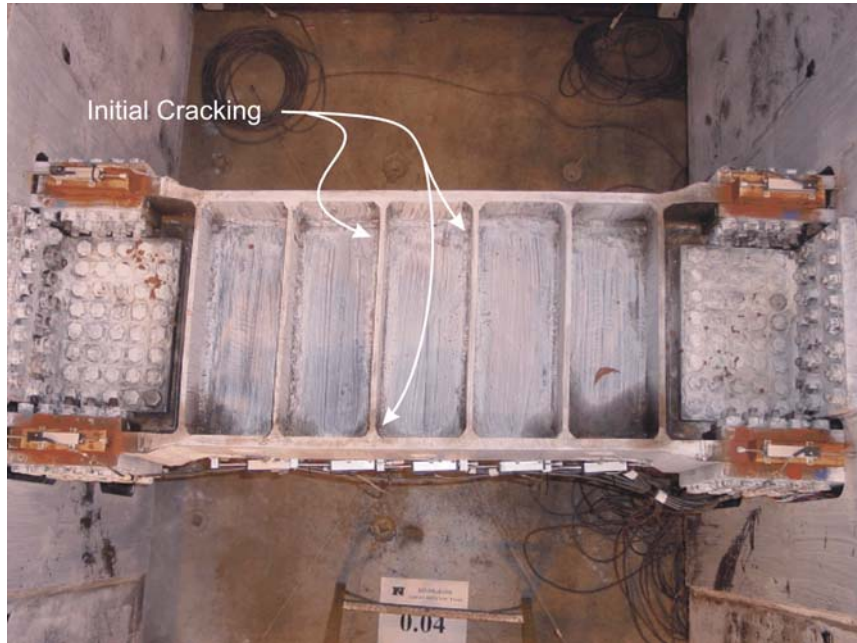


**Figure 3-4: Initial Crack Locations in Link H485**

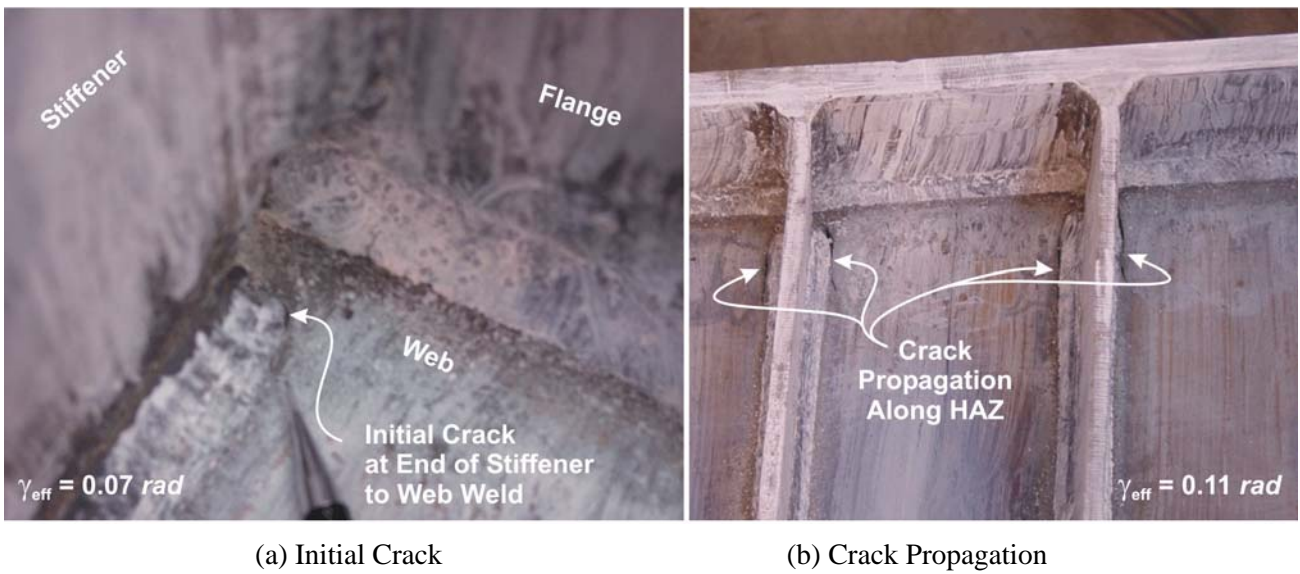


**Figure 3-5: Close-up View of Crack Initiation and Propagation**



**Figure 3-6: Deformed Link H485**

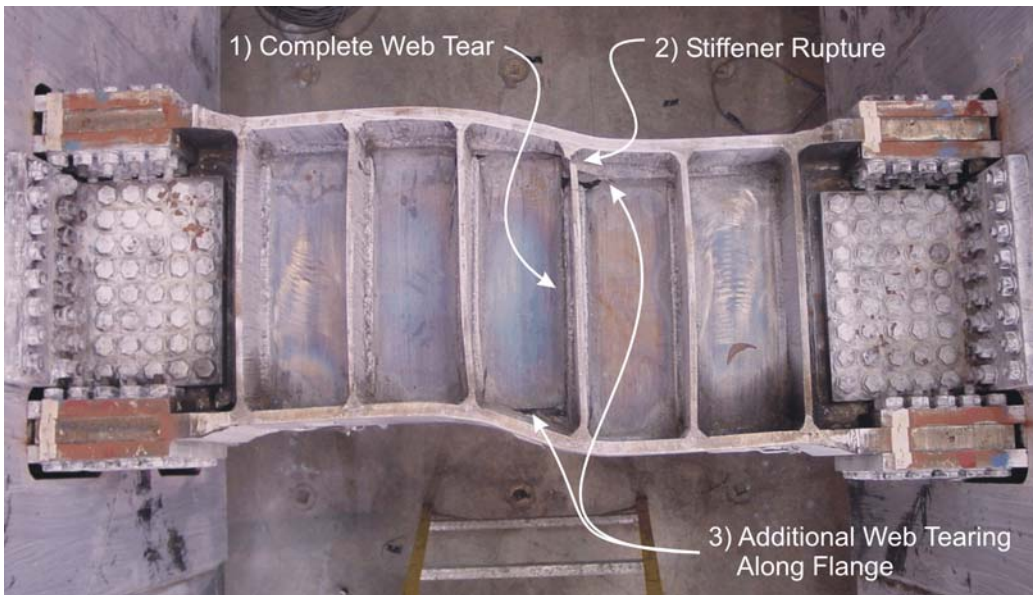


**Figure 3-7: Ultimate Failure of Link H485**

actuator command signal was affected by the instrument malfunction. After the replacement of the faulty instrument, the remainder of the deformation history followed the target values.

The plastic shear deformation calculated using Equation 1-13 is shown in Figure 3-9. The total and the plastic shear deformation are similar due to the high elastic stiffness that is characteristic to shear link

response. The maximum recorded deformations are summarized in Table 3-3. The plastic shear rotation capacity surpassed the AISC implied minimum for EBF shear links of  $0.08 \text{ rad}$  by 47%.

The shear deformation of each panel was found to be proportional to the average deformation of the effective length. As shown in Figure 3-10, the middle panel deformation demand was up to 20% higher than the average, while the demand on the panels next to the connection zone was smaller by approximately the same amount. The higher demand on the middle portion of the link is consistent with visual observations using whitewash.

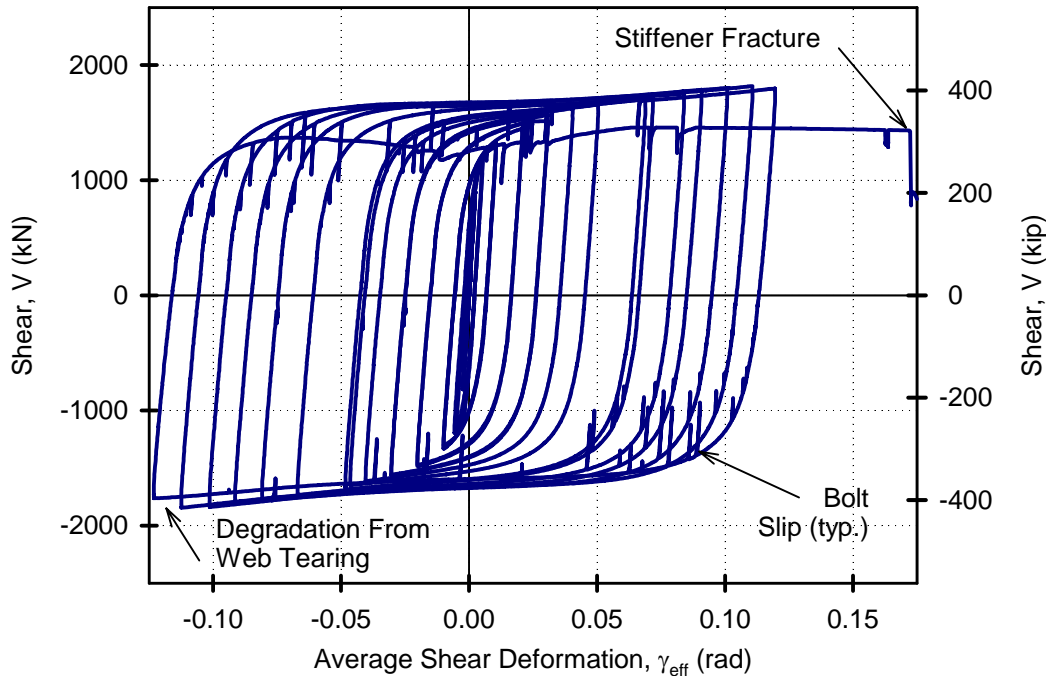


**Figure 3-8: Cyclic Behavior of Link H485**

### 3.3.4 Shear and Moment Resistance

The link shear resistance was calculated from the actuator load and the test setup geometry as described in Appendix A. The shear resistance is shown in Figure 3-8 and was normalized to the shear capacity in Figure 3-9. The shear maxima and the resulting overstrength are summarized in Table 3-3. The overstrength was found to be within the expected values of the AISC provisions for EBF links.

The moment demand at the ends of the effective length was calculated using Equation 1-1. The normalized moment, which is shown on the secondary axis in Figure 3-9, was well below the plastic moment capacity of the section. It was therefore assumed that the link deformation was dominated by shear.

### 3.3.5 Strains

Strains were continuously recorded in the web as well as the flange. Data was extracted from the recordings at each reversal of load, which allowed for data analysis at different milestones within the response.

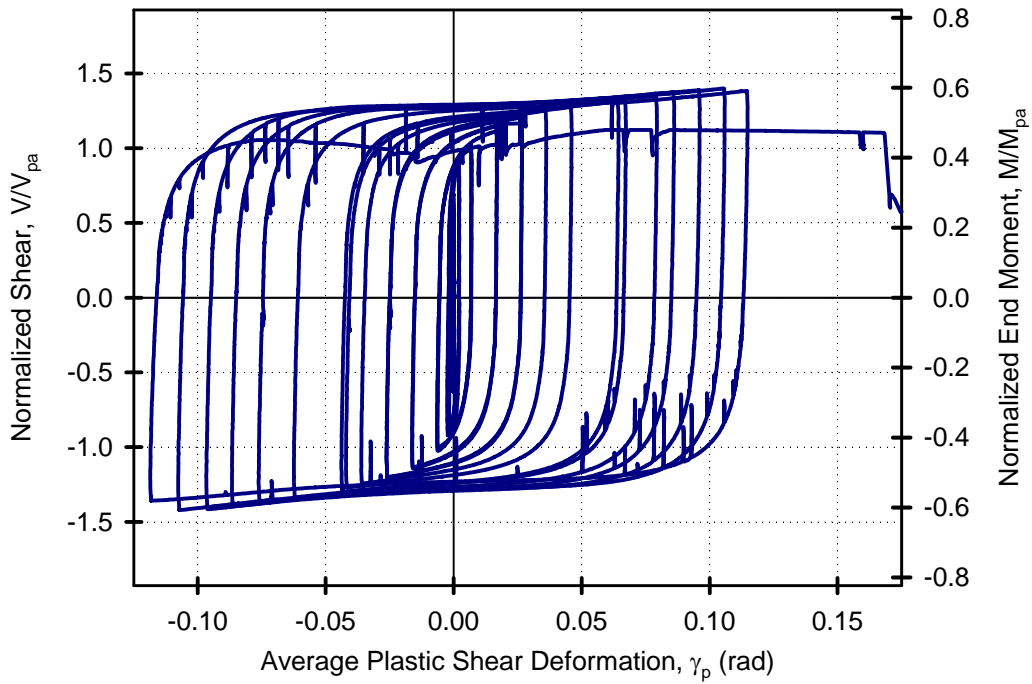


**Figure 3-9: Plastic Cyclic Behavior of Link H485**

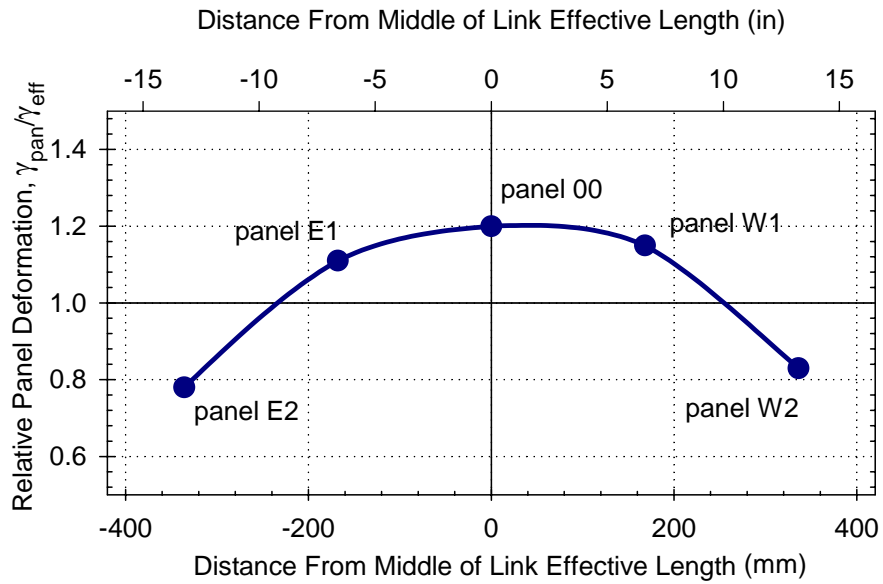


**Figure 3-10: Panel Shear Deformation Along the Length of Link H485**

**Table 3-3: Shear Link H485 Performance Summary**

Link Type	H485
$\gamma_{max}, rad$	0.123
$(\gamma_p)_{max}, rad$	0.118
$V_{max}, kN (kip)$	1845 (415)
$\Omega$	1.42
$M_{max}, kNm (kip ft)$	775 (572)
$M_{max}/M_{pa}$	0.58

The following reversal points were chosen to illustrate the values of recorded strains in the built-up shear link:

- $\gamma_{eff} = \pm 0.02 rad$  for moderate inelastic link deformations;
- $\gamma_{eff} = \pm 0.08 rad$  for the AISC Seismic Provisions implied minima of  $0.08 rad$ ; and
- $\gamma_{eff} = \pm 0.10 rad$  to represent the maximum link deformation before the onset of significant cracking in the web.

### 3.3.5.1 Web Strains

Significant plastic strains were endured by the high performance steel in the web of the shear link. Maximum shear strains were calculated from the three strain components of each rosette. The shear strain distributions through the depth of the web are shown in Figure 3-11 for the middle of panel 00. The shear strains were found to increase with increasing link deformation. In general, the strains decreased with distance away from mid-depth, but again increased at close proximity to the flanges. Shear strains next to the flanges showed significant changes within short distances as shown Figure 3-12, where the mid-depth rosette did not function. Shear strains in the end panel W2 also indicated variation of shear strain through the depth as shown in Figure 3-13 and Figure 3-14 for the middle of the panel and for the end of the effective length respectively.

The shear strain distribution at mid-depth and along the link length is shown in Figure 3-15. The shear strains were not distributed uniformly throughout the link effective length. In general the lowest shear strains occurred near the ends of the effective length. Small increase was apparent at the stiffener of panel W2 and at mid-length.

### 3.3.5.2 Flange Strains

Strains in the flanges were found to increase with increasing link deformation and reached large plastic strains as shown in Figure 3-16. The large strains were localized to the ends of the effective length and rapidly decreased towards the mid-length. Strains were not recorded past the effective length due to the flange thickness transition into the effective zone in that location. The measurements indicated that significant demand was placed near the flange welds at the transition from the thinner flanges into the thicker plate connection zone.

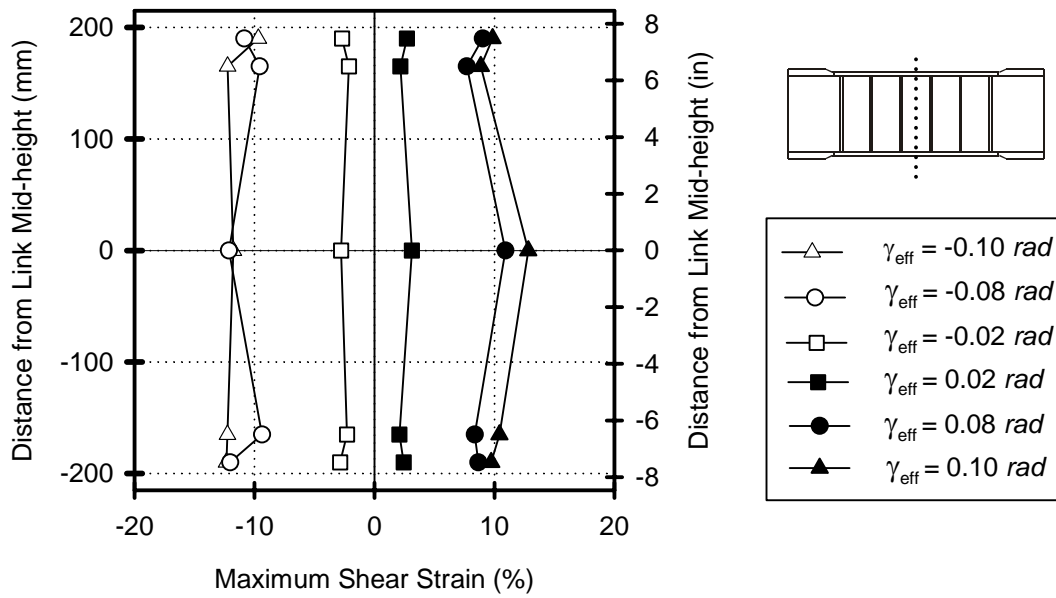


**Figure 3-11: Shear Strain at Mid-length of Link H485**

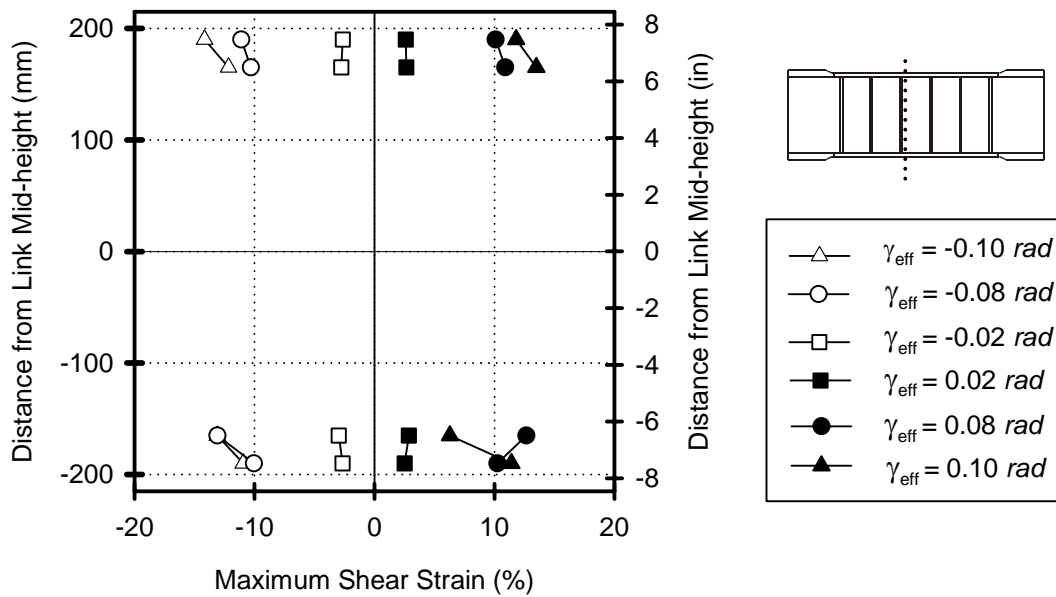


**Figure 3-12: Shear Strain Next to Stiffener in Web Panel 00 of Link H485**

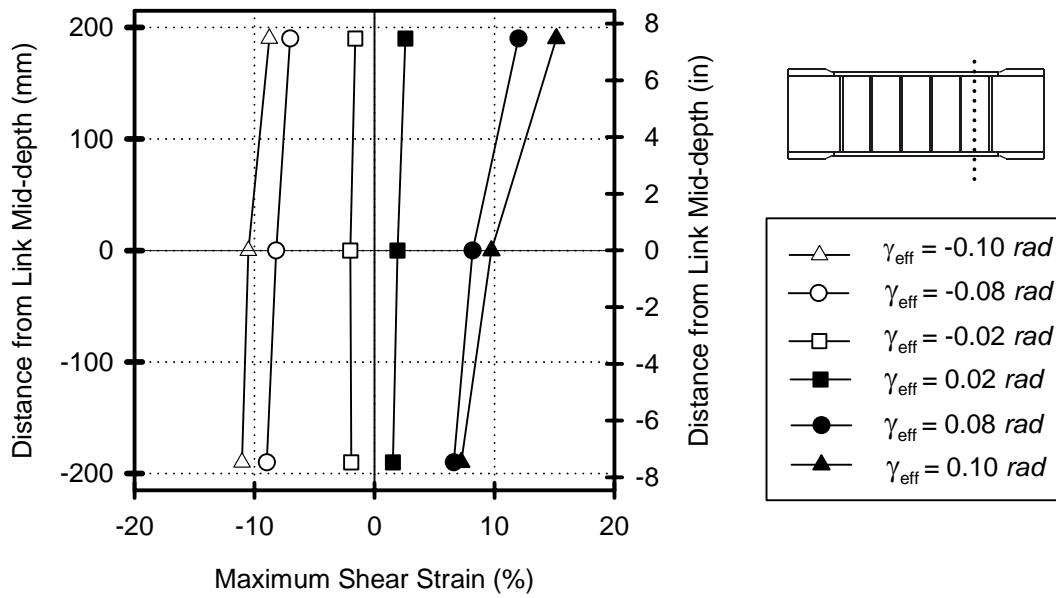


**Figure 3-13: Shear Strain at Mid-length of Link H485**

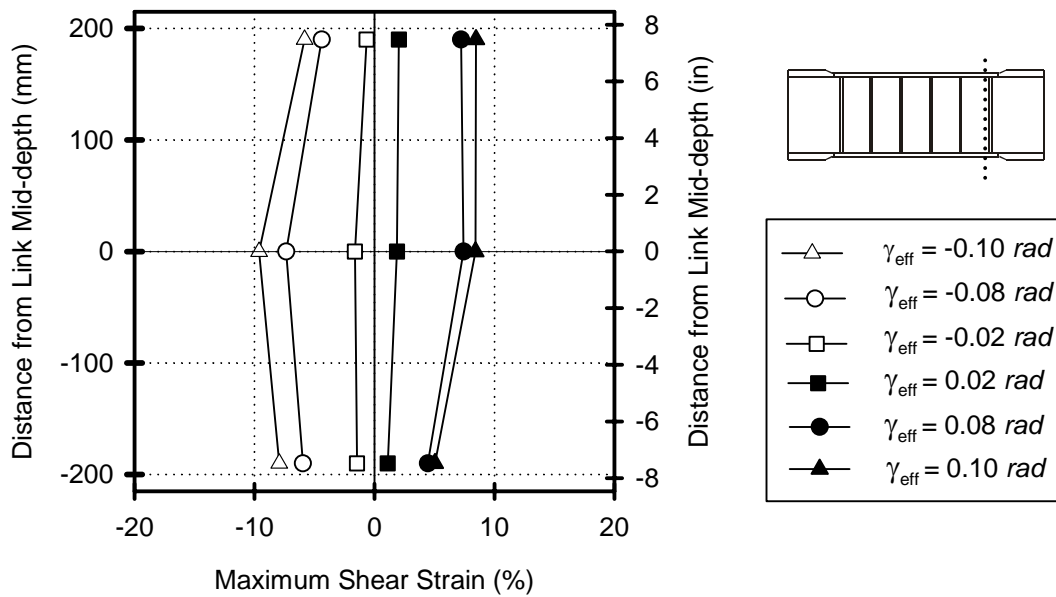


**Figure 3-14: Shear Strain in Web at End of Effective Length of Link H485**

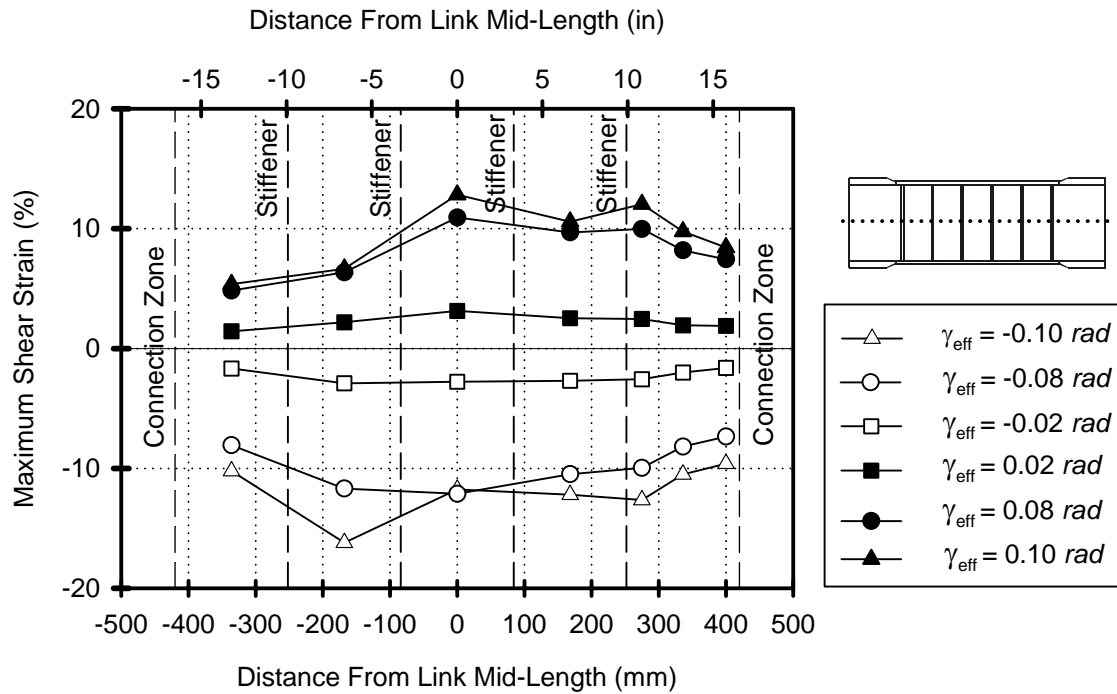


**Figure 3-15: Shear Strain in Web at Mid-depth of Link H485**

Since the moment demand was found to be significantly less than the plastic capacity, it was inferred that the moment demand did not cause the plastic strains at the ends of the effective length. Further, the strain demand at the inside of the flange was not nearly as severe as illustrated by the recorded strains in Figure 3-16. Hence, the flange strains were caused by the imposed deformation that occurred in the transition from the elastic connection zone to the deformed effective length.

### 3.3.5.3 Stiffener Strains

Strains recorded in the stiffeners of panel E2 are shown in Figure 3-18 and Figure 3-19 for the intermediate and end stiffeners respectively. The intermediate stiffener strains were considerably larger near the connection to the flange at larger link deformations. These strains were caused by the imposed relative deformation between the flanges, forcing the stiffener to deform in double curvature. The end stiffener strains were significantly smaller and remained elastic because the stiffener was adjacent to the connection zone.

## 3.4 Summary

A large-scale cyclic experiment was conducted on a built-up shear link designed and fabricated using high performance steel A709 HPS 485W (A709 HPS 70W). The shear link exhibited ductile hysteretic behavior without degradation or pinching of the hysteretic loop. The maximum shear rotation of approximately  $0.12 \text{ rad}$  exceeded the AISC Seismic Provisions implied minimum for EBF shear links, illustrating the suitability of using high performance steel in built-up shear links. The measured overstrength of 1.42 was consistent with the expected overstrength for EBF shear links when using current Seismic Provisions recommendations.

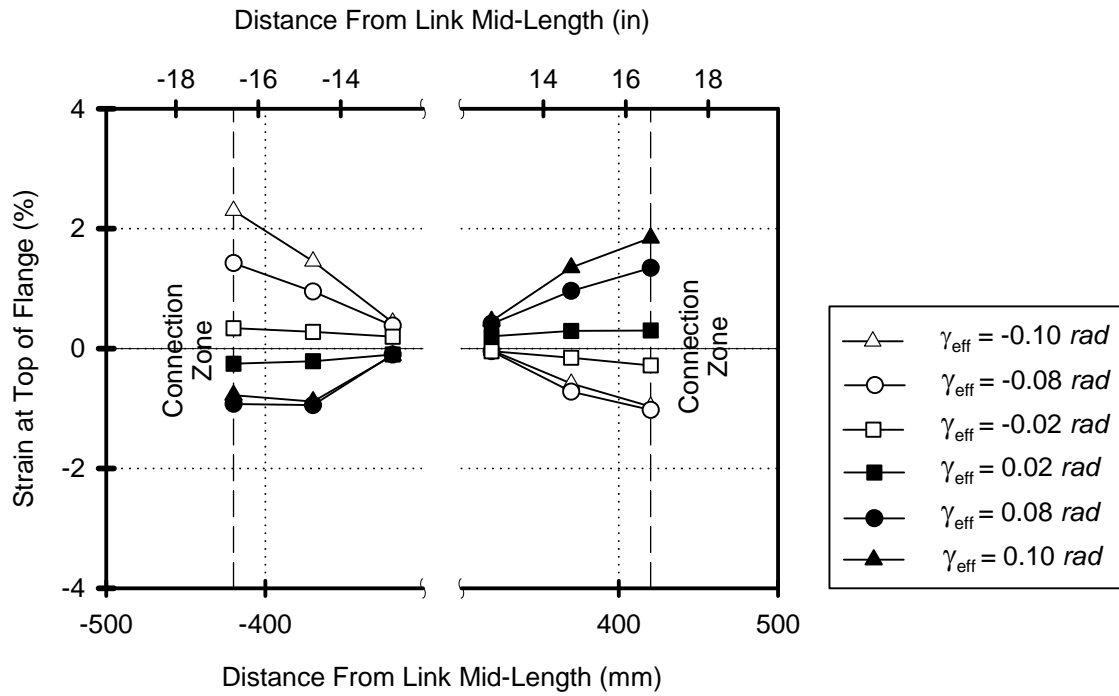


**Figure 3-16: Strains in Outside Face of Flange for Link H485**

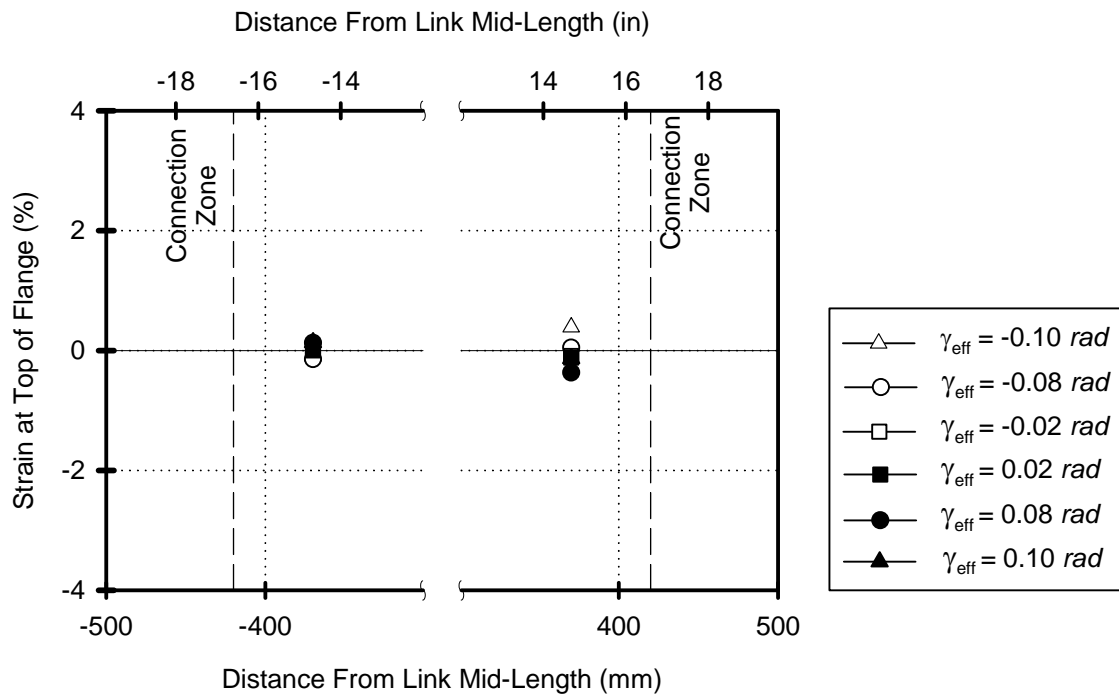


**Figure 3-17: Strains in Inside Face of Flange for Link H485**

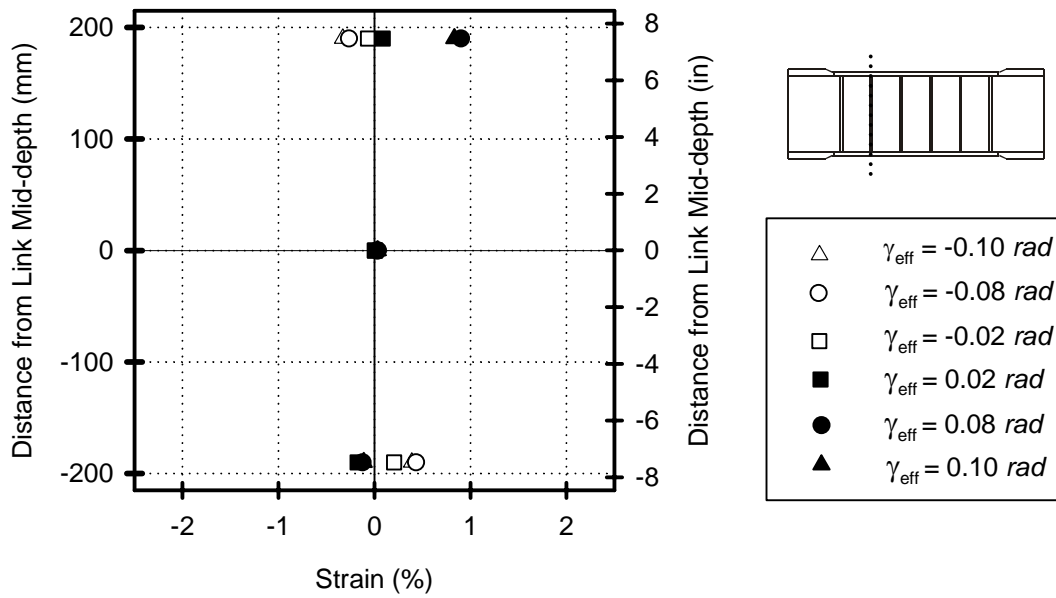


**Figure 3-18: Strains in Intermediate Stiffener of Panel E2**

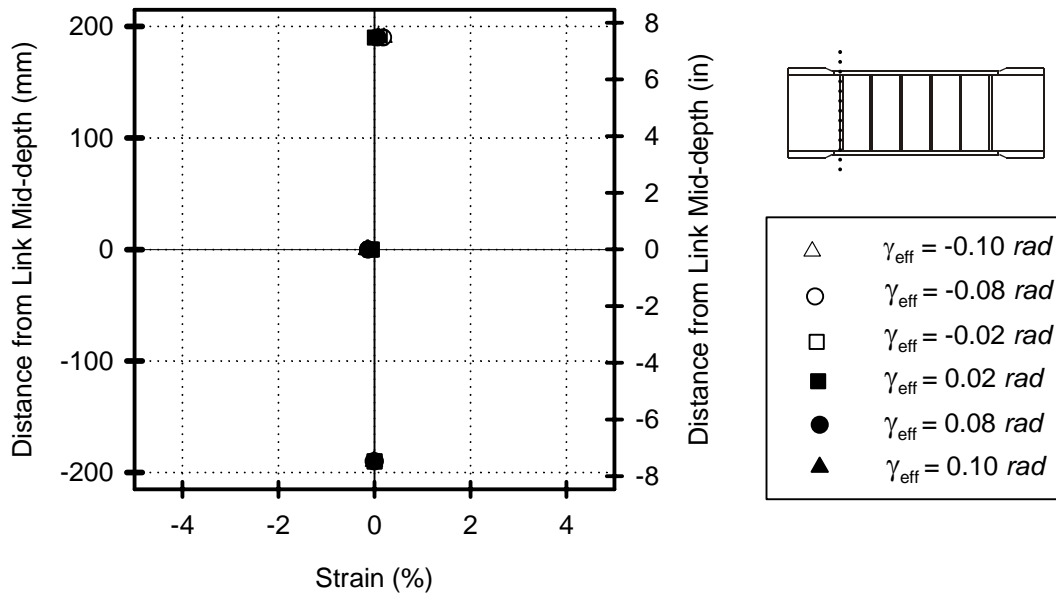


**Figure 3-19: Strains in End Stiffener of Panel E2**

Significant plastic strains were endured by the high performance steel in both the web and flange. The web shear strains were found to vary along the depth as well as the length of the effective length. Localized plastic strains were recorded in the flanges at the ends of the effective length. The flange plastic strains were not caused by the moment demand, but by the local deformations imposed by the change in geometry from the elastic connection zone to the plastically deformed effective length. Localized plastic strains were also recorded in the intermediate stiffeners near the flange welds.

The middle panel shear deformation exceeded the average link shear deformation by up to 20%, leading to the onset of cracking within that panel. The ductile failure mode was contained to within the effective length and was characterized by web tearing. The initial cracks occurred in the web metal and within the heat affected zone next to the ends of the stiffener to web welds. With additional cyclic deformations the cracks tore through the depth of the web, resulting in a ductile ultimate failure.



## SECTION 4

### CYCLIC PERFORMANCE OF SHEAR LINKS DESIGNED USING LOW YIELD POINT STEELS

#### 4.1 Evolution of Shear Link Design Philosophy

The results from experiments on built-up shear links described in previous sections show that built-up sections can exhibit ductile cyclic performance in line with the expectations of current design provisions, which were intended for rolled shapes and for use in building eccentrically braced frames. Consistent trends in the failure modes of the built-up shear links C345a, C345b and H485 were observed. Cracks first developed in the web middle panel and near the ends of the stiffener to web fillet welds. These cracks eventually tore through the web, following the heat-affected zone next to the stiffeners. In addition, increased plastic strains were found to occur in these locations as will be shown through numerical analyses later in Section 6. In order to improve performance and change this mode of failure, two options were considered:

- not welding the stiffeners to the web; or
- removing the stiffeners.

Not welding the stiffeners to the web would rely on the tight fit in restraining the web from buckling. This tight fit may be difficult to achieve without more stringent fabrication tolerances and close quality control. A more significant concern lies in the functionality of such stiffeners. When the stiffener is welded to the web, the out of plane web deformations are resisted by the combined section of the stiffener and partial length of the web. By not having the long edge of the stiffener restrained by the web, the capacity of the stiffener to resist the web out of plane buckling would be significantly reduced.

The latter option of removing the stiffeners was chosen for its simplicity. The intentional exclusion of web stiffeners represents a radical departure from traditional shear link design methodology. Stiffeners are traditionally specified to enhance the performance of shear links by delaying web buckling of rolled wide flange beams. Stiffener spacing in shear links depends on the extent of expected link shear deformation (Kasai & Popov, 1986c) and is given by a relationship involving the web depth and thickness. However, rolled wide flange beams have predetermined web compactness ratios, a limitation that does not exist in built-up shapes. A link without stiffeners can also result in simpler fabrication and potential cost savings in a labor-cost-driven construction industry.

##### 4.1.1 Need for Low Yield Point Steels

Web buckling of shear links must be delayed until the desired performance levels are reached. Without stiffeners, delaying web buckling can be achieved by decreasing the web compactness ratio. In instances where higher stiffness is desired or where depth limitations occur, decreasing the web compactness ratio can only be achieved by increasing the web thickness and thereby increasing the link shear strength. Yet, shear links are intended to act as fuses in seismic design and often require limited yield strengths to satisfy capacity design methodology and protect the integrity of the structure. Based on the relationship in Equation 1-10, lower material yield strength can be used to offset the increase in web area.

The lowest grade of structural plate steel produced in the United States is ASTM A36, with nominal yield strengths of 250 *MPa* (36 *ksi*). However, this grade should be specified with caution as mills often recycle higher strength steels while making A36 grade and the actual yield strengths are typically significantly

higher. Steel mills in Japan produce Low Yield Point (LYP) steels, which were specifically designed for use in seismic applications where the plasticity of the materials would be utilized (Yamaguchi 1998). These steels are used in the buckling restrained braces produced by Nippon Steel, which are also becoming popular in concentrically braced structures in the United States (Sabelli & Aiken 2003).

Two grades are available, with 100 *MPa* (14.5 *ksi*) and 225 *MPa* (32.5 *ksi*) specified yield strengths. The chemical composition of LYP steels is closer to pure iron, with little carbon additives for improved ductility. Both of the available grades were utilized to evaluate the performance of built-up shear links designed without stiffeners.

### 4.1.2 Objectives

Large-scale experiments were used to investigate the performance of built-up shear links and utilizing low yield point steels. Of specific interest were the deformation capacity and the effectiveness of excluding stiffeners on the failure mode. Two different deformation histories were utilized. It was also important to quantify the ultimate shear resistance and overstrength values.

### 4.1.3 Shear Link Designs

The design approach taken in developing the test specimens was to obtain shear links that had the same nominal capacity as the previously tested links, thereby allowing for a comparable evaluation. As such, the nominal plastic shear strength as well as the nominal plastic moment strength were designed to match the properties of Link C345a. Three different types of links were developed: Link L100 from specified 100 *MPa* (14.5 *ksi*) LYP steel, Link L225 from specified 225 *MPa* (32.5 *ksi*) steel and Link X100 from a combination of 100 *MPa* (32.5 *ksi*) LYP steel and high strength structural grade steel.

Each link consisted of an effective length in the middle and connection zones at the ends as shown in Figure 4-1(a). The effective lengths were designed to plastically deform, while the connection zones were used to bolt the links into the test setup and were intended to remain elastic. Mills in Japan do not produce high performance steel and hence the high strength structural grade BT-HS440C steel was substituted for use in the connection zones of the specimens. The nominal yield strength of this grade is 440 *MPa* (65 *ksi*), which is comparable to the high strength structural steels in the United States. The effective lengths of Links L100 and L225 were designed following the provisions for EBF shear links reviewed in Section 1.1.2. The connection details of the test setup restricted the web height to 430 *mm* (16.9 *in*). The web thickness was determined based on Equation 1-2 and the respective material yield strengths to achieve the plastic shear capacity. The flange dimensions were determined by simultaneously solving Equation 1-3 along with the flange compactness constraint that also matched Link C345a. The resulting dimensions of the links are shown in Figure 4-1(c) and the nominal design properties are summarized in Table 4-1.

No intermediate stiffeners were used in any of the links because the web compactness ratios were significantly lower than the ratios on which the Seismic Provision recommendations were based. The simplified Equation 1-5 and Equation 1-6 used to determine the stiffener spacing was conservatively developed on the restricted geometries of rolled shapes and web compactness ranging from  $h_w/t_w = 40$  to 57 (Kasai & Popov 1986c). Figure 4-2 summarizes the web compactness of all available wide flange shapes obtained from the Manual of Steel Construction (AISC 2001). For comparison, the web compactness ratios of all of the built-up shear link specimens are also shown. The web of the links designed using the low yield point steels did not exceed  $h_w/t_w = 20$ . If the AISC Seismic Provisions were to be applied to the links designed using low yield point steels, the implied deformation capacity would be reduced based on a linear interpolation between Equation 1-5 and Equation 1-6 and would result in an implied capacity of  $\gamma_p = 0.054 \text{ rad}$

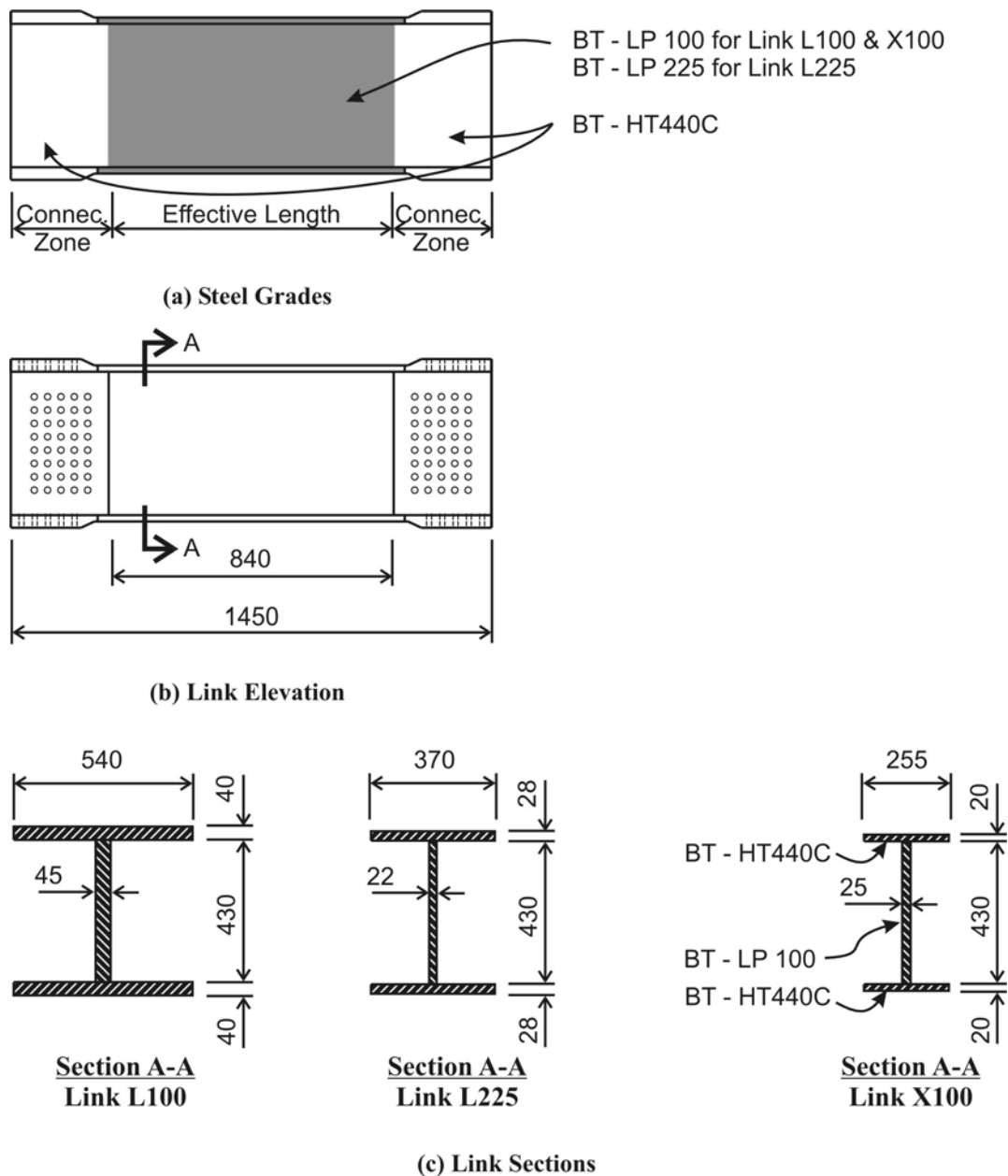


**Figure 4-1: Details of Shear Links without Stiffeners**

and  $0.067 \text{ rad}$  for the two links respectively. To investigate the applicability of the stiffener spacing recommendations of the AISC Seismic Provisions, no intermediate stiffeners were used in the shear links made from low yield point steels. Stiffeners at the ends of the effective length were also excluded because unlike EBFs, the load path did not involve a bracing element.

The incentive for developing Link X100 was to further evolve the design of built-up shear links by taking advantage of the different steel strengths and evaluate the performance of a hybrid section. The web was designed using the lower yield strength steel to decrease the web compactness ratio and reduce nominal

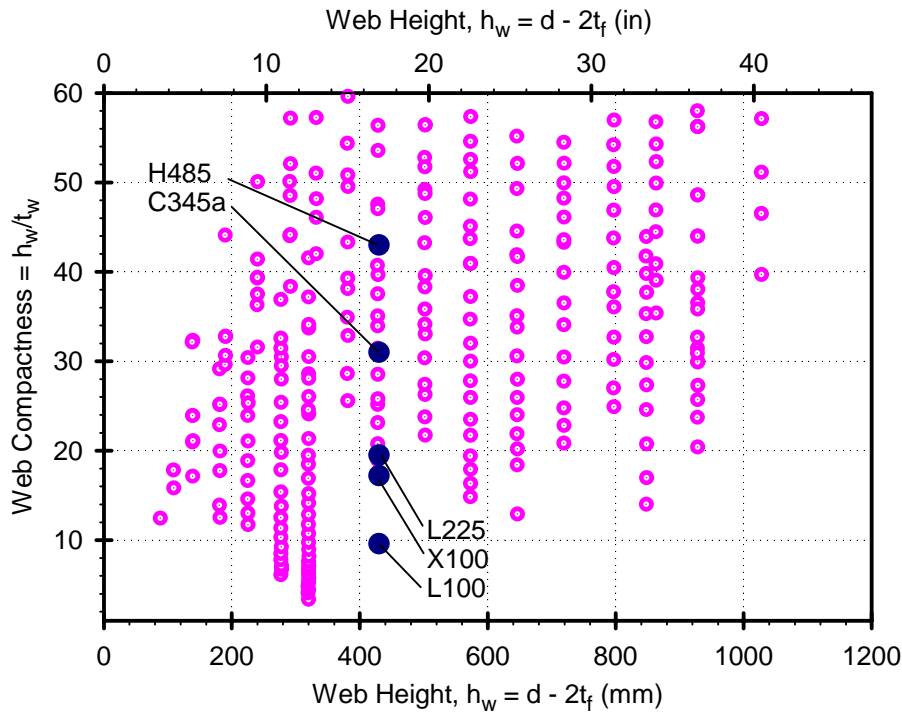


**Figure 4-2: Web Compactness Comparison to Available Rolled Sections**

shear strength. The flanges were designed using the higher grade steel to provide sufficient moment capacity while maintaining flange sizes that would be comparable with traditional beam section. The extremes of the specified yield strength range were chosen by adopting LYP with 100 MPa (14.5 ksi) specified yield strength for the web and BT-HS440C for the flanges. Initially the web of Link X100 was identical to the web of L100 so that the nominal shear design capacities were the same. However, after observing the high overstrength values and resulting connection failures in Link L100, which are discussed in detail in Section 4.3.2, the web thickness was machined down by 45% to 25 mm (1.0 in). It was reasoned that if similar overstrengths occur, the ultimate shear resistance would be similar to previously tested links.

**Table 4-1: Nominal Design Properties of Built-up Shear Links Designed Without Stiffeners**

Design Property	Link Type		
	L100	L225	X100
$e, mm (in)$	840 (33.1)	840 (33.1)	840 (33.1)
$V_p, kN (kip)$	1161 (261)	1277 (287)	645 (145)
$M_p, kNm (kip ft)$	1223 (902)	1296 (956)	1125 (830)
$e/h_w$	1.95	1.95	1.95

**Table 4-1: Nominal Design Properties of Built-up Shear Links Designed Without Stiffeners**

Design Property	Link Type		
	L100	L225	X100
$h_w/t_w$	9.5	19.5	17.2
$b_f/2t_f$	6.8	6.6	6.4

The actual yield strengths of the steels used for the webs of the link specimens were determined from a series of experiments conducted on coupons machined from the same heat steel (Dusicka et al 2004). The measured yield strengths of the plates and the shear and moment capacities based on those values are summarized in Table 4-2. The yield strength of the plates used for the flanges was obtained from the mill certificates. The measured yield strength was lower than specified for the steel in Link LYP 100 and resulted in shear link capacities that were lower than the design nominal strengths.

**Table 4-2: Capacity of Built-up Steel Shear Links Designed Without Stiffeners**

Capacity Property	Link Type		
	L100	L225	X100
$f_{yaw}$ , MPa (ksi)	76.5 (11.1)	242 (35.1)	76.5 (11.1)
$f_{yaf}$ , MPa (ksi)	88 (12.7)*	223 (32.3)*	501 (72.7)*
$V_{pa}$ , kN (kip)	888 (200)	1374 (309)	493 (111)
$M_{pa}$ , kNm (kip ft)	936 (690)	1394 (1028)	1238 (913)
$2M_{pa}/(eV_{pa})$	2.51	2.42	5.98

\* obtained from mill certificates

#### 4.1.4 Fabrication and Test Setup

The steel and the fabrication was provided by Nippon Steel, Japan. A photograph of the different types of links prior to installation is shown in Figure 4-3. The links were delivered with two attachment points welded onto the flanges of each link. These were not specified in the fabrication drawings and were ground off prior to the experiments. The test setup described in Appendix A and corresponding to the transverse orientation of the shafts was used, with one shear link installed for each test. The link connection zones were drilled on site immediately prior to each installation to ensure proper fit into the connections of the test setup.

The wide flange dimensions of Links L100 and L225 required the use of customized splice plates to accommodate the existing test setup. These splice plates fitted in the narrow opening in the shafts and widened to transfer the force from the connection to the full width of the shear link flanges. A photograph of the splice plate connection is shown in Figure 4-4. Splice plates from experiments on Link C345a were

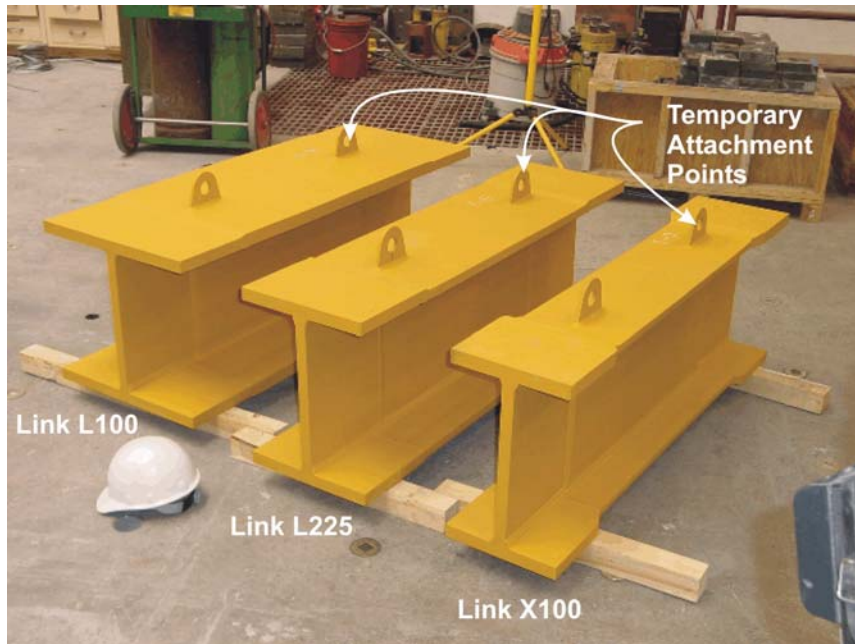


**Figure 4-3: Photograph of Shear Links without Stiffeners**

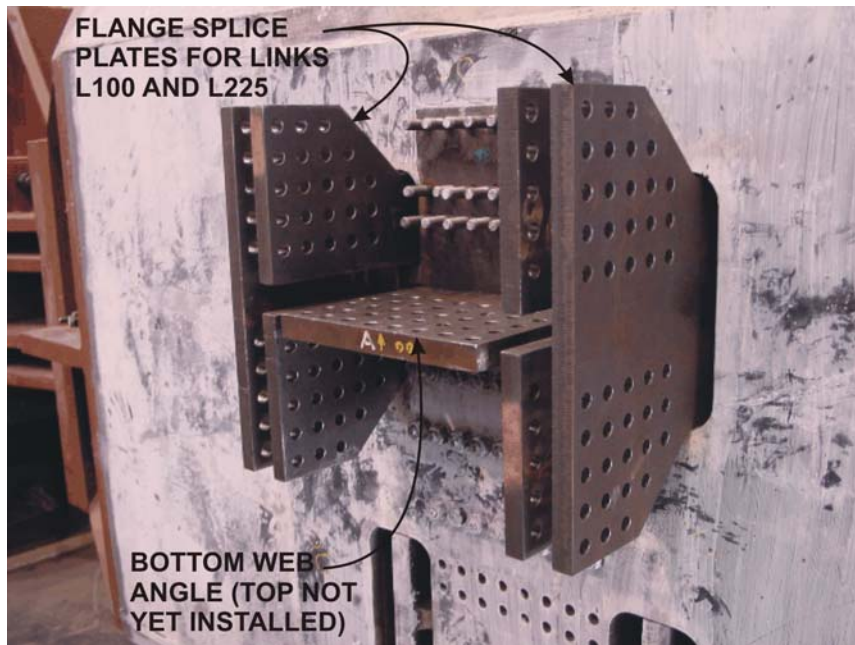


**Figure 4-4: Splice Plate Connection for Links L100 and L225**

reused for Link X100, because the flange connection zone was designed to have the same dimensions to accommodate the higher strength flanges used in the hybrid section. The link connection to the tower shafts consisted of a minimum of 232 - A490 M16 (5/8 *in*) diameter bolts.

## 4.2 Deformation History and Instrumentation

Two different deformation histories were applied to the three types of built-up shear links, resulting in six unique experiments. The link response was measured by electronic instruments and the data recorded on personal computers in tab delimited format at 1 Hz sampling frequency.

### 4.2.1 Deformation Histories

The actuator was controlled based on the link shear rotation angle  $\gamma_{eff}$ , which was calculated using displacement transducers installed across the effective length as described in Appendix A. Two displacement histories were utilized; incremental cyclic and near-fault deformation history. The incremental cyclic deformation history followed the sequence described in Section 2.2.1. This cyclic load history is suitable for evaluating the performance of structural components provided that the expected ground motion does not contain a large displacement pulse, such as those experienced from near-fault events. Response of structures to near-fault ground motions is often characterized by one large excursion, followed by smaller cycles with a mean deformation offset.

The development of a near fault loading history for built-up shear links was outside the scope of this research, but a near-fault loading history had been developed as part of the SAC Joint Venture following the Northridge earthquake to test seismic performance of moment frame components (Krawinkler et al 2000). The load history shown in Figure 4-5 was based on the storey drift angle  $\theta$ , calculated as a building's drift over height. However, the demand imposed onto the structural components depends on the overall configuration of the component within the entire structure. In the case of shear links, the lateral drift can be related to the shear deformation of the effective length  $\gamma_{eff}$  simply by the geometry, as discussed in Section 1.1.3 for eccentrically braced frames. For the results of the experiments on built-up shear links to remain as general as possible, the near-fault loading history was reformulated for shear deformation of the effective length as shown in Figure 4-5. The maximum shear rotation demand of 0.15 *rad* was chosen based on the response and achieved deformation capacity observed in specimens subjected to the incremental cyclic deformation history discussed in Section 4.3. This level of deformation was achieved in all three types of links using the incremental cyclic deformation history.

The basis for the near-fault deformation history was developed while considering the response of special moment resisting frame buildings to near-fault ground motions in the Los Angeles area. It is recognized that building structural systems utilizing shear links typically result in stiffer response and lower natural periods, which may bring into question the suitability of this load history for built-up shear links. However, the large-capacity shear links considered for this study were intended for use in bridges. Bridges are heavier structures that even when braced can have long natural periods of vibration that can exceed that of the flexible building moment frames. As an extreme example, the first transverse natural period of vibration of the new San Francisco-Oakland Bay Bridge was 3.7 *sec* (McDaniel 2003). The use of the near-field loading history developed for the moment frames was therefore reasonable in investigating the built-up shear link response to near-fault seismic events.

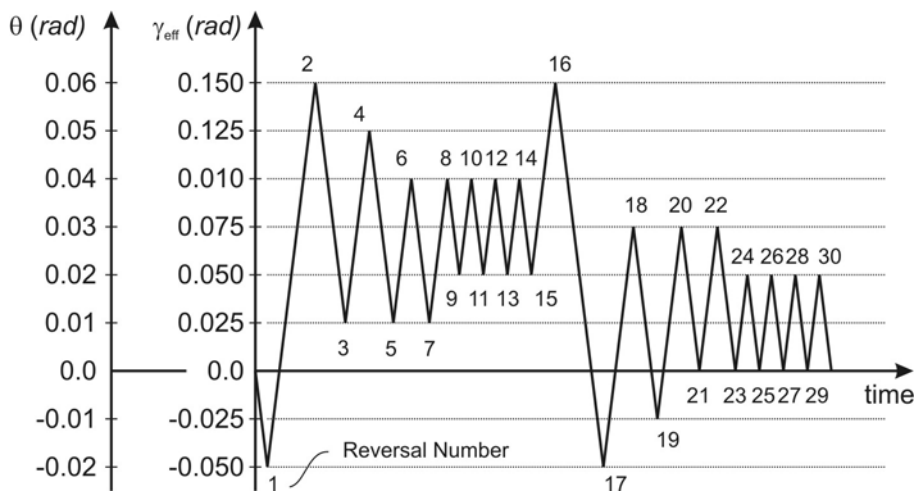


**Figure 4-5: Near-Fault Deformation History Set**

#### 4.2.2 Instrumentation and Data Acquisition

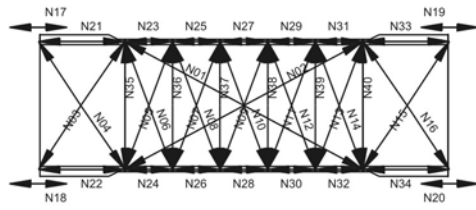
The same data acquisition system and instrument types were used as those described in Section 2.2.2. The gauge location and reference numbers of each specimen was identical among the six specimens. Typical instrumentation layout is shown in Figure 4-6. The locations of the rosette gauges were chosen to capture the shear strain distribution in the web. Seven rosettes were placed through the depth to record web shear strains at mid-length as well as the end of the effective length. Since no stiffeners were used at the ends, sufficient space was available to include shear strain measurements in the connection zone of the link. Additional rosettes were included along the length at mid-depth. Flange strains were measured at the ends of the effective length where localized deformations occurred in previous tests and where the weld transition to the connection zone was located.

#### 4.3 Results from Incremental Cyclic Experiments

This section reviews the observations and results from experiments on three types of built-up shear links designed without stiffeners and subjected to incremental cyclic deformation history. The link shear deformation was calculated from displacement transducers and the shear resistance from the actuator load and test setup geometry as described in Appendix A. Discussion and comparison of the cyclic response relative to shear links designed with stiffeners is included in Section 5.

##### 4.3.1 Visual Observations and General Comments

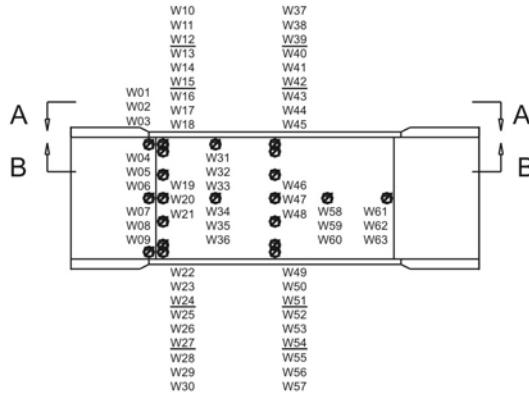
Paint was removed from the web of the effective length, but the connection zones were left painted. The paint between the splice plates and web angles aided in gradual bolt slip of the connections during testing and significantly reduced the sudden reductions in resistance that were common in previous experiments. A square grid of approximately 50 mm (2 in) spacing was drawn on the web of the effective length to aid visual observations throughout the response.



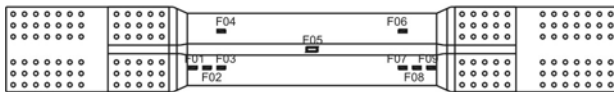
(a) Displacement Transducers

LEGEND:

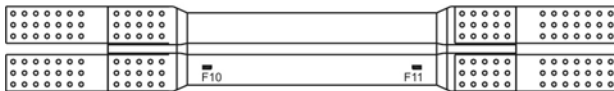
-  displacement transducer
-  rosette strain gauge
-  strain gauge



(b) Web Strain Gauges



Section A-A



Section B-B

(c) Sections with Flange and Stiffener Gauges

**Figure 4-6: Typical Instrumentation of Link without Stiffeners**

The links generated noticeable heat during testing, especially after large deformation cycles. A thermocouple was used to measure the temperature at the center of Link L100 web after the completion of deformation cycles throughout the history. The temperature of other links was not measured. The recordings of  $\Delta T$ , the temperature change from ambient of  $30^{\circ}\text{C}$  ( $85^{\circ}\text{F}$ ) to that of the link, are summarized in Table 4-3.

**Table 4-3: Nominal Design Properties of Built-up Shear Links without Stiffeners**

$\gamma_{eff}, rad$	$\Delta T, ^\circ C (F)$	$\gamma_{eff}, rad$	$\Delta T, ^\circ C (F)$
0.01	1.0 (1.8)	0.10	16 (29)
0.03	2.0 (3.6)	0.11	17 (31)
0.05	6.6 (12)	0.12	23 (41)
0.06	7.4 (13)	0.13	24 (43)
0.07	9.2 (17)	0.14	26 (47)
0.08	12 (22)	0.15	27 (49)
0.09	16 (29)	0.16	27 (49)

The elevated temperatures from these cyclic deformations illustrate the potential for developing significant heat during dynamic tests. The heat in the links does not only depend on the rate of loading, but also on the heat dissipation characteristics of the link and the surrounding structure. The temperature was found to decrease at the ends of the link and near the flanges. For example, at  $\gamma_{eff} = 0.10 rad$ , the web temperature was  $3^\circ C$  lower at the flanges at mid-length and  $5^\circ C$  lower at the connection zones.

### 4.3.2 Cyclic Response of Link L100

The experiment on Link L100 using the incremental cyclic deformation history was conducted on July 21<sup>st</sup>, 2003.

#### 4.3.2.1 Failure Mode

The first crack occurred in the web at the corners of the effective length at  $\gamma_{eff} = 0.10 rad$  as shown in Figure 4-7, but did not propagate with increasing deformations. No buckling or out of plane distortion of the web or the flange were observed. Localized cracking was observed at the inside face of the flange, next to the weld between the web and the flange as shown in Figure 4-8 at  $\gamma_{eff} = 0.15 rad$ . The cracking appeared to tear the low yield point steel at the base of the weld. The overall behavior of the effective length did not exhibit any indication of failure, but the connection regions gradually showed increasing signs of distress.

At  $\gamma_{eff} = 0.11 rad$ , a bolt in the web angle to tower shaft connection fractured. Two additional bolts fractured at similar locations during  $\gamma_{eff} = 0.15 rad$  cycle as shown in Figure 4-9. Before any failure occurred in the effective length, the connection fractured by shearing through the web bolt holes as shown in Figure 4-10. Numerous bolts were permanently deformed and flange splice plates were bent in the process.

#### 4.3.2.2 Shear Deformation Capacity

The ultimate deformation capacity of Link L100 was not achieved due to the premature connection fracture. Nonetheless, the cyclic response shown in Figure 4-11 was ductile and did not exhibit any pinching or degradation of the hysteretic loop. The plastic shear deformation was calculated using Equation 1-13 and is shown in Figure 4-12. The maximum deformation values achieved prior to the connection failure are sum-

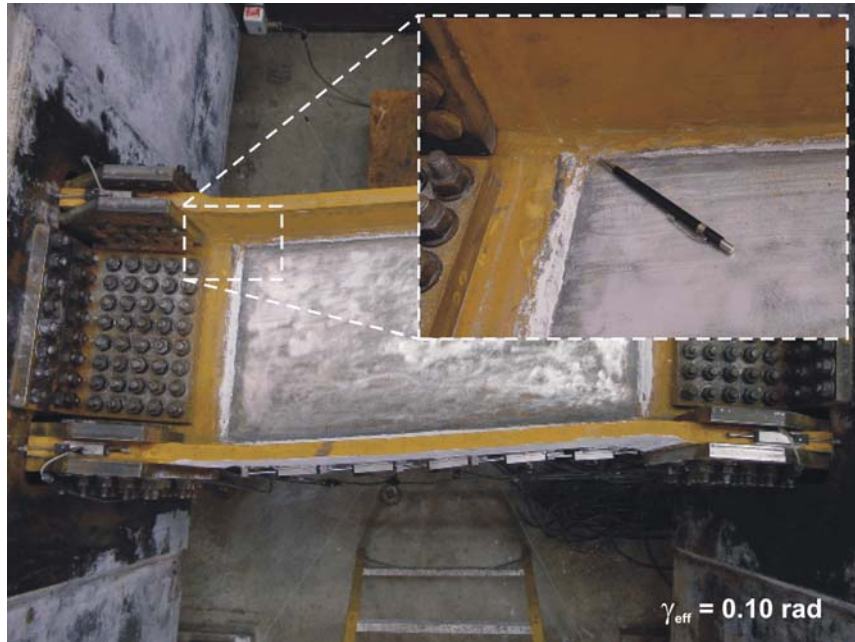


**Figure 4-7: Location of Initial Cracks in Link L100**

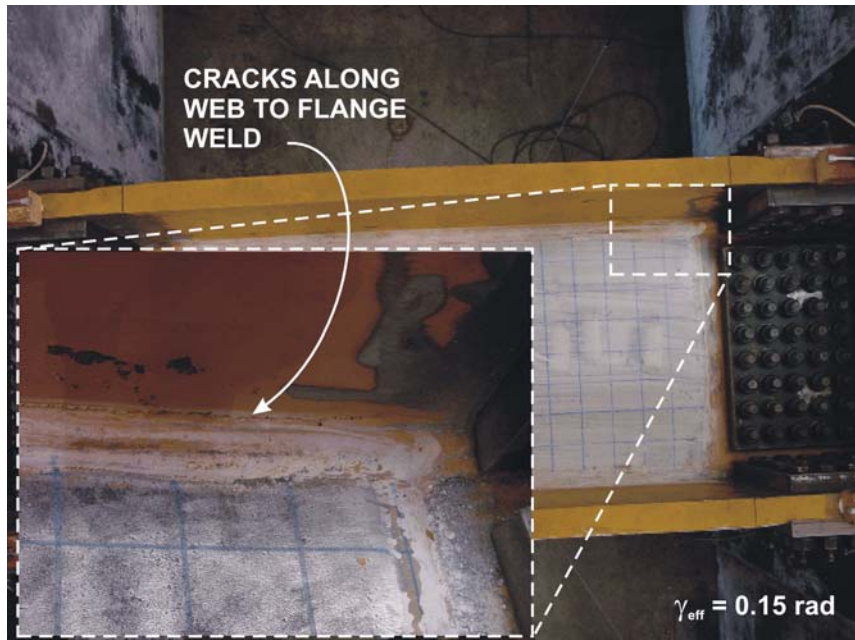


**Figure 4-8: Flange Tearing Next to Web Weld in Link L100**



**Figure 4-9: Bolt Fracture in Connection Zone of Link L100**



(a) Connection Zone

(b) Connection Zone After Angle Removal

**Figure 4-10: Fracture of Connection in Link L100**

marized in Table 4-4. The lack of significant cracking or other distress within the effective length indicated that additional deformation capacity was still possible for this type of built-up shear link.

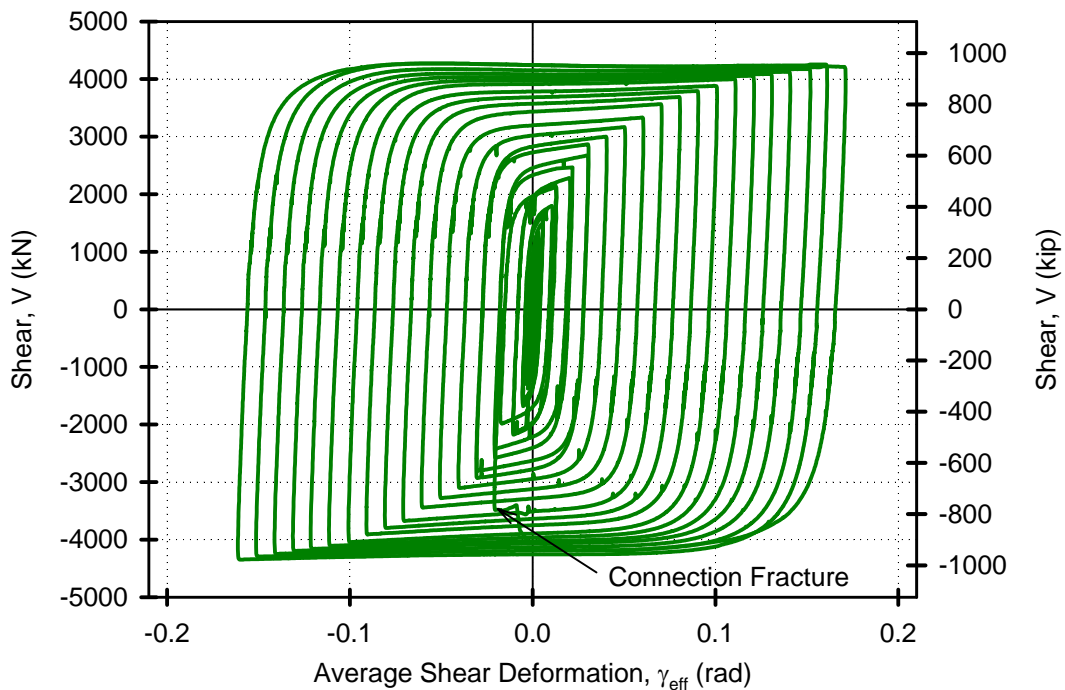


**Figure 4-11: Cyclic Behavior of Link L100**

#### 4.3.2.3 Shear and Moment Resistance

The shear resistance is shown in Figure 4-11 and was normalized to the shear capacity  $V_{pa}$  in Figure 4-12. The resulting overstrength summarized in Table 4-4 was found to be significantly higher than any expected or previously reported results. The fracture of the connection zone was a direct result of the forces generated within the effective length. The connection design strength was 2.7 times the nominal capacity of the link. The connection failure illustrated the importance of quantifying the maximum forces generated by the shear link for design. The moment demand at the ends of the effective length was calculated using Equation 1-1 and is shown on the secondary axis in Figure 4-12. Due to the high overstrength, the moment demand also exceeded the plastic moment design strength by 95%.

#### 4.3.3 Cyclic Response of Link L225

The experiment on Link L225 using the incremental cyclic deformation history was conducted on July 9<sup>th</sup>, 2003.

##### 4.3.3.1 Failure Mode

The ultimate failure mode of Link L225 was ductile and characterized by web tearing. Cracks initially appeared in the corners of the web within the effective length at  $\gamma_{eff} = 0.09 \text{ rad}$  as shown in Figure 4-13.

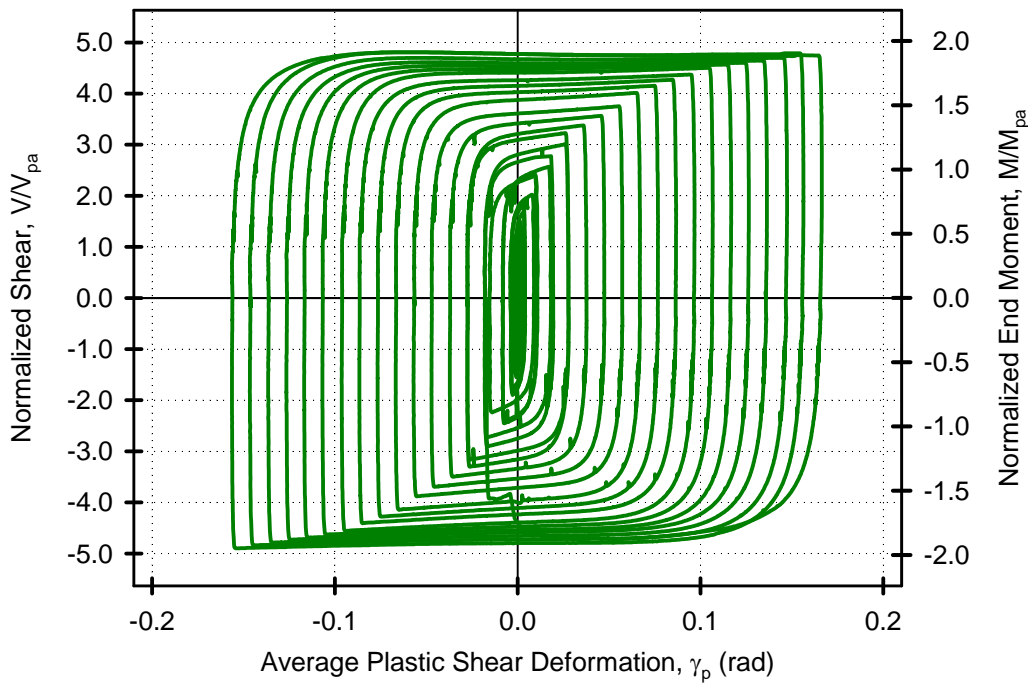


**Figure 4-12: Normalized Cyclic Plastic Behavior of Link L100**

Once formed, these cracks did not propagate with increasing deformations and remained approximately 10 mm (0.4 in) long. Out of plane web bending was first observed at  $\gamma_{eff} = 0.09 \text{ rad}$ , and was only detectable when a straight edge was placed against the web. The bending became more pronounced with increasing link shear deformations, but did not immediately degrade the shear link resistance. At large link shear deformations, the distorted web formed a strut between the diagonal corners of the effective length as shown in Figure 4-14.

At  $\gamma_{eff} = -0.18 \text{ rad}$ , the corner cracks started to grow along the flange weld with increasing link deformations. The ultimate failure was ductile and occurred after the reversal at  $\gamma_{eff} = 0.20 \text{ rad}$ . The web tearing did not extend outside the effective length and mainly travelled parallel to the full joint penetration welds along the flange and the connection zone as shown in Figure 4-15.

#### 4.3.3.2 Shear Deformation Capacity

The cyclic response was ductile and did not exhibit any pinching or degradation of the hysteretic loop until the last cycle as shown in Figure 4-16. A combination of the web out of plane distortion and crack growth contributed to the resistance decrease. The plastic shear deformation was calculated using Equation 1-13 and is shown in Figure 4-17. The shear link deformations were dominated by plastic behavior. The ultimate deformation capacities were obtained from the last completed reversal and are summarized in Table 4-4. The deformation capacity exceeded the AISC implied minimum of  $\gamma_p = 0.08 \text{ rad}$  by 246%.



**Figure 4-13: Location of Initial Cracks in Link L225**



**Figure 4-14: Web Out of Plane Web Deformation of Link L225**

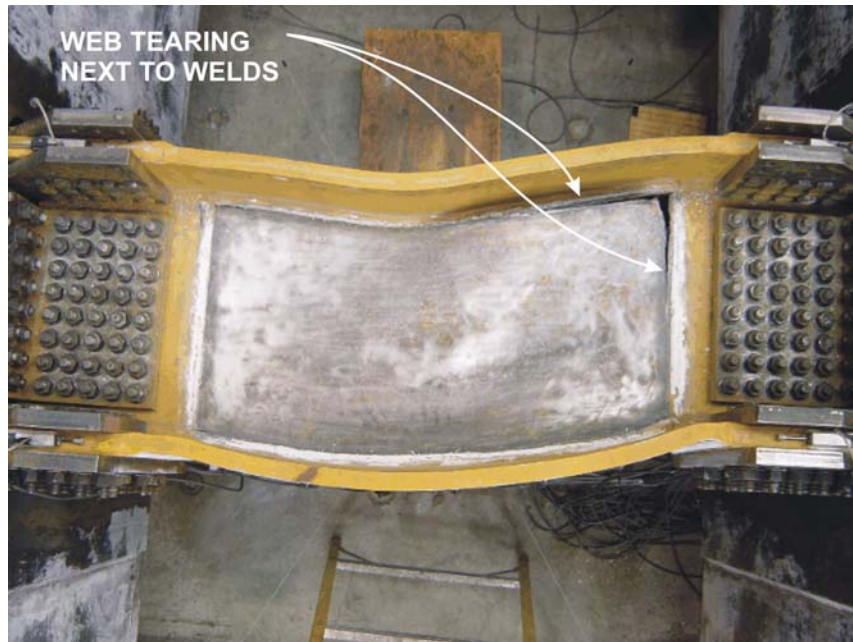


**Figure 4-15: Ultimate Failure of Link L225**

#### **4.3.3.3 Shear and Moment Resistance**

The shear resistance is shown in Figure 4-16 and was normalized to the shear capacity in Figure 4-17. The resulting overstrength summarized in Table 4-4 exceeded the expected values of the AISC provisions for EBF links by 24%. The moment demand at the ends of the effective length was calculated using Equation 1-1 and is shown on the secondary axis in Figure 4-17. The demand was well below the plastic moment capacity.

#### **4.3.4 Cyclic Response of Link X100**

The experiment on Link X100 using the incremental cyclic deformation history was conducted on September 3<sup>rd</sup>, 2003.

##### **4.3.4.1 Failure Mode**

The ultimate failure mode of Link X100 was ductile and was characterized by out of plane web bending and web tearing. The first crack first developed in one of the corners of the web within the effective length at  $\gamma_{eff} = 0.05 \text{ rad}$  as shown in Figure 4-18. The crack remained approximately 6 mm (0.25 in) in length and did not propagate with increasing deformations until the cycle  $\gamma_{eff} = 0.17 \text{ rad}$  was completed. At that time the crack grew to form a corner crack measuring 6 mm (0.25 in) by 8 mm (0.30 in). Similar web cracking occurred diagonally across on the other side of the effective length at  $\gamma_{eff} = 0.19 \text{ rad}$ . Cracking was also observed at the ends of the effective length.

In addition to the web and flange cracks, out of plane web deformations was detected using a straight edge after the completion of cycle  $\gamma_{eff} = \pm 0.11 \text{ rad}$ . These deformations became more pronounced with increas-

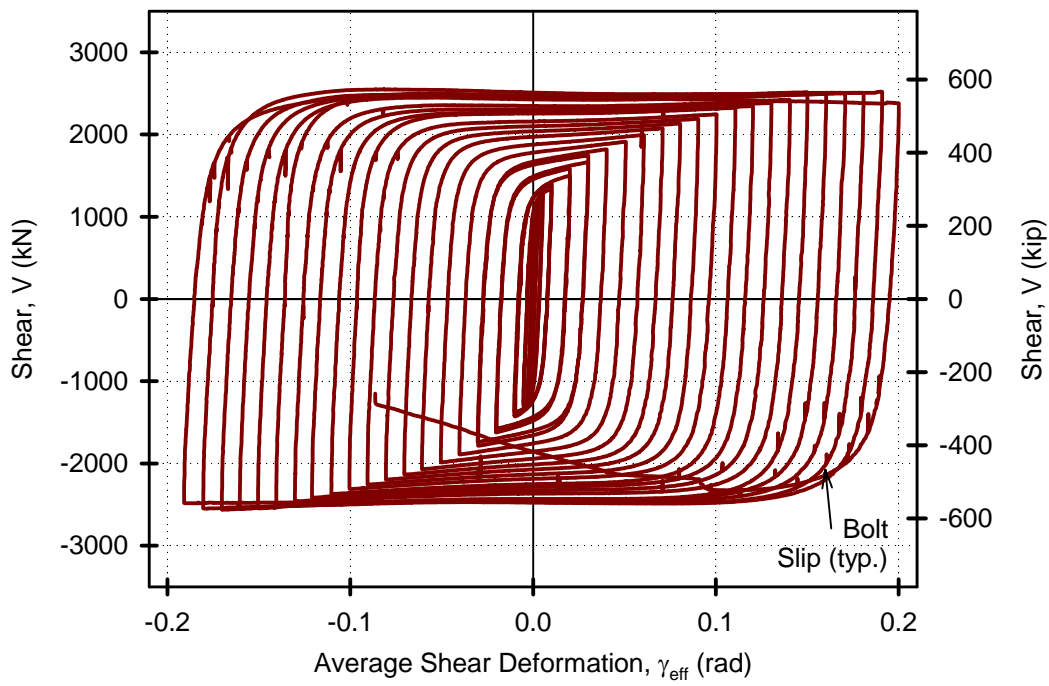


**Figure 4-16: Cyclic Behavior of Link L225**

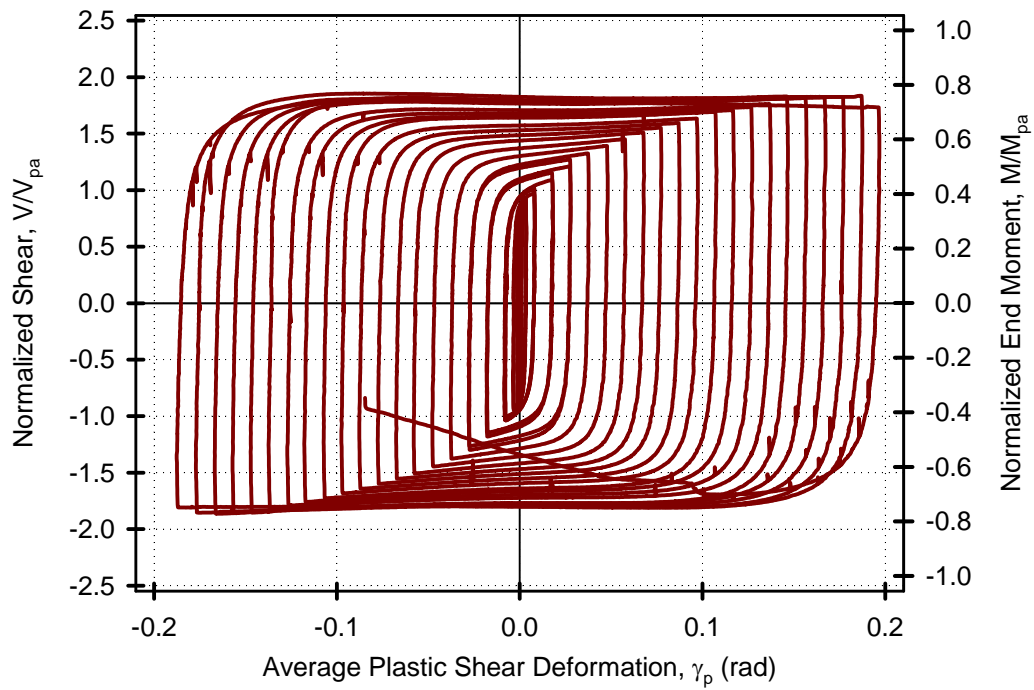


**Figure 4-17: Normalized Cyclic Plastic Behavior of Link L225**

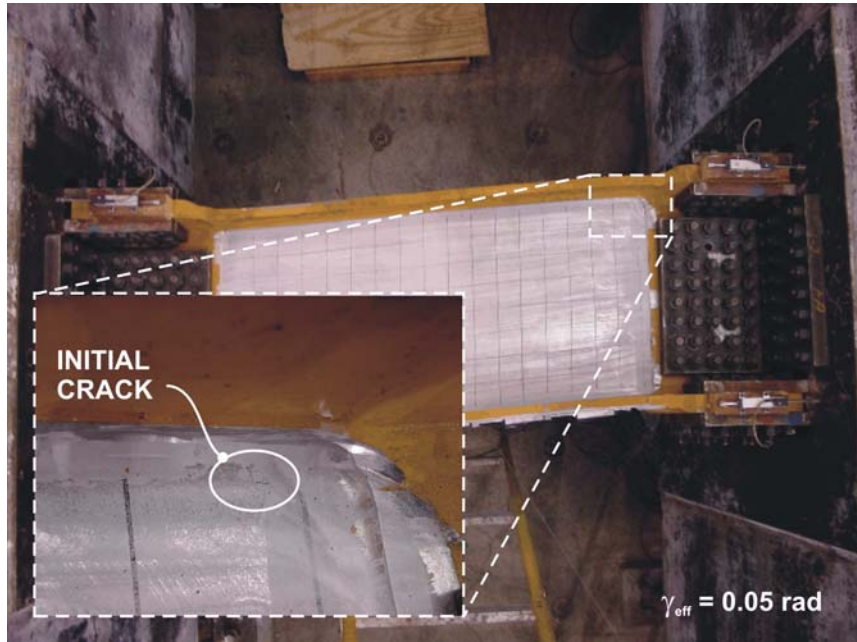


**Figure 4-18: Location of Initial Crack in Link X100**



**Figure 4-19: Web Out of Plane Web Deformation in Link X100**

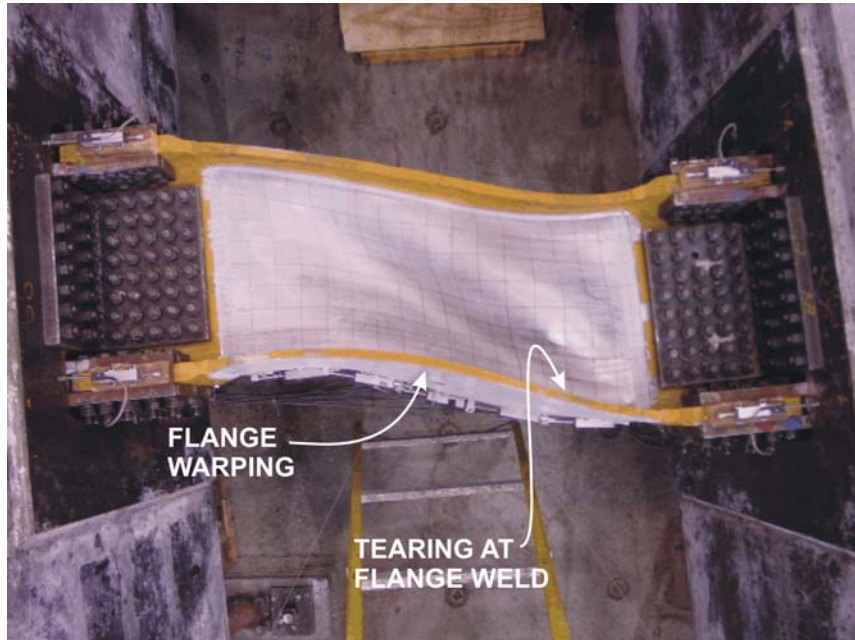


**Figure 4-20: Ultimate Failure of Link X100**

ing link shear deformation, with an example shown in Figure 4-19. The ultimate failure shown in Figure 4-20 resulted from web tearing at the flange welds, which was partially caused by the bending induced by the distorted web.

#### **4.3.4.2 Shear Deformation Capacity**

The cyclic response shown in Figure 4-21 was ductile and did not exhibit any pinching or degradation of the hysteretic loop until  $\gamma_{eff} = 0.17 \text{ rad}$ . Distortion of the web caused progressive degradation in resistance at subsequent reversals. The resistance remained above 80% of the maximum recorded force until  $\gamma_{eff} = \pm 0.23 \text{ rad}$  cycle, when the ultimate failure was reached. The maximum deformation capacities were obtained from the last completed reversal and are summarized in Table 4-4. The plastic shear deformation was calculated using Equation 1-13 and is shown in Figure 4-22.

#### **4.3.4.3 Shear and Moment Resistance**

The shear resistance is shown in Figure 4-21 is normalized to the shear capacity in Figure 4-22. The resulting overstrength summarized in Table 4-4 was similar to that observed in Link L100. The moment demand at the ends of the effective length was calculated using Equation 1-1 and is shown on the secondary axis in Figure 4-17. Despite the high overstrength, the demand did not exceed the plastic moment capacity because of the high link capacity ratio resulting from thinning the link web to decrease the shear capacity.

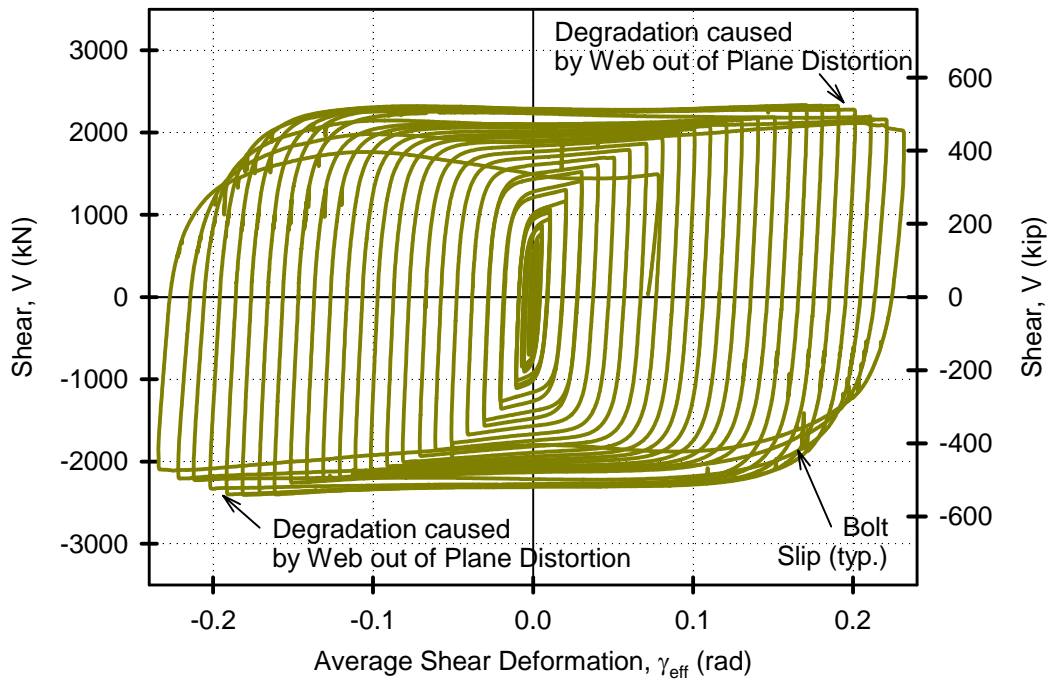


**Figure 4-21: Cyclic Behavior of Link X100**

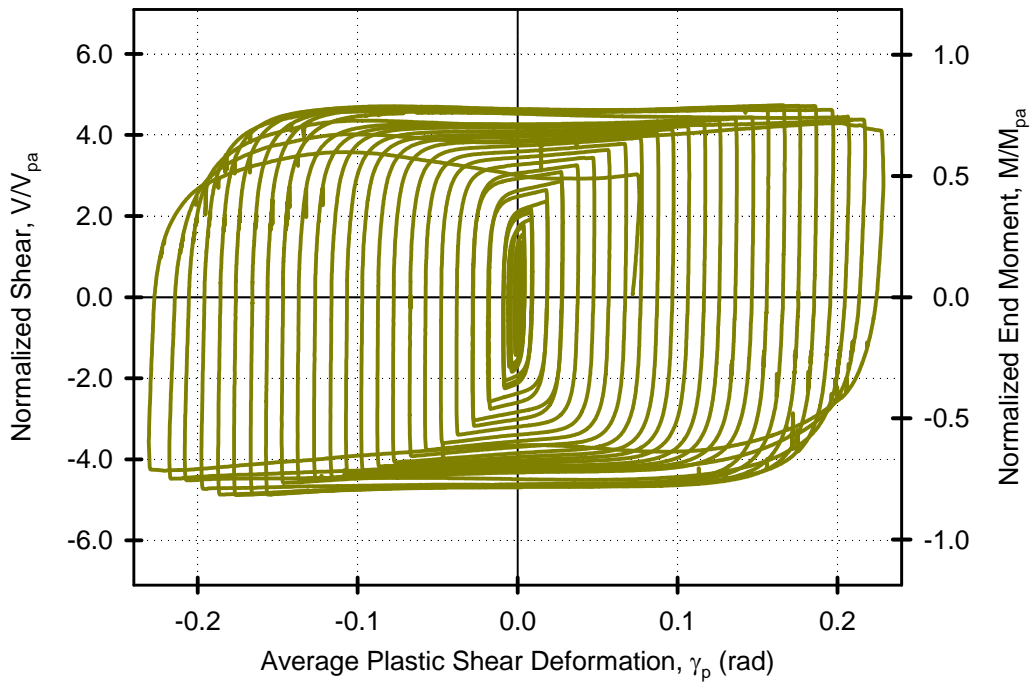


**Figure 4-22: Normalized Cyclic Plastic Behavior of Link X100**

**Table 4-4: Cyclic Performance Summary of Shear Links without Stiffeners**

Characteristic	Link Type		
	L100	L225	X100
$\gamma_{max}, rad$	0.171*	0.200	0.232
$(\gamma_p)_{max}, rad$	0.166*	0.197	0.228
$V_{max}, kN (kip)$	4348 (978)	2562 (576)	2408 (541)
$\Omega$	4.90	1.86	4.88
$M_{max}, kNm (kip ft)$	1826 (1348)	1076 (794)	1011 (746)
$M_{max}/M_{pa}$	1.95	0.77	0.82

\* capacity not reached due to premature fracture of the connection

### 4.3.5 Flange Cracking

The overall cyclic behavior of all three types of shear links showed ductile hysteretic behavior, but significant cracking in the flange was observed. Flange fracture can result in immediate drop in resistance and undesirable brittle ultimate failure mode. The flange cracks occurred in two locations; at the connection zone complete joint penetration weld and near the ends of the effective length.

The flange cracks at the connection zone welds did not occur in the complete joint penetration weld itself, but within the heat affected zone next to weld as shown in Figure 4-23 and Figure 4-24 for Link L100 and Link X100 respectively. The link flange plate extended past the end of the effective length into the connection zone where it was welded to the connection zone flange. The cracking in Link L100 may have been understandable since the moment demand was nearly twice the magnitude of the plastic moment capacity of the section. However, that was not the case for the other shear link types where similar cracking was also observed in. The cause of the cracks was the localized flange deformation caused by transition from elastic connection zone to the large deformations of the inelastically deforming effective length.

Measured flange strains at the ends of the effective length are shown Figure 4-26 through to Figure 4-28 for the three types of links. The strain measurements were only effective up to approximately  $\gamma_{eff} = 0.10 rad$  due to limitations of the strain gauges. In all cases, the strains rapidly increased towards the end of the connection zone. Although the measured values do not extend up to the flange welds where the cracks occurred, they do illustrate a trend that indicates large plastic demands near the location of the welds.

The cracks near the ends of the effective length shown in Figure 4-24 and Figure 4-25 occurred in only one side of the links. Upon closer inspection, it was discovered that the location of the cracks corresponded to the location of the temporary attachments that were ground prior to testing. The temporary hooks were welded to the flanges, thereby changing the properties at the extreme fibres of the flange. The increased strain demand at the outside fibres at the ends of the effective length coincided with the welds and resulted in the observed flange cracking. To reduce flange cracking, the flange transition weld from the effective length to the connection zone should therefore be located as far away from the ends of the effective zone as possible and no welding should be permitted for the outside faces of the flanges at the ends of the effective length.

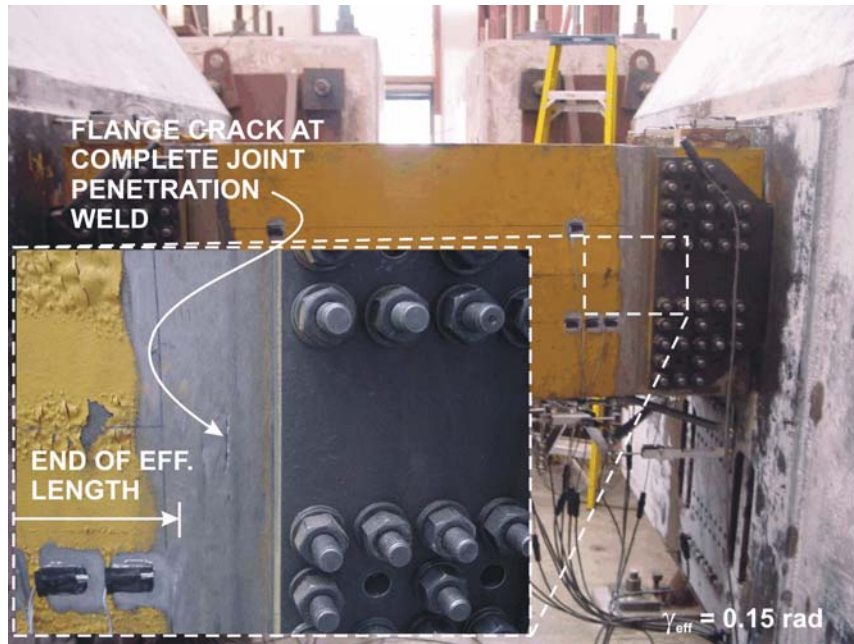


**Figure 4-23: Flange Crack Next At Connection Zone Weld in Link L100**

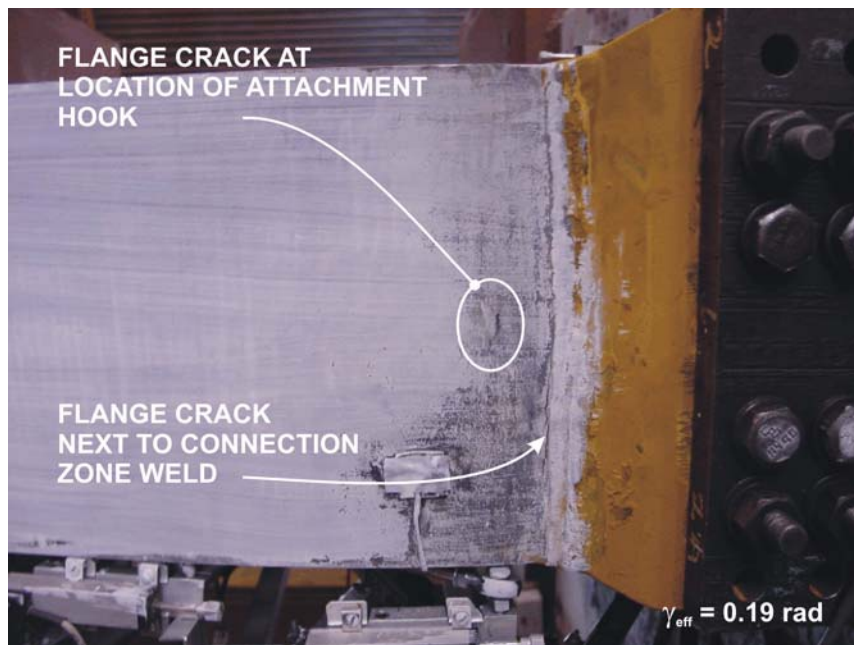


**Figure 4-24: Flange Cracks in Link X100**

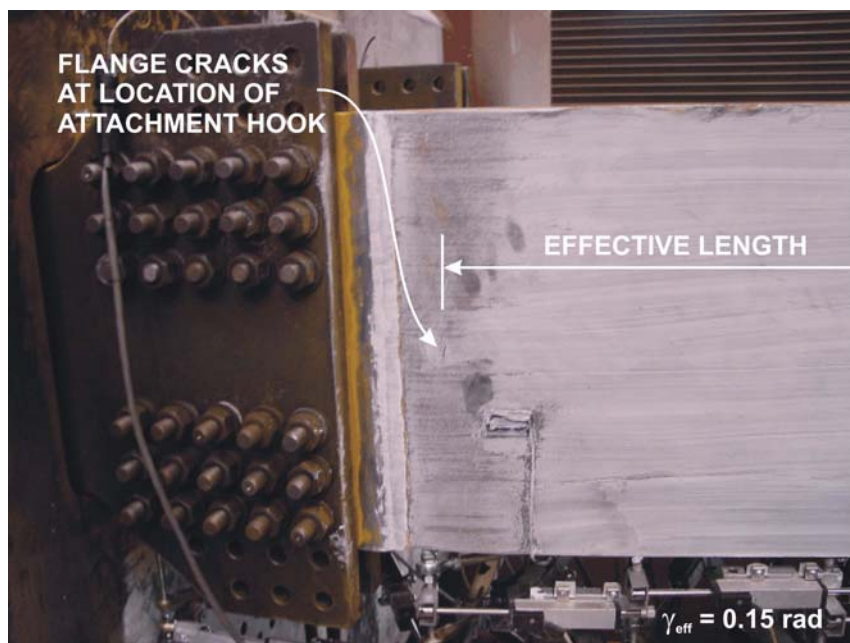


**Figure 4-25: Flange Crack at Location of Attachment Hook in Link L225**

#### **4.3.6 Web Shear Strains**

Strain gauges were effective for link shear deformations below approximately  $0.10 \text{ rad}$ . At larger deformations the strain gauge measurements became unreliable as the limits of the gauges was reached. Strain values were extracted at link deformations corresponding to  $\gamma_{eff} = \pm 0.02 \text{ rad}$ ,  $\pm 0.05 \text{ rad}$  and  $\pm 0.10 \text{ rad}$  to provide measurements from a range of link deformations.

Maximum shear strains were calculated from the three strain components of each rosette. Typical distributions of shear strain through the depth of the web are shown in Figure 4-29 and Figure 4-30 for mid-length and end of effective length respectively. The strain distribution remained relatively constant, even at the ends of the effective length. The shear strain distribution at mid-depth along the length of the link is shown in Figure 4-31. The distribution of strains is uniform along the length and indicates a reduction in demand towards the ends of the effective length. Rapid transition is evident between the shear strains at the ends of the effective length and the connection zone.

#### **4.3.7 Web Length Without Stiffeners**

The web compactness ratios of built-up shear links, especially for those utilizing low yield point steels within the web, can be significantly lower than the ratios previously considered. The equations in the AISC Seismic Provisions that govern the minimum spacing of stiffeners appear overly conservative for built-up shear links with low values of web compactness. As previously discussed in Section 4.1.3, the implied maximum deformation for built up shear links L225 and X100 based on Equation 1-5 and Equation 1-6 was lower than the  $0.08 \text{ rad}$  limit. Yet, both links significantly exceeded that limit before any out of plane web deformations were observed.

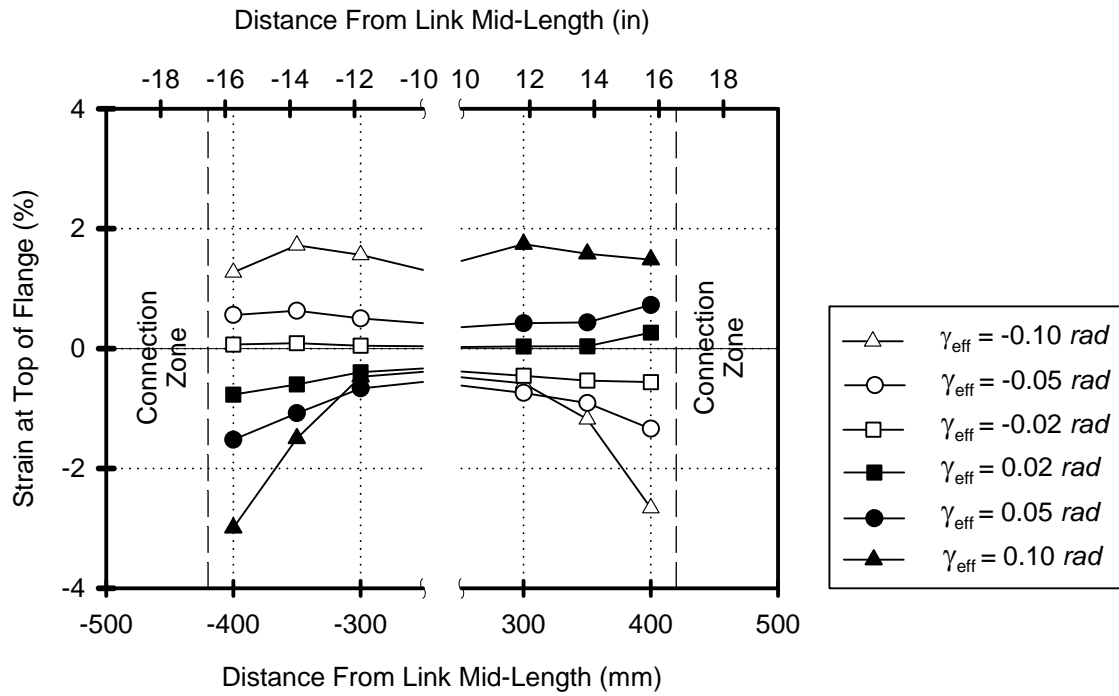


**Figure 4-26: Flange Strains at Ends of Effective Length for Link L100**

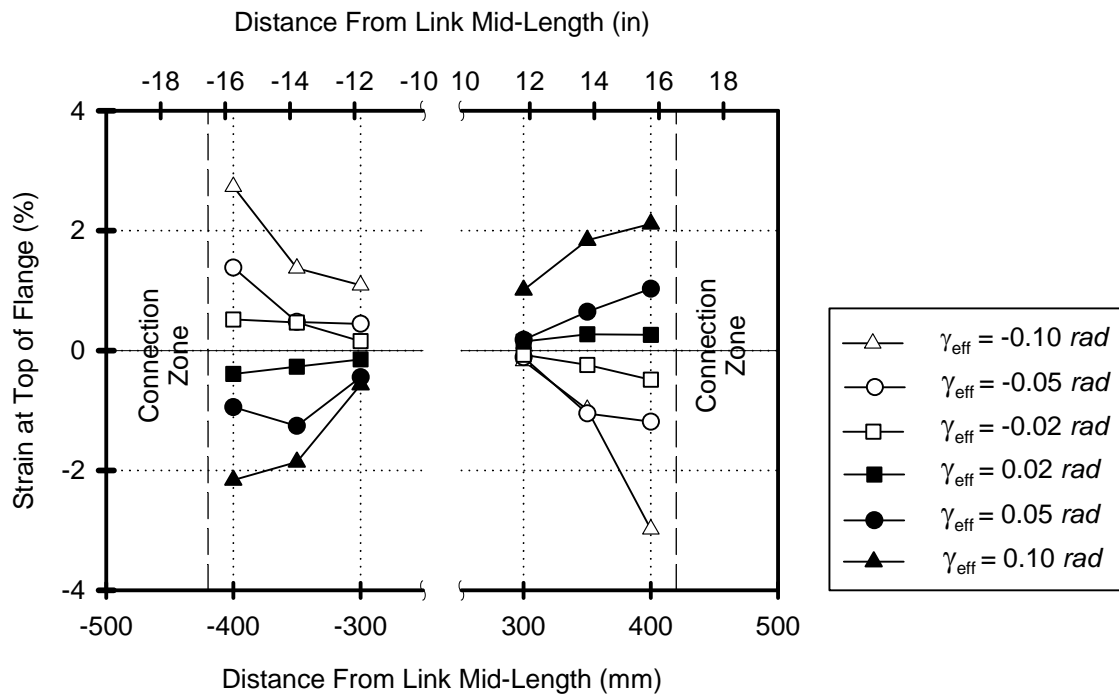


**Figure 4-27: Flange Strains at Ends of Effective Length for Link L225**

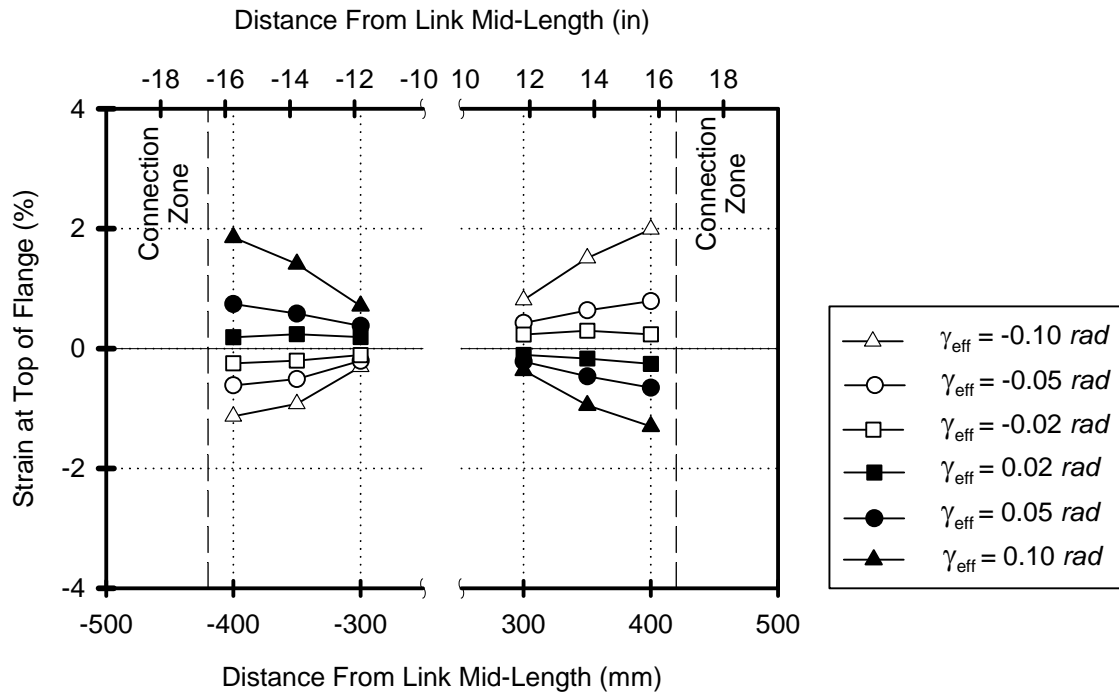


**Figure 4-28: Flange Strains at Ends of Effective Length for Link X100**

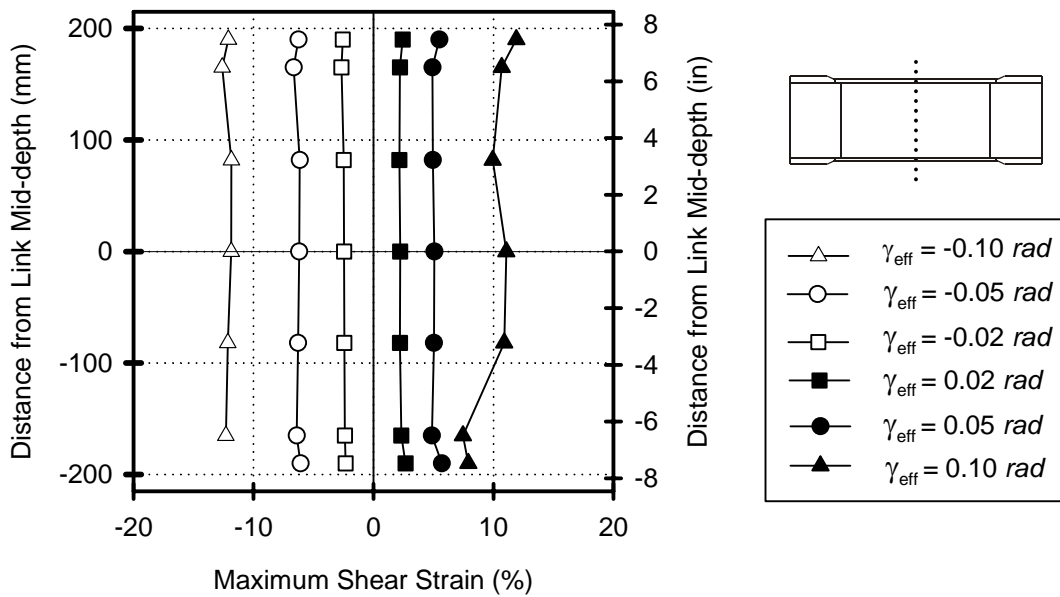


**Figure 4-29: Typical Web Shear Strain at Mid-Length (Link L100 Shown)**

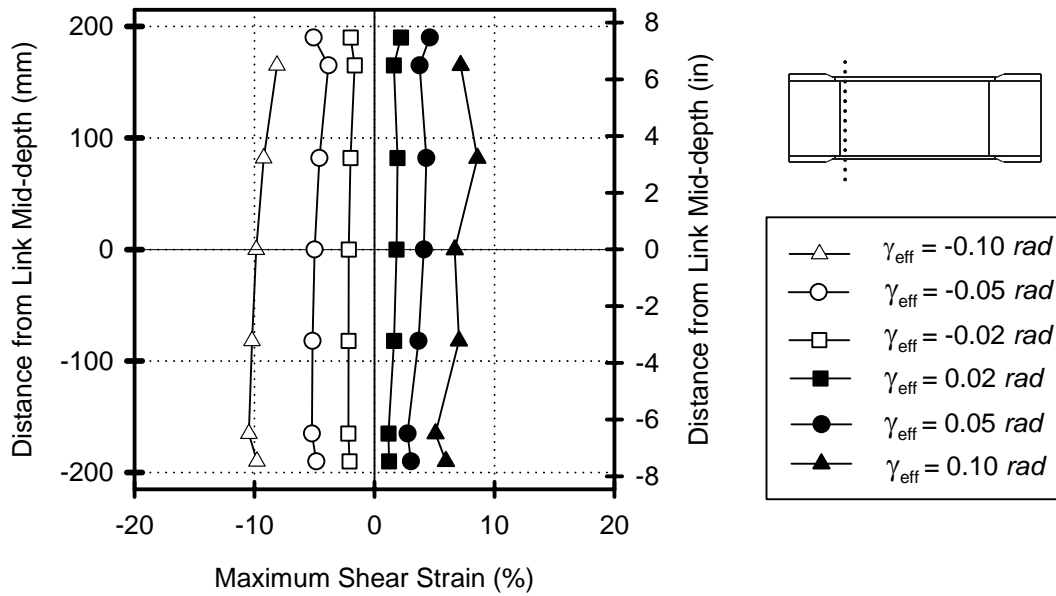


Figure 4-30: Typical Web Shear Strain at End of Effective Length (Link L100 Shown)

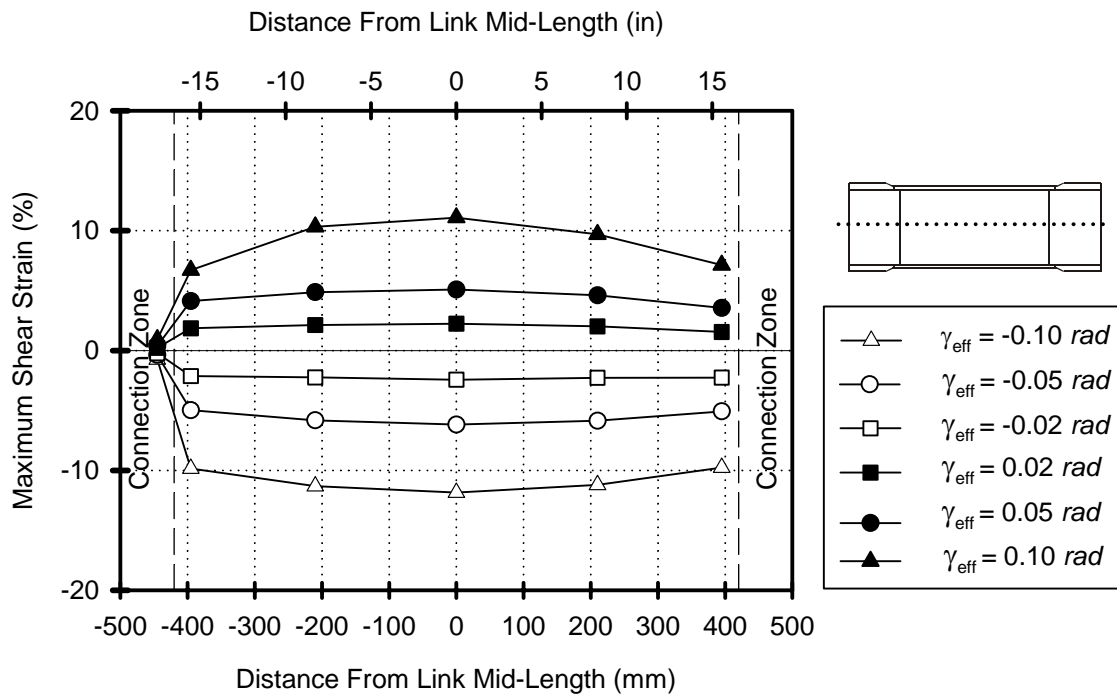


Figure 4-31: Typical Web Shear Strain Along Link at Mid-Depth (Link L100 Shown)

The potential benefits of excluding stiffeners and changing the mode of failure away from the middle of the effective length could only be achieved if out of plane web deformations are delayed until the target deformation levels are reached. Due to the limited number of experimental results, the effective lengths of built-up shear links without stiffeners should be limited to the ratios used in the experiment. As such, the aspect ratio should not exceed  $e/h_w \leq 2$  and at the same time the web compactness ratios should not exceed  $h_w/t_w \leq 20$ .

#### **4.4 Results from Near-Fault Deformation History Experiments**

This section reviews the observations and test results from experiments on three types of built-up shear links designed without stiffeners and subjected to the near-fault deformation history. The link shear deformation was calculated from displacement transducers and the shear resistance from the actuator load and test setup geometry as described in Appendix A.

##### **4.4.1 Response of Link L100**

The experiment on Link L100 using the near-fault deformation history was conducted on September 3<sup>rd</sup>, 2003.

###### **4.4.1.1 Shear Deformation Capacity**

Two sets of the near-fault deformation history were applied without any visible signs of the onset of failure and without any degradation in response. There were no cracks in the web or the flanges and no out of plane distortion of the web or the flanges. The only observed distress was a crack at the inside of the flange, next to the web weld. This localized deformation was similar to that observed under cyclic loading and shown in Figure 4-8.

###### **4.4.1.2 Shear Resistance**

The shear deformation response from the first set of applied near-field load history is shown in Figure 4-32. The response was ductile and did not exhibit any pinching or degradation. The link response was inelastic at each reversal point, and the resistance increased with increasing deformations. Some of the reversals points are shown to illustrate the gradual increase in resistance.

At the first reversal the link shear was  $-2172 \text{ kN}$  ( $488 \text{ kip}$ ) while at the second and third, the shear increased to  $3382 \text{ kN}$  ( $760 \text{ kip}$ ) and  $-3511 \text{ kN}$  ( $789 \text{ kip}$ ) respectively. Subsequent reversals continued to increase the resistance with each reversal, but to a much smaller extent. The next significant increase occurred at the 17th and 18th reversals, which defined the maximum shear values for that set. The maximum shear and the resulting overstrength values are summarized in Table 4-5. Despite the deformation offset, the positive and negative shear values were nearly identical. The response from the second set of the near-fault deformation history is shown in Figure 4-33. The shear had only marginally increased. The maximum shear and overstrength values summarized in Table 4-5 were less than 5% higher than those recorded in the first set, but were 13% smaller than the ultimate values obtained from experiments using the incremental cyclic history.

##### **4.4.2 Response of Link L225**

The experiment on Link L225 using the near-fault deformation history was conducted on August 19<sup>th</sup>, 2003.

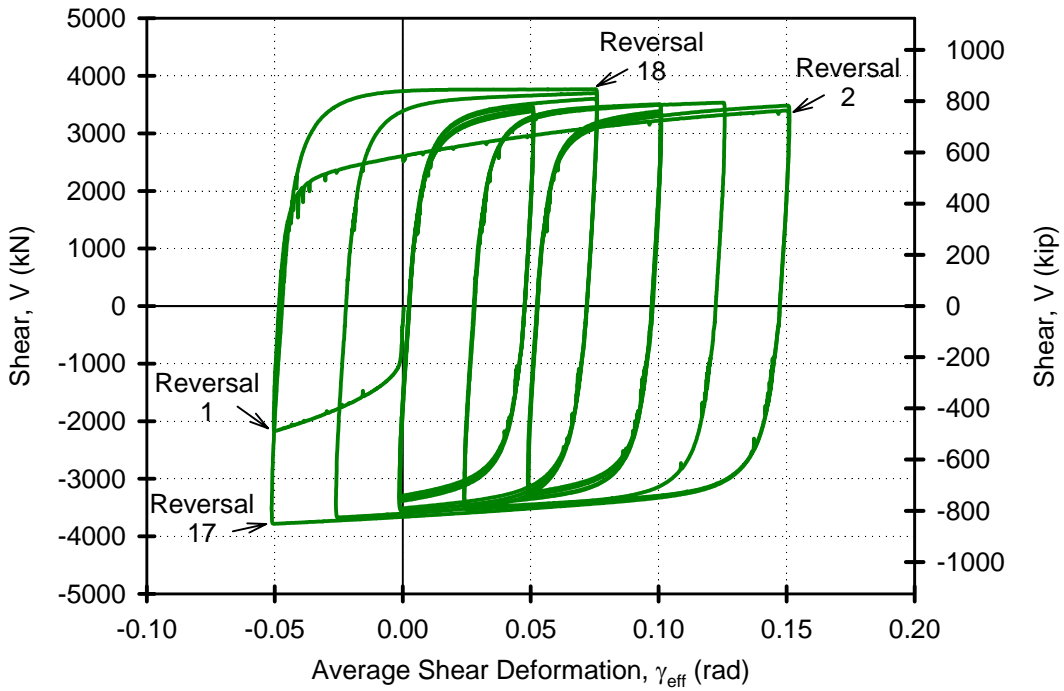


**Figure 4-32: Response of Link L100 to Near-Fault History Set 1**

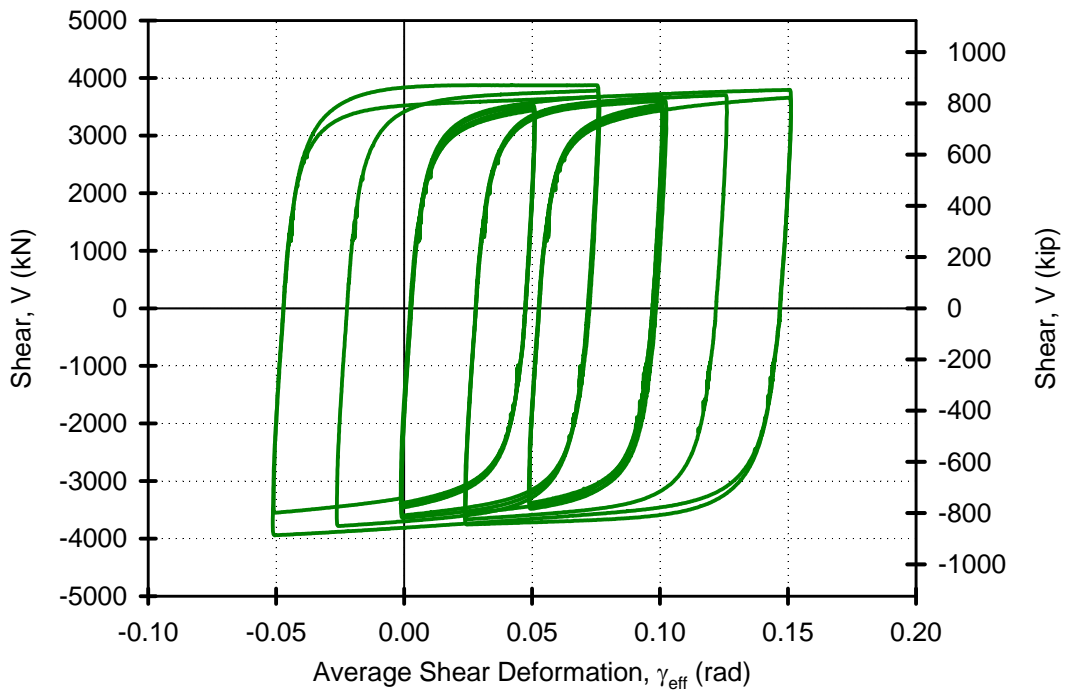


**Figure 4-33: Response of Link L100 to Near-Fault History Set 2**

### 4.4.2.1 Shear Deformation Capacity

Two sets of the near-fault deformation history were applied without any visible signs of the onset of failure and without any degradation in response. There were no cracks in the web or the flanges and no out of plane web distortion occurred. The link appeared the same after the two sets as it did before the experiment began.

### 4.4.2.2 Shear Resistance

The response was ductile and did not exhibit any pinching or degradation. The shear deformation response from the first set of applied near-field load history is shown in Figure 4-34. Connection bolt slip introduced periodic abrupt reductions in resistance which were immediately recoverable. The bolt slip was not as gradual in these tests as in the cyclic tests because the paint was removed from the connection zone while grinding the connection ends to fit into the test setup. The link response was inelastic at each deformation reversal and the resistance gradually increased with increasing deformations.

At the first reversal the link shear was  $-1530\text{ kN}$  ( $344\text{ kip}$ ) while at the second and third, the shear increased to  $2088\text{ kN}$  ( $469\text{ kip}$ ) and  $-2146\text{ kN}$  ( $482\text{ kip}$ ) respectively. The resistance remained within the envelope of the second and third reversal values until the 17th and 18th reversals further increased the shear to the maximum for that set. Despite the deformation offset, the positive and negative resistance values were nearly identical. The maximum shear and the resulting overstrength values are summarized in Table 4-5. The response from the second set of the near-fault deformation history is shown in Figure 4-35. The maximum shear was nearly identical to the first set as summarized in Table 4-5. Overall, the overstrength was 9% lower than the value achieved in experiments using the incremental cyclic deformation history.

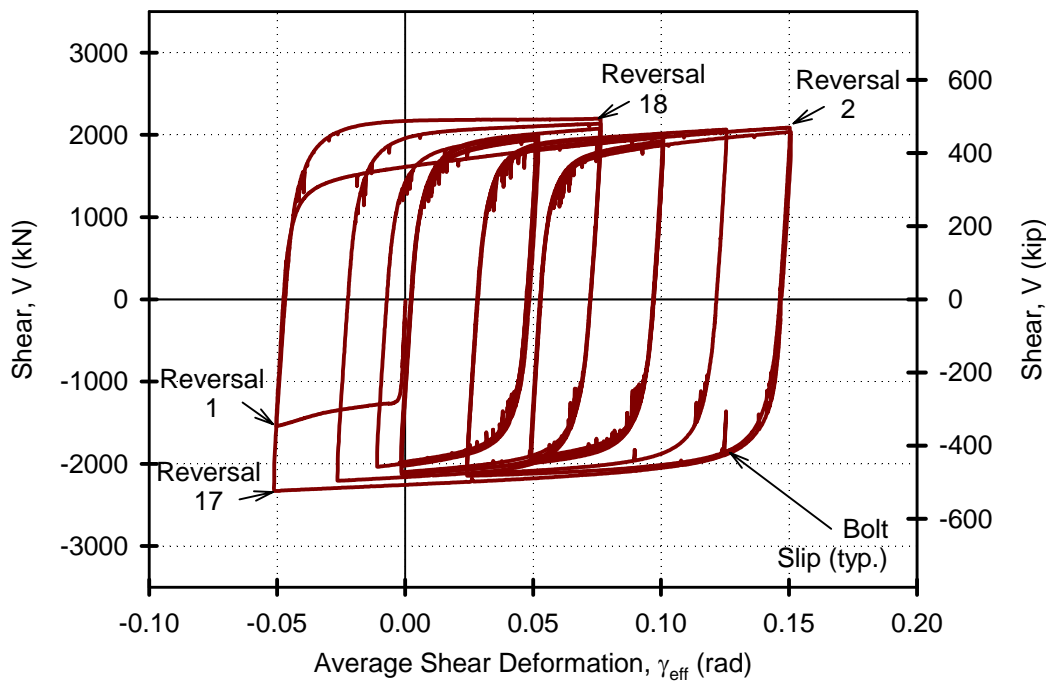
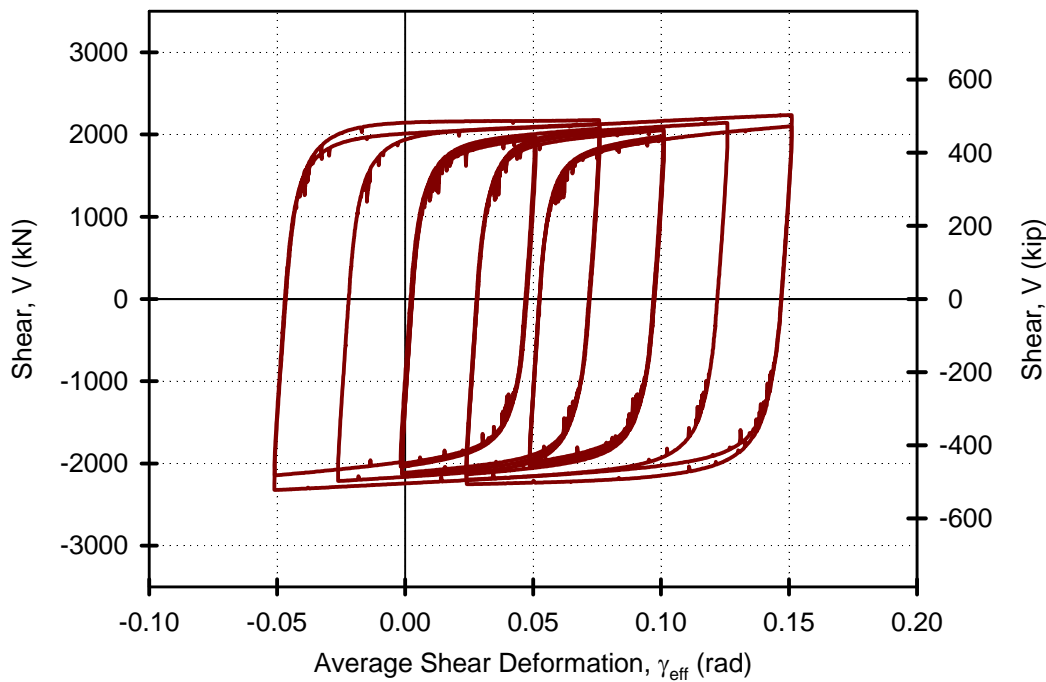


Figure 4-34: Response of Link L225 to Near-Fault History Set 1



**Figure 4-35: Response of Link L225 to Near-Fault History Set 2**

### 4.4.3 Response of Link X100

The experiment on Link X100 using the near-fault deformation history was conducted on September 24<sup>th</sup>, 2003.

#### 4.4.3.1 Shear Deformation Capacity

Two sets of the near-fault deformation history were applied without any visible signs of the onset of failure and without any degradation in response. During the second set, 3 mm (0.1 in) crack formed in the web to flange weld after the 5<sup>th</sup> reversal as shown in Figure 4-36. Hairline cracks appeared in the outside flange next to the connection zone weld after the 16<sup>th</sup> reversal. The flange cracks were in the same location as those observed in the cyclic experiments, but did not grow for the remainder of the deformation history. Out of plane web distortion was detected near the end of the second set as shown in Figure 4-37.

#### 4.4.3.2 Shear Resistance

The shear deformation response was ductile and did not exhibit any pinching or degradation. The response from the first set of applied near-field load history is shown in Figure 4-38. Connection bolt slip caused periodic sudden decrease in load. The link response was inelastic at each reversal point, but the resistance gradually increased with increasing deformations. The trend in the gradual increase in shear resistance was similar to Link L100.

At the first reversal the link shear was -1182 kN (266 kip) while at the second and third, the shear increased to 1833 kN (412 kip) and -1881 kN (423 kip) respectively. The next substantial increase occurred at the

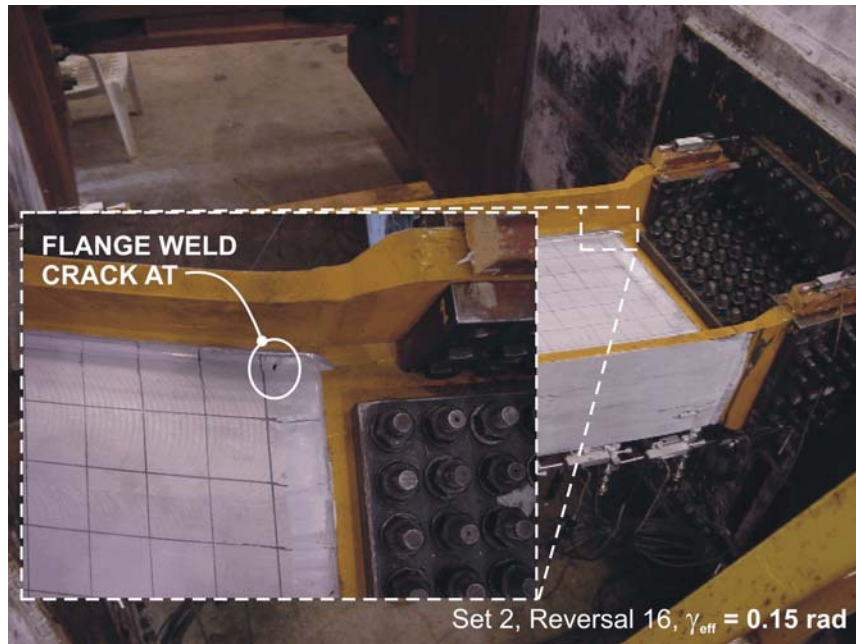


**Figure 4-36: Weld Crack in Link X100**



**Figure 4-37: Web Distortion in Link X100 at End of Second Set**

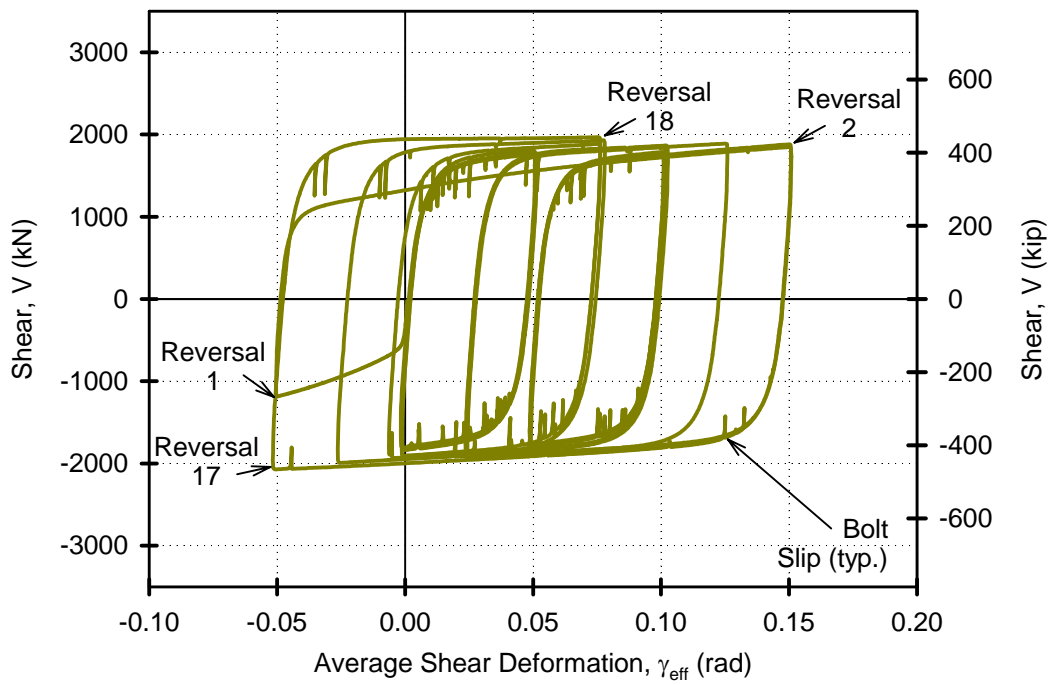


**Figure 4-38: Response of Link X100 to Near-Fault History Set 1**

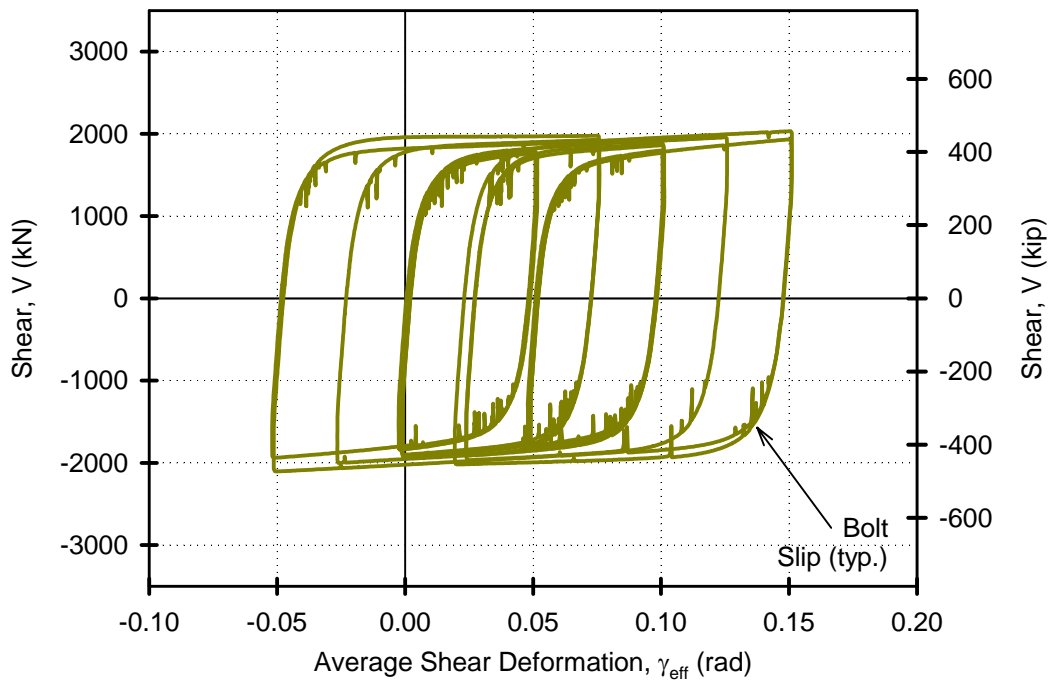


**Figure 4-39: Response of Link X100 to Near-Fault History Set 2**

17th and 18th reversals, which defined the maxima for that set. Despite the deformation offset, the positive and negative resistance values were nearly identical. The maximum shear and the resulting overstrength values are summarized in Table 4-5. The second set of applied near-fault load history is shown in Figure 4-39. The shear resistance had mainly stabilized, and the maximum shear and overstrength values summarized in Table 4-5 only marginally increased from the first set. The overstrength values developed in the link were high, but still 12% smaller than values obtained from experiments using incremental cyclic deformation history.

**Table 4-5: Performance Summary of Shear Links without Stiffeners under Near-fault History**

Deformation History	Characteristic	Link Type		
		L100	L225	X100
Near-fault Set 1	$V_{max}, kN (kip)$	3785 (851)	2330 (524)	2072 (466)
	$\Omega$	4.24	1.70	4.20
Near-fault Set 2	$V_{max}, kN (kip)$	3943 (886)	2335 (525)	2110 (474)
	$\Omega$	4.44	1.70	4.28
Additional Cyclic	$\gamma_{max}, rad$	-	0.201	0.221
	$V_{max}, kN (kip)$	-	2590 (582)	2400 (540)
	$\Omega$	-	1.88	4.87

#### 4.4.4 Response to Additional Cyclic Deformations

The ultimate capacity of the shear links was not reached after the completion of two sets of near-fault deformation histories. No degradation of the response was observed. Two options were considered for attaining the ultimate failure in the links; continue to apply the near-fault deformation history or apply incremental cyclic deformations until failure.

Applying the incremental cyclic deformation was chosen in order to obtain better understanding of the ultimate deformation capacity and failure mode. The first cycle was chosen to exceed the deformations achieved under the near-fault history. In order to be consistent with the previously tested links, the cyclic history was applied without mean deformation offset, i.e. the positive and negative deformations were of the same amplitude, and the shear deformations of each cycle were increased by 0.01 *rad* after each cycle. These cyclic deformations were not applied to Link L100 because it was expected that the connection would fail before the effective length would reach ultimate capacity.

The results for the additional cyclic deformations of Link L225 and Link X100 are shown in Figure 4-40 and Figure 4-41 respectively. In both cases, significant additional cyclic deformations were achieved. The failure mode for Link L225 was similar to that observed in the incremental cyclic deformation experiments. Out of plane web distortion became more pronounced with increased deformations, cracks formed in the corners of the effective length and outside surfaces of the flanges. The ultimate failure was characterized by web tearing in the corners and is shown in Figure 4-42.

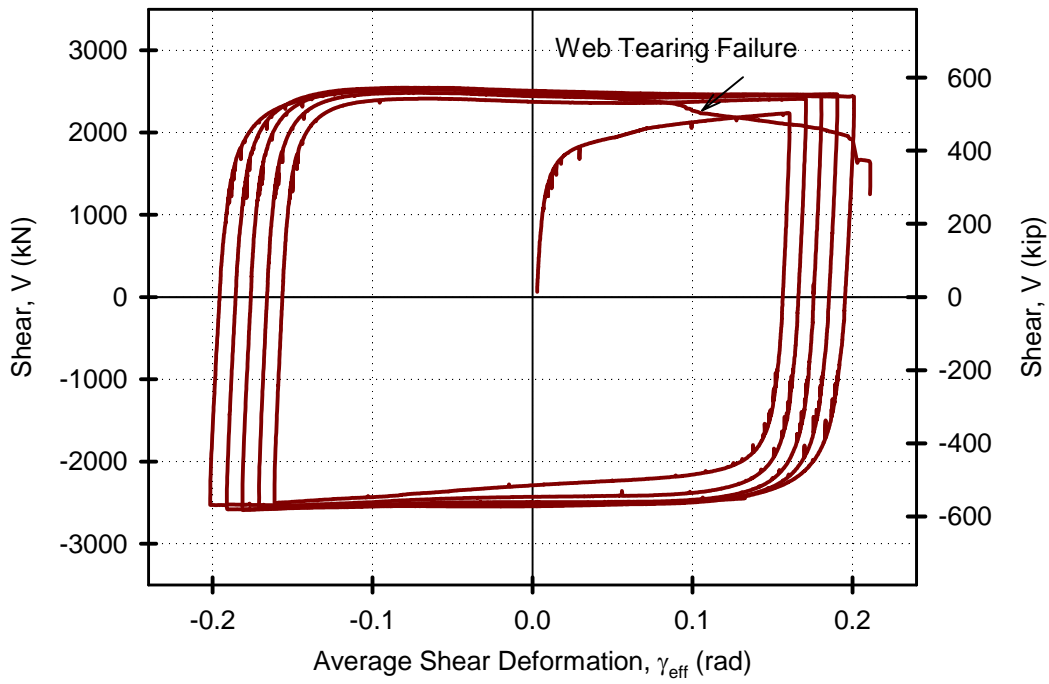


**Figure 4-40: Additional Cyclic Deformations for Link L225**

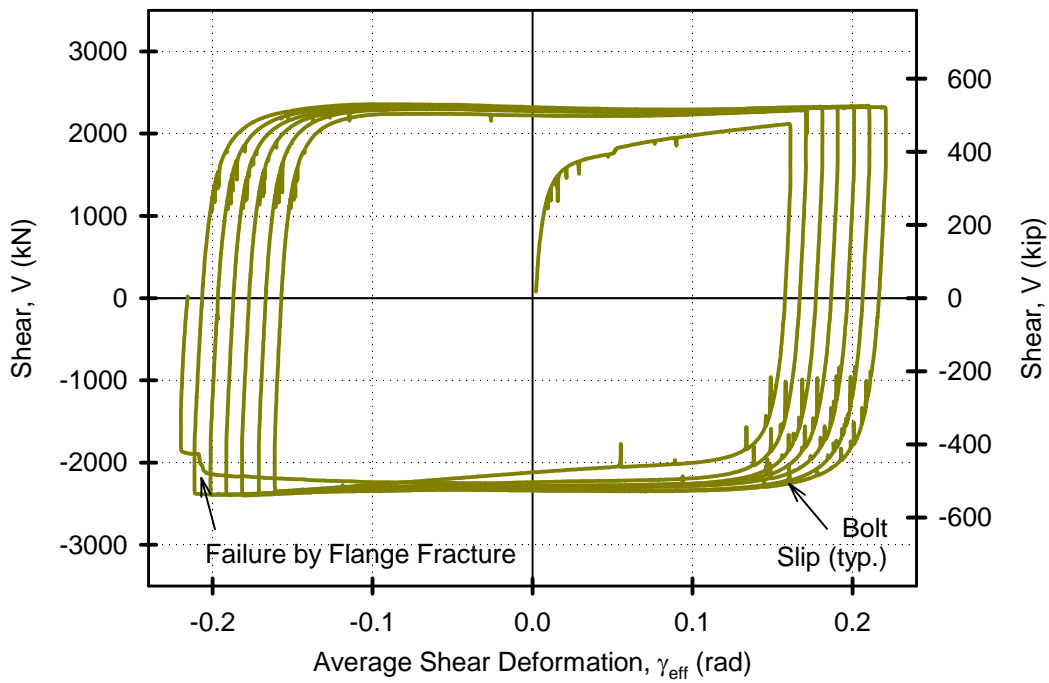


**Figure 4-41: Additional Cyclic Deformations for Link X100**

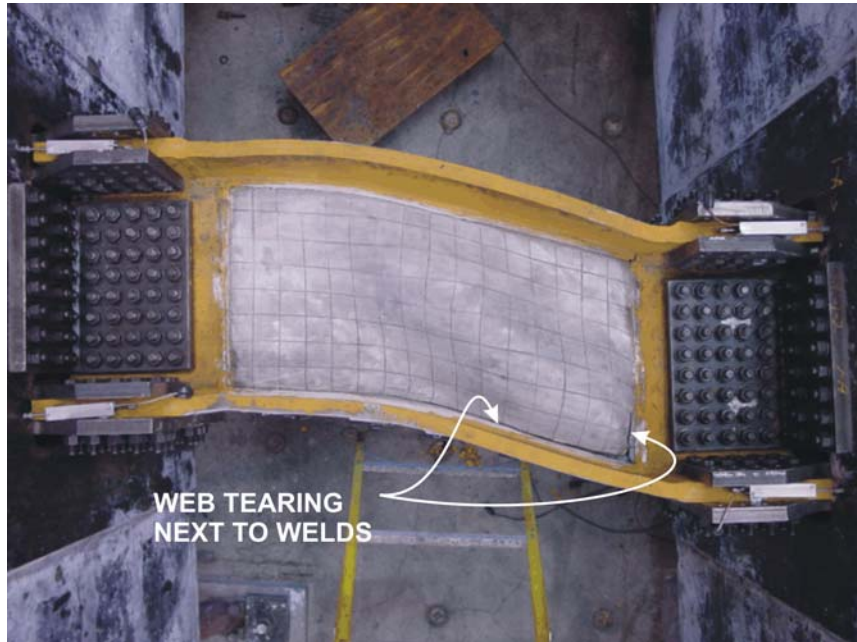


**Figure 4-42: Ultimate Failure of Link L225 After Additional Cyclic Deformations**

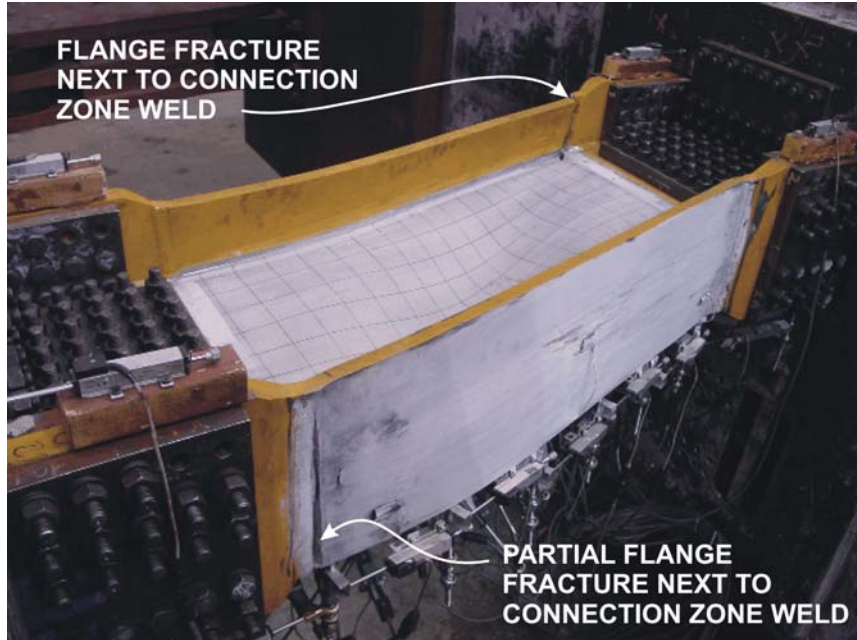


**Figure 4-43: Ultimate Failure of Link X100 After Additional Cyclic Deformations**

The failure mode for Link X100 initially followed the same pattern as that observed in the incremental cyclic deformation tests, but out of plane web distortions were not as pronounced and did not degrade the

response. The flange cracks that developed next to the connection welds became increasingly larger and caused the ultimate failure as shown in Figure 4-43. The flange fracture caused the resistance to decrease rapidly. The ultimate deformation and shear strength characteristics for both links are summarized in Table 4-5. The ultimate deformation capacities as well as the overstrength values were nearly identical to the results obtained from the incremental cyclic tests.

## 4.5 Summary

The design freedom associated with built-up shear links was used to advantage by eliminating intermediate web stiffeners in order to change the failure mode from that observed in previously tested links. To limit web buckling, the web compactness was reduced while maintaining limits on the nominal design shear strength by utilizing low yield strength steels. Three types of shear links without stiffeners were designed using low yield point steels produced in Japan. Their performance was investigated using two deformation histories; incremental cyclic and near-fault.

The cyclic response of all three types of links resulted in ductile hysteretic response. The ductile failure mode was characterized by web tearing at the corners of the effective zone. However, overstrength values as high as 4.9 were observed in links designed using low yield point steel of 100 MPa (14.5 ksi) specified yield strength. The resulting shear resistance in Link L100 caused connection fracture prior to achieving the deformation capacity of the link itself, thereby illustrating the importance of quantifying the maximum forces generated by the link for capacity seismic design.

The behavior under near-fault deformation history also showed ductile hysteretic response of the built-up links. In all cases, two complete sets of the near-fault load history were applied without reaching ultimate failure. Other than the initial increase in resistance after the first three reversals, the shear deformation response was nearly duplicated under the second near-fault history set. The overstrength was approximately 10% lower than the values obtained from the incremental deformation history. Additional cycles of increasing amplitude were used to achieve ultimate failure, which mainly followed the modes observed under incremental cyclic loading.

Of concern was the observed cracking of the flange at the connection welds, which in one case resulted in complete fracture of the flange. These flange cracks were caused by large strains at the ends of the effective length and should be avoided by locating flange welds as far away as possible from the ends of the effective length.

## SECTION 5

### BUILT-UP SHEAR LINK CYCLIC PERFORMANCE COMPARISONS

#### 5.1 Overview

An experimental program was conducted on large-scale built-up shear links that utilized steels of a broad range of nominal yield strengths. The individual performance characteristics of the different shear link types was discussed in previous sections. The objectives of this section are to compare the cyclic behavior of the different types of shear links and evaluate the influence of different parameters on their performance. Discussions are related to the cyclic behavior, overstrength, deformation capacity and failure mode. Based on the experimental results, design implications for built-up shear links are also reviewed.

##### 5.1.1 Experimental Program

The first built-up shear link specimens utilized conventional plate steels and were designed based on the AISC Seismic Provisions, which are intended for eccentrically braced frame shear links made from rolled shapes. The design further evolved by taking advantage of the design freedom associated with the use of built-up shapes to incorporate high performance steel. Finally, shear links without stiffeners were developed by utilizing low yield point steels to decrease the web compactness ratio without increasing the nominal shear capacity. This approach was a departure from not only the design provisions, but the general philosophy traditionally applied to shear link design.

The grades of steel covered a wide spectrum of nominal yield strengths. In total, six different shear link designs were investigated by imposing cyclic inelastic deformations following two deformation histories. All shear link types were subjected to incrementally increasing cyclic (IC) deformation history up to failure. Three specimens corresponding to the shear link types designed without stiffeners were subjected to near-fault (NF) deformation history. These nine unique experiments are summarized in Table 5-1 along with the some of the key shear link characteristics.

Despite the differences in specified yield strengths of the steels, a number of common characteristics were incorporated into the design of the different types of built-up shear links. Links C345a, H485, L100 and L225 were designed to have the same effective length, nominal shear and moment capacities and flange compactness ratios. The minor differences in these properties were caused by round off in plate thickness and variability in actual versus specified steel yield stresses. Link X100 had the same properties as mentioned above for the other links, except for having a lower nominal shear capacity. Link C345b was significantly different and only had the nominal shear capacity in common with the rest of the link types.

#### 5.2 Energy Dissipation

Ductile hysteretic behavior without strength degradation and without pinching of the hysteretic loop was characteristic for all shear links subjected to the incremental cyclic deformation history. In order to obtain the energy dissipated by these devices, the average relative displacement between the ends of the shear links  $\Delta_{eff}$  was calculated based on the average shear deformation  $\gamma_{eff}$  according to Equation 5-1, where  $e$  is the effective length.

$$\Delta_{eff} = e \cdot \gamma_{eff} \tag{5-1}$$

The area bound by the resulting shear-displacement cyclic response of the links as shown in Figure 5-1 represents the hysteretic energy  $E_{hyst}$  dissipated by the link. The hysteretic energy was calculated for all links and is summarized in Figure 5-2 for each cycle of link deformation. With increase in the deformation, the dissipated hysteretic energy increased as the area bound by the cyclic response became larger. Compared to other shear link specimens, Link L100 dissipated the most energy per cycle because of the significantly larger shear strength that was resisted by the link.

**Table 5-1: Summary of Tested Built-up Shear Links**

Characteristic	Link Type					
	C345a	C345b	H485	L100	L225	X100
Detailed Figure	Figure 2-1		Figure 3-1	Figure 4-1		
Deformation History	IC	IC	IC	IC	IC	IC
				NF	NF	NF
No. of Intermediate Stiffeners	2	1	4	No Web Stiffeners Used		
Steel Grade within the Effective Length	A709 Grade 345 MPa (50 ksi)	A709 Grade 345 MPa (50 ksi)	A709 HPS 485W (70 ksi)	LYP 100 MPa (14.5 ksi)	LYP 225 MPa (33 ksi)	Web: LYP 100 MPa, Flange: HT 440 MPa
$e/h_w$	1.95	1.16	1.95	1.95	1.95	1.95
$h_w/t_w$	31	31	43	9.5	19.5	17.2
$b/2t_f$	6.8	5.4	6.7	6.8	6.6	6.4
$2M_{pa}/(eV_{pa})$	2.49	3.46	2.43	2.51	2.42	5.98

The effectiveness of the shear links as hysteretic energy dissipating device was evaluated by the hysteretic efficiency factor in Equation 5-2.

$$\text{Hysteretic Efficiency Factor} = E_{hyst}/E_{max} \quad (5-2)$$

The energy  $E_{max}$  represents the maximum energy that can be achieved per cycle as bound by a rectangular area between the maximum and minimum values of shear and deformation per cycle. Hence, a hysteretic efficiency factor of 0% represents an elastic response, while a factor of 100% represents a theoretical infinitely stiff elasto-plastic response.

The hysteretic efficiency factor is summarized in Figure 5-3 for all links at each shear deformation value. The shape of the cyclic response did not significantly vary among the different shear links and hence the

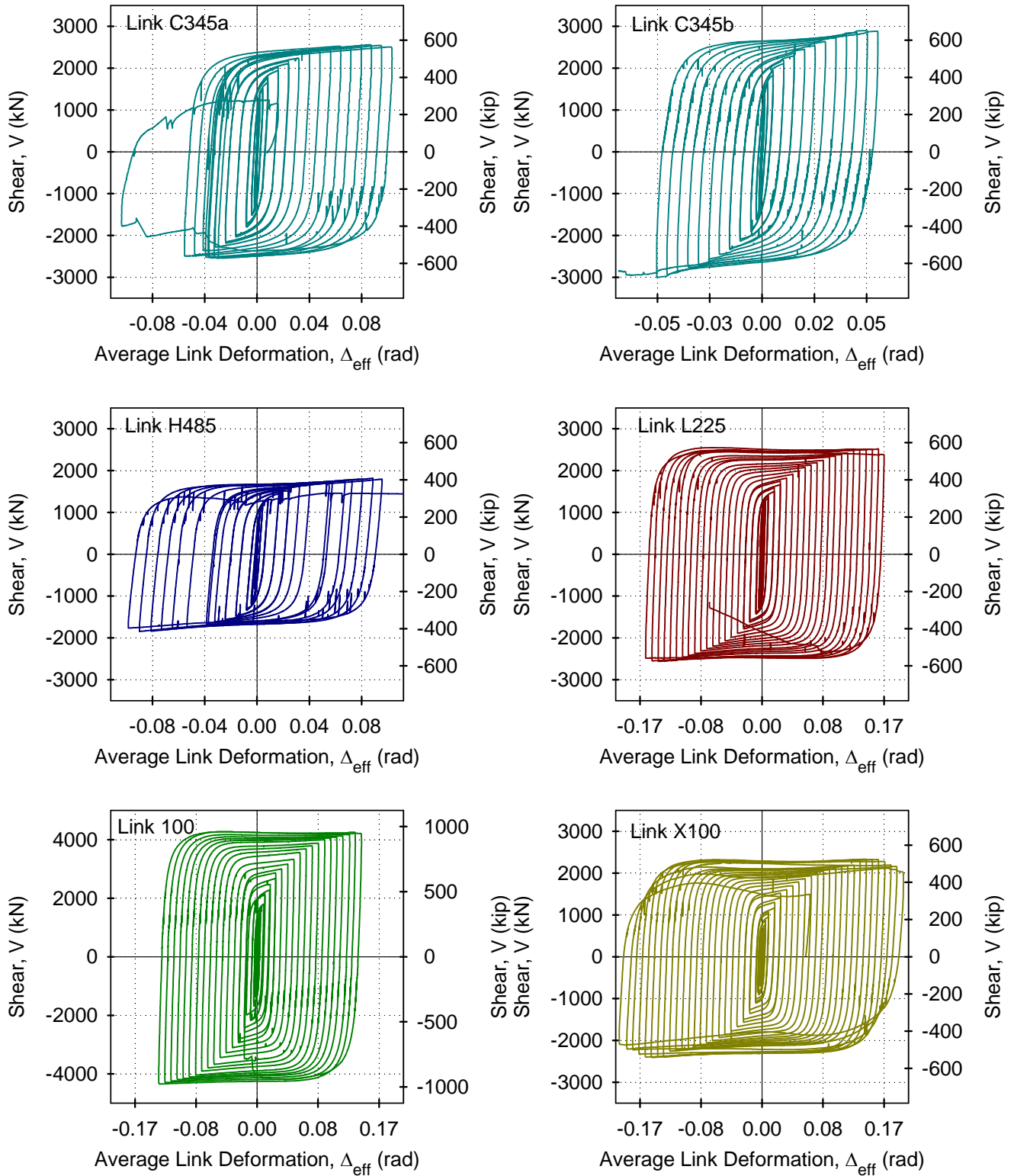


**Figure 5-1: Shear Force-Displacement Cyclic Response**

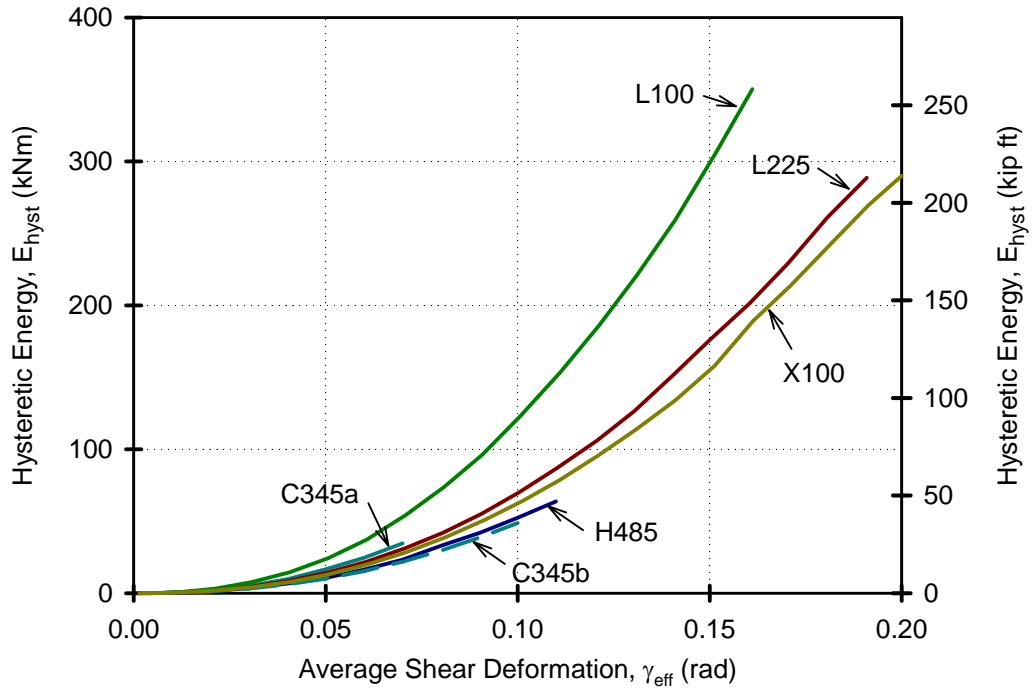


**Figure 5-2: Hysteretic Energy Dissipated per Cycle of Average Shear Deformation**

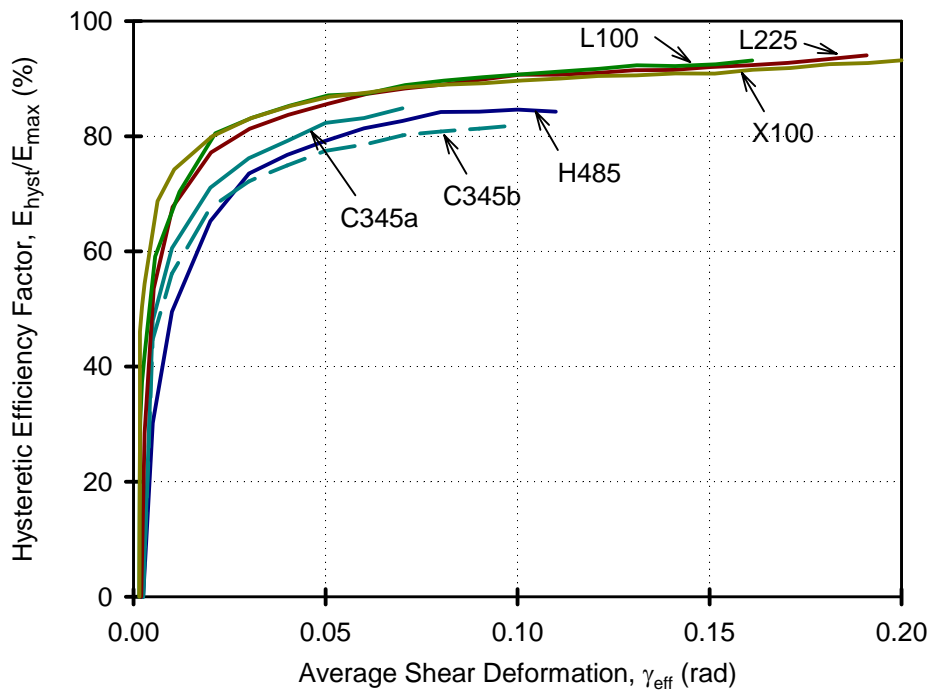


**Figure 5-3: Hysteretic Efficiency Factor**

hysteretic efficiency factor was similar for large levels of deformation among all of the links. The links with low yield point steel webs were marginally more efficient, but the hysteretic efficiency was found to be larger than 80% for all shear links.

### 5.3 Cyclic Shear Behavior and Overstrength

Large inelastic deformation was typical for all tested built-up shear links, but overstrength varied significantly. Overstrength refers to the actual recorded shear resistance normalized to the link shear capacity as discussed in Section 1.2.2. For the purpose of discussing the results of the experimental program, the overstrength definition of Equation 1-15, which uses shear capacity  $V_{pa}$  based on measured yield strength  $f_{ya}$ , is used. Based on capacity design principles, the elements outside the effective length must remain elastic under the maximum forces generated by the link. Understanding and quantifying overstrength is therefore essential such that the elements outside of the effective length are adequately designed. The expected overstrength in the AISC Seismic Provisions is based primarily on experimental results of shear links made from rolled sections, with little guidance given on the source of the overstrength. This section examines the experimental results for trends in the shear strength of built-up links.

#### 5.3.1 Cyclic Shear Strength

The maximum overstrength value recorded in all of the experiments are summarized in Table 5-2, however these maxima do not provide any indication on the development of the shear strength throughout the history. A closer examination of the shear strength was made by constructing a backbone curve from the results of the IC history tests. The shear resistance at each reversal was considered and the maximum was taken if more than one reversal occurred at the same deformation. The backbone curve represents the cyclic shear response of the specimen and is shown contrasted to the response of the six types of shear links in Figure 5-4. To represent the overstrength, the backbone curves were normalized to the shear capacity  $V_{pa}$  in Figure 5-5 up to 0.15 *rad* deformation. Links L100 and X100 had the highest overstrengths and the shear links made from conventional grade steel had the second highest. Closer comparison was made in Figure 5-6 of link types excluding the high values of L100 and X100. In all cases the shear strength increased with increasing deformations, but did so following different trends.

For comparison, the overstrengths at different levels of response were stacked in Figure 5-7 up to the maximum recorded value. Other than the maximum, three other milestones were chosen to graphically illustrate the development of overstrength;  $\gamma_p = 0.02$  *rad* for low values of plastic demand,  $\gamma_p = 0.10$  *rad* for the highest values that all links were able to achieve and  $\gamma_p = 0.05$  *rad* as an intermediate point. To obtain the relative percentage increase, each overstrength was normalized to the maximum value in Figure 5-8. Although the overstrength increased progressively with the deformation demand, large contributions of the overstrength occurred even for low values of deformation. After completing  $\gamma_p = 0.02$  *rad* cycle, an average of 78% of the overstrength was achieved for the links with conventional and high performance steel and 58% of the maximum overstrength was achieved for the links with low yield point steels. Hence, overstrength must be taken into account even for low values of expected inelastic demand.

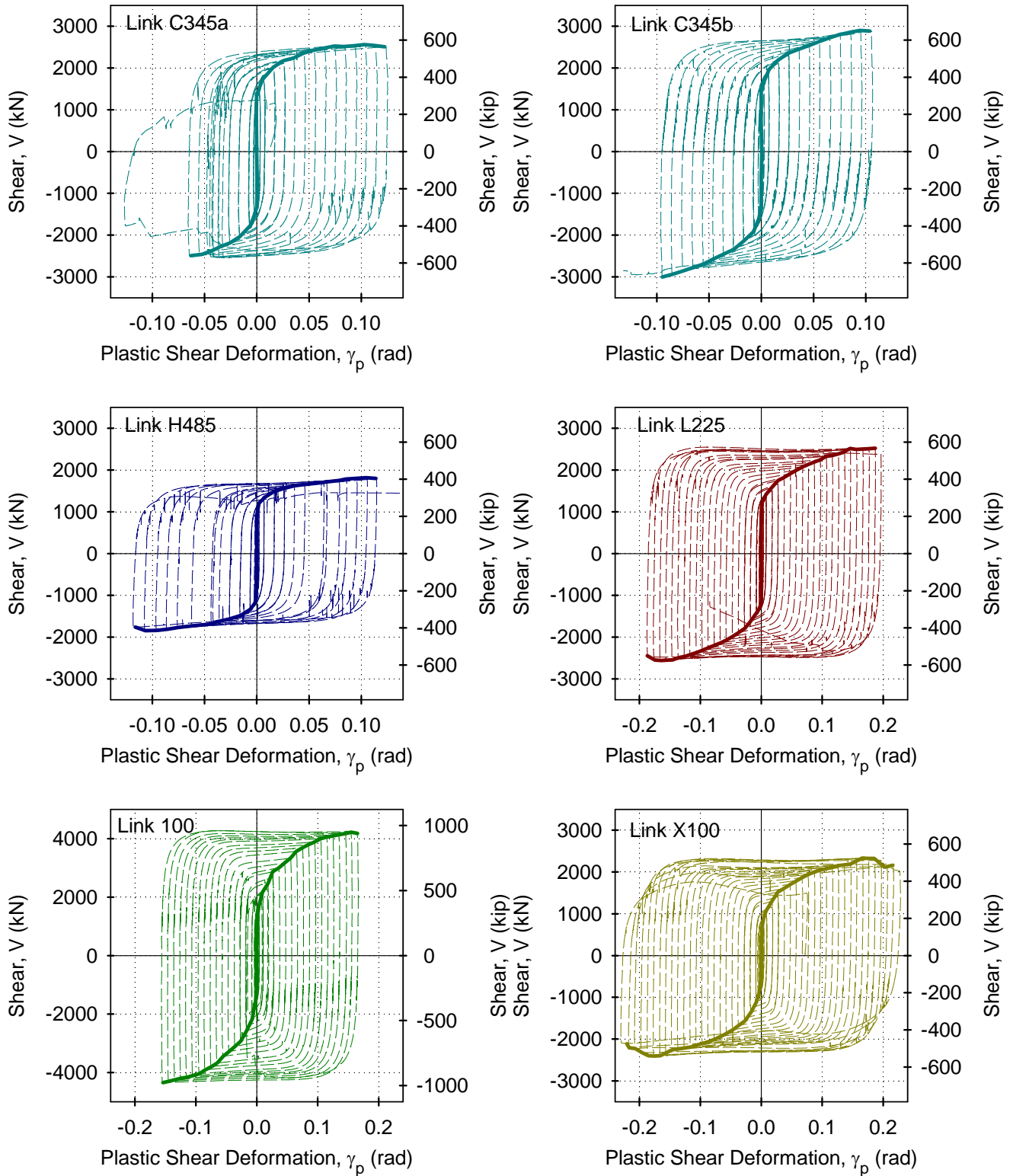


**Figure 5-4: Cyclic Backbone Curve from IC History Response**

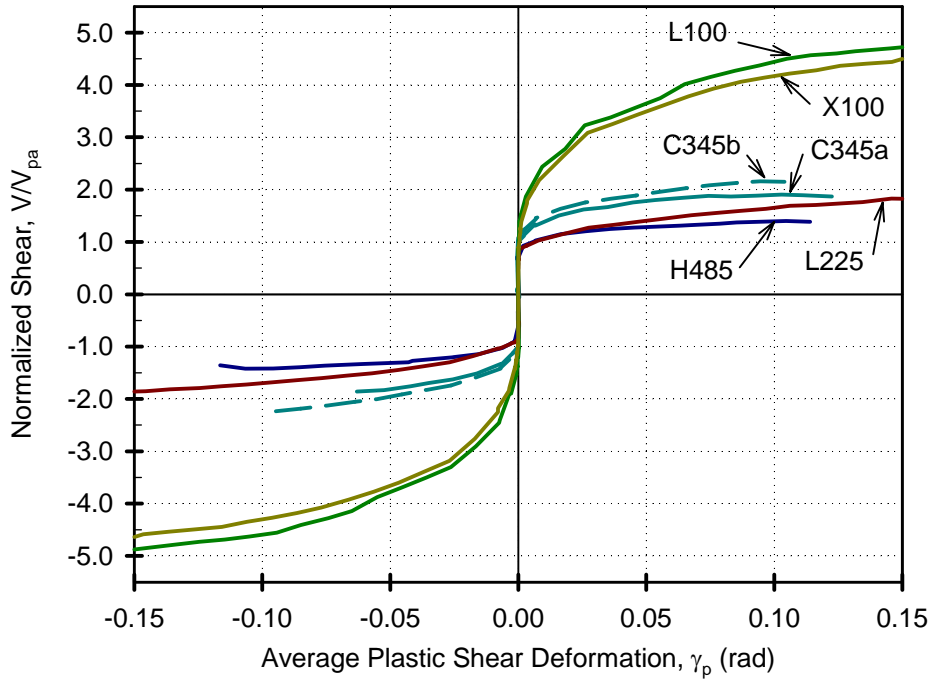


**Figure 5-5: Cyclic Backbone Curve Comparison for All Link Types**

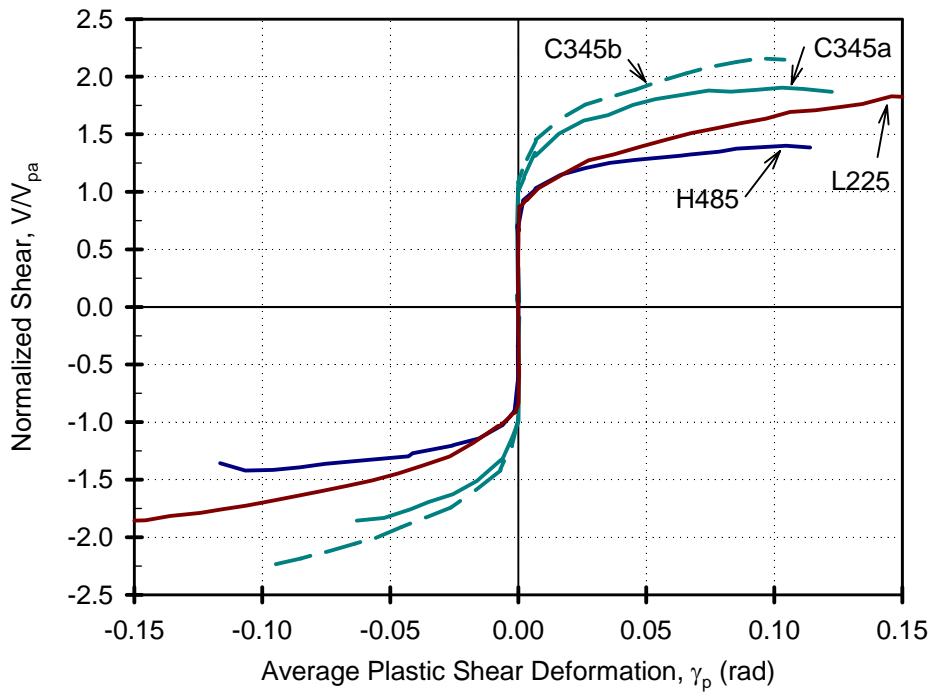


**Figure 5-6: Cyclic Backbone Curve Comparison without Link L100 and X100**

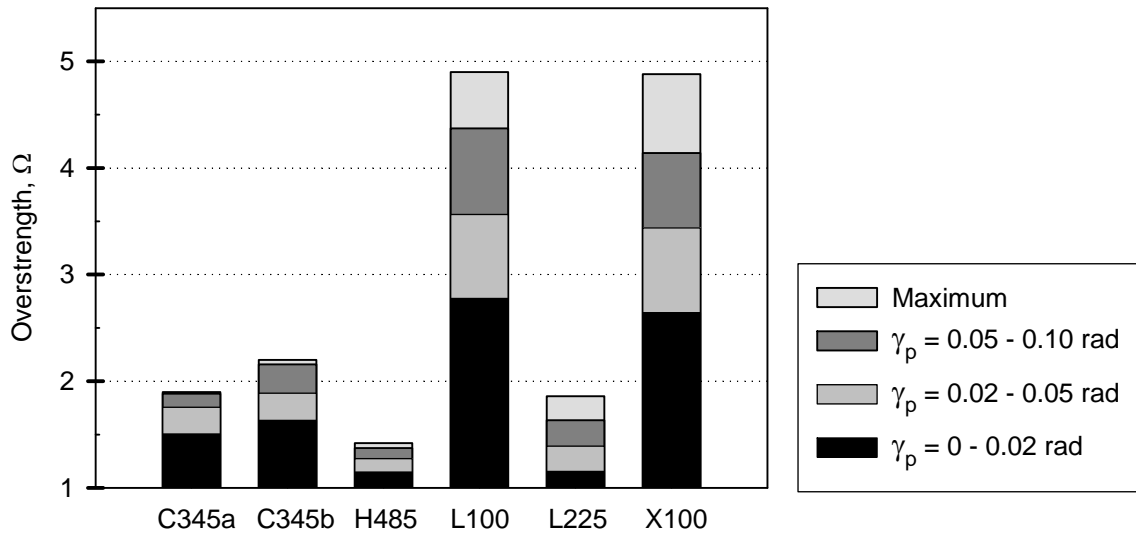


Figure 5-7: Overstrength Comparison from IC History

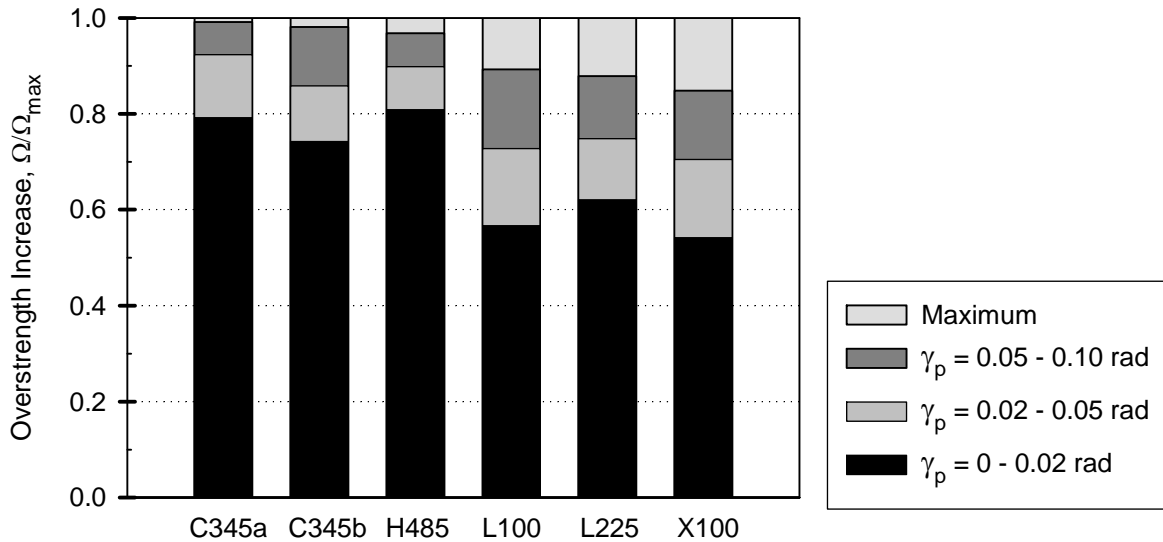


Figure 5-8: Normalized Overstrength Comparison from IC History

### 5.3.2 Influence of Material Behavior

Despite commonalities in nominal shear and moment capacities for most link types, the overstrength values varied significantly. One of the main differences among the links was the materials used within the

**Table 5-2: Summary of Maximum Overstrengths**

Deformation History	$\Omega_{max}$ for Link Type					
	C345a	C345b	H485	L100	L225	X100
IC History	1.90	2.20	1.42	4.90	1.86	4.88
After Set 2 of NF History	N.A.			4.44	1.70	4.28
After Cycles Following NF History	N.A.			-	1.88	4.87

effective length. Shear links and in specific the webs of those links that were made from the same material resulted in similar trends in the response as shown in Figure 5-5. The steel in the web of the link is important because the web inelasticity dominates the shear link behavior. Links C345a and C345b had different design characteristics, but the overstrengths followed similar trends in the lower deformation demands as well as at ultimate. Similarly Links L100 and X100 were designed with the same steel in the web and both followed similar trends in the lower deformation demands and resulted in extremely high overstrength values.

The results from the early cycles of the NF deformation history show the significance of material behavior on the resistance. The initial deformations of Link L100 subjected to the NF history are shown in Figure 5-9. After yield, the absolute value of the monotonic response increased up to the first reversal at  $\gamma_p = -0.05 \text{ rad}$ . The monotonic hardening was caused by strain hardening of the steel. The deformations reversed and for the same level of deformation, the shear resistance increased by 36%. Since the deformation was the same, only the material inelastic properties had increased the resistance of the link. Link L100 represented links with the highest overstrengths in the cases considered.

Similar trend was also observed in Link L225, which represented the second lowest overstrengths, shown in Figure 5-10. The slope of the monotonic hardening was lower and the resistance increased by 17% for the same  $\gamma_p = \pm 0.05 \text{ rad}$  points. The trend in the gradual increase in resistance for additional reversal points was described in greater detail in Section 4.4 and indicated progressive shear increase at the same deformation levels but after numerous reversals. These experimental results indicate a strong influence of material post-yield behavior on the overstrength in built-up shear links. In addition to the results from NF history, Section 5.3.3 further outlines the importance of material cyclic hardening on overstrength. The mechanical characteristics of the steels used in the specimens was further studied by Dusicka et al (2004).

### 5.3.3 Influence of Deformation History

The influence of deformation history on overstrength is related to the cyclic hardening characteristics of the individual steels. The overstrengths after the NF deformation history were consistently lower than after the IC history as summarized in Table 5-2, yet after the additional cycles following the NF history the overstrengths were nearly identical. Figure 5-11 and Figure 5-12 illustrate the difference between a monotonic response of shear links L225 and L100 to that achieved with IC history up to  $\gamma_p = \pm 0.05 \text{ rad}$  deformation. The monotonic response was obtained from the initial loading of the NF history.

Links of the same type but subjected to IC and NF histories were made from the same original plate to the same dimensions and using the same fabrication procedures. Yet, for the same deformation at  $\gamma_{eff} = -$

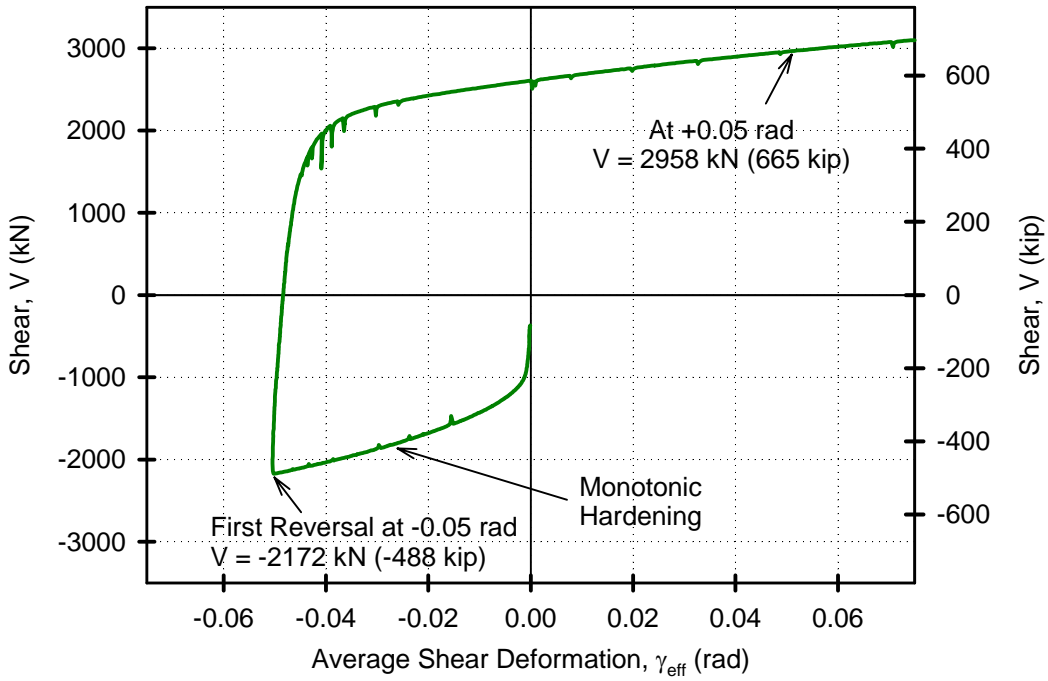


Figure 5-9: Initial Deformations of Link L100 Subjected to NF Deformation History

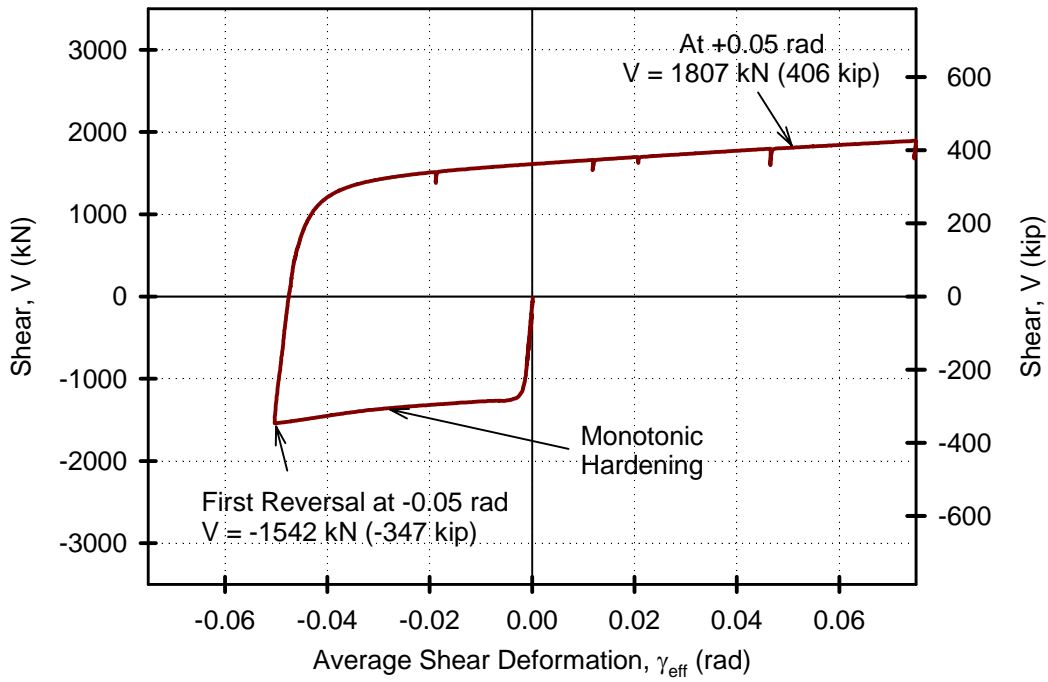
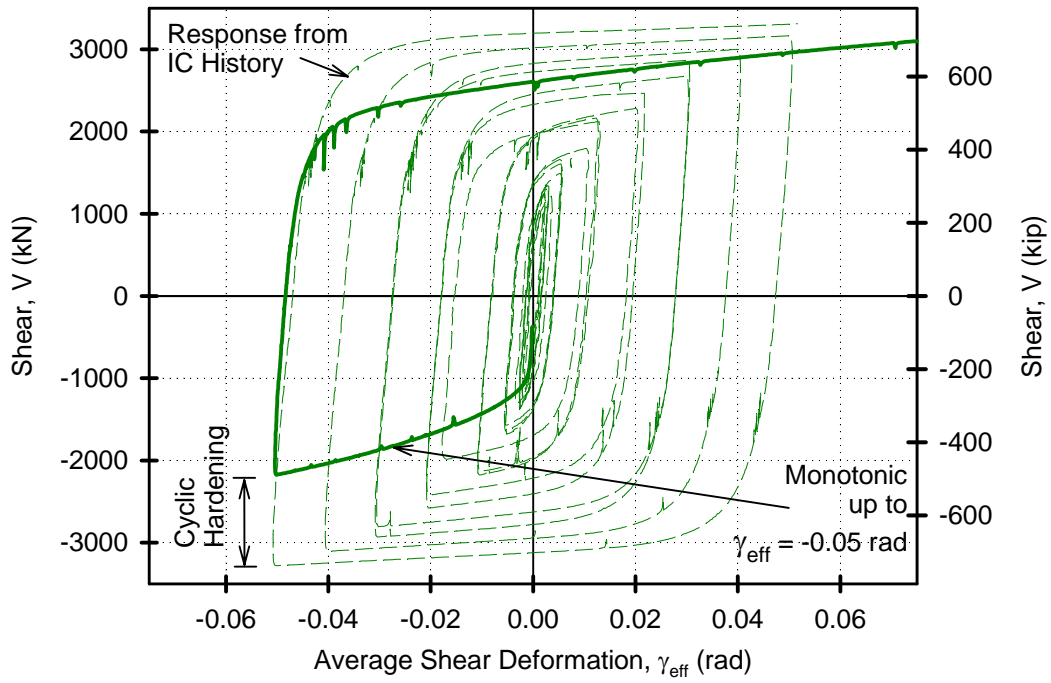
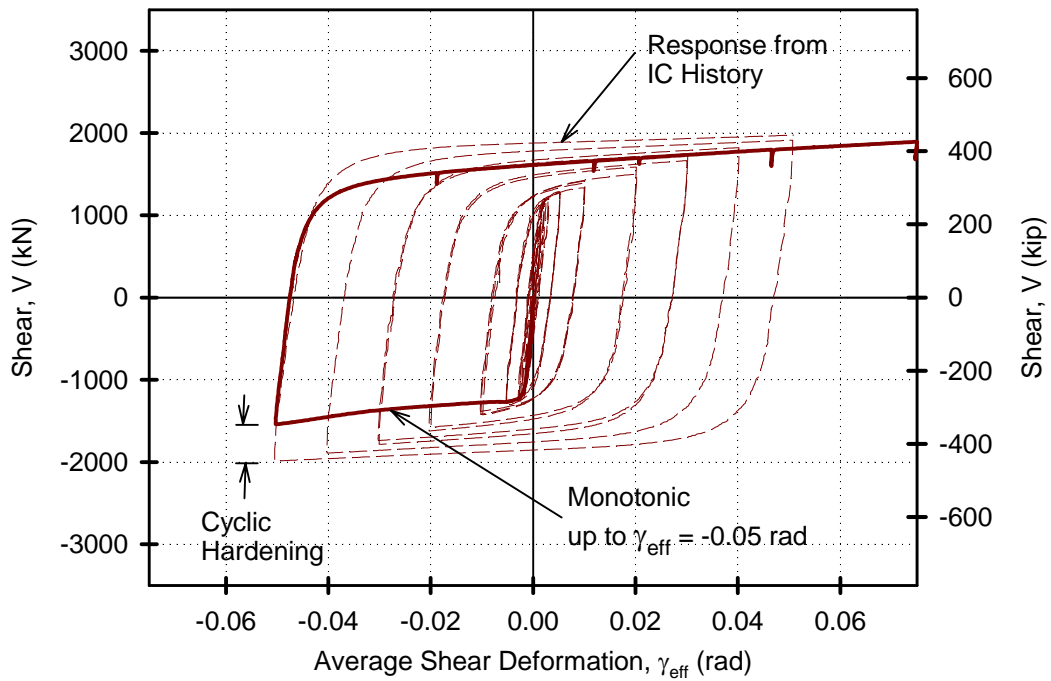


Figure 5-10: Initial Deformations of Link L225 Subjected to NF Deformation History



**Figure 5-11: Monotonic and Cyclic Response Comparison for Link L100**



**Figure 5-12: Monotonic and Cyclic Response Comparison for Link L225**

0.05 rad the resistance developed from the IC history was significantly higher than under simple monotonic loading. The only contributor to the increase in resistance was the cyclic hardening of the steel and resulted in a 56% and 28% increase for Link L100 and L225 respectively.

Under repeated cycles the shear resistance tended to stabilize throughout the NF history. During the second set, the loading and unloading parts of the stress strain curve were nearly identical and were also independent of the offset from origin. Figure 5-13 and Figure 5-14 show the bounding envelope of the response under both sets of NF deformation histories. Superimposed are the backbone curves from the IC deformation history. The original backbone curve does not approximate the shear resistance well for the absolute shear deformation values. However, when translated to the center of the NF history envelope, the backbone curve approximated closely the maximum resistance values. It is hence concluded that the resistance and thereby the overstrength are dependant on the range of shear deformations endured by the shear link, not just on the value of  $\gamma_{eff}$  achieved.

From the above discussion, the cause for the lower overstrengths after the NF history sets was due to the lower deformation range endured. The range of shear deformations in NF history was  $\Delta\gamma_{eff} = 0.20$  rad. The overstrength from IC history for the same strain range, i.e. for  $\gamma_{eff} = \pm 0.10$  rad, was 4.52 and 1.67 for Link L100 and L225 respectively. The overstrengths corresponded to within 2% in both cases. The material dependent cyclic hardening influenced the link resistance characteristics depending on the range of deformations and number of cycles.

The lower overstrength in C345a as compared to C345b was also partially influenced by the lower achieved deformation range, which resulted from reaching the actuator force capacity during the negative deformations. The deformation offset is apparent in the hysteretic response. Other factors such as differences in link geometry and test setup are also likely contributors.

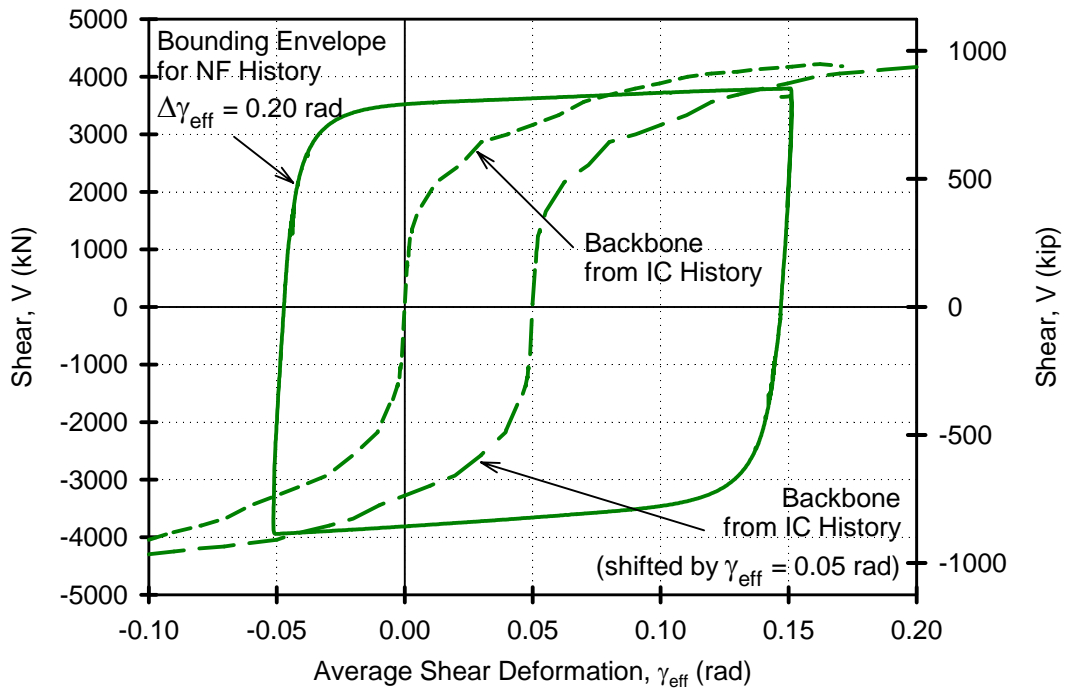


**Figure 5-13: Envelope and Backbone Comparison for Link L100**

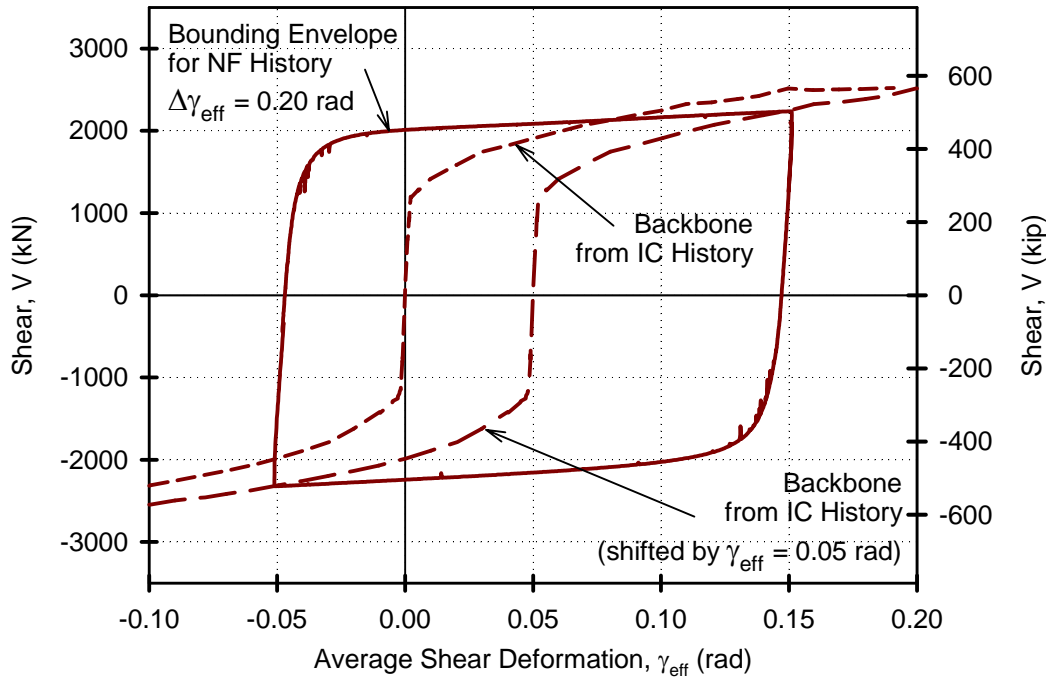


**Figure 5-14: Envelope and Backbone Comparison for Link L225**

## 5.4 Deformation Capacity and Failure Mode

One of the desirable properties of a shear link is the ductile hysteretic behavior, which is primarily characterized by high plastic shear deformation capacity. The deformation capacities were found to vary for the different shear link designs.

### 5.4.1 Effectiveness of eliminating stiffeners

The maximum shear deformation capacities obtained from the IC tests are summarized in Table 5-3 and graphically shown in Figure 5-15. All shear links significantly surpassed the implied minimum of the AISC Seismic Provisions. When considering that Link L100 capacity was not achieved due to premature failure of the connection, different levels of ultimate deformation capacity were evident. The links designed without stiffeners had on average 68% higher ultimate deformation capacity than the shear links with stiffeners. The improved performance was primarily due to the change in the mode of failure caused by eliminating stiffeners from the effective length.

The shear links with stiffeners consistently developed cracks in the heat affected zone next to the stiffener to web welds. With increasing deformations those cracks propagated through the depth of the web. This failure mode occurred near mid-length of the link where the shear deformations were larger than the average across the effective length. Failure mode of the links without stiffeners initiated in the web corners at the ends of the effective length where the shear deformation demand was lower than average. The resulting ultimate failure occurred at a significantly later point in the deformation history than the mode initiated at stiffener welds. Both types of failures were desirably ductile and contained to within the effective length.

The significance of these results lies in the inclusion or exclusion of stiffeners from the effective length, not in the number of stiffeners used. Link C345b only had one intermediate stiffener and the crack initia-

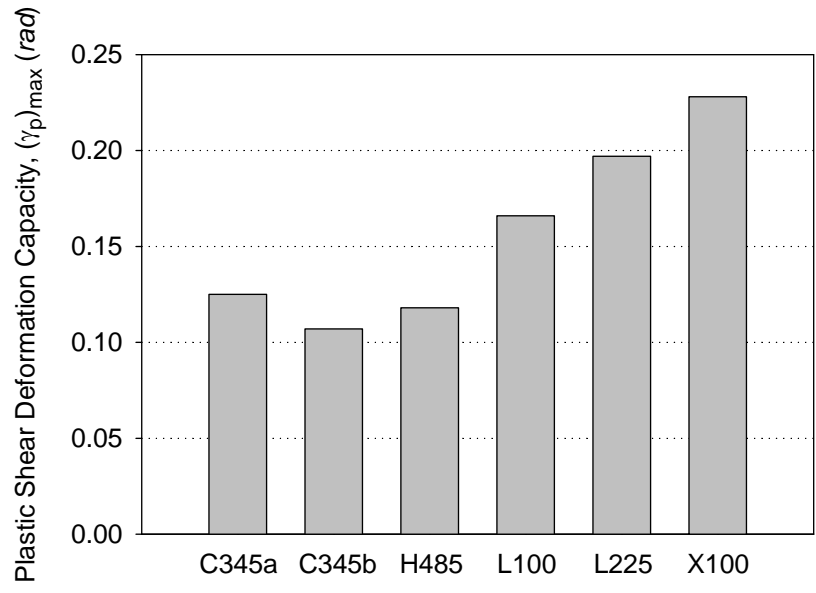


**Figure 5-15: Shear Link Maximum Cyclic Deformation Capacity**

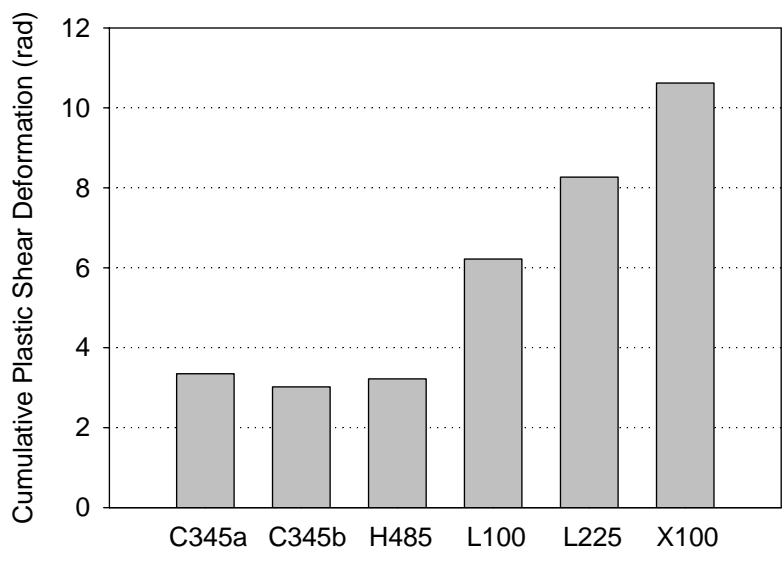


**Figure 5-16: CPSD at Failure from Incremental Deformation Tests**

tion and failure mode were similar to Link H485, which had 4 intermediate stiffeners. The absence of stiffeners eliminated welding and the associated HAZ from the face of the web where majority of the link inelasticity was generated. It should be stressed that eliminating stiffeners was only possible due to the low values of web compactness ratios. The design approach of eliminating intermediate stiffeners by decreasing the web compactness was found to be very effective in increasing the ultimate deformation capacity of the shear link.

### 5.4.2 Cumulative Plastic Shear Deformation

An additional measure of deformation performance can be made by comparing the damage sustained by the shear links throughout the deformation history. Damage was caused by plastic deformations and can be compared by calculating the cumulative plastic shear deformation (CPSD) using Equation 5-3. CPSD cumulatively adds the plastic shear deformations that was calculated based on the average shear deformation of the effective length of the shear link. The calculation of CPSD was made by considering all reversal points  $i$  up to the point of the last completed reversal  $n$  prior to failure.

$$CPSD = \sum_{i=0}^n |(\gamma_p)_{i+1} - (\gamma_p)_i| \text{ for } i = 0 \text{ to } n \quad (5-3)$$

The deformation history outlined in the AISC Seismic Provisions for eccentrically braced frame shear links would generate CPSD value of 2.77 *rad* after reaching the implied limit of  $\gamma_{eff} = 0.08 \text{ rad}$  for links made from 345 *MPa* (50 *ksi*) steels. All tested shear links surpassed that value as calculated from the IC history experiments up to failure in Table 5-3 and graphically compared in Figure 5-16. The contribution from the half-cycle during which failure occurred was not included. The difference between the CPSD values of links without stiffeners to those with stiffeners is more clearly defined than using  $(\gamma_p)_{max}$  because more plastic strain was accumulated during the larger deformation cycles. The links without stiffeners endured on average 160% more damage based on CPSD than links with stiffeners, further highlighting the benefits of excluding stiffeners from the effective length. Using CPSD instead of  $(\gamma_p)_{max}$  was also useful when comparing deformation capacity from different histories as it allowed for comparison of damage sustained by the shear link regardless of the path taken.

### 5.4.3 Influence of Deformation History

For the shear links without stiffeners, IC as well as NF deformation histories were applied on different specimens of the same shear link type. After completing two sets of the NF deformation history, Links L225 and X100 were subjected to additional cyclic deformations up to failure. Failure of Link L100 was not achieved due to failure of the connection prior to achieving capacity within the effective length. The CPSDs calculated from the near-fault history results are included in Table 5-3. Despite following the same NF deformation history, small variations in the achieved CPSD values after the second set were observed. These were caused by differences in elastic stiffness and in target versus achieved deformations. The elastic stiffness influences the calculation of the plastic shear deformation, which was calculated from the measured average shear deformation  $\gamma_{eff}$  based on Equation 1-13. The target average shear deformation were at times slightly over achieved or under achieved in the experiment as compared to the idealized targets. The accumulation of these differences resulted in small variations after completion of the NF deformation histories.

**Table 5-3: Summary of Deformation Characteristics from Built-up Shear Link Experiments**

History & Deformation Characteristic	Link Type					
	C345a	C345b	H485	L100	L225	X100
Incremental Cyclic History ( $\gamma_p$ ) <sub>max</sub> , rad	0.125	0.107	0.118	0.166*	0.197	0.228
After Cycles Following NF History ( $\gamma_p$ ) <sub>max</sub> , rad	N.A.			N.A.	0.201	0.221
CPSD at Failure After Incremental Cyclic History, rad	3.35	3.02	3.22	6.22*	8.27	10.6
CPSD at Failure After Near Fault History, rad	N.A.			4.83*	8.04	9.38

\* ultimate capacity not achieved due to connection failure

After the additional cyclic deformations that followed the two NF history sets for both Link L225 and Link X100, the maximum plastic deformations ( $\gamma_p$ )<sub>max</sub> were within 5% of the capacity achieved under IC deformation history. From this perspective, the different deformation histories did not influence the link capacity. The ultimate CPSD values were also similar. The CPSD was lower by 3% and 13% for Link L225 and X100 respectively when the near-fault deformation histories were used. The cumulation of plastic deformation during the different histories can be observed in Figure 5-17 and Figure 5-18 for Links L225 and X100 respectively. The progression is represented by the number of reversals  $2N$ , where  $N$  denotes the number of cycles. Reversals were used because cycles were not clearly defined for the NF deformation history. Since the number of reversals prior to failure varied depending on the deformation history, the reversals were normalized to the total number of reversals at failure  $2N_f$ . The ratio  $N/N_f$  therefore represents the life of the specimen from start of each deformation history up to failure.

The damage progression throughout the different deformation histories was markedly different. During the IC history, CPSD increased gradually with increasing reversals. At larger cycles, the accumulation of plastic deformation was significantly higher than during the initial cycles. The increase in  $\gamma_p$  was linear with each cycle, but the damage sustained between successive reversals at large deformations was far more significant than earlier in the deformation history. For example, the CPSD after  $\gamma_p = \pm 0.15$  rad was approximately 5 times the CPSD after  $\gamma_p = \pm 0.05$  rad.

The imposed deformations under the NF history were not symmetric and contained large and small deformation excursions. For reference, the completion of each of the two sets of near-fault histories are highlighted in the figures. The large initial deformations that are characteristic of the NF history are evident by the almost immediate increase in CPSD, showing that significantly more damage was inflicted early in the life of the specimen. At the end of the first set of NF deformation history, the damage based on CPSD corresponded to approximately the damage after 0.09 rad during the IC deformation history. Yet, the maximum achieved deformation under NF history was 0.15 rad. Based on the different progression of damage,

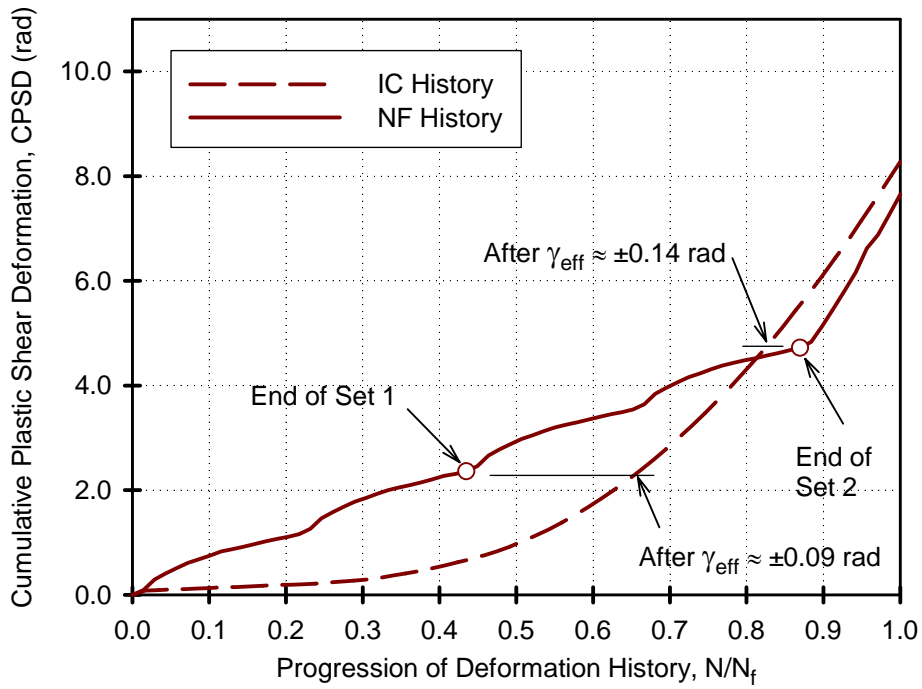


**Figure 5-17: CPSD in Link L225 Under Different Deformation Histories**

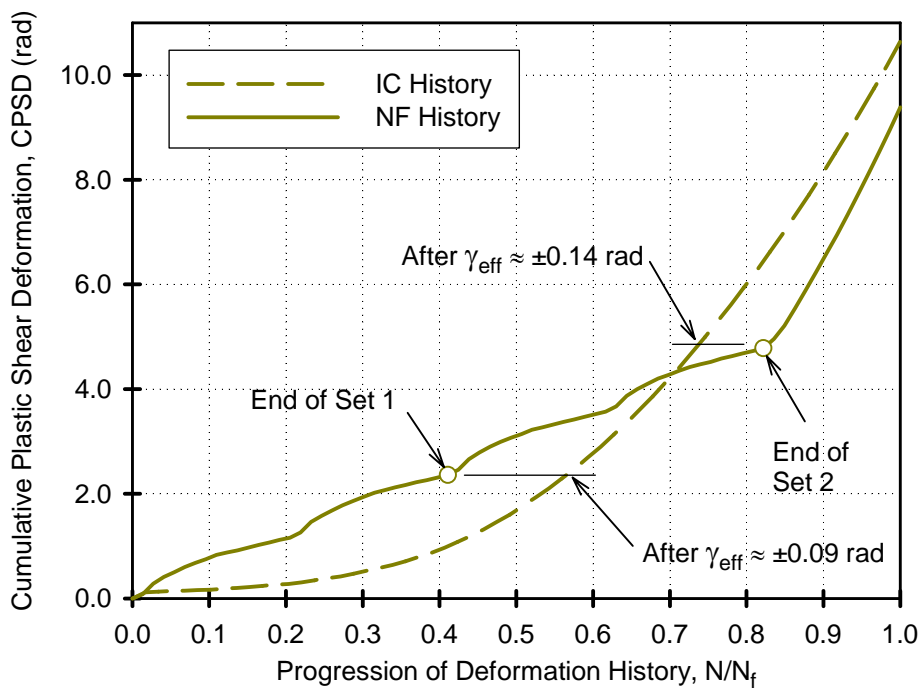


**Figure 5-18: CPSD in Link X100 Under Different Deformation Histories**

measuring the link deformation capacity using the maximum value of achieved plastic deformation is not necessarily representative of the link damage.

From these results the deformation history was found to influence the link damage throughout the life of the shear link, but not the ultimate values. The early accumulation of large plastic strain during the NF deformation history only marginally lowered the ultimate capacity in both links as compared to the values achieved under IC history. Hence, the damage measured by CPSD can be used to compare the performance of shear links subjected to both NF as well as IC deformation histories.

## 5.5 Implications on Built-up Shear Link Design

The results of the experimental program on built-up shear links lead to observations related to the design of built-up shear links. The AISC Seismic Provisions limit the expected design demand on a shear link to  $0.08 \text{ rad}$ . The cyclic deformation capacity of the built-up shear links surpassed that value and the design recommendations should at least remain at that level for built-up shear links in general. The superior deformation capacity of built-up shear links designed without stiffeners should be reflected by relaxing the maximum demand. The following are the proposed deformation limits for built-up shear links:

- $\gamma_p \leq 0.15 \text{ rad}$  for links without stiffeners and within the bounds of web compactness and effective length aspect ratios of previously tested shear links, otherwise
- $\gamma_p \leq 0.08 \text{ rad}$ .

These deformations were readily achieved by all links when considering  $(\gamma_p)_{max}$  as well as CPSD under IC deformation history. They were also achieved under NF deformation history for the shear links without stiffeners.

A single multiplication factor currently used in the AISC Seismic Provisions is inadequate in estimating the maximum resistance of built-up shear links and can be grossly unconservative. The influence of flange thickness and especially the web steel cyclic hardening characteristics must be incorporated into the calculation of overstrength. The cyclic hardening properties alone accounted for up to 50% of the resistance increase. The overstrength must be considered even for relatively small levels of plastic shear deformations and is further discussed in Section 7.7.

## 5.6 Summary

The results of large-scale cyclic experiments on six different built-up shear link types were compared. All specimens exhibited ultimate deformation capacities that exceeded the current AISC Seismic Provisions. The energy dissipated by the links was greater than 80% of the maximum theoretical energy per cycle, illustrating the effectiveness of using built-up shear links as ductile hysteretic devices. In addition to the maximum plastic shear deformations, cumulative plastic shear deformation values were calculated to compare the relative damage sustained by the links that were subjected to different load histories. The near-fault deformation history resulted in early accumulation of plastic strain as compared to the incremental cyclic deformation history. As a result, the plastic deformation at failure is only partially indicative of the damage sustained throughout the life of the link and should not be used as a sole indicator of achieved performance. The total accumulations of plastic strain for the near-fault and incremental histories were within 13% for Link L225 and X100.

The effectiveness of eliminating stiffeners and decreasing web compactness by incorporating low yield point steels within the effective length was evident by the increase in deformation capacity as compared to

the links with stiffeners. The improved performance was mainly attributed to the change in failure mode from HAZ of the stiffener welds near mid-length of the link to web tearing at the ends of the effective length.

The overstrength values significantly exceeded the expected values in the AISC Seismic Provisions in most cases. Experimental evidence pointed to the material characteristics as one of the major contributors to the maximum shear resistance. Cyclic hardening was especially evident when comparing the near-fault to the incremental cyclic deformation history. The shear resistance was found to be mainly a function of the deformation range, regardless of the offset of the history used.



## SECTION 6

### NUMERICAL INVESTIGATION OF BUILT-UP SHEAR LINKS

#### 6.1 Finite Element Modeling

Large-scale experiments are costly endeavors and one effective way to add additional value to the experimental program is to utilize the results and validate numerical models. The numerical models described in this section were developed concurrently with experimentation. These models allowed for closer investigation of the behavior of the shear links, especially in areas that were difficult to instrument, and assisted in explaining some of the observations made during the experiments.

The main objective was to develop numerical models for each type of shear link that was investigated using the large-scale experiments. In the case of inelastic behavior of shear links, both material as well as geometric non-linearities were required to account for the influence of material inelasticity and the changing geometry. The general purpose, finite element computer program ABAQUS v6.4 (HKS 2003) was used to model the built-up shear links. The software allowed for three dimensional finite element modeling and had the capability of incorporating material as well as geometric non-linear behavior, including geometrical instabilities. Local instabilities such as flange or web buckling were not significant contributors to the shear link behavior during the experiments, and therefore monotonic loading was used for the numerical models to approximate the cyclic backbone curves. The plastic strain demands in the various components of the built-up shear links were also investigated.

#### 6.2 Model Description

The models were developed in three dimensions to account for the interaction of the flange, web and stiffeners. The overall model geometry included the effective length as well as the connection zones of the shear links, but excluded the tower shafts and other components of the test setup. Since the analyses concentrated on the behavior of the effective length, the bolt holes and flange splice details were not incorporated into the link connection zones. The models of the different built-up shear link types shared a common approach in the final choice of element type, boundary conditions, material models and discretization.

##### 6.2.1 Element Type

Two types of three dimensional elements were considered for the built-up shear link models; plate and continuum elements. Plate elements are typically used to model the flanges, web and stiffeners of steel I-beams or rolled shapes (Itani et al 2003). For the shear link models, ABAQUS 8-node plate element S8R with 6 degrees of freedom per node was considered. The elements were spatially located at the plate center lines and were assigned the appropriate thickness values.

In contrast to the typical dimensions of steel girders or rolled shapes, the plate dimensions used for built-up shear links can have significant thickness. The thickness of the flanges in Link L100 made up 16% of the entire section depth. Plate thickness can have an influence on the inelastic response evidenced by the plastic strains recorded in the flanges from bending about the plate weak axis at the ends of the effective length during the experiments. For the shear link models, ABAQUS 8-node continuum element C3D8R with 3 degrees of freedom per node was considered to appropriately model the plate thickness. Section 6.3.1 discusses the applicability of these 2 elements to the shear link model and outlines both the final element choice and justification.

## 6.2.2 Boundary Conditions

A typical shear link model, utilizing either plate or solid elements is shown in Figure 6-1. The nodes at one end of the link were restrained against displacements in all directions. The nodes at the other end of the link were slaved to a single reference point RF1. The shear link deformations were imposed at RF1 by applying a displacement in the y-direction while providing a restraint against rotation about the z-axis. The reference point and thereby the end of the shear link was free to move in the x-direction. The combination of these boundary conditions imposed constant shear and equal end moments in the shear link without introducing any axial forces. The exclusion of axial force was made for clarity of results with a separate investigation on the influence of the axial force discussed later in Section 6.3.3.

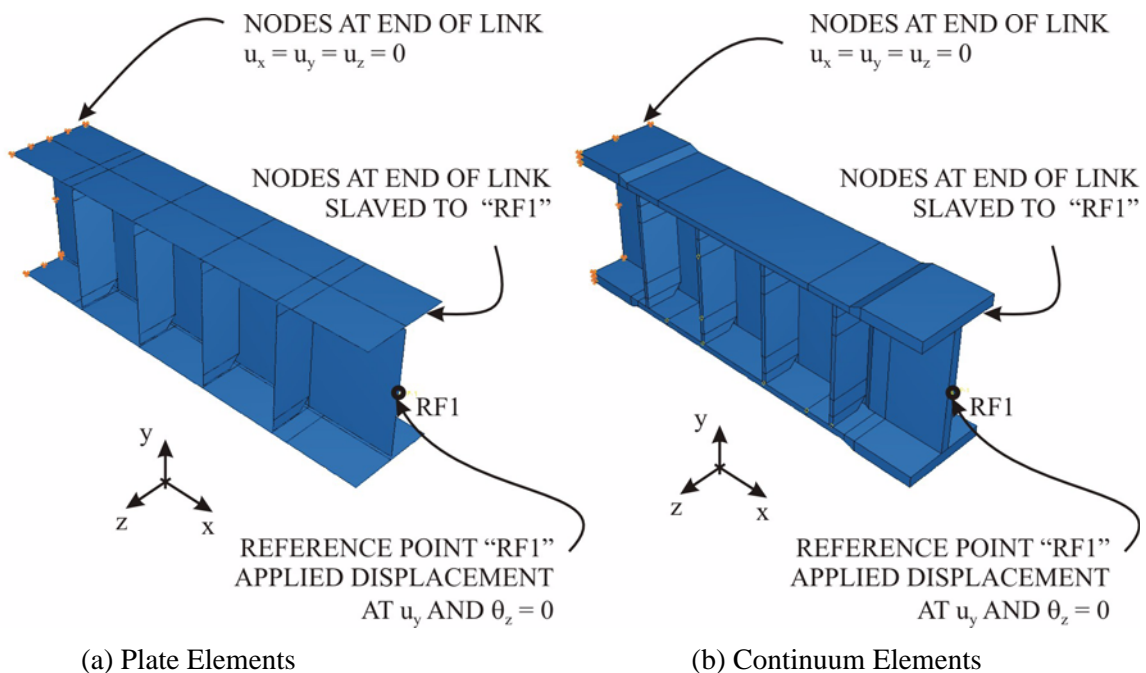


**Figure 6-1: Typical Model Layout Including Boundary Conditions**

## 6.2.3 Material Models

The material nonlinearity was defined by a yield stress along with plastic strain and associated stress data. The plasticity behavior was based on von Mises yield surface criteria, which is appropriate for the ductile behavior of steels. The yield strength for each grade of steel were obtained from the measured yield strengths of the steels previously summarized in Table 2-2, Table 3-2 and Table 4-2. The poisson ratio was assumed to be  $\nu = 0.3$  as typical for structural grade steels. Isotropic strain hardening was used for the material along with two types of post-yield material relationships, elasto-plastic and cyclic stress-strain relationships.

The elasto-plastic stress-strain relationship had no strain hardening and effectively discounted any material influence on the post-yield stiffness of the shear link. The cyclic stress-strain material behavior was incorporated by utilizing the results from cyclic coupon experiments (Dusicka et al 2004). Since monotonic

analyses of the numerical models were used to approximate the cyclic experimental results, the power law cyclic stress-strain relationships was utilized to define the plastic stress-strain material behavior of the different steels. The power-law relationship is defined by Equation 6-1 and the required parameters summarized in Table 6-1.

$$\varepsilon = \frac{\sigma}{E} + \left(\frac{\sigma}{K}\right)^{1/n} \quad (6-1)$$

where  $\varepsilon$  = true strain  
 $\sigma$  = true stress  
 $E$  = elastic modulus  
 $K$  = cyclic strain coefficient  
 $n$  = cyclic strain hardening exponent

**Table 6-1: Stress-Strain Power Function Coefficients (Dusicka et al 2004)**

Coefficient	Steel				
	A709 Grade 345 MPa (50 ksi)	A709 HPS 485W (70 ksi)	HT 440 MPa (65 ksi)	LYP 100 MPa (14.5 ksi)	LYP 225 MPa (33 ksi)
Cyclic Strain Coefficient $K$ , MPa (ksi)	1020 (148)	1010 (146)	1270 (184)	600 (87.1)	610 (88.4)
Cyclic Strain Hardening Coefficient, $n$	0.138	0.124	0.192	0.178	0.144

#### 6.2.4 Discretization

The flanges, web and stiffeners were modelled as individual components. The components included local geometric changes such as flange and web thickness transitions from the effective length to the connections and stiffener chamfer details. After spatially assembling the components, interactive constraint relationships were defined to tie together the nodes at the edges and surfaces of the intersections of the components. The welds were not included in the numerical model for reasons of computational simplicity.

The mesh density, which determined the typical element size in the model, was defined by a global seed assignment at the edges of the model. Local seeds were then assigned at specific locations to further refine the element mesh size. The meshing algorithm in ABAQUS uses the seed spacing to generate the element mesh. The mesh refinement was especially important for the models utilizing the continuum elements because closer element mesh size was required in areas of expected bending about the weak axis of the plates. As shown in Figure 6-2, the flanges at the ends of the effective length were refined to a smaller mesh size along the link length since localized yielding was recorded in those locations during the experiments. Similarly, the stiffener discretization was refined along the length at the flange connections. The

flanges and stiffeners were divided into five layers through each plate thickness. This division allowed for appropriate accommodation of the weak axis bending of those plates.

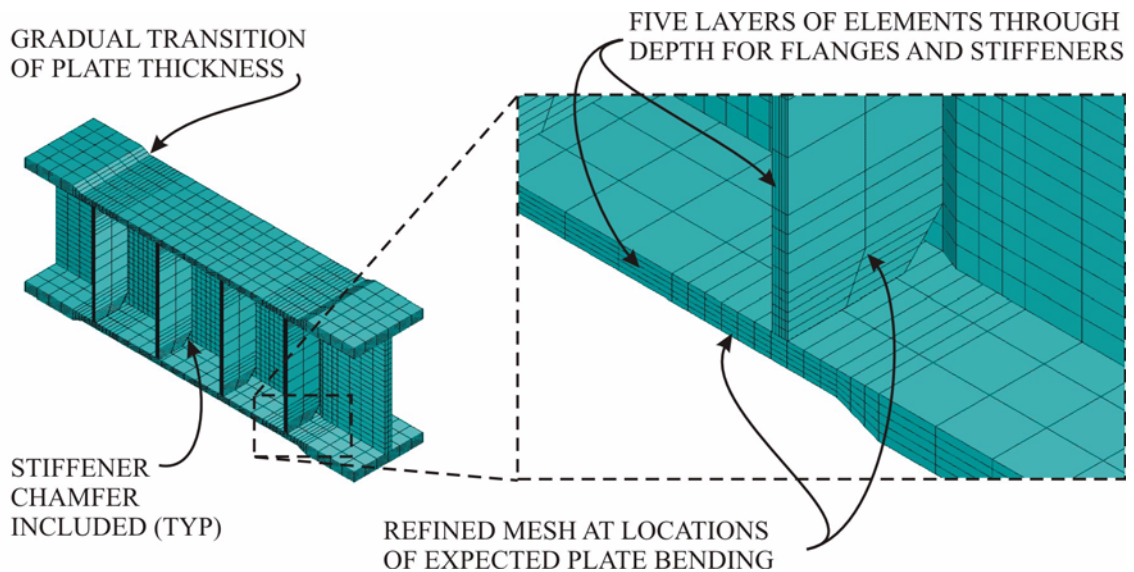


**Figure 6-2: Details of Model Discretization**

### 6.3 Results of Shear Link Analyses

During the experiments, the deformation of the effective length was measured independent of the connections and the test setup. For consistency, the average shear deformation of the numerical models was obtained using the same methodology. Diagonal displacements were measured across the effective length and the shear deformation was calculated using Equation A.3 as described in Appendix A. The numerical models were monotonically loaded until the shear deformation reached  $\gamma_{eff} = 0.15 \text{ rad}$ . The shear force was obtained from the reaction in the  $y$ -direction at the reference node RF1.

#### 6.3.1 Element Type and Size

The appropriate selection of the type of elements and the discretization of the mesh was investigated using the model for Link C345a as it was the first model to be developed. The cyclic material stress-strain relationship for A709 Grade 345 MPa (50 ksi) steel was used and the following element choice and discretization options were investigated:

- plate elements S8R with global mesh seeding of 20 mm (0.79 in).
- continuum elements C3D8R with global mesh seeding of 50 mm (2.0 in).
- continuum elements C3D8R with global mesh seeding of 20 mm (0.79 in).
- continuum elements C3D8R with global mesh seeding of 10 mm (0.39 in).

The models were pushed to  $\gamma_{eff} = 0.15 \text{ rad}$  shear deformation. As shown by the shear deformation response in Figure 6-3, the overall behavior was similar for both element types and for the considered discretization options. The response of the models using the continuum elements converged for global seeding of 20 mm

(0.79 in) or less. The shear resistance was consistently lower for the model using the plate elements for deformations exceeding approximately  $\gamma_{eff} = 0.08 \text{ rad}$ . Reducing the size of the continuum elements did not improve upon this difference, which was found to be caused by the strain distribution in weak axis bending of plates.

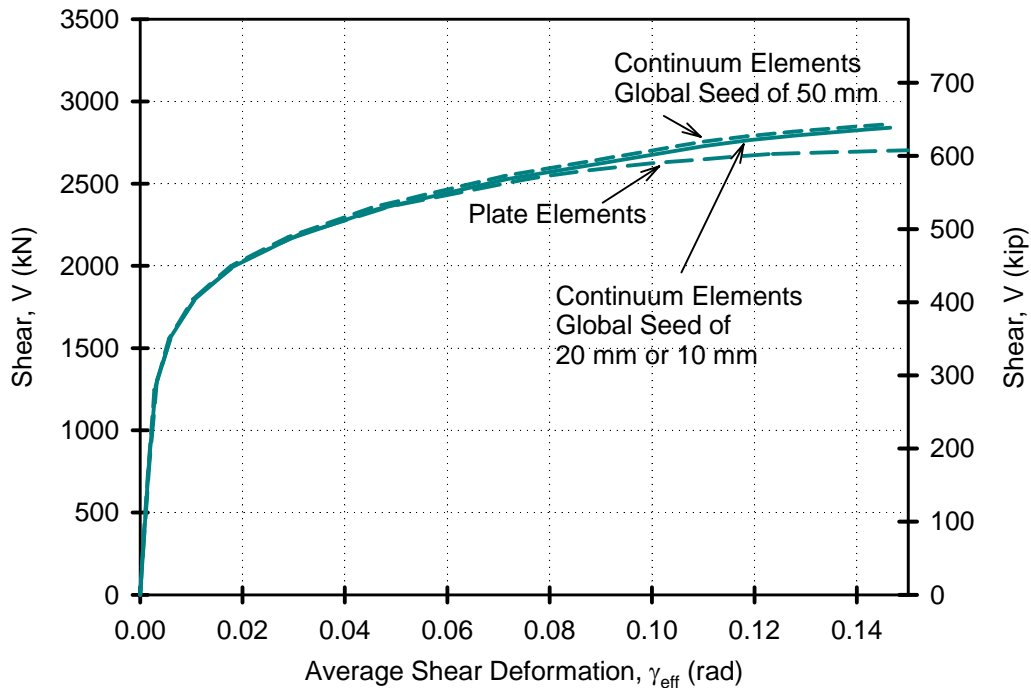
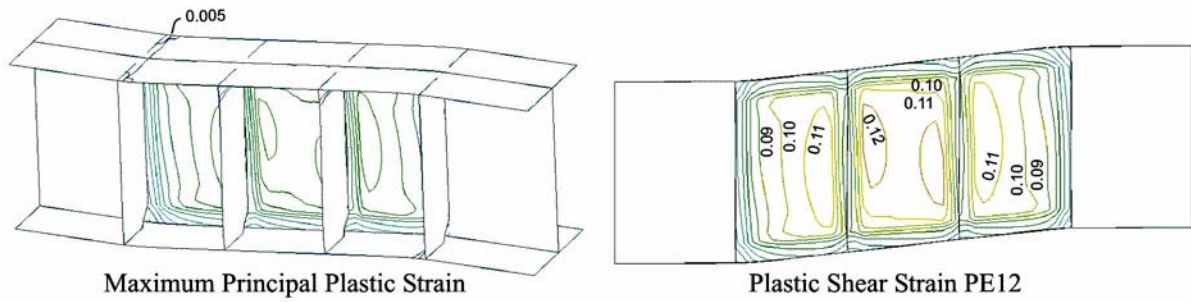


**Figure 6-3: Global Response Comparison of Considered Models of Link C345a**

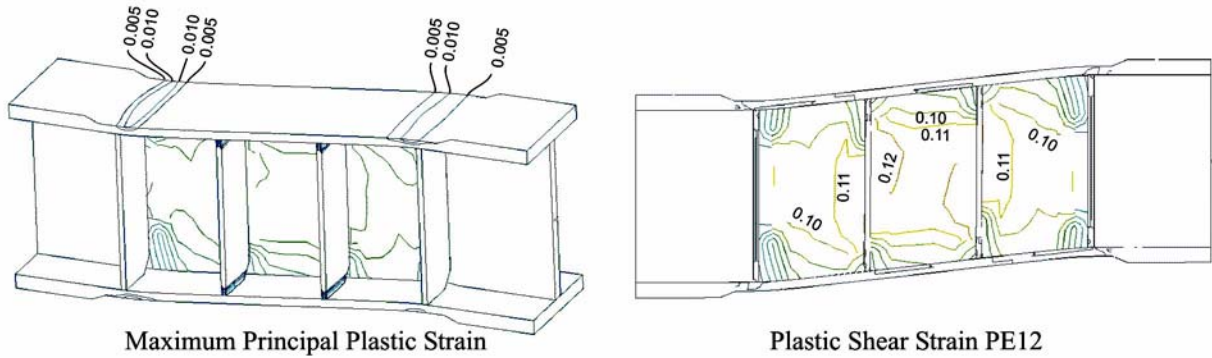
The plastic strains in the flanges of the numerical models utilizing continuum elements were more representative of the trends in the flange strains recorded from the experiments. The maximum principal plastic strains in the flanges are shown for the different models in Figure 6-4 for shear link deformation of  $\gamma_{eff} = 0.10 \text{ rad}$ . The plastic strain distribution was not uniform through the depth of the flanges and extended over a longer length for the models utilizing continuum elements. The partial plasticity of the flanges contributed to a higher resistance as compared to the fully plastic flanges of the models utilizing the plate elements.

Important differences were also observed when comparing the plastic shear strain distributions in the web of the links as shown in Figure 6-4. The plastic shear strain PE12 in the center of the web panels indicated similar levels of demand among the different model options. However, the strain demand in the web showed increased concentrations of plastic strains for the models using continuum elements. The strains concentrated in the area of the stiffener to web connections near the ends of the stiffener chamfers. This was not observed in the plate models where the stiffeners were defined along a line of nodes at the web intersections, instead of an area that was representative of the plate thickness.

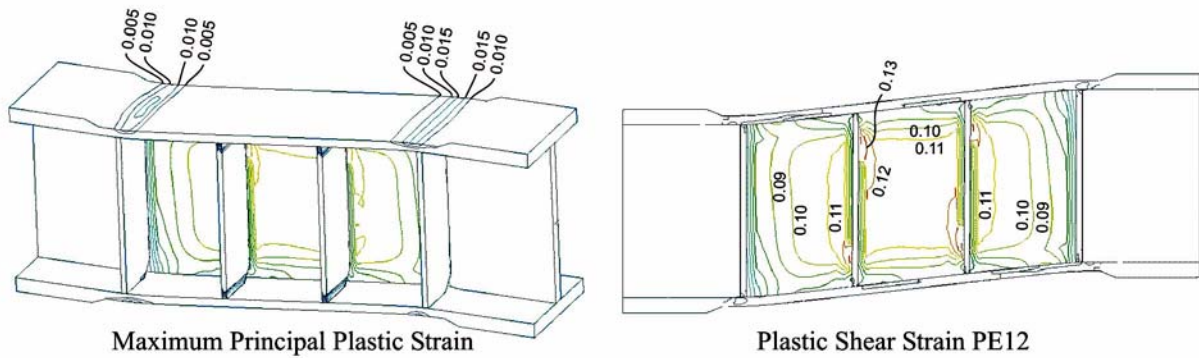
In general, the shear deformation responses were similar for the options considered, but the continuum elements allowed for modeling of plastic strains that was more closely correlated to the experimental. The final element type and discretization of the model was selected as continuum elements C3D8R at a global



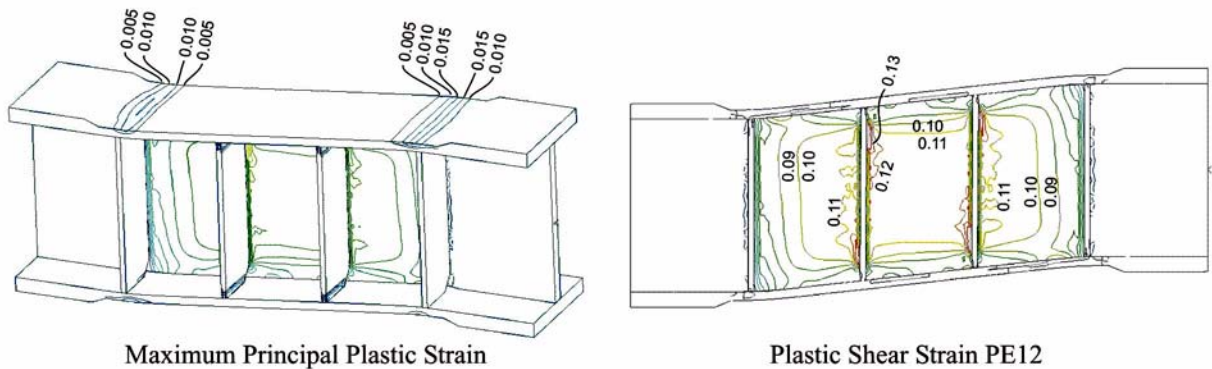
(a) Plate Elements with Global Seed at 20 mm



(b) Continuum Elements with Global Seed at 50 mm

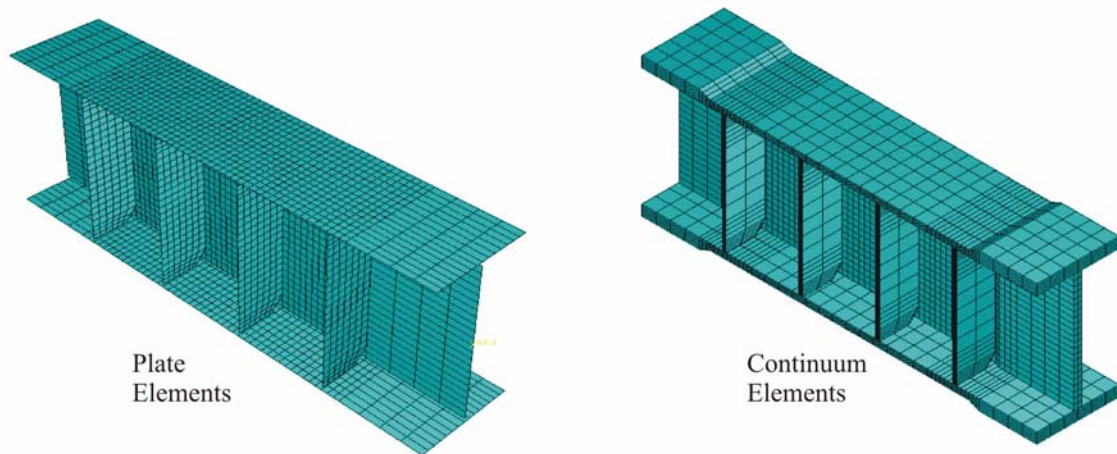


(c) Continuum Elements with Global Seed at 20 mm

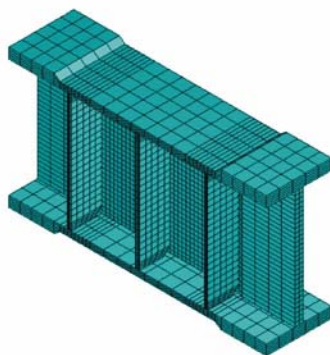


(d) Continuum Elements with Global Seed at 10 mm

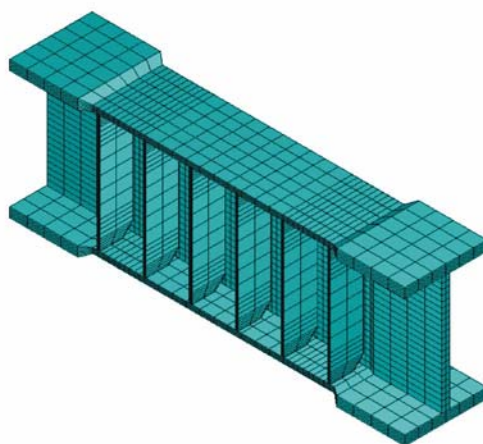
**Figure 6-4: Strain Comparison of Link C345a Models at  $\gamma_{eff} = 0.10$  rad**



(a) Link C345a

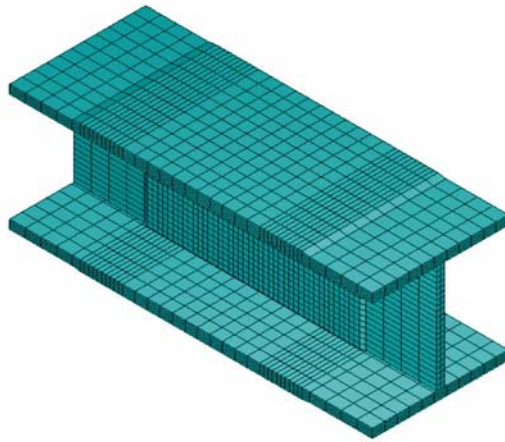


(b) Link C345b

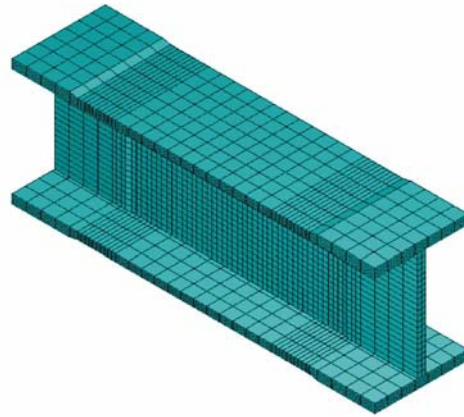


(c) Link H485

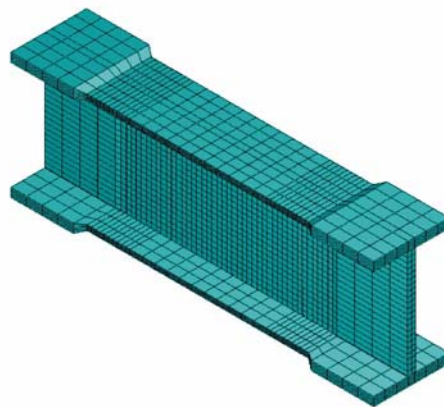
**Figure 6-5: Models of Shear Links with Stiffeners**



(a) Link L100



(b) Link L225



(c) Link X100

**Figure 6-6: Models of Shear Links without Stiffeners**

seed of 20 mm (0.79 in). At this discretization the plastic strains were well represented without the added computational effort required for finer mesh size. This choice of the three-dimensional element and discretization was extended for the other types of shear links listed in Table 5-1. The meshed models representing the shear links with stiffeners are shown in Figure 6-5 and those without in Figure 6-6.

### 6.3.2 Correlation to Cyclic Response

The force deformation response from the monotonically loaded numerical models was compared to the experimental cyclic backbone curve for the different shear link types in Figure 6-7 through to Figure 6-12. In all cases, the response of the models with elasto-plastic material relationship did not correspond well to the experimental. However, the numerical models utilizing the material cyclic stress-strain relationships exhibited a much closer correlation. These results confirmed the experimental observations that material stress-strain characteristics have significant influence on the built-up shear link behavior and illustrate the feasibility of approximating the cyclic backbone curves through the use of monotonically loaded numerical models.

The response of the numerical models correlated well to the experimental for shear links made from the structural grade steels, i.e. Links C345a, C345b and H485. This was especially the case for Link C345a where the initial hardening was nearly identical up until the point of  $\gamma_{eff} = 0.08 \text{ rad}$ , when during the experiment the cycles did not fully reverse. The response of the model for Link C345b also followed closely the shape of the backbone curve, only slightly underestimating the experimental response. The difference between experimental response of C345a and C345b was likely caused by the test setup. The geometry of the test setup for 345b was more susceptible to the development of tensile axial forces and may have contributed to the increased resistance in that shear link. The model of Link H485 was also reasonable, but did over-estimate the resistance at larger deformations. The transition from elastic response was much more gradual in Links C345a and C345b as compared to Link H485, a difference that was well captured by the numerical models.

The response of the numerical models of links made from low yield point steels, i.e. Links L225, L100 and X100, showed similar trends to the experimental backbone curve, but had consistently higher resistance than the experimental results. The discrepancy was caused by the material cyclic stress-strain relationship. The numerical model used the power law material relationships developed from the cyclic coupon tests. The cyclic response of the LYP steel coupons did not stabilize in the same manner as the structural grade steels. The power law relationship was derived from the maximum values of the stress that developed under the repeated cycles of the same amplitude strain. The deformation in the shear link experiments were incrementally increased in amplitude after just one cycle and hence the cyclic hardening did not increase the resistance to the same level as that represented by the power law relationship. The numerical model consistently overestimated the stress in the material and provided an upper bound shear resistance for the links with LYP steel.

### 6.3.3 Influence of Axial Force on Shear Resistance

It is possible that under large deformations of the shear link, axial tensile forces were introduced by the deformed test setup geometry as explained in Appendix A. The influence of the axial force on the link shear resistance was inherent in the processing of the actuator load data. It is important to quantify the influence to better understand the significance of axial loading on link shear resistance. The numerical models of all link types were re-analyzed with a tensile axial force, which has the potential of increasing the shear resistance of deformed shear links.

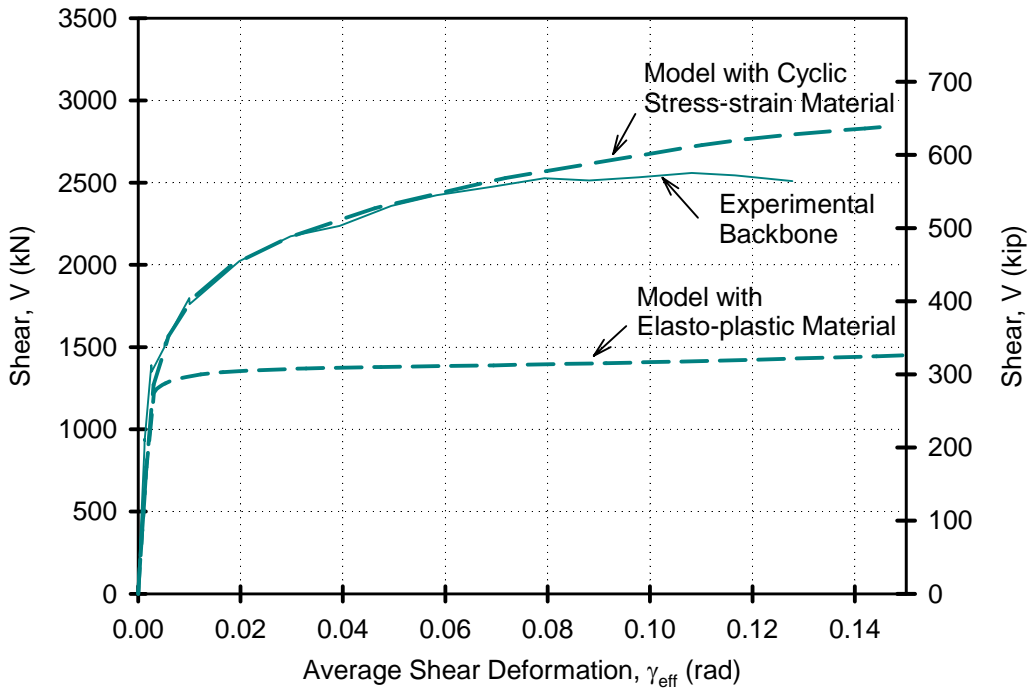


**Figure 6-7: Model and Experimental Response Comparison of Link C345a**

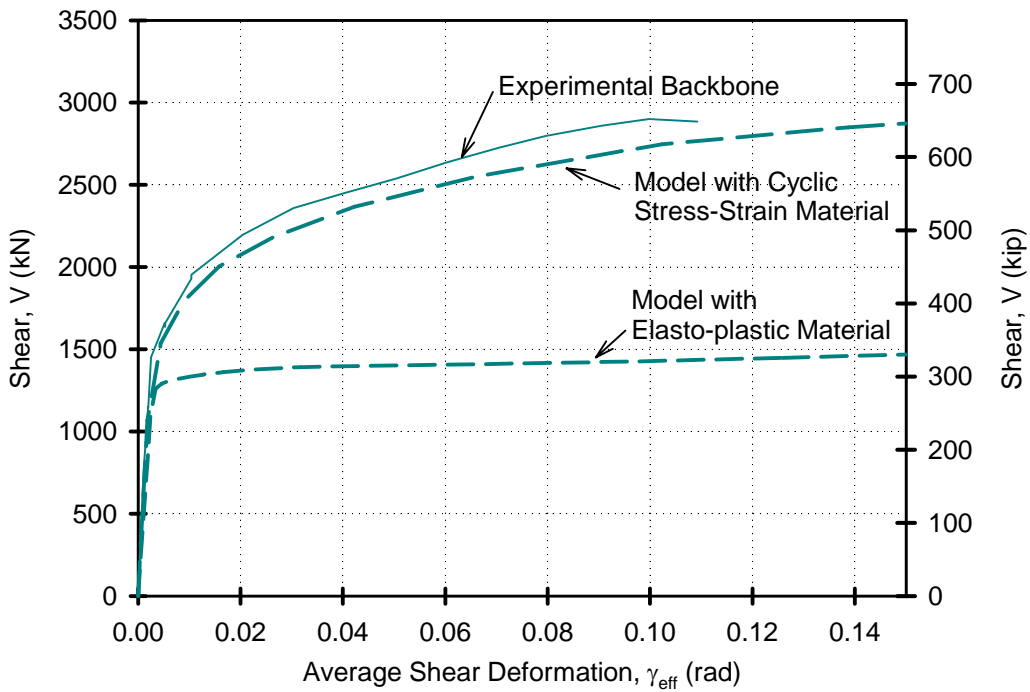


**Figure 6-8: Model and Experimental Response Comparison of Link C345b**

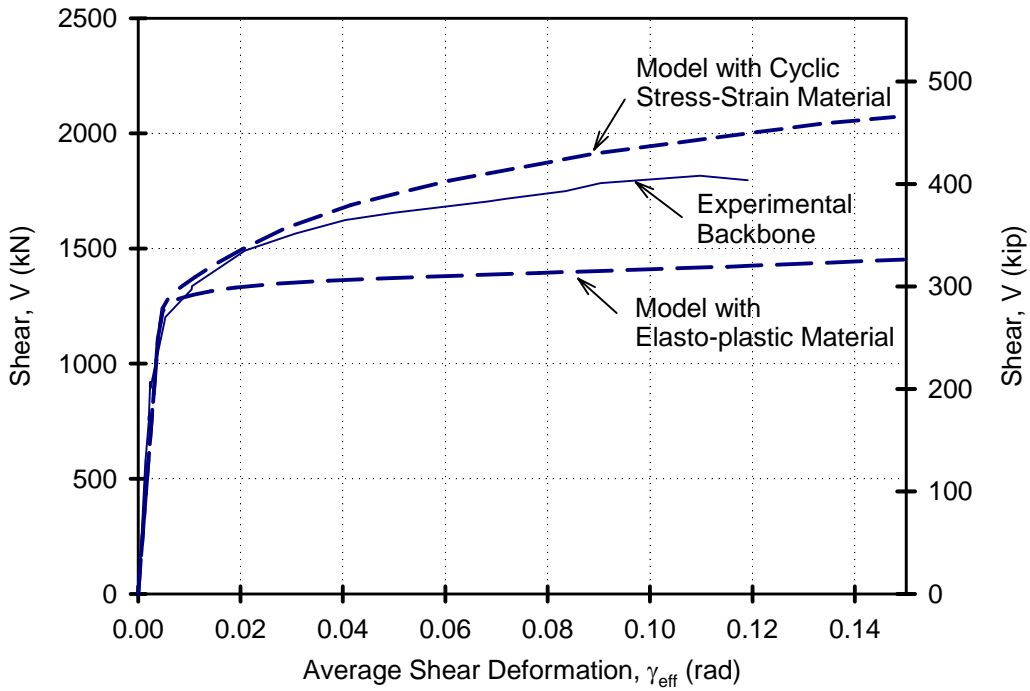


**Figure 6-9: Model and Experimental Response Comparison of Link H485**

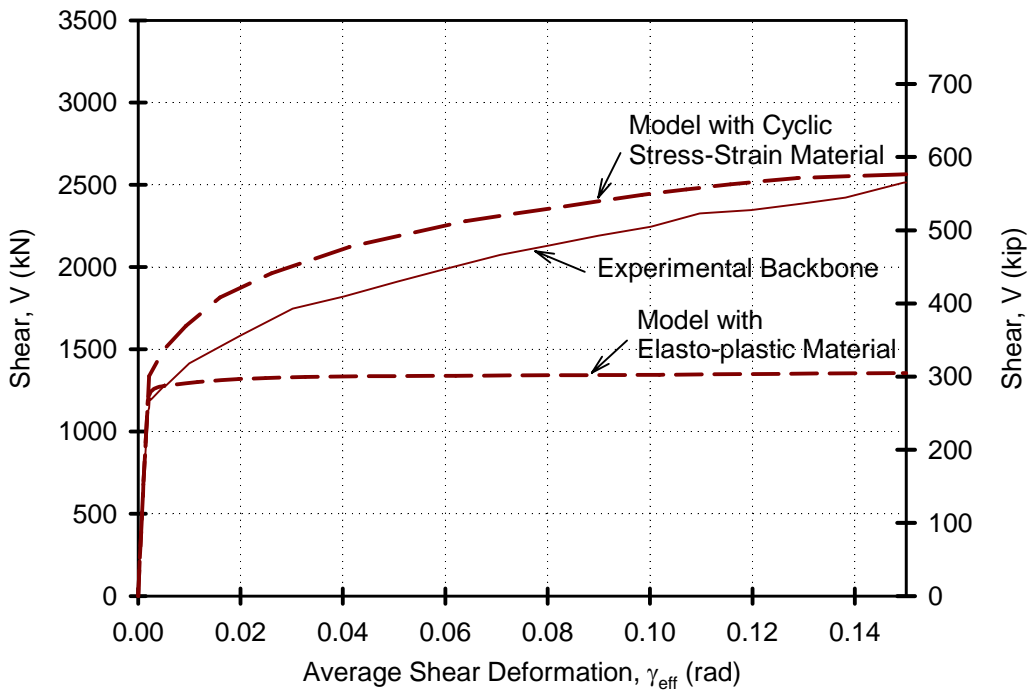


**Figure 6-10: Model and Experimental Response Comparison of Link L225**

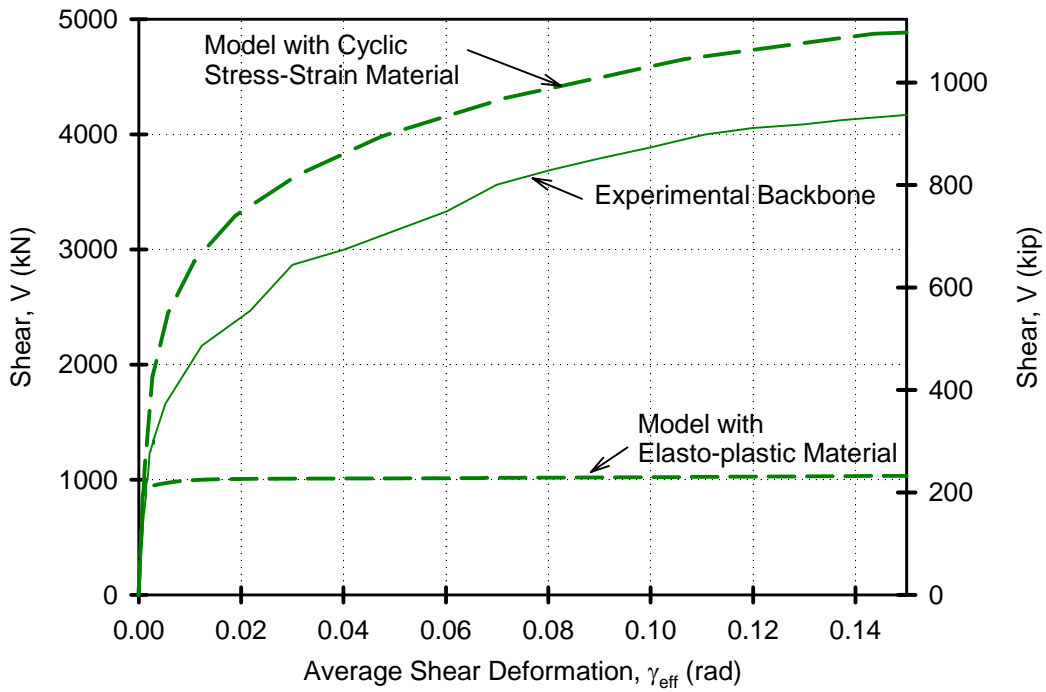


**Figure 6-11: Model and Experimental Response Comparison of Link L100**

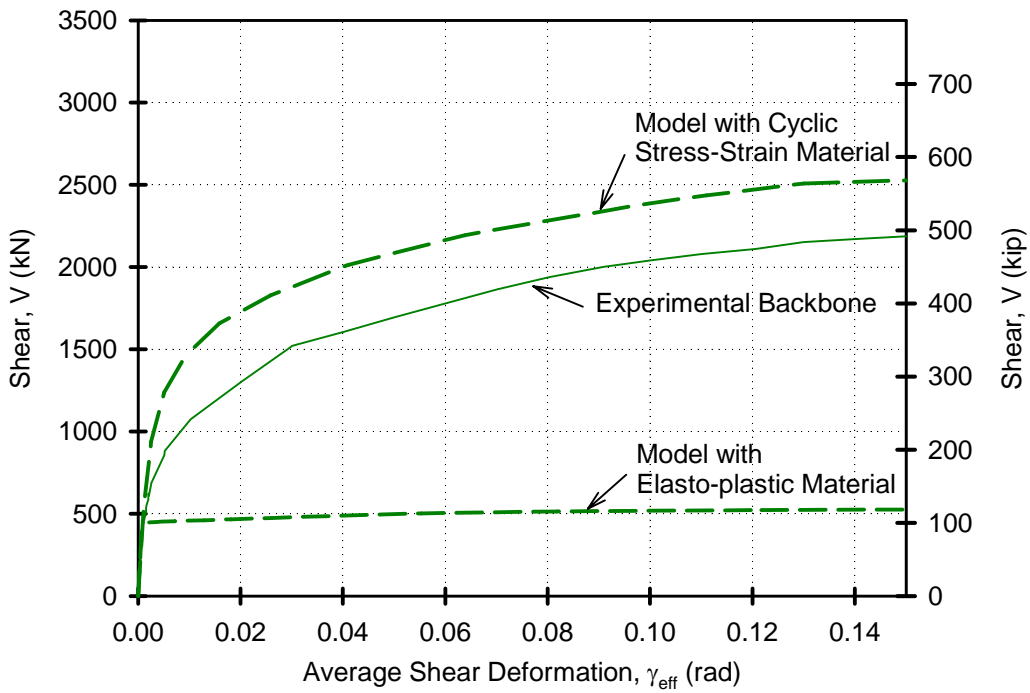


**Figure 6-12: Model and Experimental Response Comparison of Link X100**

The link axial force  $F$  was applied at RF1 and linearly increased with deformation from zero to a peak value of  $0.20P_y$ , where  $P_y$  is the axial yield capacity of the link calculated as  $P_y = Af_y$  for a link cross sectional area  $A$  and nominal yield strength  $f_y$ . The peak axial force was chosen as the axial force estimated in Appendix A for actuator displacements corresponding to approximate shear link deformations of  $\gamma_{eff} = 0.20 \text{ rad}$ .

The results of the analyses where axial force was included were compared in Figure 6-13 to the results of models without any axial forces. The tensile axial force in the link increased the shear resistance at large shear link deformations by 5% to 8%. This increase was also calculated by using equilibrium of an idealized link shown in Figure 6-14 in order to develop a method of approximating the effect of axial force without the need for detailed numerical models. Equal moments  $M$  were assumed at the ends of the effective length  $e$ . It can be shown that the shear resistance  $V$  is directly proportional to the axial force  $P$  and shear link deformation  $\gamma_{eff}$  as described by Equation 6-2.

$$V = \frac{2M}{e} - P\gamma_{eff} \quad (6-2)$$

Hence, the increase in shear resistance caused by the axial force can be approximated by  $P\gamma_{eff}$ . This increase was added to the original numerical results and is compared to the numerical models in Figure 6-13. The approximation was consistently higher than the numerical model results, but showed that the simple expression could be used to conservatively estimate the shear resistance increase.

## 6.4 Plastic Strain Demand

The detailed numerical models allowed for closer investigation of plastic strain demand in the shear links. The accumulation of plastic strain can lead to material fatigue and cracking, potential sources of failure we can investigate effectively using numerical modeling. The strains obtained from gauges during the experiments were only in specific locations whereas the strains in the model could be obtained as a distribution throughout the link. Utilizing the continuum elements allowed for realistic representation of relative plate thicknesses of the flanges and stiffeners. The strain demands in the web and the flanges were examined for correlations to the failure modes and cracking patterns observed during the experiments.

### 6.4.1 Influence of Stiffeners on Web Strains

A consistent correlation was found between the location of the initial cracking during the experiments on shear links with stiffeners and the location of localized plastic shear strain concentrations in the numerical models. The plastic shear strain demand in the built-up shear links in which stiffeners were used is shown in Figure 6-15 for deformations at  $\gamma_{eff} = 0.10 \text{ rad}$ . The increase in strain demand occurred consistently at the ends of the stiffener to web connection, next to the stiffener chamfer. The plastic strains in those locations were over 20% higher than in the middle of the panel and coincided with the welding start and stop locations of the stiffener fillet welds. This indicates that the onset of cracking in the web observed during the experiments was likely caused by the combination of the influence of the heat affected zone and the plastic strain concentrations. The ends of the effective length remained primarily elastic and hence the end stiffeners did not influence the web plastic strains.

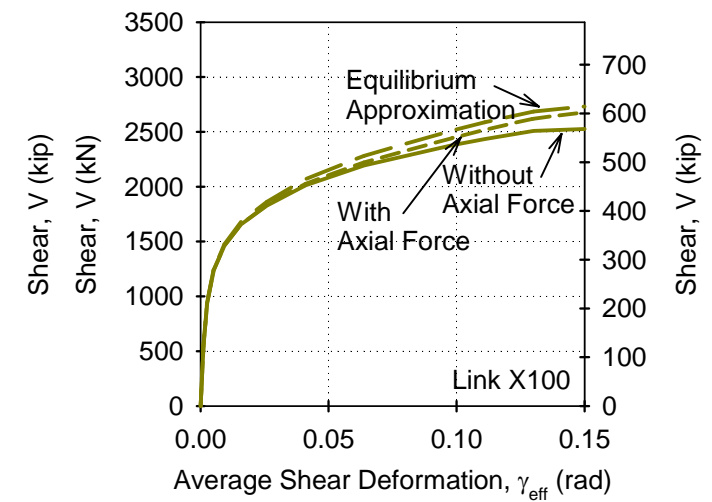
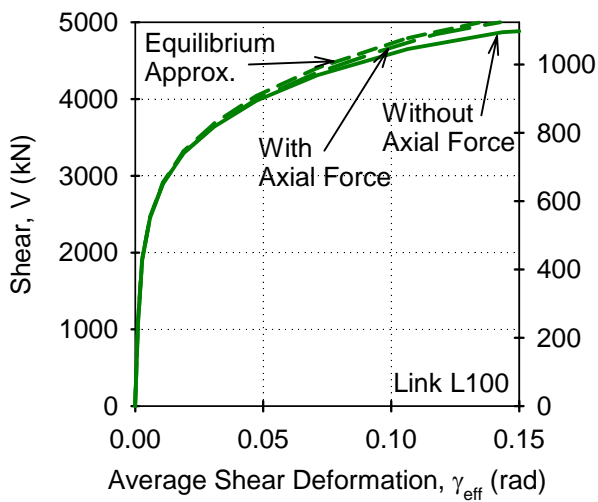
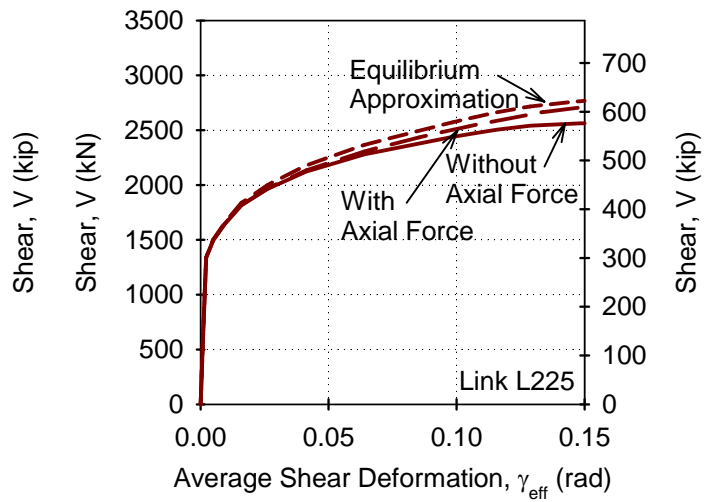
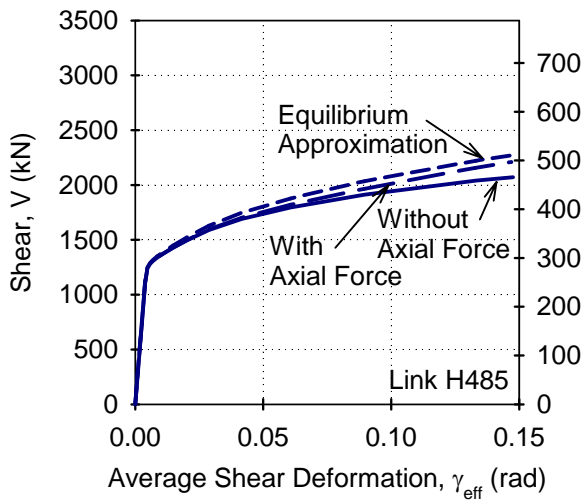
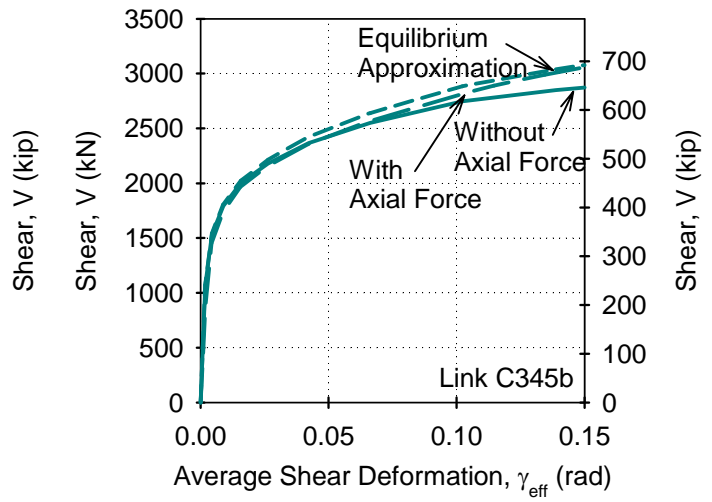
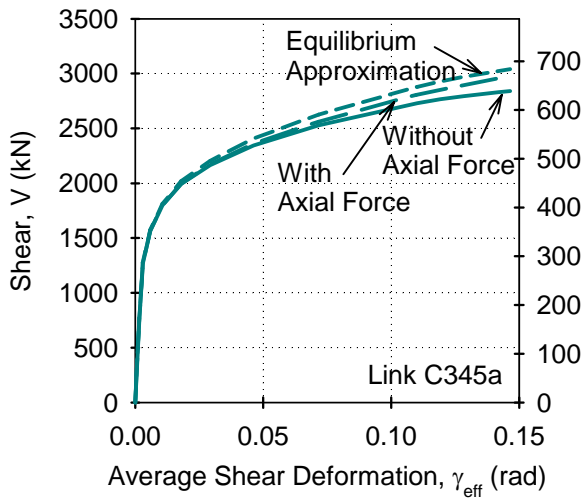


**Figure 6-13: Influence of Axial Force on Shear Resistance**

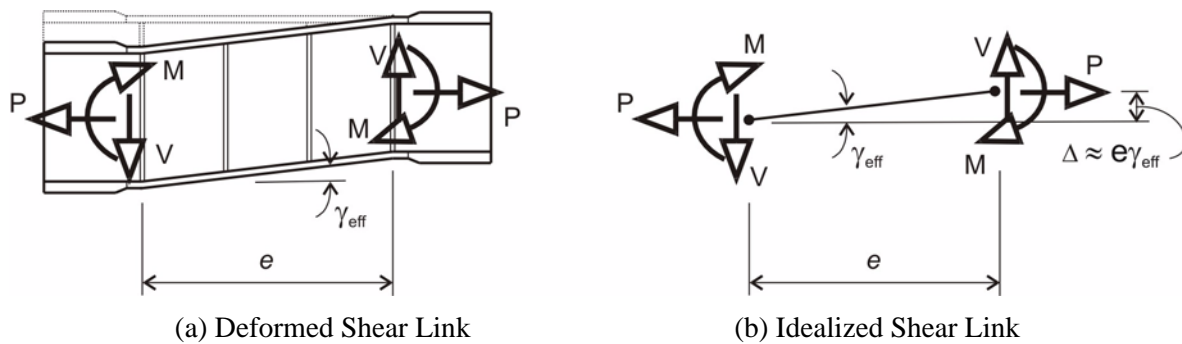


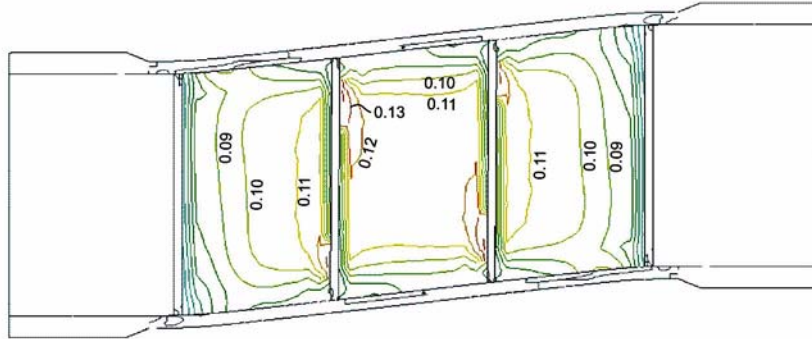
**Figure 6-14: Equilibrium of Shear Link With Axial Force**

For comparison, Figure 6-16 shows the plastic shear strain demand in the shear links types without stiffeners for deformations at  $\gamma_{eff} = 0.10 \text{ rad}$ . No localized plastic strain concentrations occurred in the web within the effective length. The contours of the plastic shear strain showed lower demand at the ends of the effective length as compared to mid-length, which confirmed the strain measurements from the experiments shown in Figure 4-31. From the strain demand perspective, removing the stiffeners from the effective length eliminated the localized plastic shear deformations caused by the presence of intermediate web stiffeners. These results along with the experimental observations of failure in Link C345a and H485 led to the investigation of shear links without stiffeners as previously discussed in Section 4.1.

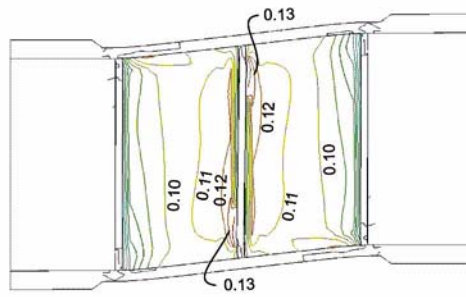
### 6.4.2 Stiffener Bending

Strain gauge measurements as well as observations during the test indicated yielding in the stiffeners near the flange connection zones. The numerical models also showed significant yielding in the stiffeners as shown in Figure 6-17 for Link C345a and H485 at deformation of  $\gamma_{eff} = 0.10 \text{ rad}$ . The distribution of strain indicated that a plastic hinge formed at the ends of each intermediate stiffener. The hinge was caused by the bending of the stiffener in accommodating the relative deformation of the flange with respect to the web. An experimental observation of the stiffener bending was previously shown in Figure 2-12 for Links C345a and C345b. Cracks in the stiffeners do not necessarily result in brittle failure of the link and hence the plastic strains were not as concerning as those in the flanges. The chamfer in the stiffener allowed for the necessary deformation to take place without potentially increasing the strain demand on the web. A large chamfer dimension is preferred over the potential of increased plastic strains in the web as shown by McDaniel et al (2003). Based on their study, the minimum size of the chamfer should be  $3t_w$ , where  $t_w$  is the thickness of the web. This dimension is sufficient to allow the formation of a plastic hinge provided that the web thickness is the same as the stiffener thickness. If the stiffener is thicker than the flanges, the chamfer may have to be increased.

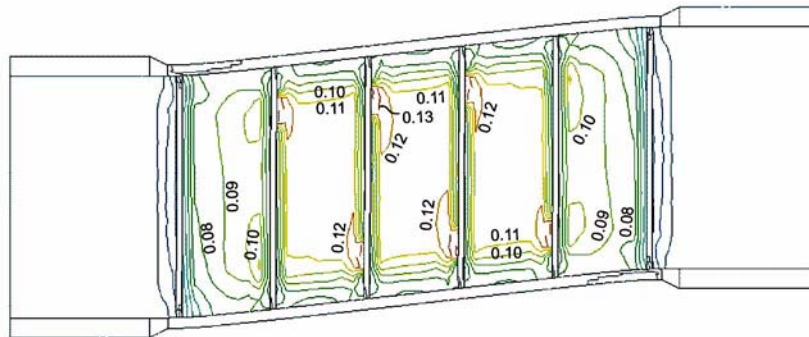
It was considered that the bending of the stiffener caused the plastic strain concentrations in the web by introducing a force at the stiffener to web connection. To investigate the influence of the stiffener bending on the web plastic strain concentrations, the tie constraint between the stiffener and the flanges were deleted in model of Link C345a. In effect, the stiffeners were considered to only be attached to the web and not the flanges. The plastic shear strain distribution resulting from the re-run analyses of the modified shear link is shown in Figure 6-18. The results showed that the stiffener bending was not the primary cause of the strain concentrations since the increased plastic strains remained at the same locations. The cause was therefore the connection of the stiffener to the web and the consequent stiffening at that location. The



(a) Link C345a at  $\gamma_{\text{eff}} = 0.10$  rad

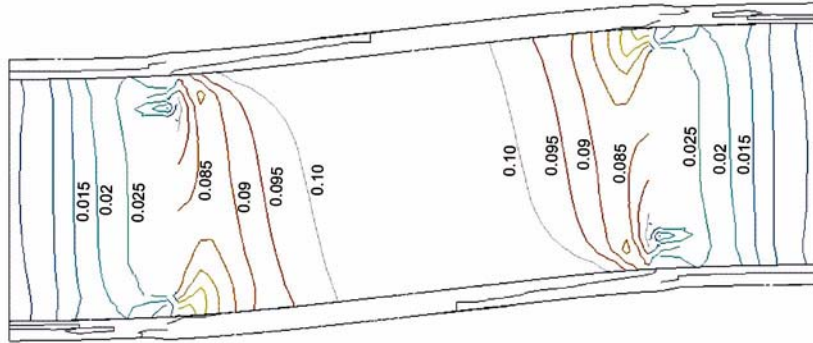


(b) Link C345b at  $\gamma_{\text{eff}} = 0.10$  rad

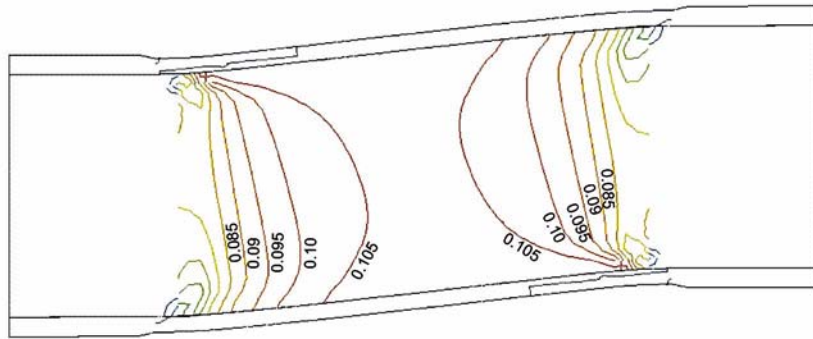


(c) Link H485 at  $\gamma_{\text{eff}} = 0.10$  rad

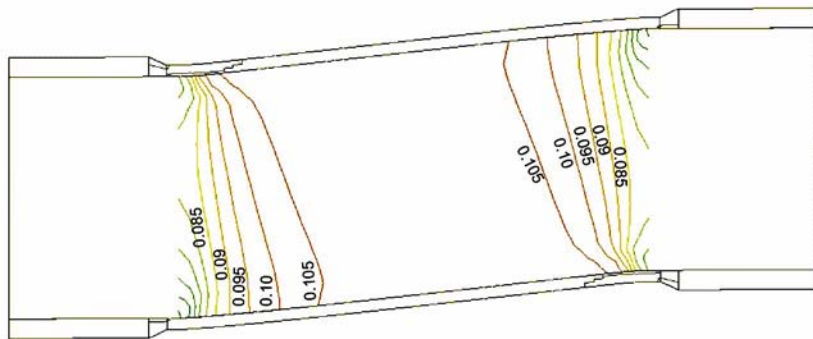
**Figure 6-15: Plastic Shear Strain Distribution in Web of Links with Stiffeners**



(a) Link L100 at  $\gamma_{\text{eff}} = 0.10$  rad

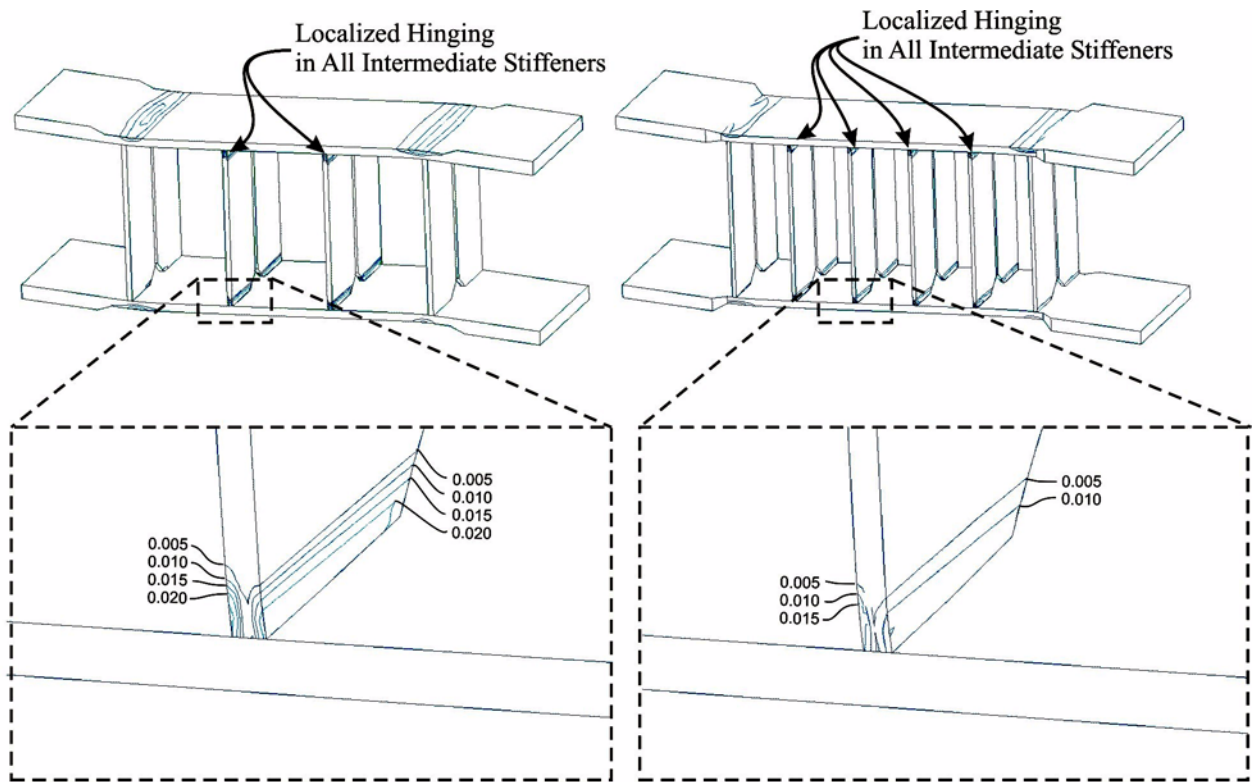


(b) Link L225 at  $\gamma_{\text{eff}} = 0.10$  rad



(c) Link X100 at  $\gamma_{\text{eff}} = 0.10$  rad

**Figure 6-16: Plastic Shear Strain Distribution in Web of Links without Stiffeners**



(a) Stiffeners of Link C345a at  $\gamma_{eff} = 0.10 \text{ rad}$

(b) Stiffeners of Link H485 at  $\gamma_{eff} = 0.10 \text{ rad}$

**Figure 6-17: Maximum Principal Plastic Strains in Stiffeners**

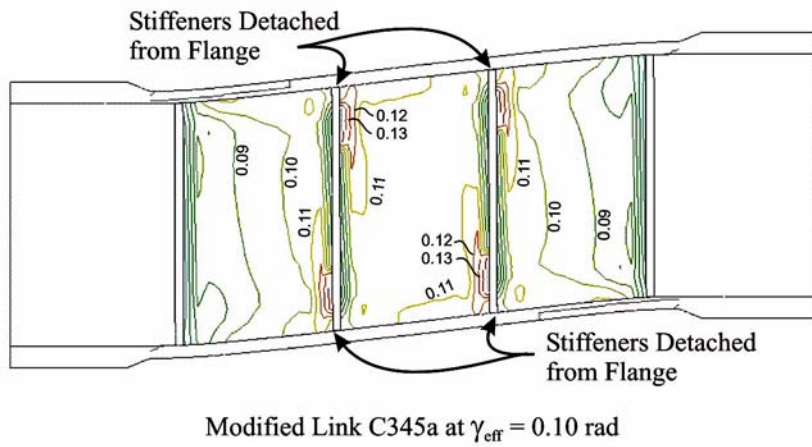


**Figure 6-18: Plastic Shear Strain with Stiffeners Detached from Flanges**

stiffening introduced a discontinuity in the plastic deformations of the web and resulted in localized plastic strains at the ends of that discontinuity. Disconnecting the stiffener from the web would not provide sufficient stiffening of the web against buckling.

### 6.4.3 Plastic Strains in Flanges

Modeling the shear links with the connection zones was important in assessing the demands in the transition zone between the plastically deformed effective length and the elastic connection zones. Localized yielding of the flanges at the ends of the effective length were recorded in all shear link experiments despite the fact that in most cases, the moment demand was below the moment capacity of the section. The numerical models also showed local plastic strains in the flanges. Two examples of the maximum plastic principal strains are shown in Figure 6-19 for two shear link types that were selected for their different flange thicknesses. Link L100 had the thickest flanges within the effective length and Link X100 the thinnest. The webs of the links were suppressed from view and only flanges shown for clarity.

The strains are shown for two link deformations which were achieved during the experiments on both link types. The strains magnitudes at  $\gamma_{eff} = 0.10 \text{ rad}$  corresponded well to the measured strains in Figure 4-26 and Figure 4-28 for Link L100 and X100 respectively. The plastic strains did not significantly grow in area with increased shear link deformations, but they did increase in magnitude. The proximity of the plastic strains to the flange welds next to the connection zone contributed to the observed flange cracking in that area. This was especially the case for Link X100 where the highest plastic strains were located within the transition between the thinner flange and thicker connection zone. To alleviate this flange cracking, welds should be located away from the flange plastic strain areas.

Although significant plasticity did occur in the flanges, a complete plastic hinge did not form. The plastic strains in the flanges did not extend through the thickness of the plates and mainly concentrated on the outside surface. Limited yielding did start to occur on the bottom of the flanges in Link L100 for larger deformations, but the strains were much lower than on the outside surfaces. These results confirm experimental strain gauge readings discussed in Section 2.3.5, Section 3.3.5 and Section 4.3.5 for the different types of links.

### 6.4.4 Strain Demand in Link L100

Although the connection zones of the shear links were simplified in the numerical models, the plastic strain demand in the connections was evident for Link L100. As shown in Figure 6-16a, the large overstrength resulted in plastic shear strains that extended into the connection zones. This link type was the only one where any plastic strains were recorded in the web of the connection zones. The severity would have been further exaggerated if bolt holes were included in the analyses and explains the premature failure of the connection.

The numerical models also helped to explain the cause of the observed cracking at the web to flange interface in Link L100 discussed in Section 4.3.2 and shown in Figure 4-8. The low yield strength of LYP 100 MPa (33 ksi) was not sufficient to elastically transfer the stresses from the web to the flanges. Plastic strains resulted along the length of the flange to web connection as shown in Figure 6-19b. These flange plastic strains did not occur when higher strength steel was used in Link X100 as shown in Figure 6-19d. Based on these results, care should be taken when low yield point steel is used for flanges and higher grades steels are recommended for flanges in built-up shear links.

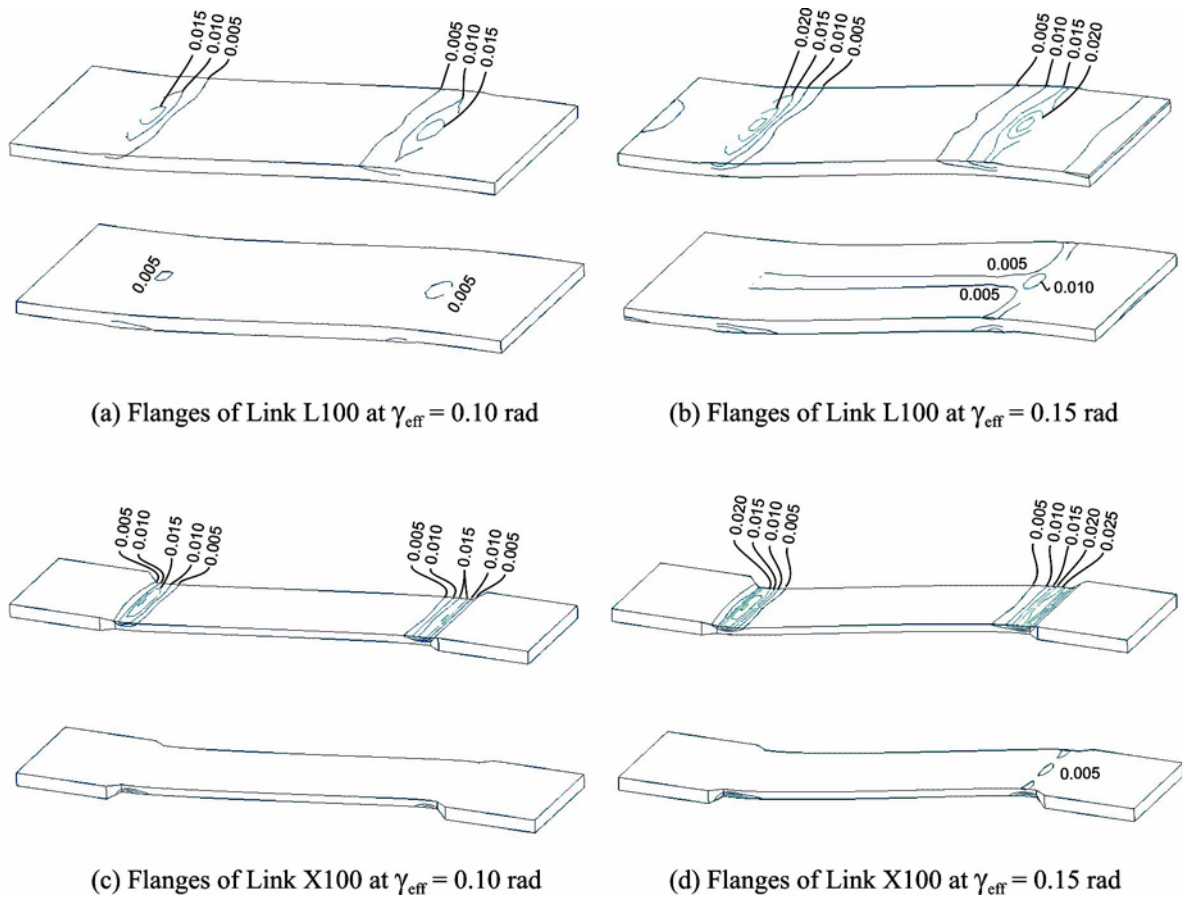


**Figure 6-19: Maximum Principal Plastic Strains in Shear Link Flanges**

## 6.5 Implications for Built-up Shear Link Design

The numerical results confirmed a number of the results and observations made during the extensive experimental program. The models also provided insight into some of the detailing requirements associated with built-up shear link design. The following details are recommended for consideration in the design for built-up shear links:

- Experimentally obtained cyclic stress-strain material behavior is essential in modeling the shear link resistance of links made from different grades of steel.
- Chamfers should be used in the stiffeners in the flange to web corners to accommodate the formation of plastic hinges at the ends of the stiffeners.
- In order to reduce the chance for cracking in the flanges, welding should be avoided at the flange outside surfaces near the ends of the effective length. Welding at the inside of the flange, i.e. the flange surface facing the web, can be performed at any location along the length of the link since the plastic strains are not as severe.
- The steel in the flanges should be of the same or higher strength than steel used for the web.

## 6.6 Summary

Finite element models were developed for the built-up shear link types that were tested during the experimental program. The force deformation response of the numerical models utilizing plate elements was similar to the models utilizing continuum elements. However, the continuum elements were able to more realistically represent the thickness of the plates and the strain distribution throughout the shear link. The response of the models was found to be significantly influenced by the material stress-strain relationships.

Estimating the force deformation response using numerical models would not have been possible without the experimental results of the material stress-strain characteristics of the different grades of steels. The monotonic response of the numerical models utilizing the cyclic power law stress strain properties approximated the shear link cyclic backbone curve from the experiments well, especially for the structural grade steels. Consistently higher resistance resulted from analyses of models utilizing the LYP steels due to the derivation procedure of the power law stress-strain relationship.

The numerical modeling showed plastic strain concentrations in the web of the shear links that used stiffeners. The increased demand was caused by the stiffening of the web and restricted plastic flow in the web caused by the stiffeners. The higher strains coincided with the heat affected zone from the stiffener to web welds and contributed to the onset of cracks in those locations during the experiments.

Plastic hinging occurred in the intermediate stiffeners at the flange connection. The hinging was caused by the imposed bending of the stiffener to accommodate the relative deformation of the flange with respect to the web. Plastic strains also occurred in the flanges at the ends of the effective length. The plastic strain increased with increasing shear link deformation, but remained localized to the ends of the effective length. The strains did not extend through the thickness of the flange and did not form a plastic hinge. Welding should be avoided on the outside surface of the flanges at the ends of the effective length to prevent cracking, although welding anywhere along the length on the inside surface of the flange would not be detrimental.



## SECTION 7

### PLASTIC SHEAR STRENGTH OF BUILT-UP SHEAR LINKS

#### 7.1 Parametric Study

One of the primary benefits of numerical modeling of built-up shear links is the ability to study the response of design alternatives and variations without additional experimentation. The calculation of shear resistance as expressed in Equation 1-10 only considered the plasticity of the web, but other factors can potentially influence the shear resistance. The experimentation and numerical modeling conducted in this study identified material stress-strain characteristics as major contributors to shear resistance and it is possible that those material properties may have over shadowed the contributions of other link components such as flanges and stiffeners.

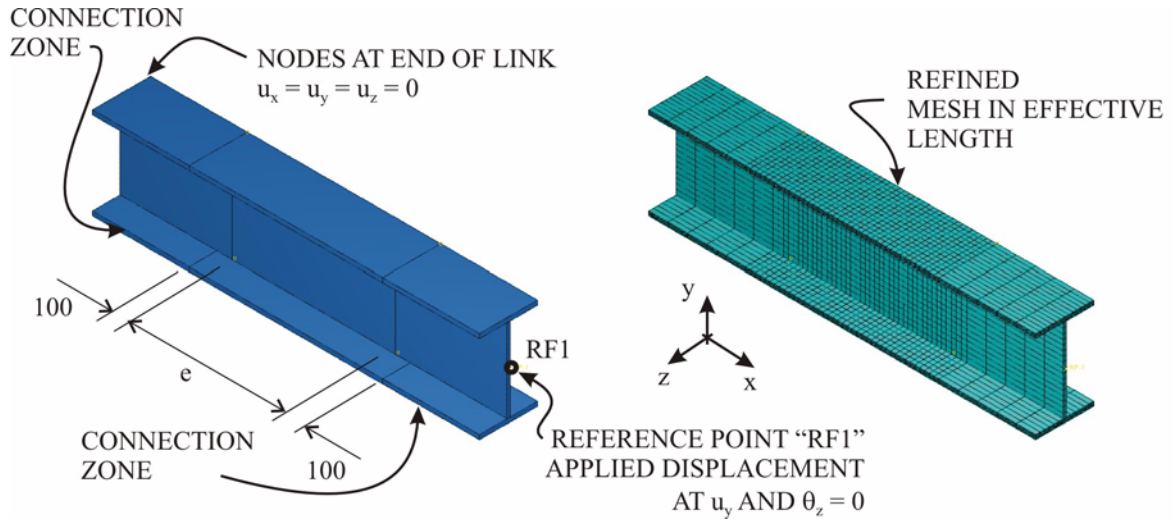
The methods and rationale used to numerically model the different types of built-up shear links in Section 6 using ABAQUS v6.4 (HKS 2003) finite element software package were extended for studying the influence of link geometry on the shear resistance. The objectives were to investigate the influence of stiffeners, flanges and the effective length on the link shear resistance by conducting parametric analyses. The results of these analyses in combination with results from the experiments served as basis for formulating an expression for determining the maximum shear resistance of built-up shear links.

#### 7.2 Model Description

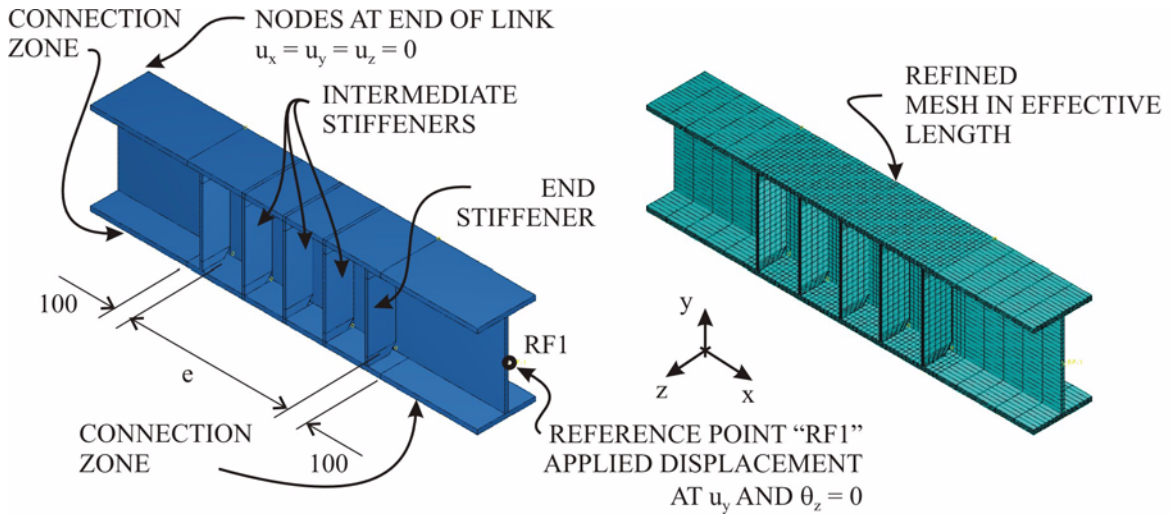
Shear link geometry was varied from a base model of a built-up shear link. The base model was chosen to be representative of the links used for the experiments in the effective length  $e$  and web height  $h_w$ . The cross sectional dimensions of Link C345a were used as initial values as summarized in Table 7-1. The connection zones were included at both ends of the effective length and were defined to have the same plate dimensions as the effective length to eliminate any thickness and width transitions for modeling and computational simplicity.

The nodes were restrained against all displacements at one end of the link and slaved to reference point RF1 as shown in Figure 7-1. Deformation of the link was imposed by applying a monotonic displacement in the y-direction at RF1 while restraining rotation about the z-axis, resulting in constant shear and equal end moments in the model. ABAQUS continuum elements C3D8R were used with discretization details chosen as discussed in Section 6.3.1, resulting in the discretization of the shear links with and without stiffeners as shown in Figure 7-1. An elasto-plastic material stress-strain relationship was used in order to eliminate the contribution of material hardening on the results and thereby isolate the influence of link geometry. The connection zones were assigned elastic properties. The flange transition from elasto-plastic to the elastic properties extended beyond the ends of the effective length in order to fully accommodate the formation of plastic strains at the ends of the effective length.

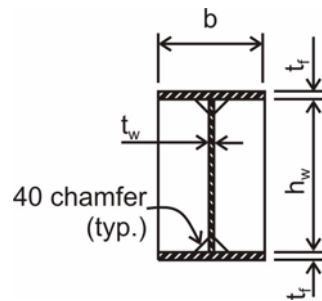
If intermediate stiffeners were used, they extended through the full depth and width of the shear link and were placed at both sides of the web. The number of intermediate stiffeners, denoted by  $n_s$ , were spaced equally through the effective length. All stiffeners included 40 mm (1.57 in) chamfers in each web to flange corner. Unless otherwise specified, the stiffener nodes were tied to the rest of the shear link at the web and flange interfaces, but the welds themselves were not modelled.



(a) Layout of Shear Link Without Stiffeners (b) Elements in Link Without Stiffeners



(c) Layout of Shear Link With Stiffeners (d) Elements in Link With Stiffeners



(d) Sectional Dimensions

**Figure 7-1: General Layout of Shear Link Model**

**Table 7-1: Summary of Base Model and Considered Variations**

Characteristic*	Base Link Model	Considered Variations from Base Model
$L, mm (in)$	2000 (78.7)	-
$e, mm (in)$	840 (33)	210 (8.23), 420 (16.5), 1260 (49.6)
$h_w, mm (in)$	430 (16.9)	-
$t_w, mm (in)$	14 (0.55)	-
$b, mm (in)$	300 (11.8)	-
$t_f, mm (in)$	22 (0.87)	11 (0.43), 33 (1.30), 44 (1.73), 55 (2.17)
$t_s, mm (in)$	0	7 (0.28), 14 (0.55), 21 (0.83), 28 (1.1)
$n_s$	0	3, 6, 12
Web Yield Strength $f_{yw}, MPa (ksi)$	345 (50)	-
Flange Yield Strength $f_{yf}, MPa (ksi)$	345 (50)	225 (33), 485 (70), 695 (100)

\* geometric characteristics are depicted in Figure 7-1

### 7.3 Flange Contribution to Shear Strength

Localized yielding of flanges at the ends of the effective length was recorded in the shear link experiments described in Section 2 through to Section 4 and verified by numerical modeling in Section 6. The yielding was caused by the bending deformations of the flanges in accommodating the transition from the elastic connection zone to the inelastic effective length. The force required to bend the flange can influence the overall shear resistance of the link. The flange flexural strength is primarily influenced by the flange steel yield strengths and the flange thicknesses.

#### 7.3.1 Influence of Flange Steel Yield Strength

Four yield strength values of steel were considered for the flanges of the base model as summarized in Table 7-1. The flange yield strengths ranged from 225 MPa (33 ksi) to 695 MPa (100 ksi), covering the practical range of strengths for structural plate steels. All of the other parameters of the shear link remained unchanged from the basic model. The lowest available yield strength of 100 MPa (33 ksi) was not used because the moment capacity of such a shear link would not be sufficient to yield the web.

The values of maximum shear resistance from the analyses are shown in Figure 7-2 for three values of shear link deformation  $\gamma_{eff} = 0.05, 0.10$  and  $0.15 rad$ . Only a moderate influence of flange steel yield strength was observed on the shear resistance of the link. The maximum shear increase from the base

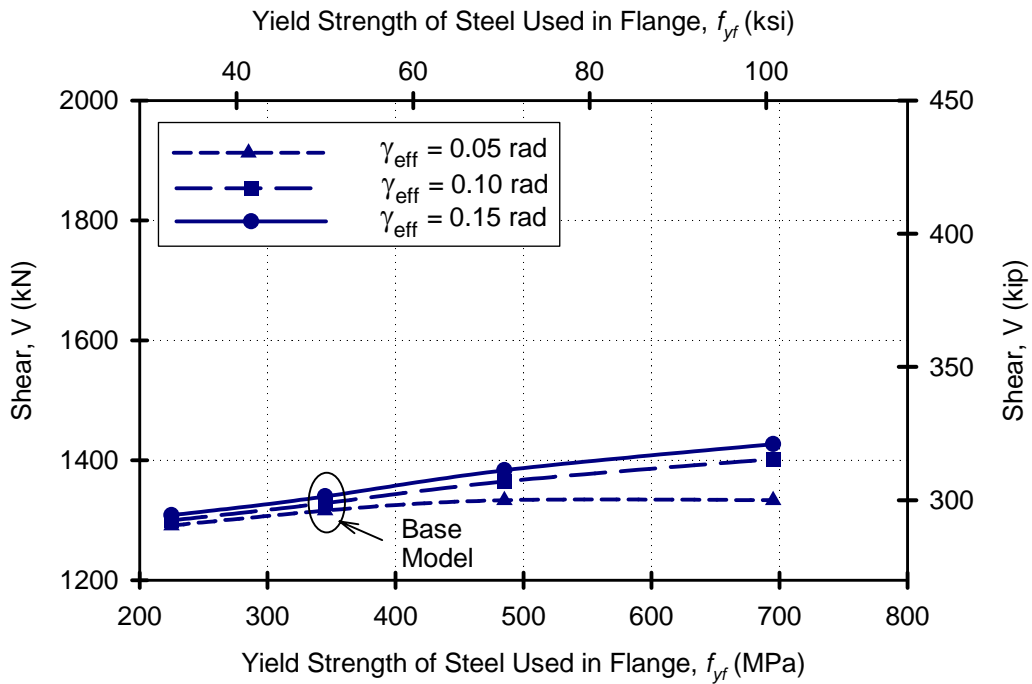


**Figure 7-2: Influence of Flange Steel Yield Strength**

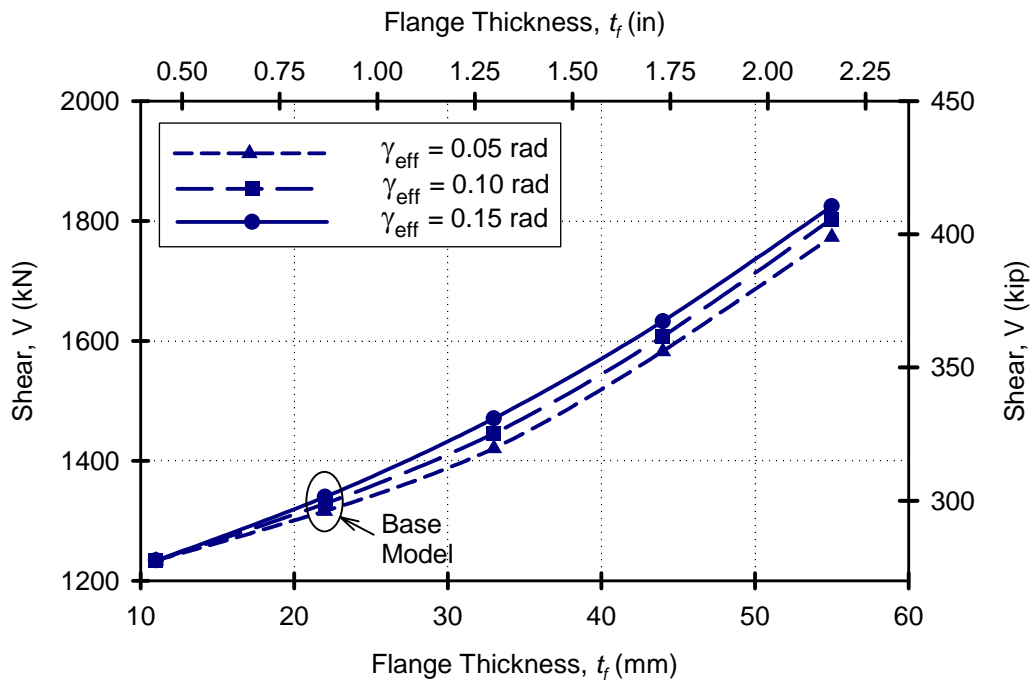


**Figure 7-3: Influence of Flange Thickness**

model was 7% at  $\gamma_{eff} = 0.15 \text{ rad}$  for the range considered and decreased with smaller shear deformations. The strength increase with link deformation was more significant for higher steel yield strengths because the plastic flange strains that would limit the resistance did not develop in the flange until later in the link deformation response.

### 7.3.2 Flange Thickness

Five different variations of flange thickness were considered as listed in Table 7-1. The flange yield strength remained constant at  $f_{yf} = 345 \text{ MPa}$  (50 ksi). The values of the maximum shear resistance from the analyses are shown in Figure 7-3. The influence of flange thickness was much more evident than the influence of flange steel yield strength. The increase in shear had a consistent trend among the three levels of shear deformations. The largest strength increase from the base model among the cases considered was approximately 46%.

## 7.4 Stiffener Contribution to Shear Resistance

End stiffeners are necessary to transfer the load from the shear link to the rest of the structure, typically through the use of braces. These stiffeners do not deform inelastically as they form part of the elastic connection zone and as a result, they do not contribute to the shear strength developed within the effective length. Intermediate stiffeners are located within the plastically deforming effective length and can potentially influence the shear resistance. These stiffeners are often necessary in delaying web buckling and their influence on the shear link resistance was considered using the mechanisms of web stiffening and stiffener bending.

### 7.4.1 Web Stiffening

The non-linear behavior of shear links relies on developing plasticity in the web within the effective length. As discussed in Section 6.4.1, stiffeners can provide discontinuities in the plastic strain distribution in the web. At the location of the stiffener to web interface, the web becomes stiffer not only against out of plane buckling but also against formation of plastic strains in that area. It is possible that with a sufficient number of stiffeners, the stiffening of the web would increase the shear link resistance by restricting the plastic strain flow.

Intermediate stiffeners were added within the effective length of the base model. In order to account for only the web stiffening effect, the stiffeners were only connected to the web and not to the flanges. Shear links with sectional properties corresponding to the base model were considered with  $n_s = 0, 3, 6$  and  $12$ , where the stiffener thickness remained constant at  $t_s = 14 \text{ mm}$  (0.55 in). Higher number of stiffeners would not be practical due to constructability considerations. The results of the numerical analyses are shown in Figure 7-4 for three shear deformation values  $\gamma_{eff} = 0.05, 0.10$  and  $0.15 \text{ rad}$ . The strength remained nearly constant over the range of stiffener ratios and hence the web stiffening effect was shown to have insignificant influence on link shear strength within the range considered.

### 7.4.2 Stiffener Bending

The development of plastic hinges in the stiffeners at the flange connections has been experimentally observed and numerically validated for the tested built-up shear links. The formation of hinges was caused by bending of the stiffeners in accommodating the relative deformation between the flange and the web. In the web stiffening investigation, the stiffeners were not connected to the flanges and hence did not bend

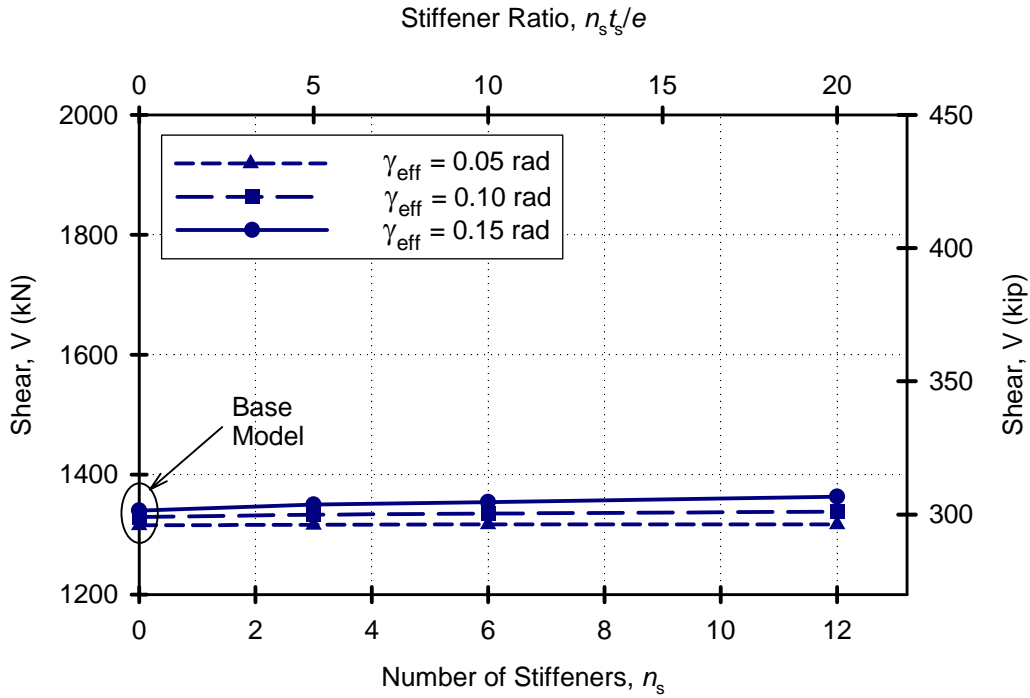


**Figure 7-4: Influence of Web Stiffening**

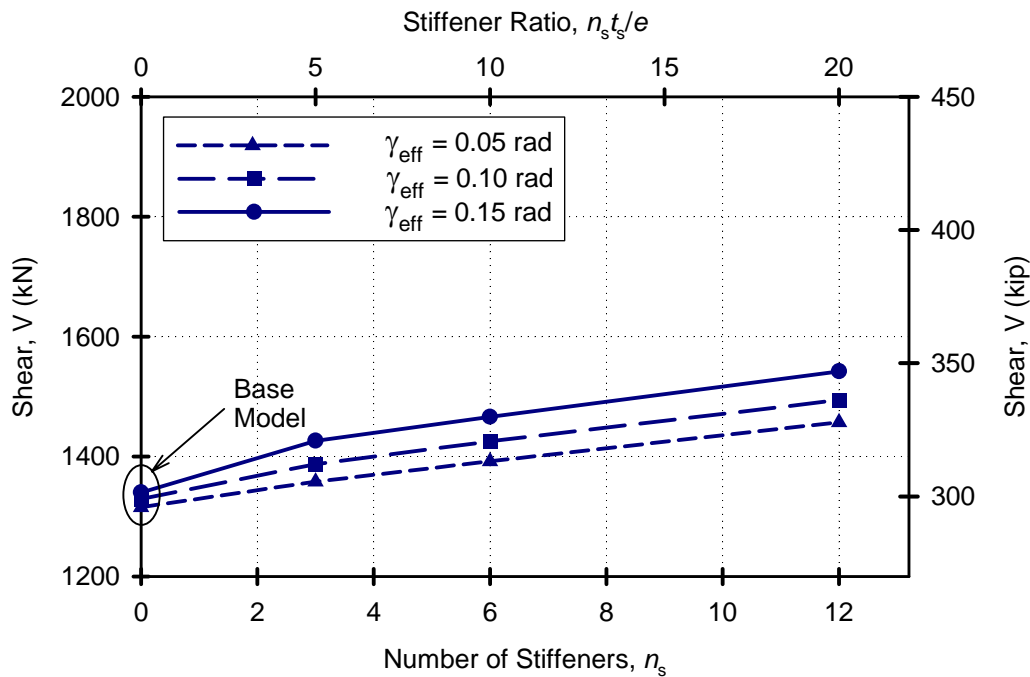


**Figure 7-5: Influence of Stiffener Bending**

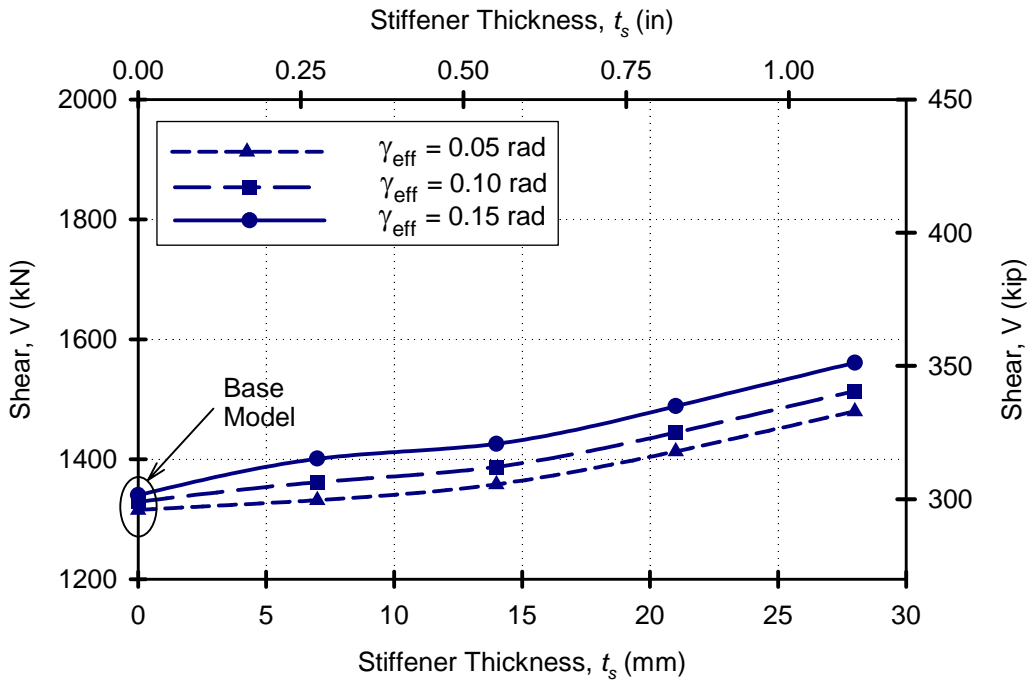


Figure 7-6: Influence of Stiffener Thickness ( $n_s = 3$ )

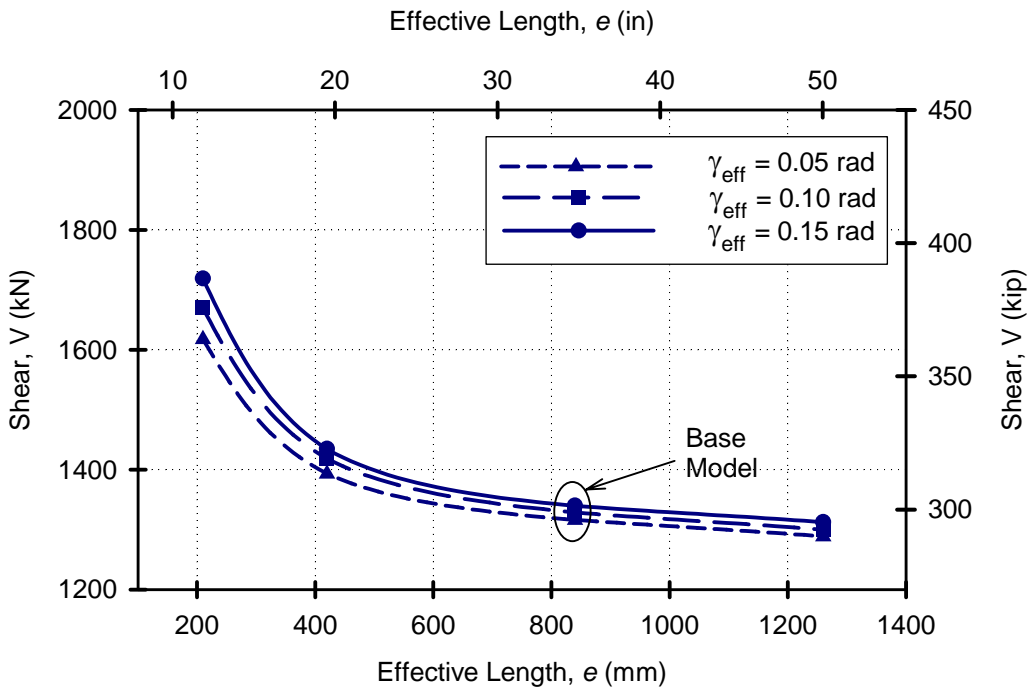


Figure 7-7: Influence of Effective Length

during the link plastic shear deformations. To investigate the effect of stiffener bending, the models considered for the web stiffening investigation in Section 7.4.1 were re-analyzed with the stiffeners connected to the flanges.

The results of the analyses are shown in Figure 7-5 for three different shear deformation values  $\gamma_{eff} = 0.05$ , 0.10 and 0.15 *rad*. An increase in shear strength with increase in shear deformation was evident in each of the model variations. The stiffener yielding progressively formed with increasing link deformations resulting in an increase in shear resistance. The increase in number of stiffeners also increased the resistance. The maximum increase from the base model was 15% for  $\gamma_{eff} = 0.15$  *rad* and for the range considered.

To investigate the influence of the stiffener thickness, three intermediate stiffeners were used in the base model with thicknesses ranging from 0 *mm* (0 *in*) to 28 *mm* (1.1 *in*) as summarized in Table 7-1. The results of the numerical analyses are shown in Figure 7-6 for three shear deformation values  $\gamma_{eff} = 0.05$ , 0.10 and 0.15 *rad*. Increase in stiffener thickness led to increase in shear resistance, with the largest increase of 11% from the base model at  $\gamma_{eff} = 0.15$  *rad*. Since the web stiffening did not significantly contribute, the shear resistance increase was caused by the bending of the stiffeners at the flange interface.

## 7.5 Influence of Effective Length on Shear Resistance

The effective length of the base model was varied as summarized in Table 7-1 with the remaining cross sectional properties of the base model constant. In all cases, shear dominated the link behavior as indicated by the lowest shear capacity ratio for the longest effective length of  $2M_p/(eV_p) > 1.6$ , which was well above the AISC Seismic Provisions minimum design criteria of 1.25. Although no stiffeners were used, web buckling did not contribute to the response during the monotonic application of link deformation. The results of the analyses are shown in Figure 7-5 and indicate a significant increase in shear resistance for short links. The influence of the effective length quickly diminished with increased length.

## 7.6 Shear Strength of Built-Up Shear Links

Estimating the maximum value of the shear strength that can develop within the effective length is important in obtaining a realistic value of overstrength as discussed in Section 1.2.2. The experimental as well as the numerical investigations showed that a constant value used to estimate the maximum shear resistance as used in the AISC Seismic Provisions is not optimal and at the current definition can also be unconservative. In addition to the influence of the material stress-strain, influence of flanges and stiffeners were shown to influence the strength as shown by the parametric study. This section outlines the development of a rational equation that can be used to calculate the maximum shear resistance of built-up shear links. The methodology is based on the numerical as well as experimental results and accounts for the contributions of the different link components as well as the material stress-strain characteristics.

### 7.6.1 Development of Equation

The total shear resistance of a built-up shear link can be superimposed from the individual influences of the web, flange and stiffener contributions. This can be expressed by the sum in Equation 7-1, where  $V_{pw}$  is the web contribution,  $V_{pf}$  is the contribution of the flanges and  $V_{ps}$  is the stiffener contribution to the total plastic shear strength  $V_{pt}$ .

$$V_{pt} = V_{pw} + V_{pf} + V_{ps} \quad (7-1)$$

The web contribution can be obtained from Equation 1-10 and recalculated for convenience in Equation 7-2, where  $f_{yw}$  is the yield strength of the web steel,  $h_w$  and  $t_w$  are the web height and thickness respectively.

$$V_{pw} = 0.6f_{yw}t_w(d - 2t_f) = 0.6f_{yw}t_w h_w \quad (7-2)$$

The built-up section is not specified by the depth  $d$  as is the case for rolled sections. The web height is a more convenient parameter than the section depth, because the cross section is combined from plate sizes that correspond to the web height.

The flange contribution to the total shear strength is based on the observations from experiments as well as the results from numerical modeling and considers the plastic strains in the flanges at the ends of the effective length. To help visualize the plastic strains and the distribution for different flange thicknesses, the numerical models used in Section 7.3.2 were utilized. The maximum principal strains in the flanges are shown in Figure 7-8 for  $\gamma_{eff} = 0.15 \text{ rad}$ . For thin flanges, plastic strains mainly concentrated on the outside surface of the flange and did not extend through the depth. For thick flanges, the plastic strain distribution formed two different patterns. The strains in the tension flange were dominated by tensile plastic strains, while the compression flange developed both compressive as well as tensile plastic strains.

Based on these observations of flange plastic strain distribution, an idealized flange deformation mechanism was developed for the case of thick flanges where the influence is the largest. The plastic strain patterns were idealized based on an elasto-plastic stress-strain relationship as illustrated in Figure 7-9. The tension flange was assumed to develop tensile yield stress through the full thickness of the flange. The force developed from these stresses was assumed to be resisted by the compression force  $C_l$  provided by the web interface. The force couple results in a moment  $M_{pf1}$  as expressed by Equation 7-3, where  $f_{yf}$  is the yield strength of the flange steel,  $b$  is the flange width and  $t_f$  is the flange thickness.

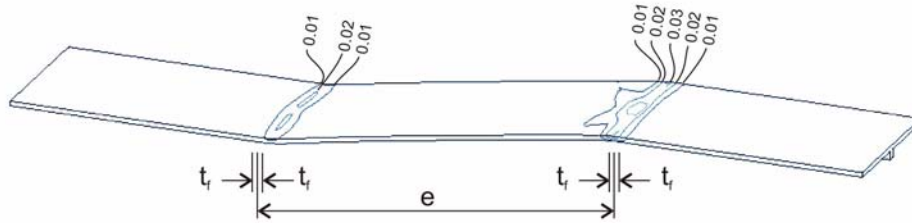
$$M_{pf1} = \frac{f_{yf} b t_f^2}{2} \quad (7-3)$$

The plastic strains in the compression side of the flange were idealized as a plastic hinge as illustrated in Figure 7-9. The force couple results in a plastic moment  $M_{pf2}$  about the center of the flange as expressed by Equation 7-3.

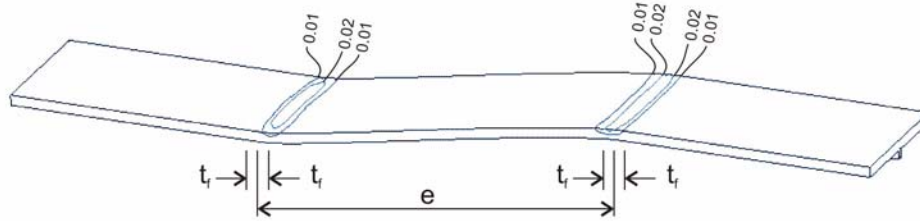
$$M_{pf2} = \frac{f_{yf} b t_f^2}{4} \quad (7-4)$$

The numerical results in Figure 7-8 showed that the peaks of the localized plastic strains occur just inside the effective length. From the design perspective, it is convenient to assume that the location of the flange plastic moments occurs consistently one flange thickness inside the ends of the effective length. From equilibrium shown in Figure 7-9, the shear contribution from the flanges can then be expressed using Equation 7-5.

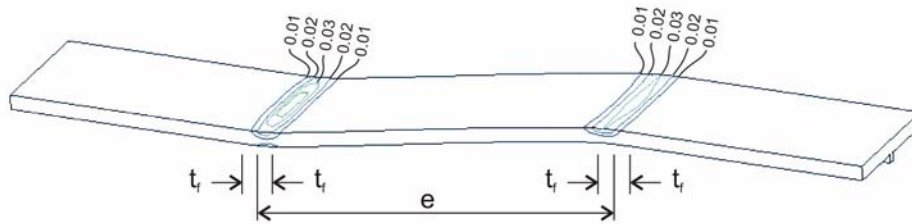
$$V_{pf} = \frac{2M_{pf1} + 2M_{pf2}}{e - 2t_f} = \frac{3f_{yf} b t_f^2}{2(e - 2t_f)} \quad (7-5)$$



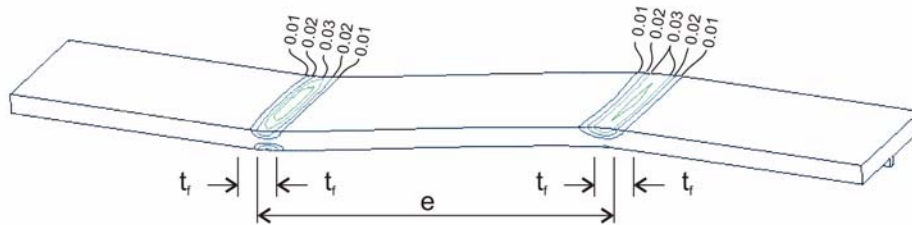
(a) Max. Principal Strains at  $\gamma_{\text{eff}} = 0.15$  rad in Flange Thickness 11 mm (0.43 in)



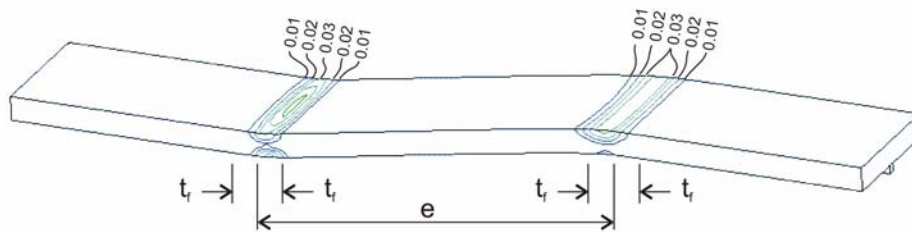
(b) Max. Principal Strains at  $\gamma_{\text{eff}} = 0.15$  rad in Flange Thickness 22 mm (0.87 in)



(c) Max. Principal Strains at  $\gamma_{\text{eff}} = 0.15$  rad in Flange Thickness 33 mm (1.30 in)



(d) Max. Principal Strains at  $\gamma_{\text{eff}} = 0.15$  rad in Flange Thickness 44 mm (1.73 in)



(e) Max. Principal Strains at  $\gamma_{\text{eff}} = 0.15$  rad in Flange Thickness 55 mm (2.17 in)

**Figure 7-8: Flange Plastic Zone at End of Effective Length**

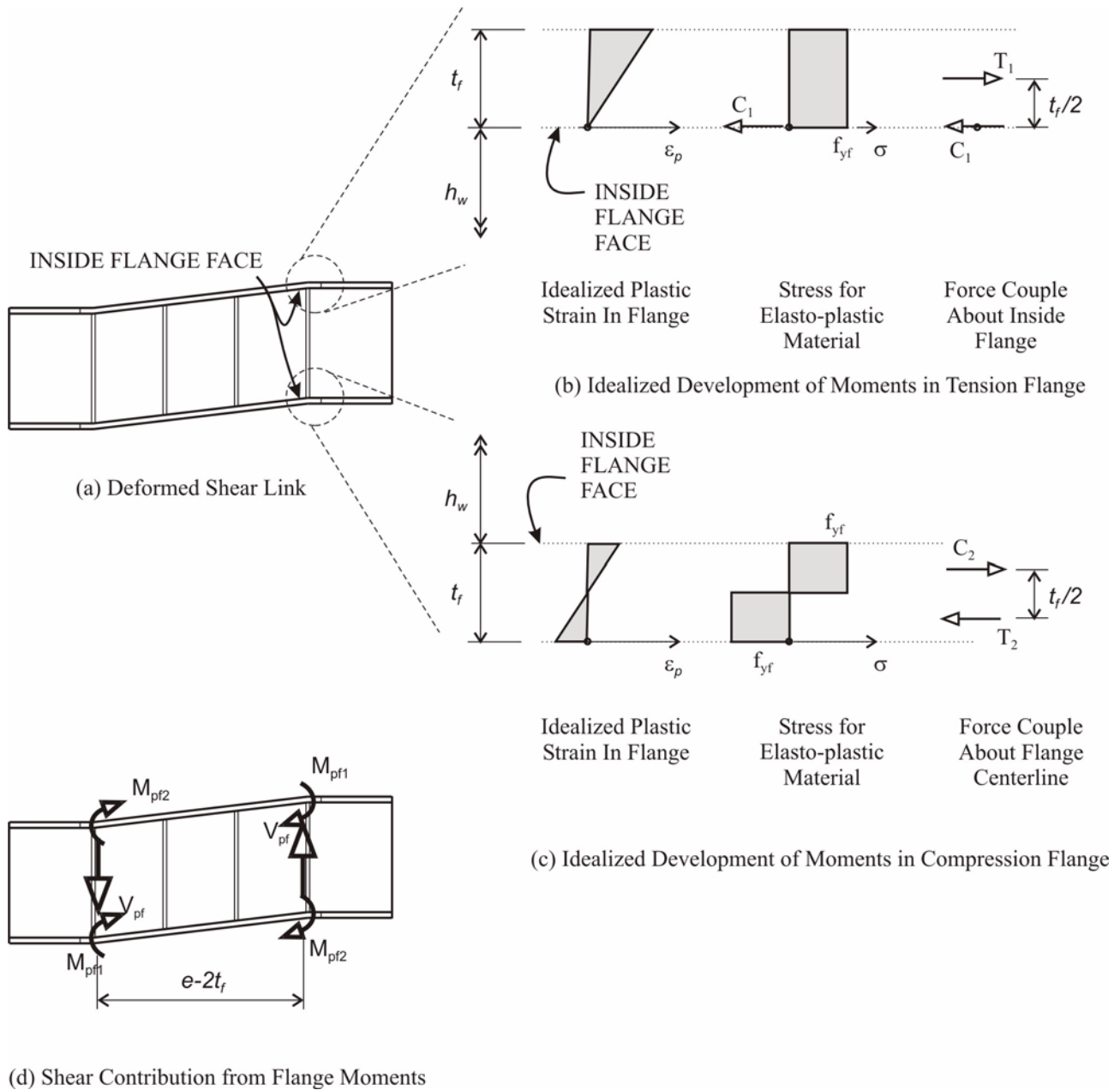


**Figure 7-9: Illustration of Flange Contribution to Link Shear Resistance**

The stiffener contribution to the total shear was derived based on the observed formation of plastic hinges at the flange connections. The plastic moment  $M_{ps}$  developed from these hinges is illustrated in Figure 7-10 and expressed by Equation 7-6, where  $f_{ys}$  is the actual yield strength of the stiffener steel,  $b$  is the flange width and  $t_s$  is the stiffener thickness.

$$M_{ps} = \frac{f_{ys} b t_s^2}{4} \quad (7-6)$$

This formulation assumes that the stiffeners are provided for the entire width of the flange and ignores any reduction in area due to stiffener chamfers. The moment was observed to form at each end of the intermediate stiffener, next to the flange connection. From equilibrium taken at the assumed location of flange moments as shown in Figure 7-10, the shear contribution from the stiffeners can be expressed using Equation 7-7, where  $n_s$  denotes the number of intermediate stiffeners within the effective length.

$$V_{ps} = \frac{2n_s M_{ps}}{e} = \frac{n_s f_{ys} b t_s^2}{2(e - 2t_f)} \quad (7-7)$$

Substituting Equation 7-2, Equation 7-5 and Equation 7-7 into Equation 7-1, results in the expression for the total plastic shear strength  $V_{pt}$  of a built-up shear link in Equation 7-8.

$$V_{pt} = 0.6f_{yw}t_w h_w + \frac{3f_{yf}bt_f^2 + n_s f_{ys} b t_s^2}{2(e - 2t_f)} \quad (7-8)$$

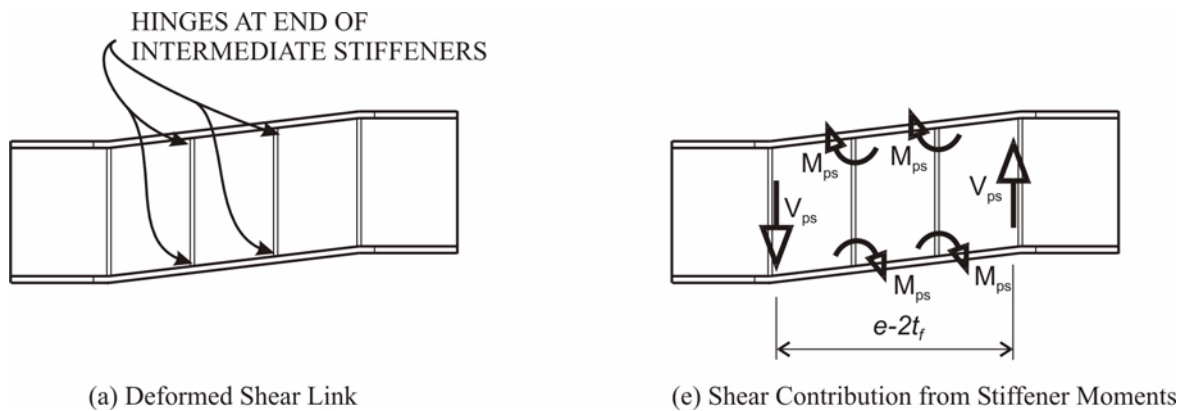


**Figure 7-10: Illustration of Stiffener Contribution to Link Shear Resistance**

### 7.6.2 Equation Comparison to FEM Analyses

The expression in Equation 7-8 does not account for material post-yield behavior other than assuming a simple elasto-plastic relationship. As such, the equation is applicable to the elasto-plastic finite element models analyzed in the parametric study. The total plastic shear strength  $V_{pt}$  was calculated using Equation 7-8 for all of the built-up shear link variations listed in Table 7-1. The calculated values of  $V_{pt}$  are compared to the results from the non-linear numerical analyses  $\gamma_{eff} = 0.15 \text{ rad}$  in Figure 7-11.

The calculated plastic shear strength followed the trends shown by the detailed numerical models in all cases. The shear increased linearly with flange yield strength based on the linear proportionality to  $f_{yf}$  and followed a quadratic increase with increase in flange thickness based on the quadratic proportionality to  $t_f$ . The trend was also consistent with the numerical results for the influence of stiffeners, although the equation did underestimate the resistance in those cases by approximately 5%. The significant influence of the

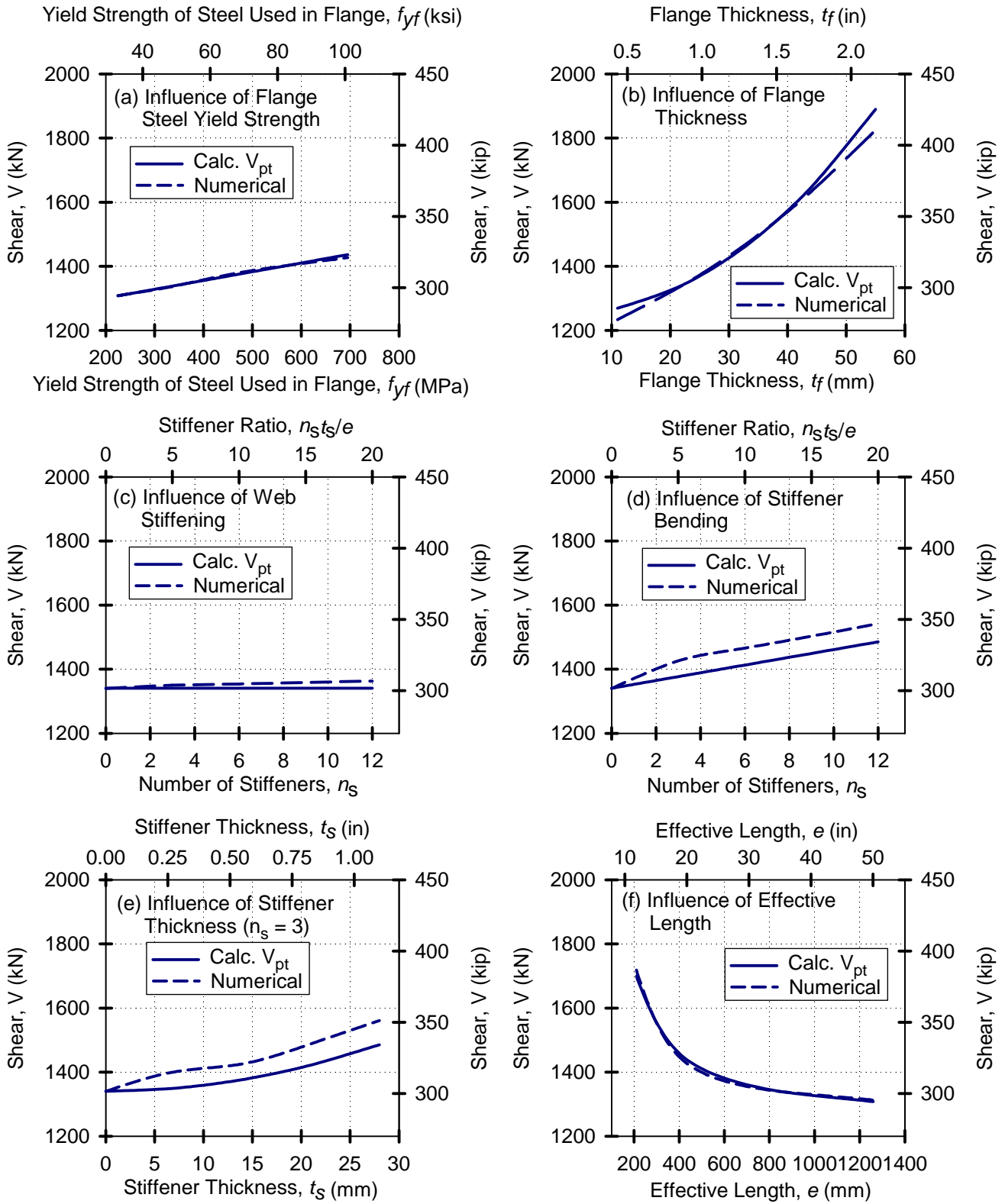


**Figure 7-11: Comparison of Shear Formula to Numerical Analyses Results**

effective length for short links was also reflected based on the inverse proportionality to  $e$ . The developed idealized relationship of Equation 7-8 for determining the plastic shear resistance of built-up shear links captured the trends as well as the shear values of the different built-up geometries.

### 7.6.3 Incorporating Material Stress-Strain Behavior

The results of the material cyclic stress strain behavior by Dusicka et al (2004) can be incorporated into the formulation of the plastic shear strength in order to account for the material cyclic stress-strain properties. It is recognized that a built-up shear link is not subjected to the same axial strains as the tested coupons, but instead to plastic multi-axial strains that are dominated by shear. Nonetheless, one of the ways to estimate the plastic strain demand is to follow the plane strain relationship between principal strains and pure shear, whereby the principal strains are half the amplitude of pure shear. In the case of shear link deforming to  $\gamma_{eff} = 0.15 \text{ rad}$ , the principal strains could be estimated as  $\epsilon = 0.075$ , which is approximately the largest cyclic amplitudes considered for the material investigation. Again this is only an approximation, but it does provide an estimate of the strain level in the deformed shear link to show that the strain amplitudes used for the coupon testing are within the range of interest for built-up shear links.

For calculating the plastic shear resistance of built-up shear links subjected to repeated plastic deformations, the maximum stresses obtained from the coupon experiments can be applied to Equation 7-8 instead of the yield stresses of the individual plates. The cyclic stress factor  $R_c$  can be used to modify the yield strength of the different grades of steel. The resulting equation for the plastic shear resistance  $V_{ptc}$  that is based on cyclic material behavior is shown in Equation 7-9, where  $R_{cw}$ ,  $R_{cf}$  and  $R_{cs}$  correspond to the cyclic stress factors for the web, flange and stiffener steels.

$$V_{ptc} = 0.6R_{cw}f_{yaw}t_w h_w + \frac{3R_{cf}f_{yaf}bt_f^2 + n_s R_{cs}f_{yas}bt_s^2}{2(e - 2t_f)} \quad (7-9)$$

The yield strengths  $f_{yaw}$ ,  $f_{yaf}$  and  $f_{yas}$  represent the actual yield strength of the steel plates. The cyclic stress factors were obtained for the different grades of steel and strain amplitudes from study by Dusicka et al (2004). Two levels of shear deformation were considered,  $\gamma_{eff} = 0.08 \text{ rad}$  for level of deformation expected in the AISC Seismic Provisions and the maximum achieved deformation of the individual links, which varied. The corresponding  $R_c$  factors based on the steel grade and deformation level are summarized in Table 7-2.

**Table 7-2: Cyclic Stress Factors at Specific Shear Deformation Levels for Tested Shear Links**

Link Shear Deformation	Link Type					
	C345a	C345b	H485	L100	L225	X100
Steel Grade Within Effective Length	A709 Grade 345 MPa (50 ksi)	A709 Grade 345 MPa (50 ksi)	A709 HPS 485W (70 ksi)	LYP 100 MPa (14.5 ksi)	LYP 225 MPa (33 ksi)	Web: LYP 100 MPa, Flange: HT 440 MPa

**Table 7-2: Cyclic Stress Factors at Specific Shear Deformation Levels for Tested Shear Links**

Link Shear Deformation	Link Type					
	C345a	C345b	H485	L100	L225	X100
$R_c$ at $\gamma_{eff} = 0.08 \text{ rad}$	1.83	1.83	1.33	4.38	1.56	4.38 (web) 1.34 (flanges)
$R_c$ at $\gamma_{max}^*$	1.94	1.89	1.40	5.00	1.80	5.27 (web) 1.64 (flanges)

\* maximum achieved deformation  $\gamma_{max}$  as summarized in Table 5-3

The plastic shear strength  $V_{ptc}$  based on cyclic stress-strain material properties was calculated using Equation 7-9 and cyclic stress factors in Table 7-2 for the link types that were tested using the large-scale experiments. The results are shown in Table 7-3, where the contributions of the web, flange and stiffeners are also shown as a ratio to the total shear resistance. In all cases, the web was the largest contributor to the shear strength, with the stiffeners contributing the least for the built-up shear link geometries considered.

The calculated plastic shear strength values were compared in Table 7-4 and graphically in Figure 7-12 to the results from detailed finite element models discussed in Section 6.3. The comparison was made using the ratio  $V_{ptc}/V_{num}$ , where  $V_{num}$  is the shear resistance obtained from the numerical models at shear deformations of  $\gamma_{eff} = 0.08 \text{ rad}$ . A close correlation of the shear resistance was obtained, where the calculated plastic shear resistance was within 2% of the shear resistance in the numerical models at both levels of deformation.

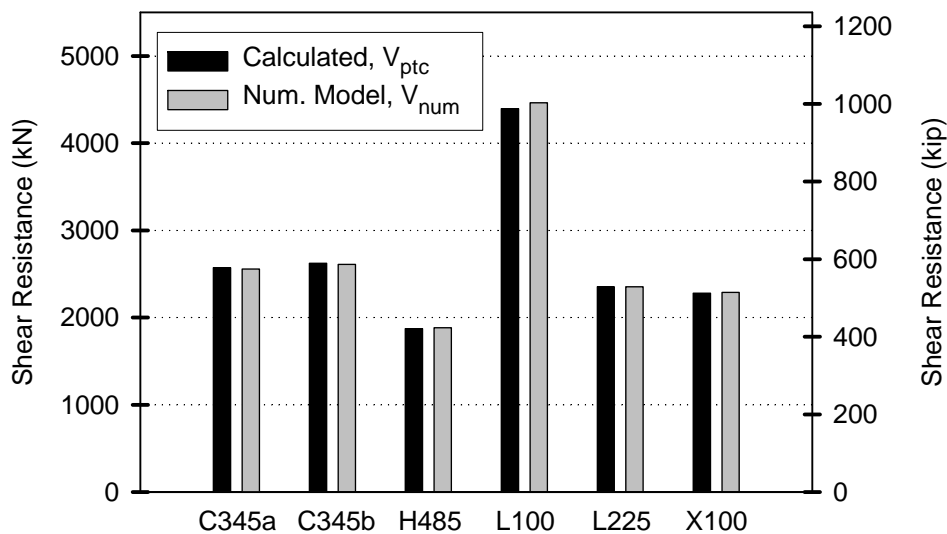


**Figure 7-12: Comparison of Equation and FEM analyses at  $\gamma_{eff} = 0.08 \text{ rad}$**

**Table 7-3: Plastic Shear Strength of Tested Built-up Shear Links**

Deformation History	Link Type					
	C345a	C345b	H485	L100	L225	X100
Detailed Figure	Figure 2-1		Figure 3-1	Figure 4-1		
Measured from Coupons Tests $f_{ya}$ MPa (ksi)	353 (51.2)	353 (51.2)	503 (73.0)	76.5 (11.1)	242 (35.1)	76.5 (11.1) & 501 (72.7)
$V_{ptc}$ , kN (kip) at $\gamma_{eff} = 0.08$ rad	2558 (575)	2611 (587)	1884 (423)	4462 (1003)	2352 (529)	2290 (515)
$V_{ptc}$ , kN (kip) at $\gamma_{max}$	2712 (610)	2768 (622)	1983 (446)	5093 (1145)	2714 (610)	2757 (620)
Web Contribution $R_{wc} V_{pw} / V_{ptc}$	0.91	0.89	0.92	0.87	0.91	0.94
Flange Contribution $R_{fc} V_{pf} / V_{ptc}$	0.07	0.09	0.06	0.13	0.09	0.06
Stiffeners Contrib. $R_{sc} V_{ps} / V_{ptc}$	0.02	0.01	0.02	0	0	0

**Table 7-4: Comparison of Plastic Shear Resistance to Finite Element Analyses Results**

Deformation Level	Strength	Link Type					
		C345a	C345b	H485	L100	L225	X100
$\gamma_{eff} = 0.08$ rad	$V_{num}$ , kN (kip)	2571 (578)	2624 (590)	1873 (421)	4394 (988)	2353 (523)	2280 (513)
	$V_{ptc} / V_{num}$	1.01	1.00	1.00	1.02	1.00	1.00

The calculated plastic shear strengths were also compared to the shear resistance recorded during the experiments  $V_{exp}$  under incrementally increasing cyclic deformation history for  $\gamma_{eff} = 0.08$  rad and the maximum achieved  $\gamma_{max}$  for each case. The results are summarized in Table 7-5 and graphically in Figure 7-13 and Figure 7-14. The ratio  $V_{ptc} / V_{max}$  indicates the relative magnitudes of the shear calculated from the developed equation with respect to the experimentally obtained values, where unity represents an exact correlation. Despite the different materials and different link geometries, the calculated plastic shear

corresponded closely to the experimental results, indicating a close relationship of the calculated plastic resistance to the experimentally measured maximum values.

**Table 7-5: Comparison of Plastic Shear Resistance to Experimental Results**

Deformation Level	Strength	Link Type					
		C345a	C345b	H485	L100	L225	X100
$\gamma_{eff} = 0.08 \text{ rad}$	$V_{exp}$ , kN (kip)	2526 (568)	2797 (629)	1749 (393)	3687 (829)	2132 (479)	1938 (436)
	$V_{ptc}/V_{exp}$	1.01	0.94	1.08	1.21	1.10	1.18
$\gamma_{max}$	$V_{exp}$ , kN (kip)	2560 (576)	2885 (649)	1815 (408)	4218 (948)	2522 (567)	2327 (523)
	$V_{ptc}/V_{exp}$	1.06	0.96	1.09	1.20	1.08	1.18

The calculated plastic shear strength was within 10% of the experimentally measured values in all cases, except for the shear links L100 and X100. The larger calculated strengths of those links were caused by the cyclic characteristics of low yield point steel used for the webs. As discussed by Dusicka et al (2004), the cyclic hardening behavior of LYP 100 MPa (15 ksi) does not stabilize as rapidly as the structural grade steels. Under the deformation history imposed on the shear links, where the deformation continuously increased, the stress of LYP 100 MPa (15 ksi) was not as cyclically hardened as it would have been under repeated deformations of the same amplitude. The factor  $R_c$  is based on the maximum cyclic stress developed under the repeated deformations of constant amplitude, whereas the deformation history of the shear links continued to increase in magnitude after just one cycle for large deformations. Hence, the  $R_c$  factor overestimated the cyclic stress in the shear links for LYP 100 MPa (15 ksi) steels. The other grades were not as affected as the cyclic stress was found to stabilize much more rapidly.

The developed equation was also applied to results of experiments on built-up shear links that were reviewed in Section 1.4. Since  $R_c$  values for the specific steels were not available for BU30 and BU16, the value of A709 Grade 345 MPa (50 ksi) was used due to the similarity in the steel grade to those used for the tests. The results of the calculations are shown in Table 7-6 along with the relative contributions of the web, flanges and stiffeners. The calculated plastic shear capacity was within 10% of the experimental results. The equation does provide conservative estimates of the maximum shear resistance. The flange thickness of BU16 and the short effective length of SFOBB Type 3 as relative to the depth resulted in significant influence of the flanges to the strength reaching up to 10%. In all cases, the stiffeners had a minor influence. The results indicate that the expression for determining the plastic shear resistance  $V_{ptc}$  can be an effective method of estimating the shear strength of the tested built-up shear links subjected to cyclic loading.

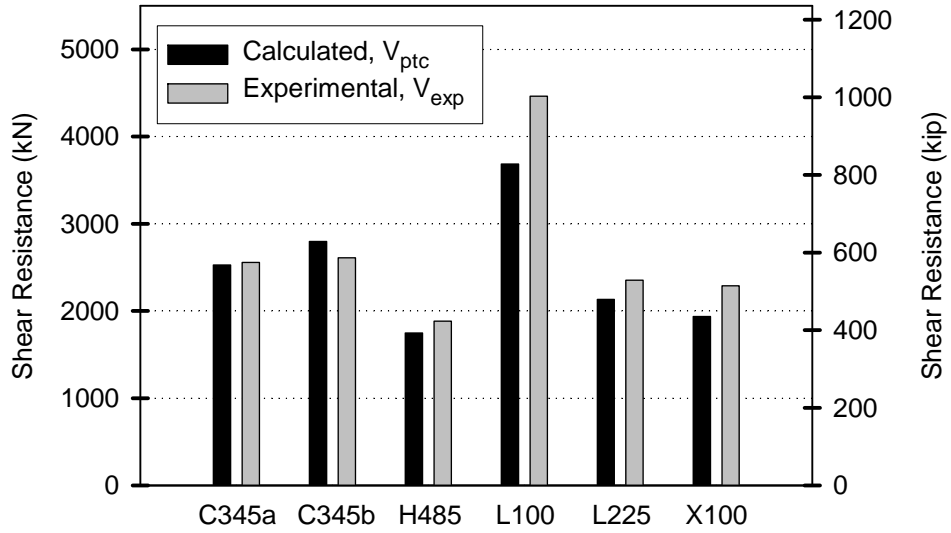


Figure 7-13: Comparison of Equation and Experimental Results at  $\gamma_{eff} = 0.08$  rad

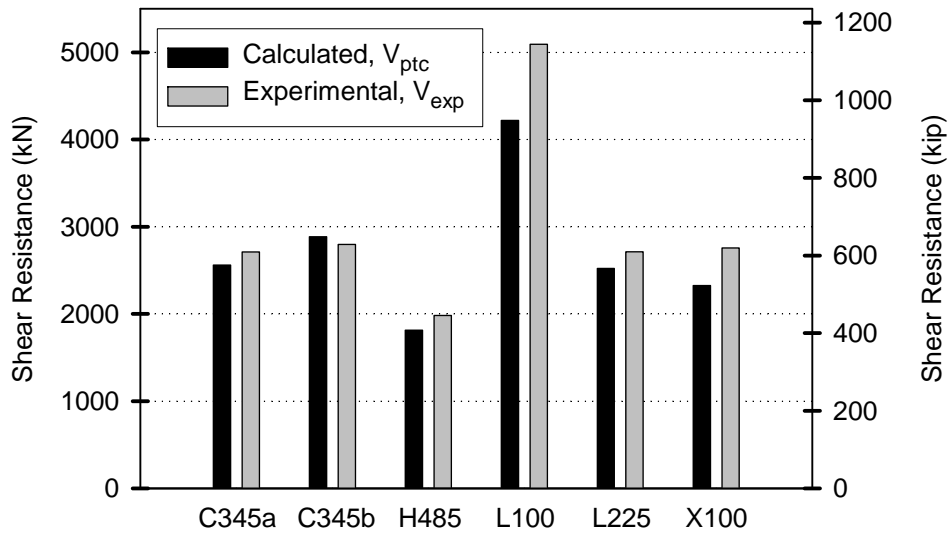


Figure 7-14: Comparison of Equation and Experimental Results at  $\gamma_{max}$

**Table 7-6: Comparison of Maximum Shear Resistance to Built-up Shear Links Tested by Others**

Parameter	Link Type			
	RSRB BU30	RSRB BU16	SFOBB Type 1	SFOBB Type 3
Coupon Yield Strength $f_{ya}$ , MPa (ksi)	372 (54)	372 (54)	354 (51)	354 (51)
$R_c$ corresponding to $\gamma_{max}$ *	1.83	1.89	1.75	1.77
From Equation 7-9 $V_{ptc}$ , kN (kip)	3040 (683)	1523 (342)	9844 (2213)	10174 (2287)
Web Contribution $R_c V_{pw}/V_{ptc}$	0.92	0.88	0.91	0.89
Flange Contribution $R_c V_{pf}/V_{ptc}$	0.05	0.10	0.07	0.10
Stiffener Contrib. $R_c V_{ps}/V_{ptc}$	0.03	0.02	0.02	0.01
From Experiments $V_{max}$ , kN (kip)	2780 (625)	1446 (325)	9363 (2105)	9919 (2230)
$V_{ptc}/(V_{max})^*$	1.09	1.05	1.05	1.03

\* maximum achieved deformation obtained from summary Table 1-1

## 7.7 Accounting for Overstrength

In general, overstrength in shear links is a ratio of the actual shear strength to the expected shear strength. As discussed in Section 1.1.2, the AISC Seismic Provisions simplify the expected shear strength to the shear strength of the web in Equation 1-2 and apply a constant factor to account for all contributive factors of overstrength. Based on the experimental and analytical study of built-up shear link cyclic behavior, an improved expression of overstrength accounting for individual contributions is introduced. Combining the contributions of variability in yield strength and inelastic steel behavior, the actual strength accounting for overstrength can be expressed by Equation 7-10.

$$V_o = R_o V_{nom} = R_y R_c V_{nom} \quad (7-10)$$

$V_{nom}$  is the nominal yield strength and the factor  $R_o$  accounts for the total contribution to overstrength, which consists of the material yield strength variability factor  $R_y$  and the cyclic stress factor  $R_c$ .

### 7.7.1 Nominal Shear Strength

Commentary in previous editions of the AISC Seismic Provisions (AISC 1997) pointed to the possibility of high overstrengths in links with relatively thick flanges. The flange and stiffener contribution to the shear resistance was shown to have an influence on shear strength in this study, leading to the development of a more refined expression for the expected shear strength in Equation 7-8. As an alternative to including the flange and stiffener influence as part of overstrength, the nominal shear strength  $V_{nom}$  can be defined. Nominal shear strength is based on specified material strengths. Rewriting Equation 7-8 for built-up shear links in which components are fabricated from the same steel grade becomes Equation 7-11.

$$V_{nom} = f_y \left( 0.6t_w h_w + \frac{3bt_f^2 + n_s b t_s^2}{2(e - 2t_f)} \right) \quad (7-11)$$

Overstrength, which is the shear strength beyond the nominal shear, can be attributed to fabrication tolerances and material characteristics.

### 7.7.2 Tolerances

Plate size variation and construction tolerances in steel fabrication are significantly more stringent than for any other types of structural construction materials. In concrete for example, the location of rebar can vary significantly from the design intent to the as-built condition. In steel fabrication, some variations do occur but are relatively minor. Welding can distort plate dimensions through the heating and cooling processes for example, but connections of members would be difficult to achieve especially with connections involving intricate bolt groups if large deviations from design existed. The variability in dimensions of the specimens is considered to provide an insignificant contribution to the structural behavior.

### 7.7.3 Material Characteristics

The characteristics of the steel can influence the resistance by the variability in yield strengths and the material inelastic behavior. The variability of yield strength from nominal to actual values was accounted for in this study by using the actual yield strength of the steels. In design codes this variability is accounted for by the  $R_y$  multiplier, which for plate steels is  $R_y = 1.1$ .

Material inelastic behavior that can contribute to the link overstrength include strain hardening and cyclic hardening of the material. Both of these types of behavior are inherent in the cyclic stress modification factor  $R_c$ , which are summarized in Table 7-2.

## 7.8 Summary

A series of parametric studies were conducted using numerical models to investigate secondary contributions to the built-up shear link strength. The numerical results showed that the flange, stiffeners and effective length influence the link shear strength. An expression for calculating the plastic shear resistance was developed based on the observations from the numerical modeling and independent of the large-scale shear link experiments. The developed equation for the plastic shear resistance followed the trends and magnitudes well with the shear resistance obtained from the detailed numerical analyses.

To account for the contribution of the steel stress-strain behavior, the results from the coupon experiments were utilized to incorporate a cyclic stress multiplication factor. The value of the multiplication factor is

highly dependant on the steel grade. A close correlation was shown between the calculated plastic shear resistance and the maximum shear obtained during the large-scale experiments as well as experiments conducted by others. Hence, the developed expression for calculating plastic shear resistance was found appropriate for estimating the maximum shear resistance of built-up shear links.



## SECTION 8

### BUILT-UP SHEAR LINK DESIGN RECOMMENDATIONS

#### 8.1 General Requirements

The eccentrically braced frame portion of the AISC Seismic Design Provisions for Structural Steel Buildings (2002) were used as the foundation for developing the design recommendations contained herein. These recommendations are based on the results and observations from the research. This section outlines the design recommendations for built-up shear links.

##### 8.1.1 Design Philosophy

Built-up shear links are expected to deform inelastically when subjected to forces from large earthquakes. The design philosophy is to contain the inelasticity to within the effective length and limit the forces and moments generated by the shear link. The effective length can be created using eccentrically placed braces or reductions in shear strength in a segment via thinner web plates or lower yield strength steels.

##### 8.1.2 Steel Grades

Based on the experimental study, Table 8-1 lists the steels that can be used for seismic applications. It should be noted the specified yield strength for ASTM specifications is a minimum, whereas lower yield strengths than the specified value may occur for low yield point steels LYP 100 MPa (15 ksi) and LYP 225 MPa (33 ksi). In the absence of coupon tests, the ratio of expected yield strength to the specified yield strength is given by  $R_y$ , which for plate steels remains constant. The cyclic stress multiplication factor is given by  $R_c$  and depends on both the steel grade and the design shear deformation of the effective length  $\gamma_{eff}$ . Two values of shear deformation are given and linear interpolation can be used for intermediate values.

##### 8.1.3 Section Compactness

The shear link cross sectional properties shall satisfy the following compactness ratios

$$\frac{b}{2t_f} \leq 0.3 \sqrt{E/f_y} \quad (8-1)$$

$$\frac{h_w}{t_w} \leq 3.14 \sqrt{E/f_y} \quad (8-2)$$

where:

$b$  = flange width, mm (in)

$t_f$  = flange thickness, mm (in)

$h_w$  = web height, mm (in)

$t_w$  = web thickness, mm (in)

$E$  = elastic modulus, MPa (ksi)

**Table 8-1: Steel Grades**

Property	Steel Specification				
	ASTM A709M Grade 345W	ASTM A709M HPS 485W	BT- HT440C*	BT- LYP100*	BT- LYP225*
Specified Yield Strength, $f_y$	345 MPa (50 ksi)	485 MPa (70 ksi)	440 MPa (64 ksi)	100 MPa (14.5 ksi)	225 MPa (32.5 ksi)
Expected to Nominal Yield Strength Ratio, $R_y$	1.1				
Cyclic Stress Multiplication Factor, $R_c$ at $\gamma_{eff} = 0.08$ rad	1.8	1.3	1.3	4.4	1.6
Cyclic Stress Multiplication Factor, $R_c$ at $\gamma_{eff} = 0.15$ rad	2.0	1.4	1.5	4.9	1.7

\* Nippon Steel (Japan) Specification

## 8.2 Shear Link Effective Length

The effective length of a built-up shear link shall be symmetric about the principal axis. The web of the link shall be a single web thickness and be free of any penetrations.

Unless otherwise noted, the required shear strength shall not exceed the design shear strength  $\phi V_{nom}$ , where:

$$\phi = \text{resistance factor} = 0.9$$

$$V_{nom} = V_w + V_f + V_s$$

$$V_w = 0.6f_{yw}t_w h_w$$

$$V_f = \frac{3f_{yf}bt_f^2}{2(e - 2t_f)}$$

$$V_s = \frac{n_s f_{ys} bt_s^2}{2(e - 2t_f)}$$

$f_{yw}, f_{yf}, f_{ys}$  = the nominal yield strength of the web, flange and stiffener steels respectively as given in Section 8.1.2

$n_s$  = number of intermediate stiffeners

$t_s$  = stiffener thickness, *mm (in)*

The nominal plastic flexural strength  $M_{nom}$  shall satisfy

$$1.6M_{nom} \geq eV_{nom} \quad (8-3)$$

where:

$$M_{nom} = f_{yf}bt_f h_w + f_{yw} \left[ \frac{t_w h_w^2}{4} \right]$$

$f_{yf}$  = nominal yield strength of the flange steel given in Section 8.1.2

$e$  = effective length, *mm (in)*

The maximum design shear deformation, which is measured by the rotation angle  $\gamma_p$  between the plastically deformed effective length and the undeformed shape, shall satisfy the following criteria:

- $\gamma_p \leq 0.15 \text{ rad}$  for built-up shear links without intermediate stiffeners, otherwise
- $\gamma_p \leq 0.08 \text{ rad}$  for built-up shear links with intermediate stiffeners.

### 8.3 Stiffener Requirements

Stiffener requirements were not the subject of this study, but the applicable recommendations from the AISC Provisions were shown to be applicable for the cases considered. Full-depth end stiffeners shall be provided at the ends of the effective length on both sides of the web. These stiffeners shall have combined width of not less than  $(b - 2t_w)$  and thickness not less than  $t_w$  or 10 *mm (3/8 in)*, whichever is larger.

Intermediate web stiffeners need not be used if the web dimensions satisfy the following criteria:

- web compactness ratio  $h_w/t_w \leq 20$ .
- effective length web aspect ratio  $e/h_w \leq 2$ , and

Otherwise, the AISC Seismic Provisions are applicable where the intermediate web stiffeners shall be provided and are required only on one side for web heights less than 635 *mm (25 in)*. These stiffeners shall have minimum width of  $(b/2 - t_w)$  and thickness not less than  $0.75t_w$  or 10 *mm (3/8 in)*, whichever is larger. The stiffener spacing  $a$  shall satisfy

$$a \leq \left( 52t_w - \frac{h_w}{5} \right) \quad (8-4)$$

#### 8.4 Connections and Members Outside the Effective Length

The built-up shear link connections and members outside the effective length shall be designed for the maximum forces and moments generated by the plastic shear resistance of the built-up shear link  $V_o$ , where

$$V_o = R_{ow}V_w + R_{of}V_f + R_{os}V_s$$

$R_{ow}, R_{of}, R_{os}$  = overstrength factors  $R_o$  for the web, flange and stiffener steels respectively  
 $R_o = R_y R_c$  as listed in Table 8-1 for the different steel grades and shear deformations

## SECTION 9 CONCLUSIONS

### 9.1 Conclusions

The following conclusions can be drawn based on the results of the research on hysteretic built-up shear links that included large-scale experiments and detailed nonlinear finite element analyses.

#### 9.1.1 General Conclusions

- As shown by others, built-up sections are a viable design option for shear links, allowing the designer greater autonomy with regard to the choice of link geometry and material selection. They are effective hysteretic devices that exhibit ductile cyclic response without strength degradation and achieve capacities exceeding the AISC Seismic Provisions for links from rolled steel sections.
- The failure mode for built-up shear links with intermediate stiffeners is characterized by web tearing that initiates with cracks in the web steel, next to the ends of the stiffener to web welds. The cracks in these locations are caused by a combination of plastic strain concentration and the effects of the welding process.
- The deformation capacity of built-up shear links designed using high performance steel A709 HPS 485W (HPS 70W) is similar to the deformation capacity of built-up shear links designed using conventional A709 Grade 345 *MPa* (50 *ksi*) steel. It follows that high performance steel is suitable for seismic applications.
- Significant improvement in the deformation capacity of built-up shear links is achieved by eliminating intermediate stiffeners from the effective length and using low yield point steels to decrease the web compactness.

#### 9.1.2 Conclusions for Design

- Eliminating intermediate stiffeners reduces the plastic shear strains in the web and removes welds from the web surface, thereby changing the failure mode and delaying the ultimate failure.
- Accurate estimation of overstrength in built-up shear links is required to protect connections and adjacent members.
- Variability of ultimate shear resistance in built-up shear links is primarily due to the steel cyclic properties with minor contribution from the link geometry. The link geometry contributes to the shear resistance primarily through the dimensions of the effective length, flange thickness and the number of stiffeners.
- Monotonic deformation response of a finite element model that incorporates the cyclic stress-strain material properties can approximate the backbone curve of a cyclic response of the shear link.
- The plastic shear resistance of built-up shear links of varied cross-sectional dimensions and material composition may be conservatively estimated using the developed relationship (Equation 7-9), which incorporates cyclic material properties and link dimensions.
- Based on limited data, the cumulative plastic shear deformation appears to be a useful parameter in predicting failure of built-up shear links under different load deformation histories.

### **9.1.3 Conclusions for Construction**

- Welding on the outside flange at the ends of the effective length should be avoided to reduce flange cracking. Plastic strains occur in these locations and are caused by flange bending that forms to accommodate the transition from the elastic connection zone to the plastically deformed effective length.
- Hybrid shear links improve cyclic performance while reducing fabrication costs. The use of low yield point steels for the web can eliminate stiffeners and the use of high strength steels for flanges can reduce material while providing sufficient moment resistance.

## REFERENCES

- AASHTO, (1998), American Association of State Highway and Transportation Officials, "LRFD Bridge Design Specifications", Second Edition, Washington, D.C.
- AISC, (2001), Manual of Steel Construction - Load and Resistance Factor Design, Third Edition, American Institute of Steel Construction, Chicago, IL.
- AISC, (2002), American Institute of Steel Construction, Seismic Provisions for Structural Steel Buildings, Chicago, IL.
- AISC, (1997), American Institute of Steel Construction, Seismic Provisions for Structural Steel Buildings, Chicago, IL; and "Supplement No. 2", November, 2000.
- ASTM, (1998), American Society for Testing and Materials, "Annual Book of ASTM Standards", Vol. 3.
- Astaneh A., Bertero, V., Bolt, B., Mahin, S., Moehle, J and Seed, R., (1989), "Preliminary Report on the Seismological and Engineering Aspects of the October 17, 1989 Santa Cruz (Loma Prieta) Earthquake", Report No. UBC/EERC-89/14, Earthquake Engineering Research Center, Bekeley, CA.
- Astaneh, A. and Shen, J., (1993), "Rocking Behavior and Retrofit of Tall Bridge Piers", Structural Engineering in Natural Hazard Mitigation, Proceeding of the Structures Congress, Vol.1, pp. 121-126.
- Astaneh-Asl, A. and Kanada, M., (1996), "Kobe Earthquake - Performance of Steel Bridges", Proceedings of the Second US Seminar on Seismic Design, Evaluation and Retrofit of Steel Bridges, Report No. UCB/CEE-STEEL-96/09, University of California at Berkeley.
- AWS, (2002), American Welding Code and American Association of State Highway and Transportation Officials, Bridge Welding Code, ANSI/AASHTO/AWS D1.5, 2002.
- Barsom, J., (1996), "Steel Properties - Effects of Constraint, Temperature, and Rate of Loading", Proceedings of the Second US Seminar on Seismic Design, Evaluation and Retrofit of Steel Bridges, Report No. UCB/CEE-STEEL-96/09, University of California at Berkeley.
- Barsom, J.M. (1996), "High-performance Steels", Advanced Materials & Processes, ASM International, v.149, n.3, pp. 27-31.
- Bertero, V., Anderson, J. and Krawinkler, H., (1994), "Performance of Steel Building Structures During the Northridge Earthquake", Report No. UBC/EERC-94/09, Earthquake Engineering Research Center, Bekeley, CA.
- Bertero, V., Borchardt, R., Clark, P, Dreger, D., Filippou, F., Foutch, D., Gee, L. Higashino, M., Kono, S., Lu, L. Moehle, J., Murray, M., Ramirez, J., Romanowicz, B., Sitar, N., Thewalt, C., Tobriner, S., Whitaker, A., Wight, J. and Xiao, Y. (1995), "Seismological and Engineering Aspects of the 1995 Hyogoken-Nanbu (Kobe) Earthquake", Report No. UBC/EERC-95/10, Earthquake Engineering Research Center, Bekeley, CA.
- Brockenbrough, R.L., (2003), "MTR Survey of Plate Material Used in Structural Fabrication", Engineering Journal, 40(1), pp. 42-49.
- CSI (2002), SAP2000 Analysis Reference, Computers and Structures Inc, Berkeley, CA.

- Dusicka, P. (2004), "Built-up Shear Links as Energy Dissipators for Seismic Protection of Bridges", Ph.D. Dissertation, Department of Civil Engineering, University of Nevada, Reno.
- Dusicka, P., Itani, A. M. and Buckle, I.G., (2002), "Cyclic Behavior of Shear Links and Tower Shaft Assembly of San Francisco-Oakland Bay Bridge Tower", Report No. CCEER02-06, Center for Civil Engineering Earthquake Research, University of Nevada, Reno.
- Engelhardt, M. D. and Popov, E. P., (1989), "Behavior of Long Links in Eccentrically Braced Frames", Report No. UCB/EERC-89/01, Earthquake Engineering Research Center, Berkeley, CA, 1989.
- Engelhardt, M. D. and Popov, E. P., (1989), "On Design of Eccentrically Braced Frames", *Earthquake Spectra*, Vol. 5, No. 3, pp. 495-511.
- Foutch, D., (1989), "Seismic Behavior of Eccentrically Braced Steel Building", *Journal of Structural Engineering*, ASCE, Vol. 115, No. 8, pp. 1857-1876.
- Goodyear, D. and Sun, J., (2003), "New Developments in Cable-stayed Bridge Design, San Francisco", *Structural Engineering International*, Vol. 13, No.1.
- Hjelmstad, K. D. and Popov, E. P., (1983) "Seismic Behavior of Active Beam Links in Eccentrically Braced Frames", Report No. UCB/EERC-83/15, Earthquake Engineering Research Center, Berkeley, CA.
- HKS (2003), *Abaqus User's Manual Version 6.4*, Hibbit, Karlsson, & Sorensen, Inc., Pawtucket, RI.
- Horton R., Power E., Ooyen K.V. and Azizinamini A., (2002), "High Performance Steel Cost Comparison Study", TRB 2002 Annual Meeting Proceedings, Transportation Research Board.
- Itani, A. M., (1997) "Cyclic Behavior of Richmond-San Rafael Tower Links", Report No. CCEER 97-04, Center for Civil Engineering Earthquake Research, University of Nevada, Reno.
- Itani, A. M., Lanaud, C. and Dusicka, P., (2003), "Analytical Evaluation of Built-up Shear Links under Large Deformations", *Computers and Structures*, v. 81, pp. 681-696.
- Kanz, R. and Bouwkamp, J.G. (1993), "Cyclic Response of Composite Steel-Concrete Shear Links of Eccentrically Braced Frames", *Proceedings of the Second European Conference on Structural Dynamics, EURO-DYN'93*, pp. 213-220.
- Kasai, I. and Popov, E. P., (1986a), "A study of Seismically Resistant Eccentrically Braced Steel Frame Systems", Report No. UCB/EERC-86/01, Earthquake Engineering Research Center, Berkeley, CA.
- Kasai, K. and Popov, E.P. (1986b), "General Behavior of WF Steel Shear Link Beams", *Journal of Structural Engineering*, Vol. 112, No. 2, (February), ASCE, Reston, VA.
- Kasai, K. and Popov, E.P. (1986c), "Cyclic Web Buckling Control for Shear Link Beams", *Journal of Structural Engineering*, Vol. 112, No. 3, (March), ASCE, Reston, VA.
- Malley, J. O. and Popov, E. P., (1983), "Design Considerations for Shear Links in Eccentrically Braced Frames", Report No. UCB/EERC-83/24, Earthquake Engineering Research Center, Berkeley, CA.
- Mans P., Yakel A.J. and Azizinamini A., (2001), "Full-scale Testing of Composite Plate Girders Constructed Using 485-MPa High-Performance Steel", *Journal of Bridge Engineering*, Vol.6, No.6.

McDaniel, C., (2002), "Influence of Inelastic Tower Links on the Seismic Response of Cable Supported Bridges", Ph.D. Dissertation, University of California, San Diego.

McDaniel, C., Uang, C.M. and Seible, F., (2003), "Cyclic Testing of Built-up Steel Shear Links for the New Bay Bridge", *Journal of Structural Engineering*, ASCE, Vol. 129, No. 6, pp. 801-809.

Nader, M., Lopez-Jara, J. and Mibelli, C. (2002), "Seismic Design Strategy of the New San Francisco-Oakland Bay Bridge Self-Anchored Suspension Span", *Proceedings of the Third National Seismic Conference and Workshop on Bridges*, Portland, OR.

Nader, M., Lopez J. and Rus L. (2004), "Seismic Reistant Design of the Single Tower of the New San Francisco-Oakland Bay Bridge", *Proceedings of the 4th National Seismic Conference and Workshop on Bridges and Highways*, Memphis, TN.

Pollino, M. and Bruneau, M., (2004), "Controlled Rocking System for Seismic Retrofit of Steel Truss Bridge Piers", *Proceedings of Fourth National Seismic Conference and Workshop on Bridges and Highway Structures*, Memphis, TN.

Ricles, J. and Popov, E. P., (1987b), "Dynamic Analysis of Seismically Resistant EBFs", Report No. UCB/EERC-87/07, Earthquake Engineering Research Center, Berkeley, CA.

Ricles, J., (1987a), "Experiments on Eccentrically Braced Frames with Composite Floors", Report No. UCB/EERC-87/06, Earthquake Engineering Research Center, Berkeley, CA.

Roeder, C.W. and Popov, E.P. (1978), "Eccentrically Braced Frames for Earthquakes", *Journal of the Structural Division*, Vol. 104, No. 3, ASCE, March 1978.

Roeder, C.W. and Popov, E.P., (1977), "Inelastic Behavior of Eccentrically Braced Steel Frames under Cyclic Loadings", Report No. UBC/EERC-77/18, Earthquake Engineering Rsearch Center, University of Californai at Berkeley, CA.

Roeder, C.W., (1998), "Overview of Hybrid and Composite Systems for Seismic Design in the United States", *Engineering Structures*, Vol. 20, pp. 355-363.

Sabelli, R. and Aiken, I. (2003), "Development of Building Code Provisions for Buckling-Restrained Braced Frames", *Proceedings of the Structural Engineers Association of California 72nd Annual Convention*, Squaw Creek, CA.

Sarraf, M. and Bruneau, M., (1998a), "Ductile Seismic Retrofit of Steel Deck-Truss Bridges I: Strategy and Modeling", *Journal of Structural Engineering*, Vol. 124, No. 11, pp. 1253-1262.

Sarraf, M. and Bruneau, M., (1998b), "Ductile Seismic Retrofit of Steel Deck-Truss Bridges II: Design Applications", *Journal of Structural Engineering*, Vol. 124, No. 11, pp. 1263-1271.

Seim, C. and Rodriguez, S, (1993), "Seismic Performance and Retrofit of the Golden Gate Bridge", *Structural Engineering in Natural Hazard Mitigation*, Proceeding of the Structures Congress, Vol.1, pp. 133-138.

Seismic Conference & Workshop on Bridges & Highways, MCEER Publications, State University of New York, Buffalo, NY.

Seyed, M.Z. and Bruneau M., (1999), "Ductile End-Diaphragms For Seismic Retrofit Of Slab-On-Girder Steel Bridges", *Journal of Structural Engineering*, Vol. 125, No. 1, pp. 71-80.

T.Y.Lin International, (1999), Design Drawings for the San Francisco Oakland Bay Bridge East Span Seismic Safety Project.

Tang, M., Manzanarez, R., Nader, M., Abbas, S. and Baker, G., (2000), "Replacing the East Bay Bridge", Civil Engineering Magazine, American Society of Civil Engineering.

Vincent, J., (1996), "Seismic Retrofit of the Richmond-San Rafael Bridge", Proceedings of the Second US Seminar on Seismic Design, Evaluation and Retrofit of Steel Bridges, Report No. UCB/CEE-STEEL-96/09, University of California at Berkeley.

Wright, W.J., (1997), "High Performance Steel: Research to Practice", Public Roads, Federal Highway Administration, Spring 1997, pp. 34-38.

Yamaguchi T., Nakata Y., Takeuchi T., Ikebe T., Nagao T., Minami A. and Suzuki T., (1998), "Seismic Control Devices Using Low-Yield-Point Steel", Nippon Steel Technical Report No. 77.

Yost, L. and Funderburk, S., (2001a), "High-performance Steels Increasingly Used for Bridge Building", Welding Journal, v.80, n.9, pp. 46-48.

Yost, L. and Funderburk, S., (2001b), "Welding High Performance Steel Bridges", Advanced Matter Processes, v.160, n.11.

Zahrai, M.S. and Bruneau, M., (1999a), "Ductile End-Diaphragms for Seismic Retrofit of Slab-on-Girder Steel Bridges", Journal of Structural Engineering, Vol. 125, No. 1, pp. 71-80.

Zahrai, M.S. and Bruneau, M., (1999b), "Cyclic Testing of Ductile End Diaphragms for Slab-on-Girder Steel Bridges", Journal of Structural Engineering, Vol. 125, No. 9, pp. 987-996.

**APPENDIX A  
TEST SETUP DETAILS**

<b>SECTION</b>	<b>TITLE</b>	<b>PAGE</b>
<b>A.1</b>	<b>OVERVIEW</b>	<b>174</b>
A.1.1	General Arrangement	174
A.1.2	Tower Shaft Description and Fabrication	176
A.1.3	Typical Shear Link Layout	177
A.1.4	Steel and Bolt Grades	178
<b>A.2</b>	<b>INSTALLATION</b>	<b>178</b>
A.2.1	Test Setup Erection Sequence	178
A.2.2	Typical Shear Link Installation Sequence	178
A.2.3	Installation Issues	179
A.2.3.1	Access to Skin Plate Bolts	179
A.2.3.2	Field Welding of Web Stiffeners	180
A.2.3.3	Flange Splice Plate Clearance	180
A.2.3.4	Bolt Accessibility	180
<b>A.3</b>	<b>MEASURING SHEAR LINK PERFORMANCE</b>	<b>182</b>
A.3.1	Friction Resistance	182
A.3.2	Calculation of Link Shear	182
A.3.3	Evaluation of Shear Link Axial Force	184
A.3.4	Calculation of Link Average Shear Deformation	185

## A.1 Overview

This appendix describes the laboratory layout, fabrication and installation of the test setup and calculations necessary for measuring shear link performance. The test setup utilized tower sections of the new San Francisco-Oakland Bay Bridge (SFOBB).

### A.1.1 General Arrangement

The tower of the suspension span portion of the SFOBB bridge consists of four shafts that are pentagonal in cross-section and interconnected by shear links. The shear links are distributed in 20 levels throughout the height of the tower. A typical section showing the tower shaft-to-link assembly at one of these levels is shown in Figure A-1. Due to the different response characteristics in the principal horizontal directions of the bridge, a single shear link connects adjacent shafts in the longitudinal direction while two parallel shear links connect adjacent shafts in the transverse direction. Sections of two tower shafts were fabricated at half-scale to replicate the conditions of both of these tower-to-shear link assemblies in the laboratory.

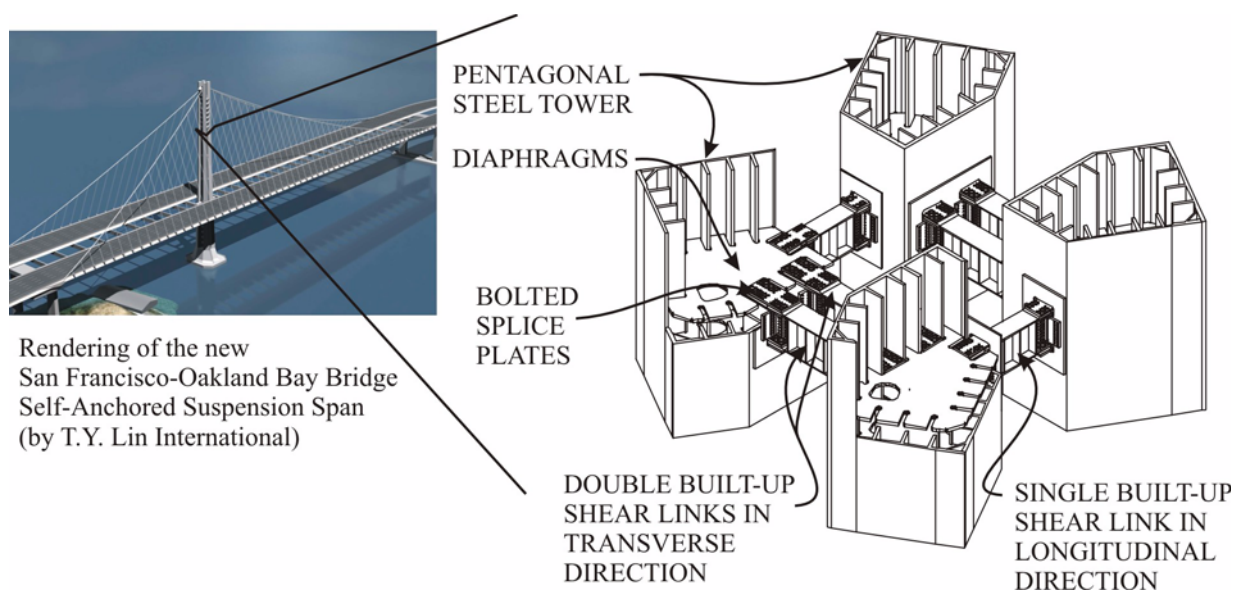


**Figure A-1: Rendering of SFOBB Tower Shaft Assembly**

The shafts were placed on their sides parallel to the laboratory floor as shown in Figure A-2. Hollow square box extensions were welded to the South end of the pentagonal sections to provide additional length as well as a flat sliding surface within the safety restraint. Teflon was used between the sliding surfaces to minimize friction. Each tower shaft was connected to concrete reaction blocks at the North end using large pins. The concrete blocks were post-tensioned to the laboratory floor. A strut with pinned connections was installed at the South end of the test setup between the two shafts. MTS made actuator model no. 243.100T with  $\pm 3115$  kN ( $\pm 700$  kip) capacity, was attached to the west box extension. The resulting assembly formed a pinned mechanism in which the shear links were installed.

Two different test setup configurations were possible and are referred to as the Longitudinal and Transverse test setups according to the shaft orientation with respect to the bridge. To change from one configuration to the other, the shafts were rotated  $90^\circ$  along their principal axis and switched East to West. The overall dimensions of the test setup arrangements are shown in Figure A-2(a). The main difference was the

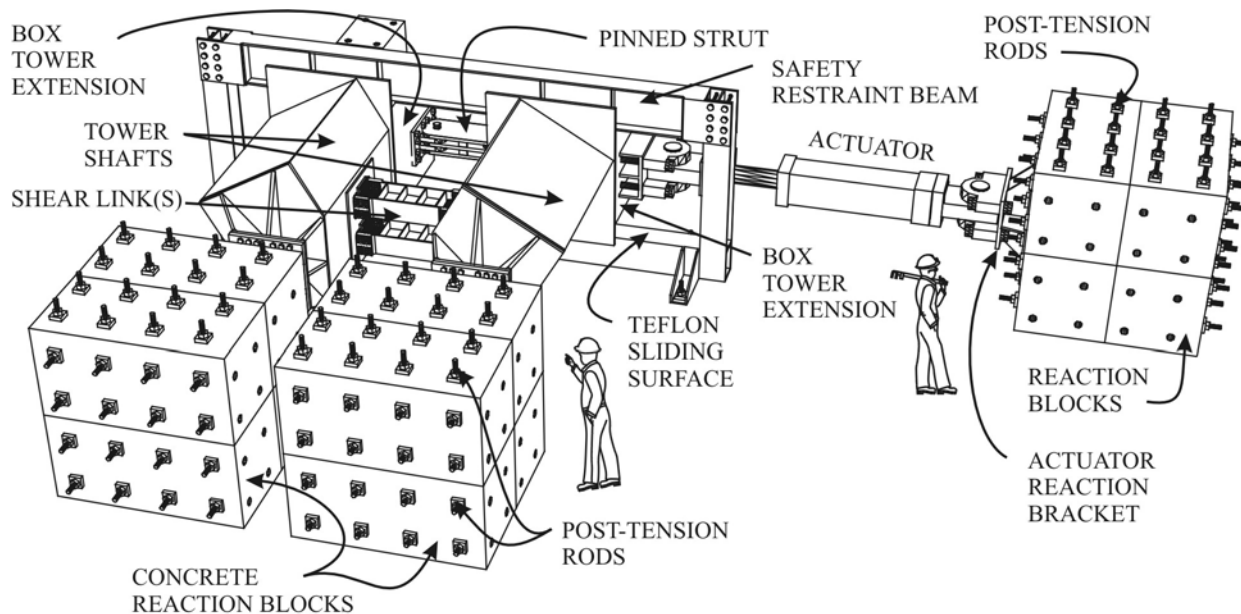
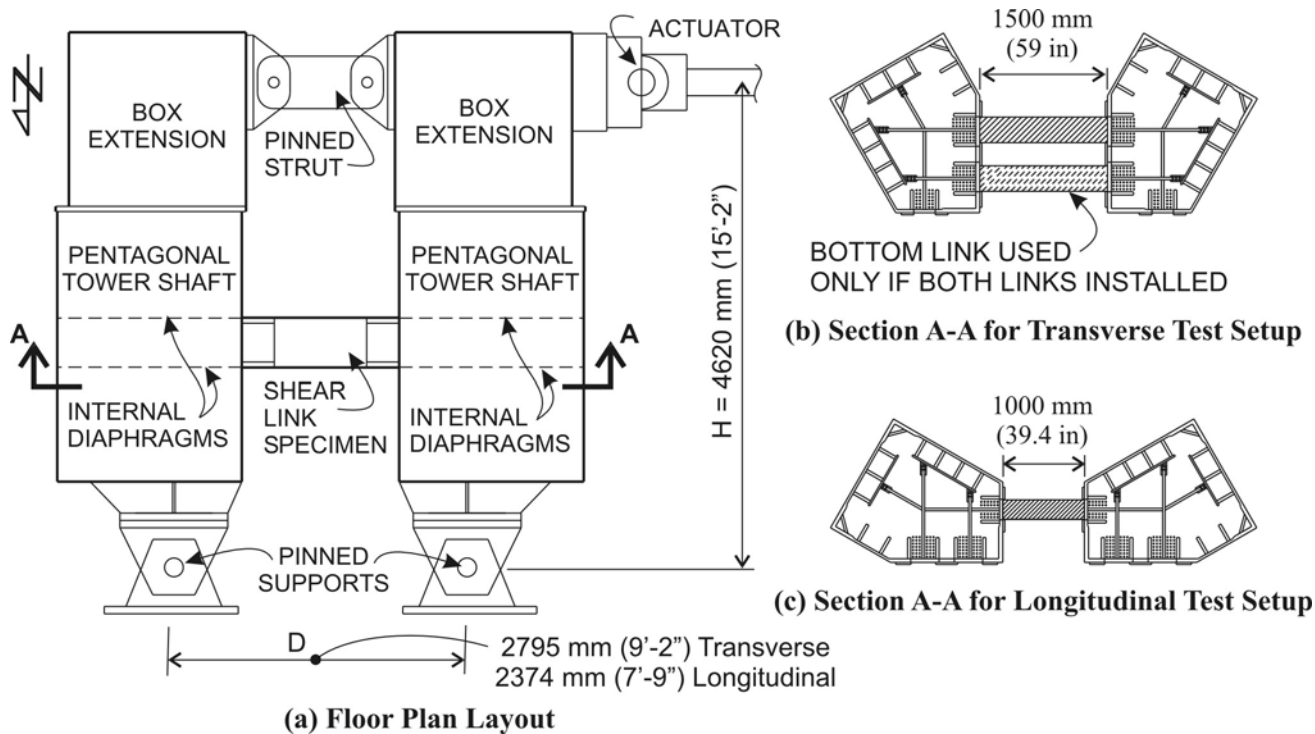


Figure A-2: Laboratory Arrangement of the Test Setup

orientation of the shafts, the distance between the shafts and the link connection details. The major advantage of utilizing the towers shafts in the test setup were the bolted connections between the shear links and the rest of the test setup, thereby allowing link replacement without field cutting and welding.

### A.1.2 Tower Shaft Description and Fabrication

Replicas of the tower shafts were designed by T.Y. Lin International in San Francisco. The test setup, including the shaft replicas, was fabricated by Christie Constructors Inc. of Richmond, CA. Quality control for the fabrication and welding was conducted by Testing Engineers Inc. of Oakland, CA, and quality assurance by Caltrans representatives from Law Crandall of San Diego, CA. The half-scale SFOBB shaft sections were 2.5 m (8.20 ft) long and were made from stiffened plates into pentagonal sections representative of the tower at 89 m (292 ft) elevation. The skin plate thicknesses varied along the perimeter between 30 mm (1.18 in) to 50 mm (1.97 in) and were reinforced by 35 mm (1.38 in) thick stiffeners. Doubler plates were welded to the skin plates at the location of shear link connections as illustrated in Figure A-3. Horizontal internal shaft diaphragms were welded in plane with the shear link flanges to facilitate load transfer from the link to the shafts.

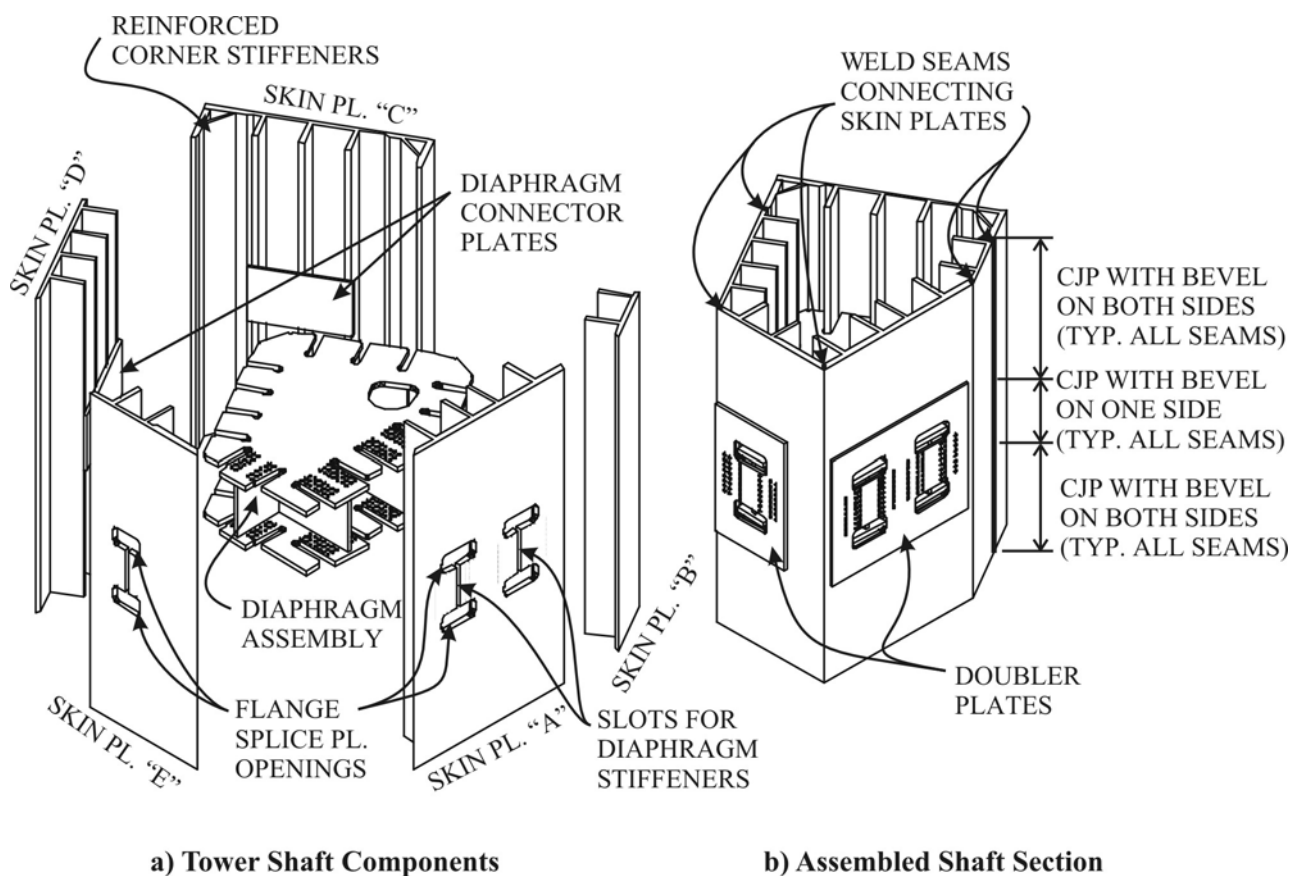


Figure A-3: Tower Shaft Details

The design provided for challenging fabrication with special attention required to the welding sequence. Each shaft was fabricated as follows:

1. The diaphragm assembly, which consisted of two pre-drilled diaphragms and diaphragm stiffening plates, was welded together.
2. Stiffened skin plates A through E were individually welded along with the stiffeners.
3. Slot openings were made in skin plates A and E between the splice plate openings to allow access for welding the stiffener of the diaphragm assembly.
4. Diaphragm connector plates were welded to stiffeners of skin plates C and D.
5. The diaphragm assembly was welded to the diaphragm connector plate of skin plate D.
6. The remaining reinforced skin plates were tack welded around the diaphragm in the order E, A, B and C.
7. The seams connecting the skin plates were welded using double bevel full penetration weld. Where access was restricted to only one side, i.e. at the locations of the diaphragms, a single bevel full penetration weld had to be made.
8. The diaphragm was welded around the perimeter to the skin plates and stiffeners from inside the shaft.
9. The diaphragm stiffener was welded using the slots in skin plates A and E.
10. Doubler plates were fillet welded and bolt holes drilled in the location of the shear link connections.

### A.1.3 Typical Shear Link Layout

To allow for the shear link bolted connections, each shear link consisted of three distinct regions as shown in Figure A-4; the deformable length in the middle and two connection zones at the ends. The link connection zone was designed to remain elastic by incorporating higher strength steel or thicker plates to compensate for the reduction in net area from the bolt holes. Each link bolted to the tower shafts using splice plates for the flanges and angles for the webs. The splice plates extended inside the shafts and bolted to the diaphragm, while the angles connected the web to the outside skin plate.

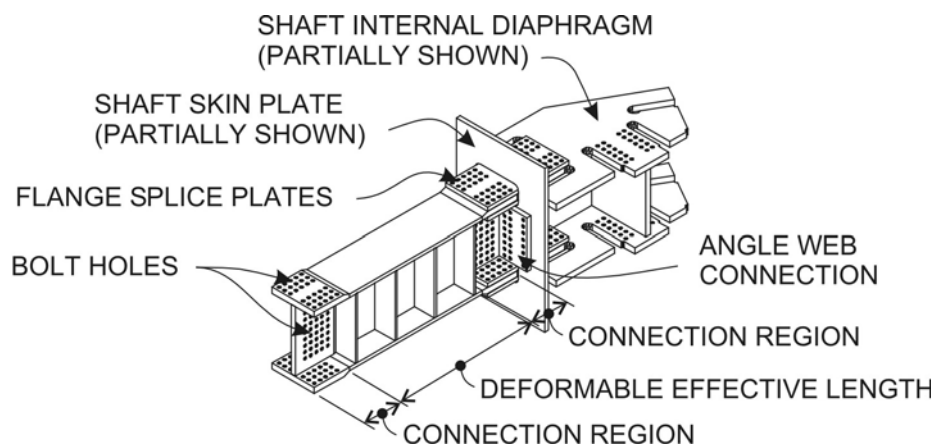


**Figure A-4: Typical Shear Link Layout**

### **A.1.4 Steel and Bolt Grades**

The shaft diaphragms, splice plates and connection angles were made from ASTM A709 grade 485 *MPa* (70 *ksi*) high performance weathering steel. The remainder of the test setup was made from ASTM A709 grade 345 *MPa* (50 *ksi*) steel. All bolts connecting the link to the tower shafts were M16 - A490 grade with threads excluded from the shear planes. The M16 bolts were tightened by a torque wrench that was calibrated to the required bolt pretension force of 107 kN (24 kip) as specified in the Manual of Steel Construction (AISC 2001). The calibration of the wrench was conducted by tightening a bolt between two representative splice plates and measuring the force using a load cell.

## **A.2 Installation**

Majority of the test setup was fabricated in Richmond, CA, and transported to the structures laboratory at the University of Nevada, Reno. This section reviews the erection and some of the installation issues encountered.

### **A.2.1 Test Setup Erection Sequence**

The erection of the test setup illustrated in Figure A-2 was conducted in the following order:

1. Concrete reaction blocks were positioned on the laboratory floor and the voids between them filled with grout.
2. Vertical post-tensioning using 45 *mm* (1.75 *in*) diameter Dywidag rods was used to secure the reaction blocks to the laboratory floor.
3. Steel brackets were installed at the North end of the towers and were post-tensioned horizontally to the concrete blocks.
4. Bottom portion of the safety restraint was post-tensioned to the floor.
5. The tower shafts were bolted to the brackets against the reaction blocks at the North end.
6. The West tower shaft was bolted to the actuator, which was then used to position the shaft as needed.
7. The pinned strut was bolted between the shafts.
8. Top beam of the safety restraint was bolted to enclose the tower shafts.

### **A.2.2 Typical Shear Link Installation Sequence**

Each shear link connection zone was drilled prior to each experiment in order to ensure proper fit. As illustrated in Figure 7, the following sequence of steps was required for successful installation of each shear link due to tolerance and potential interference issues:

1. Bolts were pre-installed in the skin plate of the tower shafts.
2. The full-width flange splice plate and one flange splice plate at the inside flange face were bolted to the shaft diaphragm.
3. One web angle was bolted onto the skin plate on the same side as the inside flange splice plate.
4. The other inside face flange splice plate was pushed inside the tower and flush with the skin plate.
5. The shear link was slid into place.
6. The splice plates on the inside flanges were pulled from inside the tower and bolted to the tower diaphragm.
7. The remaining web angles was bolted to the skin plate.

8. The link was clamped and holes marked with a portable magnetic drill using the splice plates and web angles as templates.
9. The link was removed and holes drilled according to the marked locations.
10. The link was installed by repeating steps 4 through to 8.
11. All bolts were installed and torqued.

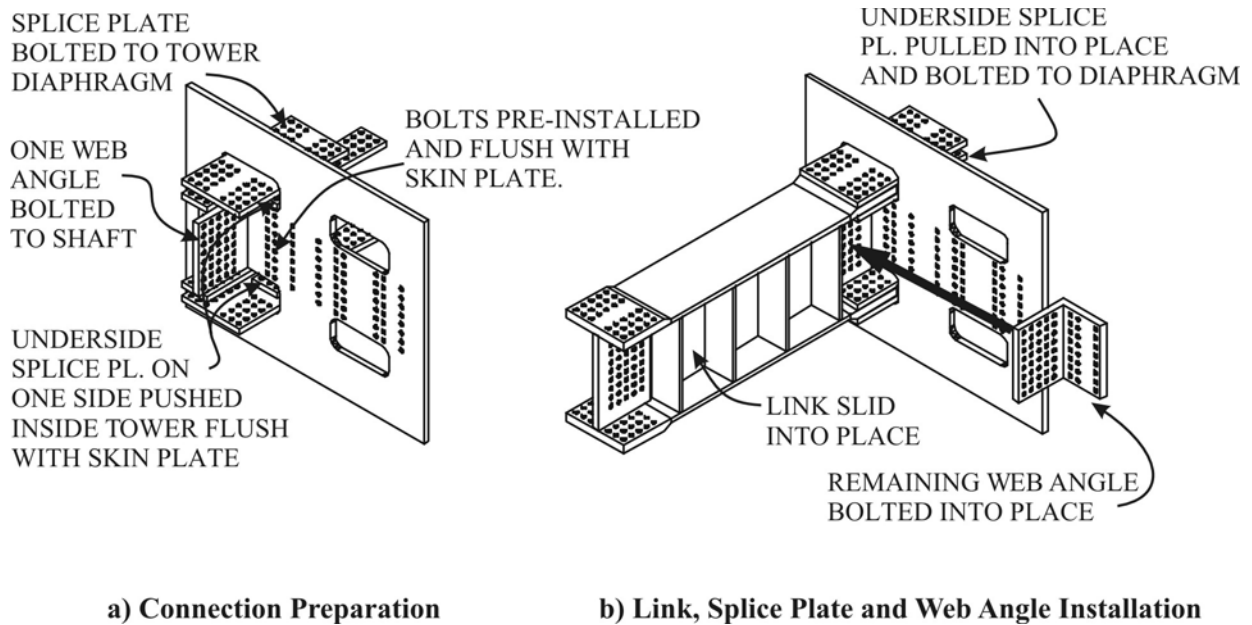


**Figure A-5: Shear Link Installation**

### A.2.3 Installation Issues

A number of issues were encountered during installation of the shear links and related to the tower shaft designs. These were mainly related to the lack of accessibility or space in parts of the tower shafts.

#### A.2.3.1 Access to Skin Plate Bolts

Majority of the bolt holes in the skin plates were not accessible from inside the tower shaft because the holes were located between the shaft diaphragms and were often hidden behind numerous stiffeners. As a result, the bolts had to be placed into the holes from outside the shaft prior to shear link plate installation. They were then retrieved using fishing wire that was attached to 3 mm (0.12 in) machine screws that were drilled and tapped at the ends of the threaded end of each bolt. These small screws did not affect the functionality of the bolts during the test, but this method would not be considered as sound bridge construction practice.

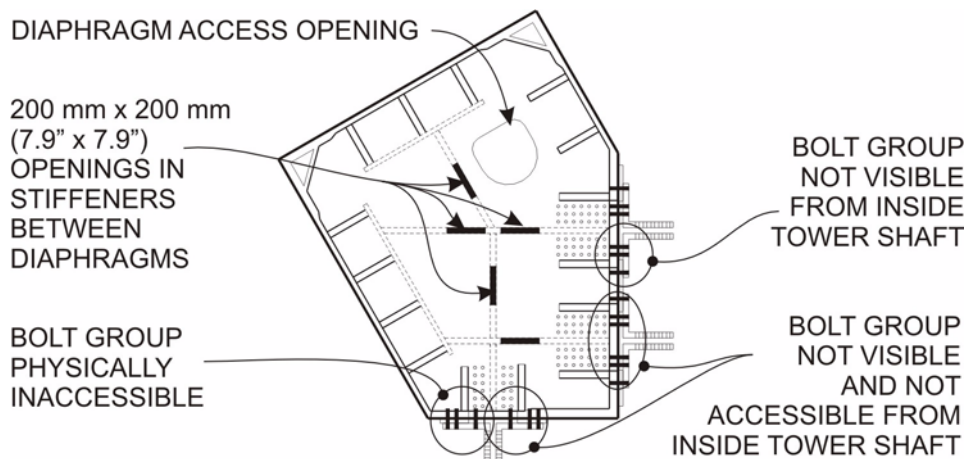


**Figure A-6: Tower Shaft Section Showing Locations of Inaccessible Bolt Areas**

### A.2.3.2 Field Welding of Web Stiffeners

Variation from the general procedure of shear link installation was needed for the shear link in the longitudinal test setup. In this case, the flange splice plate on the inside face of the link flange could not be pushed inside the tower shaft due to interference with internal tower stiffeners. The splice plates also could not be installed after the link was in place due to interference with the shear link stiffeners. As a result, the link stiffeners had to be removed on one side such that the link could be drilled and bolted into place. The stiffeners were then field welded back after the bolts were torqued.

### A.2.3.3 Flange Splice Plate Clearance

Design details of the inside flange splice plates for the transverse assembly indicated 5 mm (0.2 in) clearance between the splice plates and the stiffener inside the tower connecting the web diaphragms as shown in Figure A-7. However, the presence of welds at that location exceeded this tolerance and prevented installation of the inside flange splice plates. The inside corners of the splice plates were ground to provide adequate clearance for installation.

### A.2.3.4 Bolt Accessibility

Tightening of bolts inside the tower shafts as well as in the link connection regions was shown difficult for certain bolt groups. Inside the tower, bolts were located close to the skin plate and next to the skin plate stiffeners. While the socket was able to reach all of the bolts, the process of turning the wrench during torquing was restricted to a few degree turns at a time. The wrench either hit the stiffener next to the bolt or the stiffeners on other sides of the tower shafts as shown in Figure A-8(a). Shorter wrench would not provide sufficient lever arm for applying the required torque. Also, flange bolts closest to the skin plate within the link connection zone were not accessible as shown in Figure A-8(b). Rigs and jamming devices had to be used to hold the nut during the bolt tightening process. As a result, installation and torquing the bolts became a laborious and time consuming process.

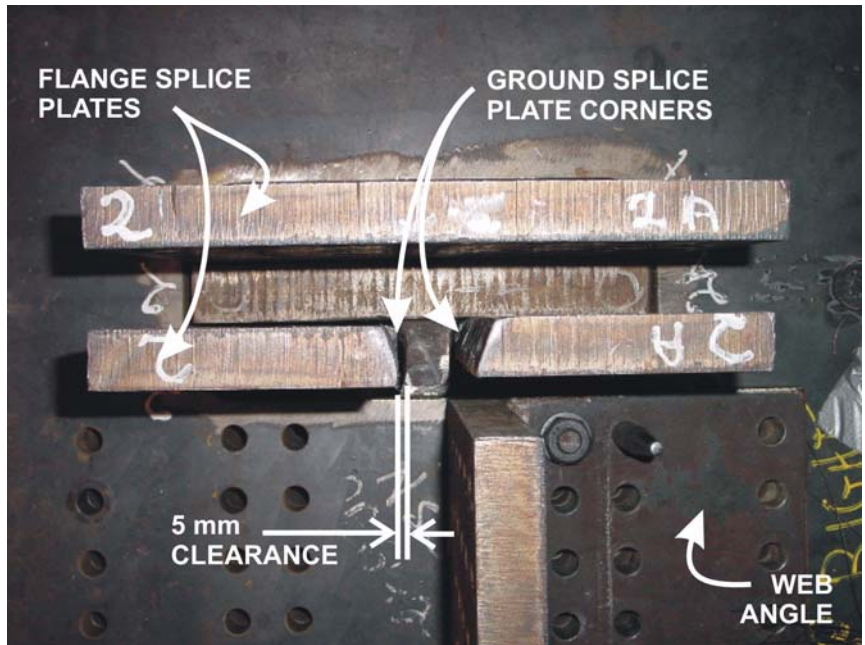
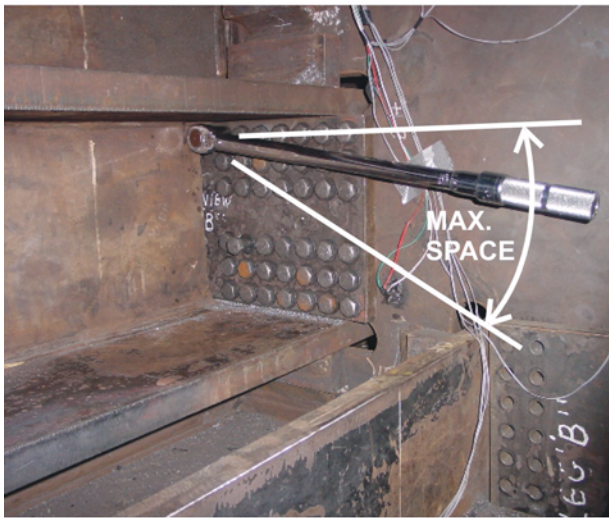
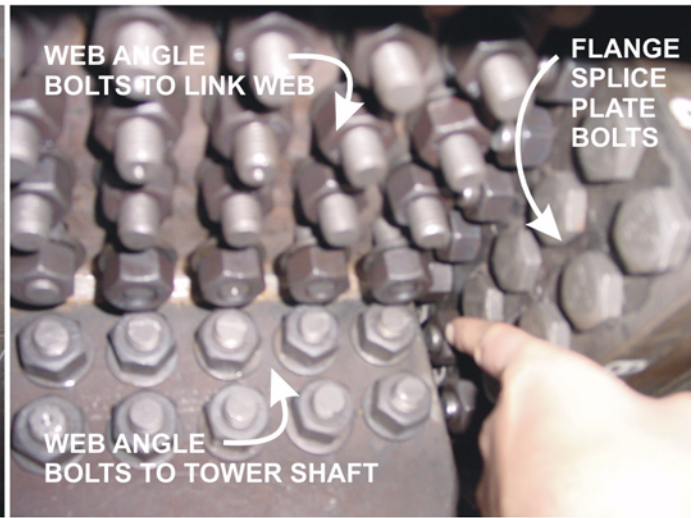


**Figure A-7: Ground Corners of Flange Splice Plates**



(a) Wrench Access Inside Tower



(b) Bolt Access at Connection Joint

**Figure A-8: Bolt Accessibility Issues**

### A.3 Measuring Shear Link Performance

The link shear forces were determined indirectly using the applied actuator force and accounted for friction and test setup geometry. The link shear deformation was measured directly and independent of any connection slippage or test setup flexibility.

#### A.3.1 Friction Resistance

The gravity loads of the shafts were supported by sliding surfaces of steel on teflon. To quantify the friction resistance, tests were carried out on the test setup mechanism without any shear links. The actuator displacement was applied at the same rate as during the shear link experiments. The actuator displacement range encompassed the maximum measured values during the shear link tests, approximately  $\pm 300 \text{ mm}$  (11.8 in) and  $\pm 150 \text{ mm}$  (5.9 in) for the Transverse and Longitudinal test setups respectively. The average friction resistance,  $F_f$ , for the two test setups are summarized in Table A-1.

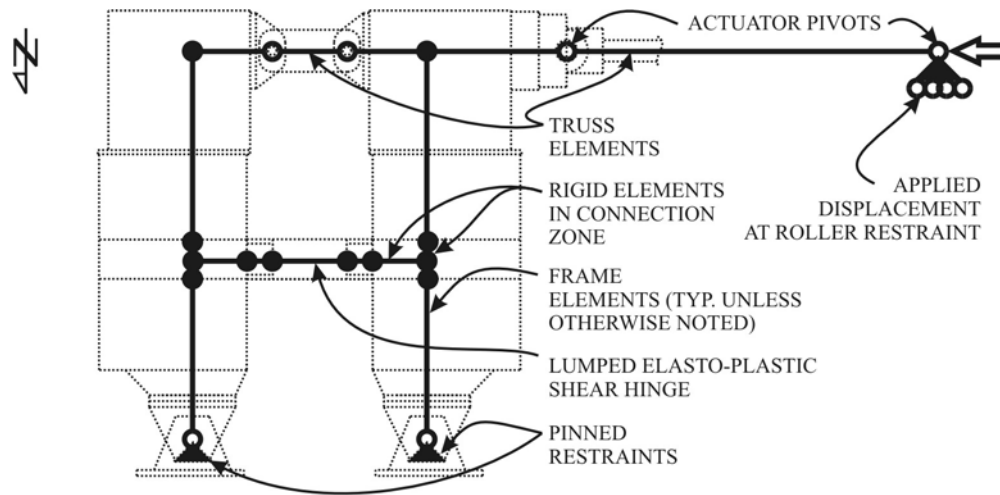
The corresponding friction coefficient values are 0.18 and 0.25 for the transverse and longitudinal test setup respectively under the assumptions that the tower legs and the actuator self weight imposed 280 kN (63 kip) force onto the bearing surface of the safety restraint. This force was determined from statics and an approximate weight of 343 kN (77.0 kip) for the two tower legs and 82 kN (18.5 kip) for the actuator. Given the slow application of load, these values correspond well to the approximate static friction coefficient of 0.2 between steel and teflon. The friction for the Longitudinal test setup was higher because the sliding surface of the box extension included welds that protruded into the teflon surface. For the Transverse test setup, the bearing surfaced was flat and without welds or other protrusions.

#### A.3.2 Calculation of Link Shear

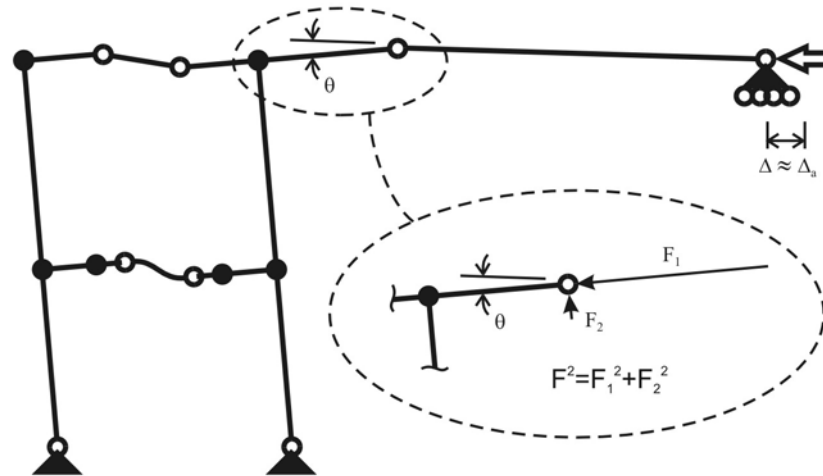
Link shear  $V$  was calculated based on the geometry and the actuator force  $F$ . The actuator force was recorded by MTS calibrated P-delta axial load cell and was positive for the push and negative for the pull force. The friction resistance was subtracted from the applied load for movement towards the East direction and added for movement towards the West. Based on the geometry shown in Figure A-2, the shear can be related to the actuator force using Equation A.1, where  $H$  is the perpendicular distance from the tower pinned reactions to the actuator line of action and  $D$  is the distance between the tower reactions.

$$V = (F \pm F_f) \cdot \left(\frac{H}{D}\right) \quad (\text{A.1})$$

However, second order effects were introduced due to the change in geometry under large actuator displacements  $\Delta_a$ . These effects were quantified using non-linear pushover analyses of the idealized test setup shown in Figure A-9(a) using SAP2000 v.8.3 structural analysis software (CSI 2002). As the actuator extended and retracted, the geometry of the mechanism caused the actuator to induce forces that were no longer perpendicular to the tower shafts as illustrated by the actuator force components  $F_1$  and  $F_2$  in Figure A-9(b). Frame and truss elements were used to model the test setup geometry and boundary conditions. Representative cross sectional properties were assigned to the elements and the tower shaft connection zone between the diaphragms and up to the skin plate was assumed to be rigid. Lumped elasto-plastic shear hinge was incorporated to limit the link shear  $V$ . The actuator displacement  $\Delta_a$  was assumed to approximately equal the imposed horizontal displacement  $\Delta$  at the West end of the actuator. The range of displacements encompassed the maximum recorded displacements for both test setups. The pushover analyses included large deformation effects to account for the changing geometry at each step increment.



(a) Finite Element Model Layout



(b) Test Setup Under Imposed Deformation

**Figure A-9: Pushover Model for Determining Second Order Effects**

The results of the analysis for both the transverse and the longitudinal test setup are shown by the discrete data points in Figure A-10. The ratio of the link shear to the axial force in the element representing the actuator illustrates the effects of the displaced geometry. The calculation of the link shear that accounts for the changing geometry was approximated by a quadratic relationship shown by Equation A.2. Constants  $c_1$  and  $c_2$  are summarized in Table A-1 for the two different test setups. These relationships are shown as continuous lines in Figure A-10 and revert to Equation A.1 for zero actuator displacement.

$$V = (F \pm F_f) \cdot \left( \frac{H}{D} + \frac{\Delta_a}{c_1} + \frac{\Delta_a^2}{c_2} \right) \quad (\text{A.2})$$

**Table A-1: Constant Used in Calculating Link Shear**

Test Setup	$F_f$ kN (kip)	$H$ mm (in)	$D$ mm (in)	$c_1$ mm (in)	$c_2$ mm <sup>2</sup> (in <sup>2</sup> )
Longitudinal	71 (16)	4620 (182)	2370 (93.3)	1830 (72)	-21900 (-862)
Transverse	50 (12)	4620 (182)	2795 (110)	2910 (115)	-25600 (-1000)

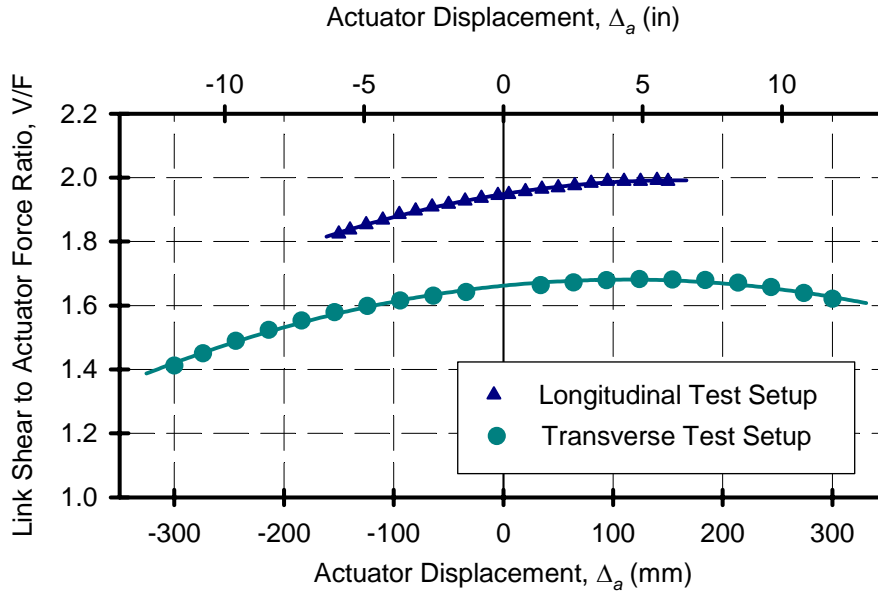


**Figure A-10: Results from Test Setup Pushover Models**

### A.3.3 Evaluation of Shear Link Axial Force

The change in geometry of the test setup under large actuator displacements can engage the link as a strut and induce axial tensile forces. The pushover model illustrated in Figure A-9 was also used to determine the significance of the shear link axial forces. Results of the analyses for the transverse as well as the longitudinal test setup are shown in Figure A-11, where the link axial force  $P$  is expressed in terms of its axial yield capacity  $P_y$ . The axial yield capacity was calculated as  $P_y = Af_y$ , where  $A$  is the link cross sectional area and  $f_y$  the nominal yield strength of the link. The link axial force was found to increase with increasing actuator displacement and was significantly higher for the Longitudinal test setup due to the closer spacing between the tower shafts. However, the bolted shear link end connections and the tower diaphragm flexibility, which were not reflected in the idealized numerical model would significantly lower the link axial forces.

Each bolt within the connection zone has 2 mm (1/16 in) clearance in a standard bolt hole (AISC 2001). Assuming bolts and bolt holes that do not deform, this clearance provides for 4 mm (1/8 in) movement at each shear link flange; i.e. between the link and the splice plate and between the splice plate and the tower diaphragm. With bolt slippage, this link movement can provide for axial force relief at the location of each flange. In order to quantify this effect, the numerical model was modified to include bolt slippage using bi-

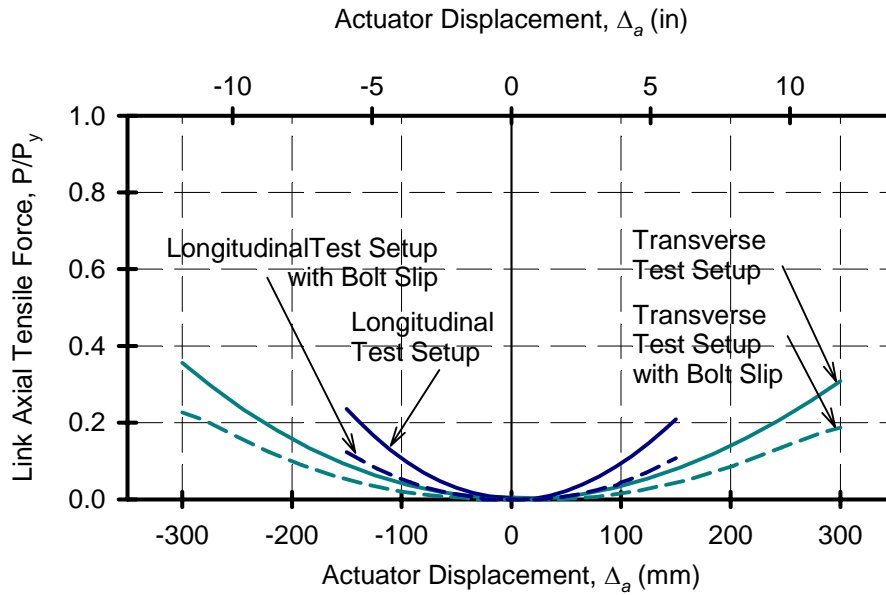


**Figure A-11: Axial Force in the Link**

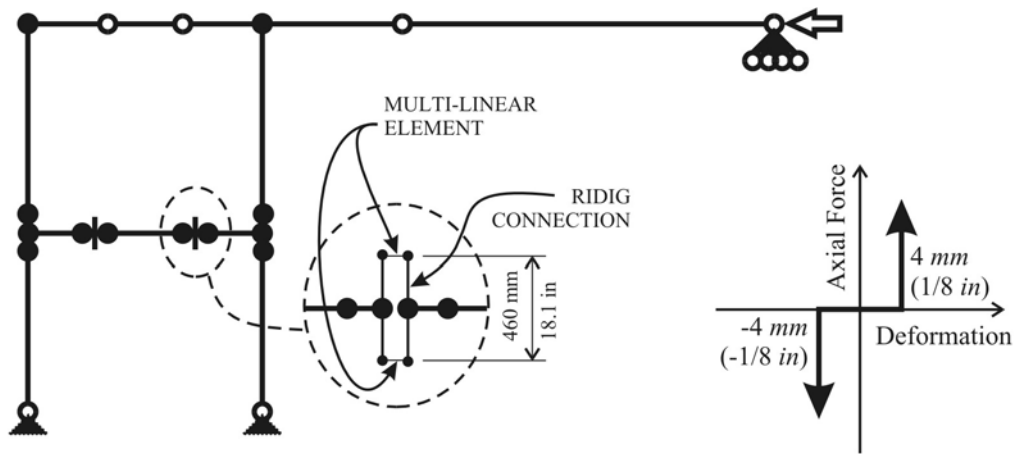
linear axial elements at the location of flange splice center lines as shown in Figure A-12. These elements were assigned stiff numerical values in all degrees of freedom except for axial force deformation. The axial force deformation allowed for 4 mm (1/8 in) displacement in both tension as well as compression before engaging the element. In effect, the numerical model assumed that all of the bolt slip occurred during the initial loading.

The resulting link axial forces for the two test setups are shown by the dashed lines in Figure A-11. Significant reduction in axial force was observed at the extreme actuator displacement. Further reduction in axial force may result if flexibility of the tower diaphragm connection was taken into account with a detailed model of the connection region. Based on the relatively low values of axial stresses induced by the test setup even at large actuator displacement, the axial force was assumed to not significantly influence the overall shear link performance.

### A.3.4 Calculation of Link Average Shear Deformation

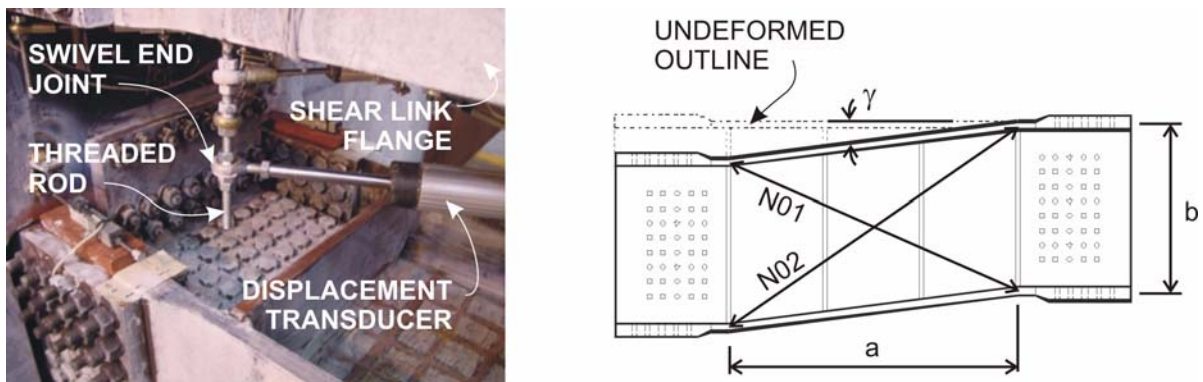
Displacement transducers were used to measure the rotation of the shear link effective length independent of the bolted connection and the rest of the test setup. Threaded rod studs were welded to the side of the flange at the ends of the deformable length as shown in Figure A-13(a). Displacement transducers were bolted to the rods with swivel joints to allow rotation at the connections. The shear deformation  $\gamma_{eff}$  was calculated using Equation A.3 (McDaniel et al 2002), where the diagonal deformations  $\delta_1$  and  $\delta_2$  were measured by transducers N01 and N02 installed across the effective length of dimensions  $a$  and  $b$  as shown in Figure A-13(b). The calculated value represented the average shear deformation across the entire effective length.

$$\gamma_{eff} = \frac{1}{2} \cdot \frac{(\delta_1 - \delta_2) \sqrt{a^2 + b^2}}{ab} \quad (A.3)$$



(a) Connection Modification for Bolt Slip      (b) Multi-Linear Link Force Deformation

**Figure A-12: Connection Modification for Including Bolt Slip**



(a) Displacement Transducer Attachment      (b) Deformable Length Shear Rotation

**Figure A-13: Illustration of Link Shear Deformation Measurements**

**APPENDIX B**  
**SUPPORT DOCUMENTS**

# OREGON STEEL MILLS

P.O. BOX 2760, Portland, Oregon 97208 • (503) 286-9851 Fax (503) 240-6288

## REPORT OF CHEMICAL/PHYSICAL TESTS

CERTIFICATE NO.	DATE	PAGE
625381	Nov 02, 2000	1
MILL ORDER NO.	DATE	
125074		
CUSTOMER ORDER NO.		
001619		
JOB/REQ. NO.		
SHIPPER NO.	DATE	
625381	11/02/2000	
CARRIER		
Melton Truck Lines		
CARTRUCK NO.		
TRL		



CHRISTIE CONSTRUCTORS, INC. 11.26.01  
 4925 SEAPORT AVE  
 RICHMOND, CA 94804

THIS MATERIAL HAS BEEN MANUFACTURED, TESTED AND FOUND TO MEET THE SPECIFICATIONS AND PURCHASE ORDER REQUIREMENTS  
 OSM HSLA STRUCTURAL QUALITY PLATE ASTM A709-00 GR 70W HPS-70W. KILLED FINE  
 GRAIN PRACTICE VACUUM DEGAUSS. REPORT ASTM G101 CORROSION INDEX. LCVN 35  
 FT/LBS AVG @ -10 F (P). FRACTURE-CRITICAL, F. ZONE 2.

### PHYSICAL PROPERTIES

HEAT NO.	SLAB	YIELD PSI X 100	TENSILE PSI X 100	% ELONG 8" X 2"	% RA	HARDNESS BHN	BEND TEST	IMPACTS
2	1.5000 X 60.000 X 380.000 THE FOLLOWING PLATES WERE AUSTENITIZED AT 1680 DEGS F FOR 76 MINUTES AND WATER QUENCHED THEN TEMPERED AT 1130 DEGS F FOR 97 MINUTES AND AIR COOLED 1 PC 9699 LBS 00K4820 + 107878 E1	865	1010	60	LCVN @ -25	110 94	100/101	egy
4	2.3600 X 48.000 X 300.000 THE FOLLOWING PLATES WERE AUSTENITIZED AT 1700 DEGS F FOR 142 MINUTES AND WATER QUENCHED THEN TEMPERED AT 1100 DEGS F FOR 158 MINUTES AND AIR COOLED 1 PC 9638 LBS 00K4821 + 101136 A20	760	915	28	LCVN @ -10	122 120	114/119	egy
5	2.9500 X 48.000 X 240.000 THE FOLLOWING PLATES WERE AUSTENITIZED AT 1700 DEGS F FOR 177 MINUTES AND WATER QUENCHED THEN TEMPERED AT 1100 DEGS F FOR 179 MINUTES AND AIR COOLED 1 PC 9638 LBS 00K4822 + 103088 D20	860	1000	23				

### CHEMICAL ANALYSIS

HEAT NO.	C	Mn	P	S	Si	Cu	Ni	V	Cr	Mo	Ti	B	Nb	Ca	CE
+107878	.11	1.21	.007	.003	.38	.31	.28	.059	.033	.53	.04				
+101136	.09	1.23	.007	.004	.40	.31	.32	.058	.034	.52	.05				
+103088	.09	1.28	.006	.003	.40	.31	.30	.058	.037	.53	.06				
ALL HEATS INDICATED WITH (+) WERE MELTED AND MANUFACTURED IN THE USA.															

*Kristine Hummer*  
 KRISTINE HUMMER  
 Q.C. RECORDS ADMINISTRATOR

I certify the above to be correct as contained in the records of OREGON STEEL MILLS By \_\_\_\_\_



# OREGON STEEL MILLS

P.O. BOX 2760, Portland, Oregon 97208 • (503) 286-9651 Fax (503) 240-5288

## REPORT OF CHEMICAL/PHYSICAL TESTS

CERTIFICATE NO.	DATE	PAGE
623982	Oct 25, 2000	1
MILL ORDER NO.	DATE	
125073		
CUSTOMER ORDER NO.		
001619		
JOURNED NO.		
SHIPPING NO.	DATE	
623982	10/25/2000	
CARRIER		
MITCHELL BROS		
CONTRACT NO.		
TRU		

**SOLD TO**  
**THE FIRST**  
**ISO9002**  
**REGISTERED**  
**TO**  
**RECOGNIZED**  
**BY PLATE**

CHRISTIE CONSTRUCTORS, INC.  
 4925 SEAPORT AVE  
 RICHMOND, CA 94804

CHRISTIE CONSTRUCTORS, INC.  
 4925 SEAPORT AVE  
 RICHMOND, CA 94804

THIS MATERIAL HAS BEEN MANUFACTURED, TESTED AND FOUND TO MEET THE SPECIFICATIONS AND PURCHASE ORDER REQUIREMENTS  
 OSM HSLA STRUCTURAL QUALITY PLATE ASTM A709-00 GR 70W HPS-70W. KILLED FINE  
 GRAIN PRACTICE VACUUM DEGAUSED. REPORT ASTM G101 CORROSION INDEX. LCVN 35  
 FT/LBS AVG @ -10 F (P). FRACTURE-CRITICAL, F, ZONE 2

QUANTITY	DESCRIPTION	HEAT NO.	SLAB	YIELD PSI X 100	TENSILE PSI X 100	% ELONG IN 2"	% RA	HARDNESS BHN	BEND TEST	IMPACTS
1	1.0000 X 88.000 X 148.000 THE FOLLOWING PLATES WERE ALUSTENITIZED AT 1680 DEGS F FOR 51 MINUTES AND WATER QUENCHED THEN TEMPERED AT 1200 DEGS F FOR 67 MINUTES AND AIR COOLED 1 PC 3694 LBS 99M0678 + 101134 H1 1 PCS 3694 LBS TOTALS CORROSION INDEX = 6.63									
										LCVN @ -25 DEG F 10.0mm 114 114 139/122 epy

CHEMICAL ANALYSIS											
HEAT NO.	C	Mn	P	S	Si	Cu	Ni	V	Cr	Mo	Ca
+101134	.11	1.27	.007	.003	.40	.30	.30	.057	.031	.52	.05
ALL HEATS INDICATED WITH (+) WERE MELTED AND MANUFACTURED IN THE USA.											
.....	END OF REPORT										

I certify the above to be correct as contained in the records of OREGON STEEL MILLS By *[Signature]*  
 KRISTINE HONWORK  
 OREGON STEEL MILLS

**OREGON STEEL MILLS**

P.O. BOX 2760, Portland, Oregon 97208 • (503) 286-9651 Fax (503) 240-5288

**REPORT OF CHEMICAL/PHYSICAL TESTS**

CERTIFICATE NO. 623983 DATE Oct 25, 2000 PAGE 1

	CHRISTIE CONSTRUCTORS, INC. 4925 SEAPORT AVE RICHMOND, CA 94804	CHRISTIE CONSTRUCTORS, INC. 4925 SEAPORT AVE RICHMOND, CA 94804	MILL ORDER NO. 125074 DATE ORDER NUMBER 001619 ORDER NO.	SHIPPING NO. 623983 DATE 10/25/2000
---	---	---	---	--

THIS MATERIAL HAS BEEN MANUFACTURED, TESTED AND FOUND TO MEET THE SPECIFICATIONS AND PURCHASE ORDER REQUIREMENTS OSM HSLA STRUCTURAL QUALITY PLATE ASTM A709-00 GR 70W HPS-70W. KILLED FINE GRAIN FRACTURE VACUUM DEGASSED. REPORT ASTM G101 CORROSION INDEX. LCVN 35 FT/LBS AVG @ -10 F (P). FRACTURE-CRITICAL, F, ZONE 2.

HEAT NO.	DESCRIPTION	HEAT NO.	SLAB	YIELD PSI X 100	TENSILE PSI X 100	% ELONG IN 2"	% RA	HARDNESS BHN	BEND TEST	IMPACTS
1	1.1800 X 48.000 X 600.000 THE FOLLOWING PLATES WERE ALSTENITIZED AT 1660 DEGS F FOR 60 MINUTES AND WATER QUENCHED THEN TEMPERED AT 1130 DEGS F FOR 73 MINUTES AND AIR COOLED 1 PC 9636 LBS 00K3053 + 107878 H3			775	965	52		LCVN @ -10	DEG F 10.0mm	88 98 83 /90 egy
3	1.9700 X 62.000 X 276.000 THE FOLLOWING PLATES WERE ALSTENITIZED AT 1660 DEGS F FOR 119 MINUTES AND WATER QUENCHED THEN TEMPERED AT 1130 DEGS F FOR 120 MINUTES AND AIR COOLED 1 PC 9560 LBS 00K3054 + 107878 H2			760	930	60		LCVN @ -10	DEG F 10.0mm	120 103 124/116 egy
2 PCS 19198 LBS TOTALS										

CHEMICAL ANALYSIS																
HEAT NO.	C	Mn	P	S	SI	CU	NI	V	CB	AL	CR	MO	TI	B	Ni	CE
+107878	.11	1.21	.007	.003	.38	.31	.28	.059	<.008	.033	.53	.04				
ALL HEATS INDICATED WITH (+) WERE MELTED AND MANUFACTURED IN THE USA.																
END OF REPORT																

I certify the above to be correct as contained in the records of OREGON STEEL MILLS BY John A. Smith CRISTINE HUNTWORK Q.C. RECORDS ADMINISTRATOR

# OREGON STEEL MILLS

P.O. BOX 2760, Portland, Oregon 97208 • (503) 286-9651 Fax (503) 240-6568



**SOLD TO**

OREGON STEEL MILLS - LAMPROS STEEL  
PO BOX 2760  
PORTLAND, OR 97208

LAMPROS STEEL  
8524 N. CRAWFORD  
PORTLAND, OR 97203

## REPORT OF CHEMICAL/PHYSICAL TESTS

CERTIFICATE NO.	DATE	PAGE
721127	Aug 23, 2002	1
MILL ORDER NO.	DATE	
147806		
CUSTOMER ORDER NO.		
UNIVERSITY OF RENNO		
JOURNAL NO.		
SHIPPING NO.	DATE	
721127	08/23/2002	
CARRIER		
GREEN TRANSFER		
CAVITRUCK NO.		
TR1.		

THIS MATERIAL HAS BEEN MANUFACTURED, TESTED AND FOUND TO MEET THE SPECIFICATIONS AND PURCHASE ORDER REQUIREMENTS  
OSK HSLA STRUCTURAL QUALITY PLATE ASTM A709-00A GRADE HPS-70M. VACUUM DEGASSED.

### PHYSICAL PROPERTIES

HEAT NO.	SLAB	YIELD PSI X 100	TENSILE % ELONG PSI X 100	% RA	HARDNESS BHN	BEND TEST	IMPACTS
1	1.3780 X 84.0000 X 340.000 HEAT #117366E2 HT#02F0717 SIZE SUBSTITUTION + 117366 E2 THE FOLLOWING PLATES WERE AUTENTIZED AT 1680 DEGS F FOR 84 MINUTES AND WATER QUENCHED THEN TEMPERED AT 1140 DEGS F FOR 94 MINUTES AND AIR COOLED 1 PC 11163 LBS 02F0717 + 117366 E2 1 PCS 11163 LBS TOTALS	8	1.3780 X 84.0000 X 340.000 (1 PC ONLY)	1.3780 X 84.0000 X 340.000 (1 PC ONLY)	340.000		

### CHEMICAL ANALYSIS

HEAT NO.	C	Mn	P	S	Si	Cu	N	V	Cr	Al	Mo	Ti	B	Ni	Ca	CE
117366	.08	1.13	.008	.002	.34	.30	.29	.053	.021	.024	.47	.04		.0055		
HEATS INDICATED WITH (+) WERE MELTED & MANUFACTURED IN THE USA. ALL OTHER HEATS WERE ROLLED IN THE USA.																
END OF REPORT																

I certify the above to be correct as contained in the records of OREGON STEEL MILLS By Angie McCalister





新日本製鋼所株式会社  
Nippon Steel Corporation

鋼材検査証明書  
INSPECTION CERTIFICATE

注文書: HORISHA  
SHIPPING MARK: 鋼材検査  
REFERENCE No.: 000  
CONTRACT No.: 0-280-011-3-2-0302  
品名: STEEL PLATE  
仕様書: ST-HY4400 (SA4400)  
文書番号: 01

本社: 〒106-8071 東京都千代田区大塚二丁目5番3号  
HEAD OFFICE: 2-5-3, OHSUMI, OHTSUKA, SAIYAMA-KU, TOKYO 106-8071, JAPAN  
東京営業所: 〒104-1141 千葉県千葉市若葉区津田3番5号  
KANTO OFFICE: 3-5-5, TSUDA, KAMETAMA-CITY, CHIBA-KEN, 104-1141, JAPAN  
検査番号: Y-4D17B PAGE: 1  
発行年月日: 2003-04-02

寸法 DIMENSIONS	鋼種 GRADE	鋼種番号 CASTING	検査番号 TEST NO.	検査結果 TEST RESULT	化学成分 CHEMICAL COMPOSITION		機械試験 MECHANICAL TEST		引張試験 TENSILE TEST		衝撃試験 IMPACT TEST		表面検査 SURFACE TEST	
					C	Mn	P	S	σ <sub>b</sub>	σ <sub>s</sub>	ε	α <sub>k</sub>	Y <sub>2</sub>	Y <sub>1</sub>
28X1000X3000	01	471	04133	13905011106	0.11	0.52	38	706	11	266	17	70	70	70
30X1000X3000	02	286	31647	13805020106	0.07	0.68	26	74	11	247	17	70	70	

検査項目: 化学成分, 機械試験, 引張試験, 衝撃試験, 表面検査  
検査結果: 合格  
検査場所: 新日本製鋼所株式会社 検査部  
検査員: A. Date  
検査日: 2003年4月2日



A. Date  
検査部長  
INSPECTION SUPERVISOR  
KANTO WORKS





Laboratory No. R573

**TENSILE TESTS**

Date: 10-26-00

Page 1 of 3

Client No.

P.O. No.: 1333725

Project: University of Reno

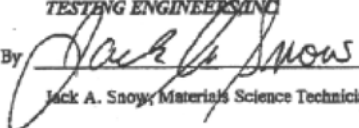
Description or Mark Identification	14mm	22mm			Specified Min. Requirement
	#1	#2			
Actual Dimensions, Ins.	0.505	0.505			
Actual Area, Sq. Ins.	0.200	0.200			
Yield Point, Lbs.	10040	10560			
Maximum Load, Lbs.	14770	15730			
Yield Strength, Lbs. Per Sq. In.	50200	52800			
Tensile Strength Lbs. Per Sq. In.	73900	78700			
Elongation In 2 Inches	0.64	0.60			
Elongation, Percent	32%	30%			
Reduction of Area, Percent	75%	71%			
Fracture	Cup cone	Cup cone			
Modulus of Elasticity, PSI	27,800,000	27,200,000			

Remarks: Yield @ 0.2 % Offset  
Machined and tested in accordance with ASTM A370.

Results Reported To: Dr. Itani

TESTING ENGINEERS, INC.

By

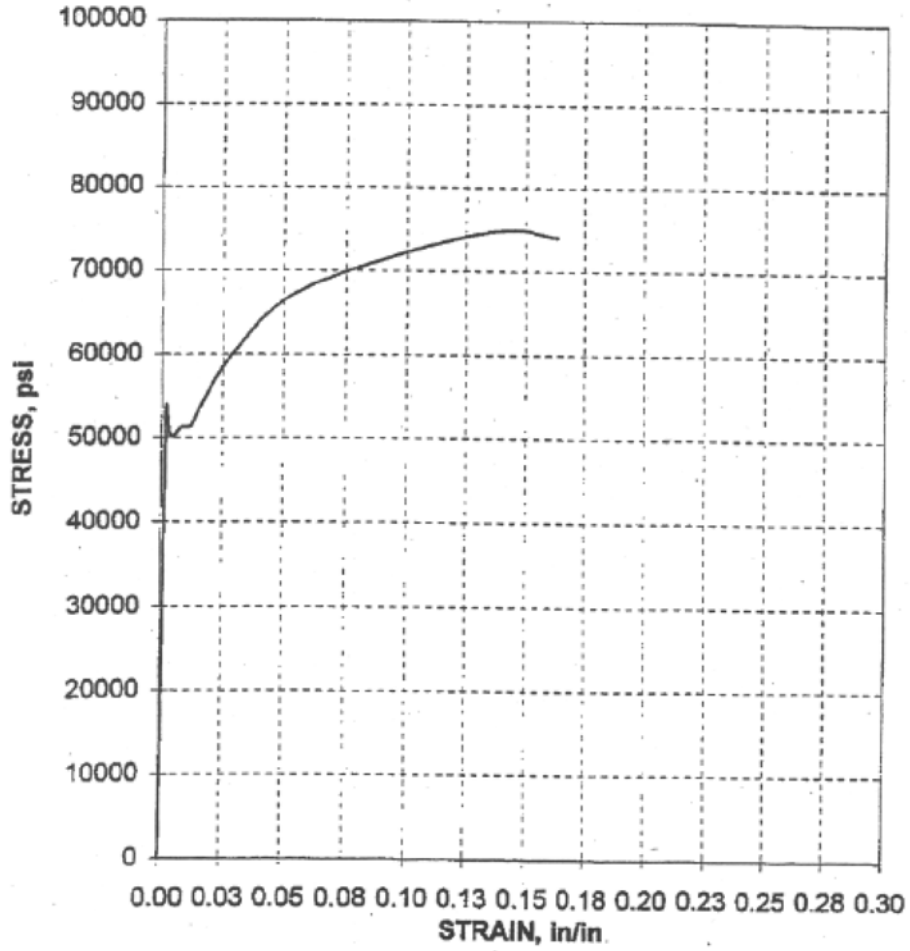
  
Jack A. Snow, Materials Science Technician

MSL 859

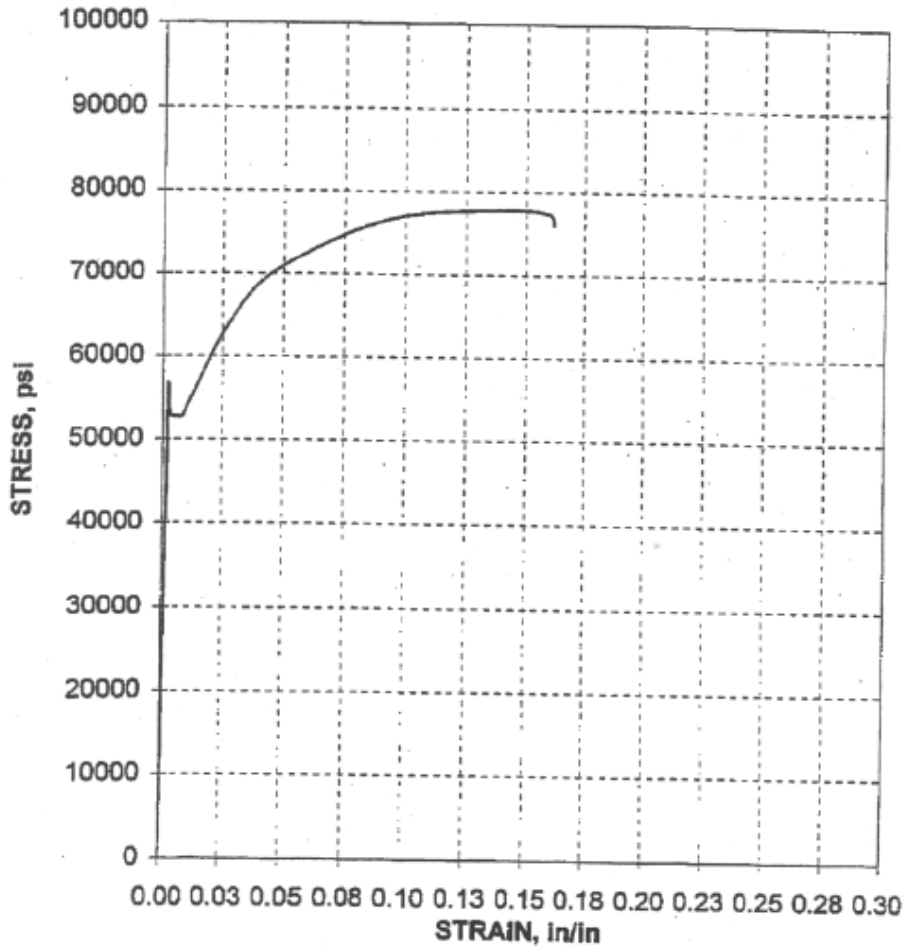
The results presented in this report relate only to the item(s) tested.  
This report can be reproduced only in its entirety unless written permission from TEI is obtained.  
Samples pertaining to this report will be discarded 30 days from the date of this report unless otherwise advised.

Copyright © 1999 MSL, Patent MSL, Patent Pending MSL, Inc. 01/00

**Graph 1**  
**Stress Strain Curve**  
**14MM Plate**



**Graph 2**  
**Stress Strain Curve**  
**22MM Plate**



# Christie Constructors, Inc.

4925 Seaport Avenue  
 Richmond, CA 94804  
 (510)215-4820  
 Fax (510) 236-0586

California License No. 237587

Date:	December 14, 2000
Attn:	Chia Ming Uang
Re:	SPOBD Shear Link Test
Contract #	
Subject:	Procedure Qualification Record(s)

TO:

University of California, San Diego  
 Department of Structural Engineering  
 LaJolla, CA 92093-0085 / 3  
 Fax 12/14/00 1-858-534-6373 (3 pages)  
 UNR Fax 1-775-784-1390

Gentlemen:

We are sending you: Christie Constructors' Procedure Qualification Record(s)  
 Shop Drawings  Attached  
 Copy of Letter  Prints  
 Specifications  Change Order

Copies	Date	No.	Description
One	11/27/00	WPS111280	Welding Procedure Specification, Procedure No. 111280 Plate up to 1 1/2"
			Material Spec. ASTM A709 GR 70/HPS-70W, 30mm
			Welding Process FCAW, Filler Metal E91T1-G, Position 1G
	12/13/00	CCI 111280	Consolidated Engineering Laboratories
			Procedure Qualification Record-CCI 111280
			Welding Process FCAW, AWS Classification E91T1-G, Position 1G
			Material Spec. ASTM A709 GR 485W (HPS 485W)
	11/27/00	WPS111281	Welding Procedure Specification, Procedure No. 111281 Plate 1 1/2" & up
			Material Spec. ASTM A709 GR 70/HPS-70W, 30mm
			Welding Process FCAW, Filler Metal E91T1-G, Position 1G
	12/13/00	CCI 111281	Consolidated Engineering Laboratories
			Procedure Qualification Record-CCI 111281
			Welding Process FCAW, AWS Classification E91T1-G, Position 1G
			Material Spec. ASTM A709 GR 485W (HPS 485W)

For your use  Approved as noted  
 As Requested  Return for corrections  
 For review and comment  Resubmittal  
 For Approval  For information as requested

Remarks:

Attached are the WPS(s) and PQR(s) test results for welding of the HPS 70W material for approval. It is noted that PQR CCI 111281 indicates an unsatisfactory RT result. However the mechanical test results all indicate satisfactory results. The deficiencies in the RT results were minor and localized at the root and did not effect the mechanical tests. The deficiencies were not detectable using UT testing and macroetch tests indicated they were very minor in nature. Upon approval from UCSD/UNR and Caltrans welding will commence on the Built-up Shear Link Specimen and the UNR work.

Copy to: Dr. A. Ilani (UNR), L. Pyle

Signed:

*W.A. Sellberg*  
 William A. Sellberg, Sales Manager

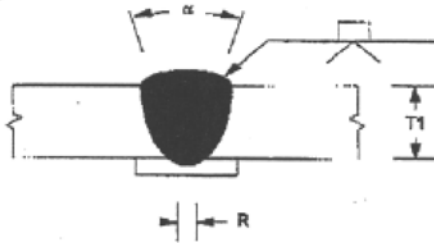


CHRISTIE CONSTRUCTORS INC  
WELDING PROCEDURE SPECIFICATION

Page 2 of 2  
111280

Joint Detail

Single-V-groove weld (2)  
Butt joint (B)



Welding Process	Joint Designation	Base Metal Thickness (Unlimited)		Groove Preparation				Permitted Welding Positions	Gas Shielding for FCAW	Notes	
		T1	T2	Root Opening	Groove Angle	Tolerances					
						As Detailed (see 3.13.1)	As Fit Up (see 3.13.1)				
GMAW FCAW	B-U2a-GF	U	-	R = 3/16	$\alpha = 30^\circ$	R = +1/16, -0	+1/4, -1/16	F,V,OH	Required	A N	
				R = 3/8	$\alpha = 30^\circ$			$\alpha = +10^\circ, -0^\circ$	F,V,OH		Not req.
				R = 1/4	$\alpha = 45^\circ$			+10°, -5°	F,V,OH		Not req.

MEMO

SEE AWS D1.5 / 96, SECTION 12.  
USE FOR PLATE UP TO 1 1/2" THICKNESS

Per AWS D1.5

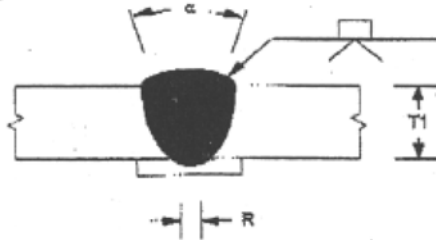


CHRISTIE CONSTRUCTORS INC  
WELDING PROCEDURE SPECIFICATION

Page 2 of 2  
111281

Joint Detail

Single-V-groove weld (2)  
Butt Joint (B)



Welding Process	Joint Designation	Base Metal Thickness (Unlimited)		Groove Preparation				Permitted Welding Positions	Gas Shielding for FCAW	Notes		
		T1	T2	Root Opening	Groove Angle	Tolerances						
						As Detailed (see 3.13.1)	As Fit Up (see 3.13.1)					
GMAW FCAW	B-U2a-G#	U	-	R = 3/16	$\alpha = 30^\circ$	R = +1/16, -0	+1/4, -1/16	F,V,OH	Required	A N		
				R = 3/8	$\alpha = 30^\circ$			$\alpha = +10^\circ, -0^\circ$	$+10^\circ, -5^\circ$		F,V,OH	Not req.
				R = 1/4	$\alpha = 45^\circ$						F,V,OH	Not req.

MEMO

SEE AWS D1.5 / 96, SECTION 12.  
USE FOR PLATE 1 1/2" AND UP.

Per AWS D1.5



CONSOLIDATED ENGINEERING  
LABORATORIES

CHRISTIE CONSTRUCTORS, INC.

Procedure Qualification Record

00111288

PCR No. <u>CC111288</u> Revision <u>0</u> Date <u>12/13/2009</u> by <u>THOMAS E. DICKSON</u> Authorized By _____ Date <u>12/22/2009</u> Type Manual <input type="checkbox"/> Machine <input type="checkbox"/> Welding Process(es) <u>ECM</u> Reference WPS No. <u>EC1-018 EC</u> Semi-Auto <input checked="" type="checkbox"/> Auto <input type="checkbox"/>	
<b>JOINT</b> Type <u>SINGLE V - CJP FIG. 8.1</u> Backing Yes <input checked="" type="checkbox"/> No <input type="checkbox"/> Single Weld <input checked="" type="checkbox"/> Double Weld <input type="checkbox"/> Backing Material <u>A709 - 48RW</u> Root Opening <u>1/8</u> Root Face Dimension <u>0</u> Groove Angle <u>20 DEG</u> Radius (J-U) <u>ns</u> Beak Gauging Yes <input type="checkbox"/> No <input checked="" type="checkbox"/> Method <u>ns</u>	<b>WITNESS LOT #B4831A</b> 
<b>BASE METALS</b> Material Spec. <u>A572GR</u> to <u>A709</u> Type or Grade <u>A572 (MS) 48RW</u> to <u>48RW</u> Thickness: Groove (mm) <u>3/8</u> Fillet ( ) _____ Diameter (Pipe, ) _____	<b>POSITION</b> Position of Groove <u>1G</u> Fillet _____ Vertical Progression: Up <input type="checkbox"/> Down <input type="checkbox"/> <b>ELECTRICAL CHARACTERISTICS</b> Transfer Mode (GMAW): Short-Circuiting <input type="checkbox"/> Globular <input type="checkbox"/> Spray <input type="checkbox"/> Current: AC <input type="checkbox"/> OCEP <input checked="" type="checkbox"/> DCEN <input type="checkbox"/> Pulse <input type="checkbox"/> Other <u>CONSTANT VOLTAGE</u> Tungsten Electrode (GTAW): Size <u>1/8</u> Type <u>ns</u>
<b>FILLER METALS</b> AWS Specification <u>A5.9</u> <u>ER70S-6</u> <u>ER70S-6</u> AWS Classification <u>E70T-6</u> <u>E70T-6</u>	<b>TECHNIQUE</b> Stringer or Weave Bead <u>STRINGER</u> Multi-pass or Single Pass (per side) <u>MULTIPLE</u> Number of Electrodes <u>1</u> Electrode Spacing: Longitudinal <u>ns</u> Lateral <u>ns</u> Angle <u>ns</u> Contact Tube to Work Distance <u>12.7-16mm</u> Peening <u>NONE</u> Interpass Cleaning <u>WIRE BRUSH / SLAG PICK</u>
<b>SHIELDING</b> Flux Gas <u>AR / CO2</u> SR _____ Composition <u>ZR / ZS</u> Electrode-Flux (Class) Flow Rate <u>27 CFH</u> SR _____ Gas Cup Size <u>15.8 mm</u>	
<b>PREHEAT</b> Preheat Temp., Min. <u>149 C</u> Interpass Temp., Min. <u>149 C</u> Max. <u>232 C</u>	
<b>POSTWELD HEAT TREATMENT</b> Required <input type="checkbox"/> Temp. <u>ns</u> Time _____	



**CHRISTIE CONSTRUCTORS, INC.**  
Procedure Qualification Record

Page 2 of 3

COI 111280

**TEST RESULTS**  
**TENSILE TEST**

Specimen no.	Width	Thickness	Area	Ultimate tensile load, lb	Ultimate unit stress, psi	Character of failure and location
1	24.1	29.86	719.4	594,899 N	742 MPa	BASE / DUCTILE
2	26.7	29.72	783.8	558,478 N	721 MPa	BASE / DUCTILE

**GUIDED BEND TEST**

Specimen no.	Type of bend	Result	Remark
1	SIDE	SATISFACTORY	5,19.2
2	SIDE	SATISFACTORY	
3	SIDE	SATISFACTORY	
4	SIDE	SATISFACTORY	

**VISUAL INSPECTION**

Appearance SATISFACTORY  
Undercut NONE  
Piping porosity NONE  
Convexity N/A  
Test date 11/28/2008  
Witnessed by MARK WANGZYHAK, GWI

**Other Test**

WELD CVN @ -30 C (J) 81", 81, 83, 84, 92" = 83 AVE. RADIOGRAPHY WAS WITNESSED BY K CARPENTER ON 11/29/00, 86176. TRANSVERSE BEND & TENSION TESTS WITNESSED BY R. VATCHER, 88808 ON 12/4/00. CVN WITNESSED BY R. VATCHER ON 12/11/00, 88811. AWWT WITNESSED BY H. BOYLES, 87021.

**Radiographic-ultrasonic examination**

RT report no: 4186 Result SATISFACTORY  
UT report no: N/A Result N/A

**FILLET WELD TEST RESULTS**

Minimum plate multiple pass	Medium size single pass
Macroetch	Macroetch
1. <u>N/A</u> 3. <u>N/A</u>	1. <u>N/A</u> 3. <u>N/A</u>
2. <u>N/A</u>	2. <u>N/A</u>

**AS-weld-metal tension test**

Tensile strength, psi 786 MPa  
Yield point strength, psi 748 MPa  
Elongation in 2 in., % 21  
Laboratory test no. (7E)

Welder's name BRAD DUNCAN

Clock no. 553-70481Z Stamp no. \_\_\_\_\_

Test conducted by [Signature] Laboratory \_\_\_\_\_

Test number MS-11928 Per ASME D1.8-98

We, the undersigned, certify that the statements herein are correct and that the test welds were prepared, welded, and tested in accordance with the requirements of sections 5-6.1.2 of ANSI/AASHTO/MWS D1.8-98 - Bridge Welding Code, and the requirements of the Special Provisions of Contract # 04-012011.

Manufacturer CHRISTIE CONSTRUCTORS, INC. By \_\_\_\_\_ Date \_\_\_\_\_  
Title \_\_\_\_\_

**CHRISTIE CONSTRUCTORS, INC.**  
Procedure Qualification Record

WELDING PROCEDURE								
Layer/Pass	Process	Filler Metal Class	Diameter	Cut. Type	Amps or WPS	Volts	Travel Speed	Other Notes
1	FCAW	E81T1-G	0.045"	DCEP	240	27.4	305 in/min	
2	FCAW	E81T1-G	0.045"	DCEP	232	27.4	349	
3	FCAW	E81T1-G	0.045"	DCEP	232	27.4	349	
4	FCAW	E81T1-G	0.045"	DCEP	232	27.4	408	
5	FCAW	E81T1-G	0.045"	DCEP	232	27.4	359	
6	FCAW	E81T1-G	0.045"	DCEP	232	27.4	381	
7	FCAW	E81T1-G	0.045"	DCEP	232	27.4	406	
8	FCAW	E81T1-G	0.045"	DCEP	232	27.4	321	
9	FCAW	E81T1-G	0.045"	DCEP	232	27.4	407	
10	FCAW	E81T1-G	0.045"	DCEP	232	27.4	407	
11	FCAW	E81T1-G	0.045"	DCEP	232	27.4	339	
12	FCAW	E81T1-G	0.045"	DCEP	232	27.4	350	
13	FCAW	E81T1-G	0.045"	DCEP	232	27.4	407	
14	FCAW	E81T1-G	0.045"	DCEP	232	27.4	407	
15	FCAW	E81T1-G	0.045"	DCEP	232	27.4	339	
16	FCAW	E81T1-G	0.045"	DCEP	232	27.4	407	
17	FCAW	E81T1-G	0.045"	DCEP	232	27.4	437	
18	FCAW	E81T1-G	0.045"	DCEP	232	27.4	358	
19	FCAW	E81T1-G	0.045"	DCEP	232	27.4	407	
20	FCAW	E81T1-G	0.045"	DCEP	232	27.4	339	
21	FCAW	E81T1-G	0.045"	DCEP	232	27.4	339	
22	FCAW	E81T1-G	0.045"	DCEP	232	27.4	407	
					232 AVE.	27.4	374 AVE.	1.02 kJ/mm



CONSOLIDATED ENGINEERING LABORATORIES

CHRISTIE CONSTRUCTORS, INC. Procedure Qualification Record

PQR No. <u>CCI 11281</u> Revision <u>0</u> Date <u>12/13/2000</u> by <u>THOMAS E. DICKSON</u> Authorized By _____ Date <u>12/13/2000</u> Type Manual <input type="checkbox"/> Machine <input type="checkbox"/> Welding Process(es) <u>FC-MW</u> Reference WPS No. <u>633-010-1-FC</u> Semi-Auto <input checked="" type="checkbox"/> Auto <input type="checkbox"/>	
<b>JOINT</b> Type <u>SINGLE V - GJP FIG. 6-1</u> Backing Yes <input checked="" type="checkbox"/> No <input type="checkbox"/> Single Weld <input checked="" type="checkbox"/> Double Weld <input type="checkbox"/> Backing Material <u>A709 - 50BW</u> Root Opening <u>18</u> Root Face Dimension <u>0</u> Groove Angle <u>30 DEG</u> Radius (J-U) <u>0</u> Back Gauging Yes <input type="checkbox"/> No <input checked="" type="checkbox"/> Method <u>08</u>	<b>WITNESS LOT #04832</b> 
<b>BASE METALS</b> Material Spec. <u>A572/A709</u> to <u>A709</u> Type or Grade <u>A572/A709 50BW</u> to <u>A572/A709</u> Thickness: Groove (mm) <u>28</u> Fillet ( ) _____ Diameter (Pipe, ) _____	<b>POSITION</b> Position of Groove <u>1B</u> Fillet _____ Vertical Progression: Up <input type="checkbox"/> Down <input type="checkbox"/>
<b>FILLER METALS</b> AWS Specification <u>A5.29</u> <u>ER60S2-DUAL SHIELD</u> AWS Classification <u>ER60S2-D</u> <u>E101H5P</u>	<b>ELECTRICAL CHARACTERISTICS</b> Transfer Mode (GMAW): Short-Circuiting <input type="checkbox"/> Globular <input type="checkbox"/> Spray <input type="checkbox"/> Current: AC <input type="checkbox"/> DCEP <input checked="" type="checkbox"/> DCEN <input type="checkbox"/> Pulsed <input type="checkbox"/> Other <u>CONSTANT VOLTAGE</u> Tungsten Electrode (GTAW): Size <u>08</u> Type <u>08</u>
<b>SHIELDING</b> Flux _____ Gas <u>AR/CO2</u> nr _____ Composition <u>78/22</u> Electrode-Flux (Class) _____ Flow Rate <u>37 CFH</u> ml _____ Gas Cup Size <u>3/8 RSP</u>	<b>TECHNIQUE</b> Stringer or Weave Bead <u>STRINGER</u> Multi-pass or Single Pass (per side) <u>MULTIPLE</u> Number of Electrodes <u>1</u> Electrode Spacing: Longitudinal <u>08</u> Lateral <u>08</u> Angle <u>08</u> Contact Tube to Work Distance <u>12.7 - 19mm</u> Peening <u>NONE</u> Interpass Cleaning <u>WIRE BRUSH / SLAG PICK</u>
<b>PREHEAT</b> Preheat Temp., Min. <u>149 C</u> Interpass Temp., Min. <u>149 C</u> Max. <u>232 C</u>	<b>POSTWELD HEAT TREATMENT</b> Required <input type="checkbox"/> Temp. <u>08</u> Time _____

**CHRISTIE CONSTRUCTORS, INC.**  
Procedure Qualification Record

TEST RESULTS						
TENSILE TEST						
Specimen no.	Width	Thickness	Area	Ultimate tensile load, lb	Ultimate unit stress, psi	Character of failure and location
1	26.94	37.26	932.49	674,899 N	733 MPa	BASE / DUCTILE
2	26.1	37.82	944.26	679,070 N	718 MPa	BASE / DUCTILE
				635-760 MPa		

GUIDED BEND TEST			
Specimen no.	Type of bend	Result	REMARK
1	SIDE	SATISFACTORY	S-19.3
2	SIDE	SATISFACTORY	
3	SIDE	SATISFACTORY	
4	SIDE	SATISFACTORY	

<p><b>VISUAL INSPECTION</b></p> <p>Appearance <u>SATISFACTORY</u></p> <p>Undercut <u>NONE</u></p> <p>Piping porosity <u>NONE</u></p> <p>Convexity <u>N/A</u></p> <p>Test date <u>11/28/2009</u></p> <p>Witnessed by <u>MARK WARCZYNSKI, CMI</u></p> <p>Other Test</p> <p>WELD CVN @ -30 C (J) 111, 114, 120, 128, 133" = 121 AVE. RADIOGRAPHY WAS WITNESSED BY K CARPENTER ON 11/22/00, 88174. TRANSVERSE BEND &amp; TENSION TESTS WITNESSED BY R. VATCHER, 85608 ON 12/8/00. CVN &amp; ANMT WITNESSED BY R. VATCHER ON 12/11/00, 85609.</p>	<p><b>Radiographic-ultrasonic examination</b></p> <p>RT report no: <u>4195</u> Result <u>UNSATISFACTORY</u></p> <p>UT report no: <u>N/A</u> Result <u>N/A</u></p> <p style="text-align: center;"><b>FILLET WELD TEST RESULTS</b></p> <table style="width: 100%;"> <tr> <td>Minimum size multiple pass</td> <td>Maximum size single pass</td> </tr> <tr> <td>Macroetch</td> <td>Macroetch</td> </tr> <tr> <td>1. <u>N/A</u> 3. <u>N/A</u></td> <td>1. <u>N/A</u> 3. <u>N/A</u></td> </tr> <tr> <td>2. <u>N/A</u></td> <td>2. <u>N/A</u></td> </tr> </table> <p><b>As-weld-metal tension test</b></p> <p>Tensile strength, psi <u>783 MPa</u></p> <p>Yield point strength, psi <u>743 MPa</u></p> <p>Elongation in 2 in., % <u>26</u></p> <p>Laboratory test no. <u>8888 (X2)</u></p>	Minimum size multiple pass	Maximum size single pass	Macroetch	Macroetch	1. <u>N/A</u> 3. <u>N/A</u>	1. <u>N/A</u> 3. <u>N/A</u>	2. <u>N/A</u>	2. <u>N/A</u>
Minimum size multiple pass	Maximum size single pass								
Macroetch	Macroetch								
1. <u>N/A</u> 3. <u>N/A</u>	1. <u>N/A</u> 3. <u>N/A</u>								
2. <u>N/A</u>	2. <u>N/A</u>								

Welder's name BRAD DUNCAN Clock no. 663-704817 Stamp no. \_\_\_\_\_

Test conducted by Thomas E. Nichols Laboratory \_\_\_\_\_

Test number NS-11638 Per ANSI D1.5-96



We, the undersigned, certify that the statements in this report are correct and that the test welds were prepared, welded, and tested (with the exception of failed RT) in accordance with the requirements of sections 5 & 12 of ANSI/AASHTO/AWS D1.5-08 - Bridge Welding Code, and the requirements of the Special Provisions of Contract # 04-012011.

Manufacturer CHRISTIE CONSTRUCTORS INC. By \_\_\_\_\_ Date \_\_\_\_\_

Title \_\_\_\_\_

**CHRISTIE CONSTRUCTORS, INC.**  
Procedure Qualification Record

WELDING PROCEDURE							
Layer/Pass	Process	Filler Metal Class	Diameter	Cur. Type	Amps or WFS	Volts	Travel Speed Other Notes
1	FCAW	E91T1-G	0.046"	DCEP	240	27.4	306 mm/min
2	FCAW	E91T1-G	0.045"	DCEP	232	27.4	321
3	FCAW	E91T1-G	0.045"	DCEP	232	27.4	407
4	FCAW	E91T1-G	0.045"	DCEP	232	27.4	381
5	FCAW	E91T1-G	0.045"	DCEP	232	27.4	321
6	FCAW	E91T1-G	0.046"	DCEP	232	27.4	407
7	FCAW	E91T1-G	0.045"	DCEP	232	27.4	348
8	FCAW	E91T1-G	0.045"	DCEP	232	27.4	306
9	FCAW	E91T1-G	0.045"	DCEP	232	27.4	306
10	FCAW	E91T1-G	0.045"	DCEP	232	27.4	348
11	FCAW	E91T1-G	0.045"	DCEP	200	27.4	407
12	FCAW	E91T1-G	0.045"	DCEP	232	27.4	381
13	FCAW	E91T1-G	0.045"	DCEP	232	27.4	407
14	FCAW	E91T1-G	0.045"	DCEP	232	27.4	438
15	FCAW	E91T1-G	0.045"	DCEP	232	27.4	330
16	FCAW	E91T1-G	0.045"	DCEP	232	27.4	407
17	FCAW	E91T1-G	0.045"	DCEP	232	27.4	407
18	FCAW	E91T1-G	0.045"	DCEP	232	27.4	339
19	FCAW	E91T1-G	0.045"	DCEP	232	27.4	407
20	FCAW	E91T1-G	0.045"	DCEP	232	27.4	508
21	FCAW	E91T1-G	0.045"	DCEP	232	27.4	407
22	FCAW	E91T1-G	0.045"	DCEP	232	27.4	407
23	FCAW	E91T1-G	0.045"	DCEP	232	27.4	407
24	FCAW	E91T1-G	0.045"	DCEP	232	27.4	328
25	FCAW	E91T1-G	0.045"	DCEP	232	27.4	306
26	FCAW	E91T1-G	0.045"	DCEP	232	27.4	407
27	FCAW	E91T1-G	0.045"	DCEP	232	27.4	610
28	FCAW	E91T1-G	0.045"	DCEP	232	27.4	566
29	FCAW	E91T1-G	0.045"	DCEP	232	27.4	671
					232 AVE.		407 AVE. 0.94 kJ/mm

## **Multidisciplinary Center for Earthquake Engineering Research List of Technical Reports**

The Multidisciplinary Center for Earthquake Engineering Research (MCEER) publishes technical reports on a variety of subjects related to earthquake engineering written by authors funded through MCEER. These reports are available from both MCEER Publications and the National Technical Information Service (NTIS). Requests for reports should be directed to MCEER Publications, Multidisciplinary Center for Earthquake Engineering Research, State University of New York at Buffalo, Red Jacket Quadrangle, Buffalo, New York 14261. Reports can also be requested through NTIS, 5285 Port Royal Road, Springfield, Virginia 22161. NTIS accession numbers are shown in parenthesis, if available.

- NCEER-87-0001 "First-Year Program in Research, Education and Technology Transfer," 3/5/87, (PB88-134275, A04, MF-A01).
- NCEER-87-0002 "Experimental Evaluation of Instantaneous Optimal Algorithms for Structural Control," by R.C. Lin, T.T. Soong and A.M. Reinhorn, 4/20/87, (PB88-134341, A04, MF-A01).
- NCEER-87-0003 "Experimentation Using the Earthquake Simulation Facilities at University at Buffalo," by A.M. Reinhorn and R.L. Ketter, to be published.
- NCEER-87-0004 "The System Characteristics and Performance of a Shaking Table," by J.S. Hwang, K.C. Chang and G.C. Lee, 6/1/87, (PB88-134259, A03, MF-A01). This report is available only through NTIS (see address given above).
- NCEER-87-0005 "A Finite Element Formulation for Nonlinear Viscoplastic Material Using a Q Model," by O. Gyebe and G. Dasgupta, 11/2/87, (PB88-213764, A08, MF-A01).
- NCEER-87-0006 "Symbolic Manipulation Program (SMP) - Algebraic Codes for Two and Three Dimensional Finite Element Formulations," by X. Lee and G. Dasgupta, 11/9/87, (PB88-218522, A05, MF-A01).
- NCEER-87-0007 "Instantaneous Optimal Control Laws for Tall Buildings Under Seismic Excitations," by J.N. Yang, A. Akbarpour and P. Ghaemmaghami, 6/10/87, (PB88-134333, A06, MF-A01). This report is only available through NTIS (see address given above).
- NCEER-87-0008 "IDARC: Inelastic Damage Analysis of Reinforced Concrete Frame - Shear-Wall Structures," by Y.J. Park, A.M. Reinhorn and S.K. Kunnath, 7/20/87, (PB88-134325, A09, MF-A01). This report is only available through NTIS (see address given above).
- NCEER-87-0009 "Liquefaction Potential for New York State: A Preliminary Report on Sites in Manhattan and Buffalo," by M. Budhu, V. Vijayakumar, R.F. Giese and L. Baumgras, 8/31/87, (PB88-163704, A03, MF-A01). This report is available only through NTIS (see address given above).
- NCEER-87-0010 "Vertical and Torsional Vibration of Foundations in Inhomogeneous Media," by A.S. Veletsos and K.W. Dotson, 6/1/87, (PB88-134291, A03, MF-A01). This report is only available through NTIS (see address given above).
- NCEER-87-0011 "Seismic Probabilistic Risk Assessment and Seismic Margins Studies for Nuclear Power Plants," by Howard H.M. Hwang, 6/15/87, (PB88-134267, A03, MF-A01). This report is only available through NTIS (see address given above).
- NCEER-87-0012 "Parametric Studies of Frequency Response of Secondary Systems Under Ground-Acceleration Excitations," by Y. Yong and Y.K. Lin, 6/10/87, (PB88-134309, A03, MF-A01). This report is only available through NTIS (see address given above).
- NCEER-87-0013 "Frequency Response of Secondary Systems Under Seismic Excitation," by J.A. HoLung, J. Cai and Y.K. Lin, 7/31/87, (PB88-134317, A05, MF-A01). This report is only available through NTIS (see address given above).
- NCEER-87-0014 "Modelling Earthquake Ground Motions in Seismically Active Regions Using Parametric Time Series Methods," by G.W. Ellis and A.S. Cakmak, 8/25/87, (PB88-134283, A08, MF-A01). This report is only available through NTIS (see address given above).

- NCEER-87-0015 "Detection and Assessment of Seismic Structural Damage," by E. DiPasquale and A.S. Cakmak, 8/25/87, (PB88-163712, A05, MF-A01). This report is only available through NTIS (see address given above).
- NCEER-87-0016 "Pipeline Experiment at Parkfield, California," by J. Isenberg and E. Richardson, 9/15/87, (PB88-163720, A03, MF-A01). This report is available only through NTIS (see address given above).
- NCEER-87-0017 "Digital Simulation of Seismic Ground Motion," by M. Shinozuka, G. Deodatis and T. Harada, 8/31/87, (PB88-155197, A04, MF-A01). This report is available only through NTIS (see address given above).
- NCEER-87-0018 "Practical Considerations for Structural Control: System Uncertainty, System Time Delay and Truncation of Small Control Forces," J.N. Yang and A. Akbarpour, 8/10/87, (PB88-163738, A08, MF-A01). This report is only available through NTIS (see address given above).
- NCEER-87-0019 "Modal Analysis of Nonclassically Damped Structural Systems Using Canonical Transformation," by J.N. Yang, S. Sarkani and F.X. Long, 9/27/87, (PB88-187851, A04, MF-A01).
- NCEER-87-0020 "A Nonstationary Solution in Random Vibration Theory," by J.R. Red-Horse and P.D. Spanos, 11/3/87, (PB88-163746, A03, MF-A01).
- NCEER-87-0021 "Horizontal Impedances for Radially Inhomogeneous Viscoelastic Soil Layers," by A.S. Veletsos and K.W. Dotson, 10/15/87, (PB88-150859, A04, MF-A01).
- NCEER-87-0022 "Seismic Damage Assessment of Reinforced Concrete Members," by Y.S. Chung, C. Meyer and M. Shinozuka, 10/9/87, (PB88-150867, A05, MF-A01). This report is available only through NTIS (see address given above).
- NCEER-87-0023 "Active Structural Control in Civil Engineering," by T.T. Soong, 11/11/87, (PB88-187778, A03, MF-A01).
- NCEER-87-0024 "Vertical and Torsional Impedances for Radially Inhomogeneous Viscoelastic Soil Layers," by K.W. Dotson and A.S. Veletsos, 12/87, (PB88-187786, A03, MF-A01).
- NCEER-87-0025 "Proceedings from the Symposium on Seismic Hazards, Ground Motions, Soil-Liquefaction and Engineering Practice in Eastern North America," October 20-22, 1987, edited by K.H. Jacob, 12/87, (PB88-188115, A23, MF-A01). This report is available only through NTIS (see address given above).
- NCEER-87-0026 "Report on the Whittier-Narrows, California, Earthquake of October 1, 1987," by J. Pantelic and A. Reinhorn, 11/87, (PB88-187752, A03, MF-A01). This report is available only through NTIS (see address given above).
- NCEER-87-0027 "Design of a Modular Program for Transient Nonlinear Analysis of Large 3-D Building Structures," by S. Srivastav and J.F. Abel, 12/30/87, (PB88-187950, A05, MF-A01). This report is only available through NTIS (see address given above).
- NCEER-87-0028 "Second-Year Program in Research, Education and Technology Transfer," 3/8/88, (PB88-219480, A04, MF-A01).
- NCEER-88-0001 "Workshop on Seismic Computer Analysis and Design of Buildings With Interactive Graphics," by W. McGuire, J.F. Abel and C.H. Conley, 1/18/88, (PB88-187760, A03, MF-A01). This report is only available through NTIS (see address given above).
- NCEER-88-0002 "Optimal Control of Nonlinear Flexible Structures," by J.N. Yang, F.X. Long and D. Wong, 1/22/88, (PB88-213772, A06, MF-A01).
- NCEER-88-0003 "Substructuring Techniques in the Time Domain for Primary-Secondary Structural Systems," by G.D. Manolis and G. Juhn, 2/10/88, (PB88-213780, A04, MF-A01).
- NCEER-88-0004 "Iterative Seismic Analysis of Primary-Secondary Systems," by A. Singhal, L.D. Lutes and P.D. Spanos, 2/23/88, (PB88-213798, A04, MF-A01).

- NCEER-88-0005 "Stochastic Finite Element Expansion for Random Media," by P.D. Spanos and R. Ghanem, 3/14/88, (PB88-213806, A03, MF-A01).
- NCEER-88-0006 "Combining Structural Optimization and Structural Control," by F.Y. Cheng and C.P. Pantelides, 1/10/88, (PB88-213814, A05, MF-A01).
- NCEER-88-0007 "Seismic Performance Assessment of Code-Designed Structures," by H.H-M. Hwang, J-W. Jaw and H-J. Shau, 3/20/88, (PB88-219423, A04, MF-A01). This report is only available through NTIS (see address given above).
- NCEER-88-0008 "Reliability Analysis of Code-Designed Structures Under Natural Hazards," by H.H-M. Hwang, H. Ushiba and M. Shinozuka, 2/29/88, (PB88-229471, A07, MF-A01). This report is only available through NTIS (see address given above).
- NCEER-88-0009 "Seismic Fragility Analysis of Shear Wall Structures," by J-W Jaw and H.H-M. Hwang, 4/30/88, (PB89-102867, A04, MF-A01).
- NCEER-88-0010 "Base Isolation of a Multi-Story Building Under a Harmonic Ground Motion - A Comparison of Performances of Various Systems," by F-G Fan, G. Ahmadi and I.G. Tadjbakhsh, 5/18/88, (PB89-122238, A06, MF-A01). This report is only available through NTIS (see address given above).
- NCEER-88-0011 "Seismic Floor Response Spectra for a Combined System by Green's Functions," by F.M. Lavelle, L.A. Bergman and P.D. Spanos, 5/1/88, (PB89-102875, A03, MF-A01).
- NCEER-88-0012 "A New Solution Technique for Randomly Excited Hysteretic Structures," by G.Q. Cai and Y.K. Lin, 5/16/88, (PB89-102883, A03, MF-A01).
- NCEER-88-0013 "A Study of Radiation Damping and Soil-Structure Interaction Effects in the Centrifuge," by K. Weissman, supervised by J.H. Prevost, 5/24/88, (PB89-144703, A06, MF-A01).
- NCEER-88-0014 "Parameter Identification and Implementation of a Kinematic Plasticity Model for Frictional Soils," by J.H. Prevost and D.V. Griffiths, to be published.
- NCEER-88-0015 "Two- and Three- Dimensional Dynamic Finite Element Analyses of the Long Valley Dam," by D.V. Griffiths and J.H. Prevost, 6/17/88, (PB89-144711, A04, MF-A01).
- NCEER-88-0016 "Damage Assessment of Reinforced Concrete Structures in Eastern United States," by A.M. Reinhorn, M.J. Seidel, S.K. Kunnath and Y.J. Park, 6/15/88, (PB89-122220, A04, MF-A01). This report is only available through NTIS (see address given above).
- NCEER-88-0017 "Dynamic Compliance of Vertically Loaded Strip Foundations in Multilayered Viscoelastic Soils," by S. Ahmad and A.S.M. Israil, 6/17/88, (PB89-102891, A04, MF-A01).
- NCEER-88-0018 "An Experimental Study of Seismic Structural Response With Added Viscoelastic Dampers," by R.C. Lin, Z. Liang, T.T. Soong and R.H. Zhang, 6/30/88, (PB89-122212, A05, MF-A01). This report is available only through NTIS (see address given above).
- NCEER-88-0019 "Experimental Investigation of Primary - Secondary System Interaction," by G.D. Manolis, G. Juhn and A.M. Reinhorn, 5/27/88, (PB89-122204, A04, MF-A01).
- NCEER-88-0020 "A Response Spectrum Approach For Analysis of Nonclassically Damped Structures," by J.N. Yang, S. Sarkani and F.X. Long, 4/22/88, (PB89-102909, A04, MF-A01).
- NCEER-88-0021 "Seismic Interaction of Structures and Soils: Stochastic Approach," by A.S. Veletsos and A.M. Prasad, 7/21/88, (PB89-122196, A04, MF-A01). This report is only available through NTIS (see address given above).
- NCEER-88-0022 "Identification of the Serviceability Limit State and Detection of Seismic Structural Damage," by E. DiPasquale and A.S. Cakmak, 6/15/88, (PB89-122188, A05, MF-A01). This report is available only through NTIS (see address given above).

- NCEER-88-0023 "Multi-Hazard Risk Analysis: Case of a Simple Offshore Structure," by B.K. Bhartia and E.H. Vanmarcke, 7/21/88, (PB89-145213, A05, MF-A01).
- NCEER-88-0024 "Automated Seismic Design of Reinforced Concrete Buildings," by Y.S. Chung, C. Meyer and M. Shinozuka, 7/5/88, (PB89-122170, A06, MF-A01). This report is available only through NTIS (see address given above).
- NCEER-88-0025 "Experimental Study of Active Control of MDOF Structures Under Seismic Excitations," by L.L. Chung, R.C. Lin, T.T. Soong and A.M. Reinhorn, 7/10/88, (PB89-122600, A04, MF-A01).
- NCEER-88-0026 "Earthquake Simulation Tests of a Low-Rise Metal Structure," by J.S. Hwang, K.C. Chang, G.C. Lee and R.L. Ketter, 8/1/88, (PB89-102917, A04, MF-A01).
- NCEER-88-0027 "Systems Study of Urban Response and Reconstruction Due to Catastrophic Earthquakes," by F. Kozin and H.K. Zhou, 9/22/88, (PB90-162348, A04, MF-A01).
- NCEER-88-0028 "Seismic Fragility Analysis of Plane Frame Structures," by H.H-M. Hwang and Y.K. Low, 7/31/88, (PB89-131445, A06, MF-A01).
- NCEER-88-0029 "Response Analysis of Stochastic Structures," by A. Kardara, C. Bucher and M. Shinozuka, 9/22/88, (PB89-174429, A04, MF-A01).
- NCEER-88-0030 "Nonnormal Accelerations Due to Yielding in a Primary Structure," by D.C.K. Chen and L.D. Lutes, 9/19/88, (PB89-131437, A04, MF-A01).
- NCEER-88-0031 "Design Approaches for Soil-Structure Interaction," by A.S. Veletsos, A.M. Prasad and Y. Tang, 12/30/88, (PB89-174437, A03, MF-A01). This report is available only through NTIS (see address given above).
- NCEER-88-0032 "A Re-evaluation of Design Spectra for Seismic Damage Control," by C.J. Turkstra and A.G. Tallin, 11/7/88, (PB89-145221, A05, MF-A01).
- NCEER-88-0033 "The Behavior and Design of Noncontact Lap Splices Subjected to Repeated Inelastic Tensile Loading," by V.E. Sagan, P. Gergely and R.N. White, 12/8/88, (PB89-163737, A08, MF-A01).
- NCEER-88-0034 "Seismic Response of Pile Foundations," by S.M. Mamoon, P.K. Banerjee and S. Ahmad, 11/1/88, (PB89-145239, A04, MF-A01).
- NCEER-88-0035 "Modeling of R/C Building Structures With Flexible Floor Diaphragms (IDARC2)," by A.M. Reinhorn, S.K. Kunnath and N. Panahshahi, 9/7/88, (PB89-207153, A07, MF-A01).
- NCEER-88-0036 "Solution of the Dam-Reservoir Interaction Problem Using a Combination of FEM, BEM with Particular Integrals, Modal Analysis, and Substructuring," by C-S. Tsai, G.C. Lee and R.L. Ketter, 12/31/88, (PB89-207146, A04, MF-A01).
- NCEER-88-0037 "Optimal Placement of Actuators for Structural Control," by F.Y. Cheng and C.P. Pantelides, 8/15/88, (PB89-162846, A05, MF-A01).
- NCEER-88-0038 "Teflon Bearings in Aseismic Base Isolation: Experimental Studies and Mathematical Modeling," by A. Mokha, M.C. Constantinou and A.M. Reinhorn, 12/5/88, (PB89-218457, A10, MF-A01). This report is available only through NTIS (see address given above).
- NCEER-88-0039 "Seismic Behavior of Flat Slab High-Rise Buildings in the New York City Area," by P. Weidlinger and M. Ettouney, 10/15/88, (PB90-145681, A04, MF-A01).
- NCEER-88-0040 "Evaluation of the Earthquake Resistance of Existing Buildings in New York City," by P. Weidlinger and M. Ettouney, 10/15/88, to be published.
- NCEER-88-0041 "Small-Scale Modeling Techniques for Reinforced Concrete Structures Subjected to Seismic Loads," by W. Kim, A. El-Attar and R.N. White, 11/22/88, (PB89-189625, A05, MF-A01).

- NCEER-88-0042 "Modeling Strong Ground Motion from Multiple Event Earthquakes," by G.W. Ellis and A.S. Cakmak, 10/15/88, (PB89-174445, A03, MF-A01).
- NCEER-88-0043 "Nonstationary Models of Seismic Ground Acceleration," by M. Grigoriu, S.E. Ruiz and E. Rosenblueth, 7/15/88, (PB89-189617, A04, MF-A01).
- NCEER-88-0044 "SARCF User's Guide: Seismic Analysis of Reinforced Concrete Frames," by Y.S. Chung, C. Meyer and M. Shinozuka, 11/9/88, (PB89-174452, A08, MF-A01).
- NCEER-88-0045 "First Expert Panel Meeting on Disaster Research and Planning," edited by J. Pantelic and J. Stoyke, 9/15/88, (PB89-174460, A05, MF-A01).
- NCEER-88-0046 "Preliminary Studies of the Effect of Degrading Infill Walls on the Nonlinear Seismic Response of Steel Frames," by C.Z. Chrysostomou, P. Gergely and J.F. Abel, 12/19/88, (PB89-208383, A05, MF-A01).
- NCEER-88-0047 "Reinforced Concrete Frame Component Testing Facility - Design, Construction, Instrumentation and Operation," by S.P. Pessiki, C. Conley, T. Bond, P. Gergely and R.N. White, 12/16/88, (PB89-174478, A04, MF-A01).
- NCEER-89-0001 "Effects of Protective Cushion and Soil Compliancy on the Response of Equipment Within a Seismically Excited Building," by J.A. HoLung, 2/16/89, (PB89-207179, A04, MF-A01).
- NCEER-89-0002 "Statistical Evaluation of Response Modification Factors for Reinforced Concrete Structures," by H.H-M. Hwang and J-W. Jaw, 2/17/89, (PB89-207187, A05, MF-A01).
- NCEER-89-0003 "Hysteretic Columns Under Random Excitation," by G-Q. Cai and Y.K. Lin, 1/9/89, (PB89-196513, A03, MF-A01).
- NCEER-89-0004 "Experimental Study of 'Elephant Foot Bulge' Instability of Thin-Walled Metal Tanks," by Z-H. Jia and R.L. Ketter, 2/22/89, (PB89-207195, A03, MF-A01).
- NCEER-89-0005 "Experiment on Performance of Buried Pipelines Across San Andreas Fault," by J. Isenberg, E. Richardson and T.D. O'Rourke, 3/10/89, (PB89-218440, A04, MF-A01). This report is available only through NTIS (see address given above).
- NCEER-89-0006 "A Knowledge-Based Approach to Structural Design of Earthquake-Resistant Buildings," by M. Subramani, P. Gergely, C.H. Conley, J.F. Abel and A.H. Zaghaw, 1/15/89, (PB89-218465, A06, MF-A01).
- NCEER-89-0007 "Liquefaction Hazards and Their Effects on Buried Pipelines," by T.D. O'Rourke and P.A. Lane, 2/1/89, (PB89-218481, A09, MF-A01).
- NCEER-89-0008 "Fundamentals of System Identification in Structural Dynamics," by H. Imai, C-B. Yun, O. Maruyama and M. Shinozuka, 1/26/89, (PB89-207211, A04, MF-A01).
- NCEER-89-0009 "Effects of the 1985 Michoacan Earthquake on Water Systems and Other Buried Lifelines in Mexico," by A.G. Ayala and M.J. O'Rourke, 3/8/89, (PB89-207229, A06, MF-A01).
- NCEER-89-R010 "NCEER Bibliography of Earthquake Education Materials," by K.E.K. Ross, Second Revision, 9/1/89, (PB90-125352, A05, MF-A01). This report is replaced by NCEER-92-0018.
- NCEER-89-0011 "Inelastic Three-Dimensional Response Analysis of Reinforced Concrete Building Structures (IDARC-3D), Part I - Modeling," by S.K. Kunnath and A.M. Reinhorn, 4/17/89, (PB90-114612, A07, MF-A01). This report is available only through NTIS (see address given above).
- NCEER-89-0012 "Recommended Modifications to ATC-14," by C.D. Poland and J.O. Malley, 4/12/89, (PB90-108648, A15, MF-A01).
- NCEER-89-0013 "Repair and Strengthening of Beam-to-Column Connections Subjected to Earthquake Loading," by M. Corazao and A.J. Durrani, 2/28/89, (PB90-109885, A06, MF-A01).

- NCEER-89-0014 "Program EXKAL2 for Identification of Structural Dynamic Systems," by O. Maruyama, C-B. Yun, M. Hoshiya and M. Shinozuka, 5/19/89, (PB90-109877, A09, MF-A01).
- NCEER-89-0015 "Response of Frames With Bolted Semi-Rigid Connections, Part I - Experimental Study and Analytical Predictions," by P.J. DiCorso, A.M. Reinhorn, J.R. Dickerson, J.B. Radzinski and W.L. Harper, 6/1/89, to be published.
- NCEER-89-0016 "ARMA Monte Carlo Simulation in Probabilistic Structural Analysis," by P.D. Spanos and M.P. Mignolet, 7/10/89, (PB90-109893, A03, MF-A01).
- NCEER-89-P017 "Preliminary Proceedings from the Conference on Disaster Preparedness - The Place of Earthquake Education in Our Schools," Edited by K.E.K. Ross, 6/23/89, (PB90-108606, A03, MF-A01).
- NCEER-89-0017 "Proceedings from the Conference on Disaster Preparedness - The Place of Earthquake Education in Our Schools," Edited by K.E.K. Ross, 12/31/89, (PB90-207895, A012, MF-A02). This report is available only through NTIS (see address given above).
- NCEER-89-0018 "Multidimensional Models of Hysteretic Material Behavior for Vibration Analysis of Shape Memory Energy Absorbing Devices, by E.J. Graesser and F.A. Cozzarelli, 6/7/89, (PB90-164146, A04, MF-A01).
- NCEER-89-0019 "Nonlinear Dynamic Analysis of Three-Dimensional Base Isolated Structures (3D-BASIS)," by S. Nagarajaiah, A.M. Reinhorn and M.C. Constantinou, 8/3/89, (PB90-161936, A06, MF-A01). This report has been replaced by NCEER-93-0011.
- NCEER-89-0020 "Structural Control Considering Time-Rate of Control Forces and Control Rate Constraints," by F.Y. Cheng and C.P. Pantelides, 8/3/89, (PB90-120445, A04, MF-A01).
- NCEER-89-0021 "Subsurface Conditions of Memphis and Shelby County," by K.W. Ng, T-S. Chang and H-H.M. Hwang, 7/26/89, (PB90-120437, A03, MF-A01).
- NCEER-89-0022 "Seismic Wave Propagation Effects on Straight Jointed Buried Pipelines," by K. Elhadi and M.J. O'Rourke, 8/24/89, (PB90-162322, A10, MF-A02).
- NCEER-89-0023 "Workshop on Serviceability Analysis of Water Delivery Systems," edited by M. Grigoriu, 3/6/89, (PB90-127424, A03, MF-A01).
- NCEER-89-0024 "Shaking Table Study of a 1/5 Scale Steel Frame Composed of Tapered Members," by K.C. Chang, J.S. Hwang and G.C. Lee, 9/18/89, (PB90-160169, A04, MF-A01).
- NCEER-89-0025 "DYNA1D: A Computer Program for Nonlinear Seismic Site Response Analysis - Technical Documentation," by Jean H. Prevost, 9/14/89, (PB90-161944, A07, MF-A01). This report is available only through NTIS (see address given above).
- NCEER-89-0026 "1:4 Scale Model Studies of Active Tendon Systems and Active Mass Dampers for Aseismic Protection," by A.M. Reinhorn, T.T. Soong, R.C. Lin, Y.P. Yang, Y. Fukao, H. Abe and M. Nakai, 9/15/89, (PB90-173246, A10, MF-A02). This report is available only through NTIS (see address given above).
- NCEER-89-0027 "Scattering of Waves by Inclusions in a Nonhomogeneous Elastic Half Space Solved by Boundary Element Methods," by P.K. Hadley, A. Askar and A.S. Cakmak, 6/15/89, (PB90-145699, A07, MF-A01).
- NCEER-89-0028 "Statistical Evaluation of Deflection Amplification Factors for Reinforced Concrete Structures," by H.H.M. Hwang, J-W. Jaw and A.L. Ch'ng, 8/31/89, (PB90-164633, A05, MF-A01).
- NCEER-89-0029 "Bedrock Accelerations in Memphis Area Due to Large New Madrid Earthquakes," by H.H.M. Hwang, C.H.S. Chen and G. Yu, 11/7/89, (PB90-162330, A04, MF-A01).
- NCEER-89-0030 "Seismic Behavior and Response Sensitivity of Secondary Structural Systems," by Y.Q. Chen and T.T. Soong, 10/23/89, (PB90-164658, A08, MF-A01).
- NCEER-89-0031 "Random Vibration and Reliability Analysis of Primary-Secondary Structural Systems," by Y. Ibrahim, M. Grigoriu and T.T. Soong, 11/10/89, (PB90-161951, A04, MF-A01).

- NCEER-89-0032 "Proceedings from the Second U.S. - Japan Workshop on Liquefaction, Large Ground Deformation and Their Effects on Lifelines, September 26-29, 1989," Edited by T.D. O'Rourke and M. Hamada, 12/1/89, (PB90-209388, A22, MF-A03).
- NCEER-89-0033 "Deterministic Model for Seismic Damage Evaluation of Reinforced Concrete Structures," by J.M. Bracci, A.M. Reinhorn, J.B. Mander and S.K. Kunnath, 9/27/89, (PB91-108803, A06, MF-A01).
- NCEER-89-0034 "On the Relation Between Local and Global Damage Indices," by E. DiPasquale and A.S. Cakmak, 8/15/89, (PB90-173865, A05, MF-A01).
- NCEER-89-0035 "Cyclic Undrained Behavior of Nonplastic and Low Plasticity Silts," by A.J. Walker and H.E. Stewart, 7/26/89, (PB90-183518, A10, MF-A01).
- NCEER-89-0036 "Liquefaction Potential of Surficial Deposits in the City of Buffalo, New York," by M. Budhu, R. Giese and L. Baumgrass, 1/17/89, (PB90-208455, A04, MF-A01).
- NCEER-89-0037 "A Deterministic Assessment of Effects of Ground Motion Incoherence," by A.S. Veletsos and Y. Tang, 7/15/89, (PB90-164294, A03, MF-A01).
- NCEER-89-0038 "Workshop on Ground Motion Parameters for Seismic Hazard Mapping," July 17-18, 1989, edited by R.V. Whitman, 12/1/89, (PB90-173923, A04, MF-A01).
- NCEER-89-0039 "Seismic Effects on Elevated Transit Lines of the New York City Transit Authority," by C.J. Costantino, C.A. Miller and E. Heymsfield, 12/26/89, (PB90-207887, A06, MF-A01).
- NCEER-89-0040 "Centrifugal Modeling of Dynamic Soil-Structure Interaction," by K. Weissman, Supervised by J.H. Prevost, 5/10/89, (PB90-207879, A07, MF-A01).
- NCEER-89-0041 "Linearized Identification of Buildings With Cores for Seismic Vulnerability Assessment," by I-K. Ho and A.E. Aktan, 11/1/89, (PB90-251943, A07, MF-A01).
- NCEER-90-0001 "Geotechnical and Lifeline Aspects of the October 17, 1989 Loma Prieta Earthquake in San Francisco," by T.D. O'Rourke, H.E. Stewart, F.T. Blackburn and T.S. Dickerman, 1/90, (PB90-208596, A05, MF-A01).
- NCEER-90-0002 "Nonnormal Secondary Response Due to Yielding in a Primary Structure," by D.C.K. Chen and L.D. Lutes, 2/28/90, (PB90-251976, A07, MF-A01).
- NCEER-90-0003 "Earthquake Education Materials for Grades K-12," by K.E.K. Ross, 4/16/90, (PB91-251984, A05, MF-A05). This report has been replaced by NCEER-92-0018.
- NCEER-90-0004 "Catalog of Strong Motion Stations in Eastern North America," by R.W. Busby, 4/3/90, (PB90-251984, A05, MF-A01).
- NCEER-90-0005 "NCEER Strong-Motion Data Base: A User Manual for the GeoBase Release (Version 1.0 for the Sun3)," by P. Friberg and K. Jacob, 3/31/90 (PB90-258062, A04, MF-A01).
- NCEER-90-0006 "Seismic Hazard Along a Crude Oil Pipeline in the Event of an 1811-1812 Type New Madrid Earthquake," by H.H.M. Hwang and C-H.S. Chen, 4/16/90, (PB90-258054, A04, MF-A01).
- NCEER-90-0007 "Site-Specific Response Spectra for Memphis Sheahan Pumping Station," by H.H.M. Hwang and C.S. Lee, 5/15/90, (PB91-108811, A05, MF-A01).
- NCEER-90-0008 "Pilot Study on Seismic Vulnerability of Crude Oil Transmission Systems," by T. Ariman, R. Dobry, M. Grigoriu, F. Kozin, M. O'Rourke, T. O'Rourke and M. Shinozuka, 5/25/90, (PB91-108837, A06, MF-A01).
- NCEER-90-0009 "A Program to Generate Site Dependent Time Histories: EQGEN," by G.W. Ellis, M. Srinivasan and A.S. Cakmak, 1/30/90, (PB91-108829, A04, MF-A01).
- NCEER-90-0010 "Active Isolation for Seismic Protection of Operating Rooms," by M.E. Talbott, Supervised by M. Shinozuka, 6/8/9, (PB91-110205, A05, MF-A01).

- NCEER-90-0011 "Program LINEARID for Identification of Linear Structural Dynamic Systems," by C-B. Yun and M. Shinozuka, 6/25/90, (PB91-110312, A08, MF-A01).
- NCEER-90-0012 "Two-Dimensional Two-Phase Elasto-Plastic Seismic Response of Earth Dams," by A.N. Yiagos, Supervised by J.H. Prevost, 6/20/90, (PB91-110197, A13, MF-A02).
- NCEER-90-0013 "Secondary Systems in Base-Isolated Structures: Experimental Investigation, Stochastic Response and Stochastic Sensitivity," by G.D. Manolis, G. Juhn, M.C. Constantinou and A.M. Reinhorn, 7/1/90, (PB91-110320, A08, MF-A01).
- NCEER-90-0014 "Seismic Behavior of Lightly-Reinforced Concrete Column and Beam-Column Joint Details," by S.P. Pessiki, C.H. Conley, P. Gergely and R.N. White, 8/22/90, (PB91-108795, A11, MF-A02).
- NCEER-90-0015 "Two Hybrid Control Systems for Building Structures Under Strong Earthquakes," by J.N. Yang and A. Danielians, 6/29/90, (PB91-125393, A04, MF-A01).
- NCEER-90-0016 "Instantaneous Optimal Control with Acceleration and Velocity Feedback," by J.N. Yang and Z. Li, 6/29/90, (PB91-125401, A03, MF-A01).
- NCEER-90-0017 "Reconnaissance Report on the Northern Iran Earthquake of June 21, 1990," by M. Mehrain, 10/4/90, (PB91-125377, A03, MF-A01).
- NCEER-90-0018 "Evaluation of Liquefaction Potential in Memphis and Shelby County," by T.S. Chang, P.S. Tang, C.S. Lee and H. Hwang, 8/10/90, (PB91-125427, A09, MF-A01).
- NCEER-90-0019 "Experimental and Analytical Study of a Combined Sliding Disc Bearing and Helical Steel Spring Isolation System," by M.C. Constantinou, A.S. Mokha and A.M. Reinhorn, 10/4/90, (PB91-125385, A06, MF-A01). This report is available only through NTIS (see address given above).
- NCEER-90-0020 "Experimental Study and Analytical Prediction of Earthquake Response of a Sliding Isolation System with a Spherical Surface," by A.S. Mokha, M.C. Constantinou and A.M. Reinhorn, 10/11/90, (PB91-125419, A05, MF-A01).
- NCEER-90-0021 "Dynamic Interaction Factors for Floating Pile Groups," by G. Gazetas, K. Fan, A. Kaynia and E. Kausel, 9/10/90, (PB91-170381, A05, MF-A01).
- NCEER-90-0022 "Evaluation of Seismic Damage Indices for Reinforced Concrete Structures," by S. Rodriguez-Gomez and A.S. Cakmak, 9/30/90, PB91-171322, A06, MF-A01).
- NCEER-90-0023 "Study of Site Response at a Selected Memphis Site," by H. Desai, S. Ahmad, E.S. Gazetas and M.R. Oh, 10/11/90, (PB91-196857, A03, MF-A01).
- NCEER-90-0024 "A User's Guide to Strongmo: Version 1.0 of NCEER's Strong-Motion Data Access Tool for PCs and Terminals," by P.A. Friberg and C.A.T. Susch, 11/15/90, (PB91-171272, A03, MF-A01).
- NCEER-90-0025 "A Three-Dimensional Analytical Study of Spatial Variability of Seismic Ground Motions," by L-L. Hong and A.H.-S. Ang, 10/30/90, (PB91-170399, A09, MF-A01).
- NCEER-90-0026 "MUMOID User's Guide - A Program for the Identification of Modal Parameters," by S. Rodriguez-Gomez and E. DiPasquale, 9/30/90, (PB91-171298, A04, MF-A01).
- NCEER-90-0027 "SARCF-II User's Guide - Seismic Analysis of Reinforced Concrete Frames," by S. Rodriguez-Gomez, Y.S. Chung and C. Meyer, 9/30/90, (PB91-171280, A05, MF-A01).
- NCEER-90-0028 "Viscous Dampers: Testing, Modeling and Application in Vibration and Seismic Isolation," by N. Makris and M.C. Constantinou, 12/20/90 (PB91-190561, A06, MF-A01).
- NCEER-90-0029 "Soil Effects on Earthquake Ground Motions in the Memphis Area," by H. Hwang, C.S. Lee, K.W. Ng and T.S. Chang, 8/2/90, (PB91-190751, A05, MF-A01).

- NCEER-91-0001 "Proceedings from the Third Japan-U.S. Workshop on Earthquake Resistant Design of Lifeline Facilities and Countermeasures for Soil Liquefaction, December 17-19, 1990," edited by T.D. O'Rourke and M. Hamada, 2/1/91, (PB91-179259, A99, MF-A04).
- NCEER-91-0002 "Physical Space Solutions of Non-Proportionally Damped Systems," by M. Tong, Z. Liang and G.C. Lee, 1/15/91, (PB91-179242, A04, MF-A01).
- NCEER-91-0003 "Seismic Response of Single Piles and Pile Groups," by K. Fan and G. Gazetas, 1/10/91, (PB92-174994, A04, MF-A01).
- NCEER-91-0004 "Damping of Structures: Part 1 - Theory of Complex Damping," by Z. Liang and G. Lee, 10/10/91, (PB92-197235, A12, MF-A03).
- NCEER-91-0005 "3D-BASIS - Nonlinear Dynamic Analysis of Three Dimensional Base Isolated Structures: Part II," by S. Nagarajaiah, A.M. Reinhorn and M.C. Constantinou, 2/28/91, (PB91-190553, A07, MF-A01). This report has been replaced by NCEER-93-0011.
- NCEER-91-0006 "A Multidimensional Hysteretic Model for Plasticity Deforming Metals in Energy Absorbing Devices," by E.J. Graesser and F.A. Cozzarelli, 4/9/91, (PB92-108364, A04, MF-A01).
- NCEER-91-0007 "A Framework for Customizable Knowledge-Based Expert Systems with an Application to a KBES for Evaluating the Seismic Resistance of Existing Buildings," by E.G. Ibarra-Anaya and S.J. Fenves, 4/9/91, (PB91-210930, A08, MF-A01).
- NCEER-91-0008 "Nonlinear Analysis of Steel Frames with Semi-Rigid Connections Using the Capacity Spectrum Method," by G.G. Deierlein, S-H. Hsieh, Y-J. Shen and J.F. Abel, 7/2/91, (PB92-113828, A05, MF-A01).
- NCEER-91-0009 "Earthquake Education Materials for Grades K-12," by K.E.K. Ross, 4/30/91, (PB91-212142, A06, MF-A01). This report has been replaced by NCEER-92-0018.
- NCEER-91-0010 "Phase Wave Velocities and Displacement Phase Differences in a Harmonically Oscillating Pile," by N. Makris and G. Gazetas, 7/8/91, (PB92-108356, A04, MF-A01).
- NCEER-91-0011 "Dynamic Characteristics of a Full-Size Five-Story Steel Structure and a 2/5 Scale Model," by K.C. Chang, G.C. Yao, G.C. Lee, D.S. Hao and Y.C. Yeh," 7/2/91, (PB93-116648, A06, MF-A02).
- NCEER-91-0012 "Seismic Response of a 2/5 Scale Steel Structure with Added Viscoelastic Dampers," by K.C. Chang, T.T. Soong, S-T. Oh and M.L. Lai, 5/17/91, (PB92-110816, A05, MF-A01).
- NCEER-91-0013 "Earthquake Response of Retaining Walls; Full-Scale Testing and Computational Modeling," by S. Alampalli and A-W.M. Elgamal, 6/20/91, to be published.
- NCEER-91-0014 "3D-BASIS-M: Nonlinear Dynamic Analysis of Multiple Building Base Isolated Structures," by P.C. Tsopelas, S. Nagarajaiah, M.C. Constantinou and A.M. Reinhorn, 5/28/91, (PB92-113885, A09, MF-A02).
- NCEER-91-0015 "Evaluation of SEAOC Design Requirements for Sliding Isolated Structures," by D. Theodossiou and M.C. Constantinou, 6/10/91, (PB92-114602, A11, MF-A03).
- NCEER-91-0016 "Closed-Loop Modal Testing of a 27-Story Reinforced Concrete Flat Plate-Core Building," by H.R. Somaprasad, T. Toksoy, H. Yoshiyuki and A.E. Aktan, 7/15/91, (PB92-129980, A07, MF-A02).
- NCEER-91-0017 "Shake Table Test of a 1/6 Scale Two-Story Lightly Reinforced Concrete Building," by A.G. El-Attar, R.N. White and P. Gergely, 2/28/91, (PB92-222447, A06, MF-A02).
- NCEER-91-0018 "Shake Table Test of a 1/8 Scale Three-Story Lightly Reinforced Concrete Building," by A.G. El-Attar, R.N. White and P. Gergely, 2/28/91, (PB93-116630, A08, MF-A02).
- NCEER-91-0019 "Transfer Functions for Rigid Rectangular Foundations," by A.S. Veletsos, A.M. Prasad and W.H. Wu, 7/31/91, to be published.

- NCEER-91-0020 "Hybrid Control of Seismic-Excited Nonlinear and Inelastic Structural Systems," by J.N. Yang, Z. Li and A. Daniellians, 8/1/91, (PB92-143171, A06, MF-A02).
- NCEER-91-0021 "The NCEER-91 Earthquake Catalog: Improved Intensity-Based Magnitudes and Recurrence Relations for U.S. Earthquakes East of New Madrid," by L. Seeber and J.G. Armbruster, 8/28/91, (PB92-176742, A06, MF-A02).
- NCEER-91-0022 "Proceedings from the Implementation of Earthquake Planning and Education in Schools: The Need for Change - The Roles of the Changemakers," by K.E.K. Ross and F. Winslow, 7/23/91, (PB92-129998, A12, MF-A03).
- NCEER-91-0023 "A Study of Reliability-Based Criteria for Seismic Design of Reinforced Concrete Frame Buildings," by H.H.M. Hwang and H-M. Hsu, 8/10/91, (PB92-140235, A09, MF-A02).
- NCEER-91-0024 "Experimental Verification of a Number of Structural System Identification Algorithms," by R.G. Ghanem, H. Gavin and M. Shinozuka, 9/18/91, (PB92-176577, A18, MF-A04).
- NCEER-91-0025 "Probabilistic Evaluation of Liquefaction Potential," by H.H.M. Hwang and C.S. Lee," 11/25/91, (PB92-143429, A05, MF-A01).
- NCEER-91-0026 "Instantaneous Optimal Control for Linear, Nonlinear and Hysteretic Structures - Stable Controllers," by J.N. Yang and Z. Li, 11/15/91, (PB92-163807, A04, MF-A01).
- NCEER-91-0027 "Experimental and Theoretical Study of a Sliding Isolation System for Bridges," by M.C. Constantinou, A. Kartoum, A.M. Reinhorn and P. Bradford, 11/15/91, (PB92-176973, A10, MF-A03).
- NCEER-92-0001 "Case Studies of Liquefaction and Lifeline Performance During Past Earthquakes, Volume 1: Japanese Case Studies," Edited by M. Hamada and T. O'Rourke, 2/17/92, (PB92-197243, A18, MF-A04).
- NCEER-92-0002 "Case Studies of Liquefaction and Lifeline Performance During Past Earthquakes, Volume 2: United States Case Studies," Edited by T. O'Rourke and M. Hamada, 2/17/92, (PB92-197250, A20, MF-A04).
- NCEER-92-0003 "Issues in Earthquake Education," Edited by K. Ross, 2/3/92, (PB92-222389, A07, MF-A02).
- NCEER-92-0004 "Proceedings from the First U.S. - Japan Workshop on Earthquake Protective Systems for Bridges," Edited by I.G. Buckle, 2/4/92, (PB94-142239, A99, MF-A06).
- NCEER-92-0005 "Seismic Ground Motion from a Haskell-Type Source in a Multiple-Layered Half-Space," A.P. Theoharis, G. Deodatis and M. Shinozuka, 1/2/92, to be published.
- NCEER-92-0006 "Proceedings from the Site Effects Workshop," Edited by R. Whitman, 2/29/92, (PB92-197201, A04, MF-A01).
- NCEER-92-0007 "Engineering Evaluation of Permanent Ground Deformations Due to Seismically-Induced Liquefaction," by M.H. Baziar, R. Dobry and A-W.M. Elgamal, 3/24/92, (PB92-222421, A13, MF-A03).
- NCEER-92-0008 "A Procedure for the Seismic Evaluation of Buildings in the Central and Eastern United States," by C.D. Poland and J.O. Malley, 4/2/92, (PB92-222439, A20, MF-A04).
- NCEER-92-0009 "Experimental and Analytical Study of a Hybrid Isolation System Using Friction Controllable Sliding Bearings," by M.Q. Feng, S. Fujii and M. Shinozuka, 5/15/92, (PB93-150282, A06, MF-A02).
- NCEER-92-0010 "Seismic Resistance of Slab-Column Connections in Existing Non-Ductile Flat-Plate Buildings," by A.J. Durrani and Y. Du, 5/18/92, (PB93-116812, A06, MF-A02).
- NCEER-92-0011 "The Hysteretic and Dynamic Behavior of Brick Masonry Walls Upgraded by Ferrocement Coatings Under Cyclic Loading and Strong Simulated Ground Motion," by H. Lee and S.P. Prawl, 5/11/92, to be published.
- NCEER-92-0012 "Study of Wire Rope Systems for Seismic Protection of Equipment in Buildings," by G.F. Demetriades, M.C. Constantinou and A.M. Reinhorn, 5/20/92, (PB93-116655, A08, MF-A02).

- NCEER-92-0013 "Shape Memory Structural Dampers: Material Properties, Design and Seismic Testing," by P.R. Witting and F.A. Cozzarelli, 5/26/92, (PB93-116663, A05, MF-A01).
- NCEER-92-0014 "Longitudinal Permanent Ground Deformation Effects on Buried Continuous Pipelines," by M.J. O'Rourke, and C. Nordberg, 6/15/92, (PB93-116671, A08, MF-A02).
- NCEER-92-0015 "A Simulation Method for Stationary Gaussian Random Functions Based on the Sampling Theorem," by M. Grigoriu and S. Balopoulou, 6/11/92, (PB93-127496, A05, MF-A01).
- NCEER-92-0016 "Gravity-Load-Designed Reinforced Concrete Buildings: Seismic Evaluation of Existing Construction and Detailing Strategies for Improved Seismic Resistance," by G.W. Hoffmann, S.K. Kunnath, A.M. Reinhorn and J.B. Mander, 7/15/92, (PB94-142007, A08, MF-A02).
- NCEER-92-0017 "Observations on Water System and Pipeline Performance in the Limón Area of Costa Rica Due to the April 22, 1991 Earthquake," by M. O'Rourke and D. Ballantyne, 6/30/92, (PB93-126811, A06, MF-A02).
- NCEER-92-0018 "Fourth Edition of Earthquake Education Materials for Grades K-12," Edited by K.E.K. Ross, 8/10/92, (PB93-114023, A07, MF-A02).
- NCEER-92-0019 "Proceedings from the Fourth Japan-U.S. Workshop on Earthquake Resistant Design of Lifeline Facilities and Countermeasures for Soil Liquefaction," Edited by M. Hamada and T.D. O'Rourke, 8/12/92, (PB93-163939, A99, MF-E11).
- NCEER-92-0020 "Active Bracing System: A Full Scale Implementation of Active Control," by A.M. Reinhorn, T.T. Soong, R.C. Lin, M.A. Riley, Y.P. Wang, S. Aizawa and M. Higashino, 8/14/92, (PB93-127512, A06, MF-A02).
- NCEER-92-0021 "Empirical Analysis of Horizontal Ground Displacement Generated by Liquefaction-Induced Lateral Spreads," by S.F. Bartlett and T.L. Youd, 8/17/92, (PB93-188241, A06, MF-A02).
- NCEER-92-0022 "IDARC Version 3.0: Inelastic Damage Analysis of Reinforced Concrete Structures," by S.K. Kunnath, A.M. Reinhorn and R.F. Lobo, 8/31/92, (PB93-227502, A07, MF-A02).
- NCEER-92-0023 "A Semi-Empirical Analysis of Strong-Motion Peaks in Terms of Seismic Source, Propagation Path and Local Site Conditions, by M. Kamiyama, M.J. O'Rourke and R. Flores-Berrones, 9/9/92, (PB93-150266, A08, MF-A02).
- NCEER-92-0024 "Seismic Behavior of Reinforced Concrete Frame Structures with Nonductile Details, Part I: Summary of Experimental Findings of Full Scale Beam-Column Joint Tests," by A. Beres, R.N. White and P. Gergely, 9/30/92, (PB93-227783, A05, MF-A01).
- NCEER-92-0025 "Experimental Results of Repaired and Retrofitted Beam-Column Joint Tests in Lightly Reinforced Concrete Frame Buildings," by A. Beres, S. El-Borgi, R.N. White and P. Gergely, 10/29/92, (PB93-227791, A05, MF-A01).
- NCEER-92-0026 "A Generalization of Optimal Control Theory: Linear and Nonlinear Structures," by J.N. Yang, Z. Li and S. Vongchavalitkul, 11/2/92, (PB93-188621, A05, MF-A01).
- NCEER-92-0027 "Seismic Resistance of Reinforced Concrete Frame Structures Designed Only for Gravity Loads: Part I - Design and Properties of a One-Third Scale Model Structure," by J.M. Bracci, A.M. Reinhorn and J.B. Mander, 12/1/92, (PB94-104502, A08, MF-A02).
- NCEER-92-0028 "Seismic Resistance of Reinforced Concrete Frame Structures Designed Only for Gravity Loads: Part II - Experimental Performance of Subassemblages," by L.E. Aycaardi, J.B. Mander and A.M. Reinhorn, 12/1/92, (PB94-104510, A08, MF-A02).
- NCEER-92-0029 "Seismic Resistance of Reinforced Concrete Frame Structures Designed Only for Gravity Loads: Part III - Experimental Performance and Analytical Study of a Structural Model," by J.M. Bracci, A.M. Reinhorn and J.B. Mander, 12/1/92, (PB93-227528, A09, MF-A01).

- NCEER-92-0030 "Evaluation of Seismic Retrofit of Reinforced Concrete Frame Structures: Part I - Experimental Performance of Retrofitted Subassemblages," by D. Choudhuri, J.B. Mander and A.M. Reinhorn, 12/8/92, (PB93-198307, A07, MF-A02).
- NCEER-92-0031 "Evaluation of Seismic Retrofit of Reinforced Concrete Frame Structures: Part II - Experimental Performance and Analytical Study of a Retrofitted Structural Model," by J.M. Bracci, A.M. Reinhorn and J.B. Mander, 12/8/92, (PB93-198315, A09, MF-A03).
- NCEER-92-0032 "Experimental and Analytical Investigation of Seismic Response of Structures with Supplemental Fluid Viscous Dampers," by M.C. Constantinou and M.D. Symans, 12/21/92, (PB93-191435, A10, MF-A03). This report is available only through NTIS (see address given above).
- NCEER-92-0033 "Reconnaissance Report on the Cairo, Egypt Earthquake of October 12, 1992," by M. Khater, 12/23/92, (PB93-188621, A03, MF-A01).
- NCEER-92-0034 "Low-Level Dynamic Characteristics of Four Tall Flat-Plate Buildings in New York City," by H. Gavin, S. Yuan, J. Grossman, E. Pekelis and K. Jacob, 12/28/92, (PB93-188217, A07, MF-A02).
- NCEER-93-0001 "An Experimental Study on the Seismic Performance of Brick-Infilled Steel Frames With and Without Retrofit," by J.B. Mander, B. Nair, K. Wojtkowski and J. Ma, 1/29/93, (PB93-227510, A07, MF-A02).
- NCEER-93-0002 "Social Accounting for Disaster Preparedness and Recovery Planning," by S. Cole, E. Pantoja and V. Razak, 2/22/93, (PB94-142114, A12, MF-A03).
- NCEER-93-0003 "Assessment of 1991 NEHRP Provisions for Nonstructural Components and Recommended Revisions," by T.T. Soong, G. Chen, Z. Wu, R-H. Zhang and M. Grigoriu, 3/1/93, (PB93-188639, A06, MF-A02).
- NCEER-93-0004 "Evaluation of Static and Response Spectrum Analysis Procedures of SEAOC/UBC for Seismic Isolated Structures," by C.W. Winters and M.C. Constantinou, 3/23/93, (PB93-198299, A10, MF-A03).
- NCEER-93-0005 "Earthquakes in the Northeast - Are We Ignoring the Hazard? A Workshop on Earthquake Science and Safety for Educators," edited by K.E.K. Ross, 4/2/93, (PB94-103066, A09, MF-A02).
- NCEER-93-0006 "Inelastic Response of Reinforced Concrete Structures with Viscoelastic Braces," by R.F. Lobo, J.M. Bracci, K.L. Shen, A.M. Reinhorn and T.T. Soong, 4/5/93, (PB93-227486, A05, MF-A02).
- NCEER-93-0007 "Seismic Testing of Installation Methods for Computers and Data Processing Equipment," by K. Kosar, T.T. Soong, K.L. Shen, J.A. HoLung and Y.K. Lin, 4/12/93, (PB93-198299, A07, MF-A02).
- NCEER-93-0008 "Retrofit of Reinforced Concrete Frames Using Added Dampers," by A. Reinhorn, M. Constantinou and C. Li, to be published.
- NCEER-93-0009 "Seismic Behavior and Design Guidelines for Steel Frame Structures with Added Viscoelastic Dampers," by K.C. Chang, M.L. Lai, T.T. Soong, D.S. Hao and Y.C. Yeh, 5/1/93, (PB94-141959, A07, MF-A02).
- NCEER-93-0010 "Seismic Performance of Shear-Critical Reinforced Concrete Bridge Piers," by J.B. Mander, S.M. Waheed, M.T.A. Chaudhary and S.S. Chen, 5/12/93, (PB93-227494, A08, MF-A02).
- NCEER-93-0011 "3D-BASIS-TABS: Computer Program for Nonlinear Dynamic Analysis of Three Dimensional Base Isolated Structures," by S. Nagarajaiah, C. Li, A.M. Reinhorn and M.C. Constantinou, 8/2/93, (PB94-141819, A09, MF-A02).
- NCEER-93-0012 "Effects of Hydrocarbon Spills from an Oil Pipeline Break on Ground Water," by O.J. Helweg and H.H.M. Hwang, 8/3/93, (PB94-141942, A06, MF-A02).
- NCEER-93-0013 "Simplified Procedures for Seismic Design of Nonstructural Components and Assessment of Current Code Provisions," by M.P. Singh, L.E. Suarez, E.E. Matheu and G.O. Maldonado, 8/4/93, (PB94-141827, A09, MF-A02).
- NCEER-93-0014 "An Energy Approach to Seismic Analysis and Design of Secondary Systems," by G. Chen and T.T. Soong, 8/6/93, (PB94-142767, A11, MF-A03).

- NCEER-93-0015 "Proceedings from School Sites: Becoming Prepared for Earthquakes - Commemorating the Third Anniversary of the Loma Prieta Earthquake," Edited by F.E. Winslow and K.E.K. Ross, 8/16/93, (PB94-154275, A16, MF-A02).
- NCEER-93-0016 "Reconnaissance Report of Damage to Historic Monuments in Cairo, Egypt Following the October 12, 1992 Dahshur Earthquake," by D. Sykora, D. Look, G. Croci, E. Karaesmen and E. Karaesmen, 8/19/93, (PB94-142221, A08, MF-A02).
- NCEER-93-0017 "The Island of Guam Earthquake of August 8, 1993," by S.W. Swan and S.K. Harris, 9/30/93, (PB94-141843, A04, MF-A01).
- NCEER-93-0018 "Engineering Aspects of the October 12, 1992 Egyptian Earthquake," by A.W. Elgamal, M. Amer, K. Adalier and A. Abul-Fadl, 10/7/93, (PB94-141983, A05, MF-A01).
- NCEER-93-0019 "Development of an Earthquake Motion Simulator and its Application in Dynamic Centrifuge Testing," by I. Krstelj, Supervised by J.H. Prevost, 10/23/93, (PB94-181773, A-10, MF-A03).
- NCEER-93-0020 "NCEER-Taisei Corporation Research Program on Sliding Seismic Isolation Systems for Bridges: Experimental and Analytical Study of a Friction Pendulum System (FPS)," by M.C. Constantinou, P. Tsopelas, Y-S. Kim and S. Okamoto, 11/1/93, (PB94-142775, A08, MF-A02).
- NCEER-93-0021 "Finite Element Modeling of Elastomeric Seismic Isolation Bearings," by L.J. Billings, Supervised by R. Shepherd, 11/8/93, to be published.
- NCEER-93-0022 "Seismic Vulnerability of Equipment in Critical Facilities: Life-Safety and Operational Consequences," by K. Porter, G.S. Johnson, M.M. Zadeh, C. Scawthorn and S. Eder, 11/24/93, (PB94-181765, A16, MF-A03).
- NCEER-93-0023 "Hokkaido Nansei-oki, Japan Earthquake of July 12, 1993, by P.I. Yanev and C.R. Scawthorn, 12/23/93, (PB94-181500, A07, MF-A01).
- NCEER-94-0001 "An Evaluation of Seismic Serviceability of Water Supply Networks with Application to the San Francisco Auxiliary Water Supply System," by I. Markov, Supervised by M. Grigoriu and T. O'Rourke, 1/21/94, (PB94-204013, A07, MF-A02).
- NCEER-94-0002 "NCEER-Taisei Corporation Research Program on Sliding Seismic Isolation Systems for Bridges: Experimental and Analytical Study of Systems Consisting of Sliding Bearings, Rubber Restoring Force Devices and Fluid Dampers," Volumes I and II, by P. Tsopelas, S. Okamoto, M.C. Constantinou, D. Ozaki and S. Fujii, 2/4/94, (PB94-181740, A09, MF-A02 and PB94-181757, A12, MF-A03).
- NCEER-94-0003 "A Markov Model for Local and Global Damage Indices in Seismic Analysis," by S. Rahman and M. Grigoriu, 2/18/94, (PB94-206000, A12, MF-A03).
- NCEER-94-0004 "Proceedings from the NCEER Workshop on Seismic Response of Masonry Infills," edited by D.P. Abrams, 3/1/94, (PB94-180783, A07, MF-A02).
- NCEER-94-0005 "The Northridge, California Earthquake of January 17, 1994: General Reconnaissance Report," edited by J.D. Goltz, 3/11/94, (PB94-193943, A10, MF-A03).
- NCEER-94-0006 "Seismic Energy Based Fatigue Damage Analysis of Bridge Columns: Part I - Evaluation of Seismic Capacity," by G.A. Chang and J.B. Mander, 3/14/94, (PB94-219185, A11, MF-A03).
- NCEER-94-0007 "Seismic Isolation of Multi-Story Frame Structures Using Spherical Sliding Isolation Systems," by T.M. Al-Hussaini, V.A. Zayas and M.C. Constantinou, 3/17/94, (PB94-193745, A09, MF-A02).
- NCEER-94-0008 "The Northridge, California Earthquake of January 17, 1994: Performance of Highway Bridges," edited by I.G. Buckle, 3/24/94, (PB94-193851, A06, MF-A02).
- NCEER-94-0009 "Proceedings of the Third U.S.-Japan Workshop on Earthquake Protective Systems for Bridges," edited by I.G. Buckle and I. Friedland, 3/31/94, (PB94-195815, A99, MF-A06).

- NCEER-94-0010 "3D-BASIS-ME: Computer Program for Nonlinear Dynamic Analysis of Seismically Isolated Single and Multiple Structures and Liquid Storage Tanks," by P.C. Tsopelas, M.C. Constantinou and A.M. Reinhorn, 4/12/94, (PB94-204922, A09, MF-A02).
- NCEER-94-0011 "The Northridge, California Earthquake of January 17, 1994: Performance of Gas Transmission Pipelines," by T.D. O'Rourke and M.C. Palmer, 5/16/94, (PB94-204989, A05, MF-A01).
- NCEER-94-0012 "Feasibility Study of Replacement Procedures and Earthquake Performance Related to Gas Transmission Pipelines," by T.D. O'Rourke and M.C. Palmer, 5/25/94, (PB94-206638, A09, MF-A02).
- NCEER-94-0013 "Seismic Energy Based Fatigue Damage Analysis of Bridge Columns: Part II - Evaluation of Seismic Demand," by G.A. Chang and J.B. Mander, 6/1/94, (PB95-18106, A08, MF-A02).
- NCEER-94-0014 "NCEER-Taisei Corporation Research Program on Sliding Seismic Isolation Systems for Bridges: Experimental and Analytical Study of a System Consisting of Sliding Bearings and Fluid Restoring Force/Damping Devices," by P. Tsopelas and M.C. Constantinou, 6/13/94, (PB94-219144, A10, MF-A03).
- NCEER-94-0015 "Generation of Hazard-Consistent Fragility Curves for Seismic Loss Estimation Studies," by H. Hwang and J-R. Huo, 6/14/94, (PB95-181996, A09, MF-A02).
- NCEER-94-0016 "Seismic Study of Building Frames with Added Energy-Absorbing Devices," by W.S. Pong, C.S. Tsai and G.C. Lee, 6/20/94, (PB94-219136, A10, A03).
- NCEER-94-0017 "Sliding Mode Control for Seismic-Excited Linear and Nonlinear Civil Engineering Structures," by J. Yang, J. Wu, A. Agrawal and Z. Li, 6/21/94, (PB95-138483, A06, MF-A02).
- NCEER-94-0018 "3D-BASIS-TABS Version 2.0: Computer Program for Nonlinear Dynamic Analysis of Three Dimensional Base Isolated Structures," by A.M. Reinhorn, S. Nagarajaiah, M.C. Constantinou, P. Tsopelas and R. Li, 6/22/94, (PB95-182176, A08, MF-A02).
- NCEER-94-0019 "Proceedings of the International Workshop on Civil Infrastructure Systems: Application of Intelligent Systems and Advanced Materials on Bridge Systems," Edited by G.C. Lee and K.C. Chang, 7/18/94, (PB95-252474, A20, MF-A04).
- NCEER-94-0020 "Study of Seismic Isolation Systems for Computer Floors," by V. Lambrou and M.C. Constantinou, 7/19/94, (PB95-138533, A10, MF-A03).
- NCEER-94-0021 "Proceedings of the U.S.-Italian Workshop on Guidelines for Seismic Evaluation and Rehabilitation of Unreinforced Masonry Buildings," Edited by D.P. Abrams and G.M. Calvi, 7/20/94, (PB95-138749, A13, MF-A03).
- NCEER-94-0022 "NCEER-Taisei Corporation Research Program on Sliding Seismic Isolation Systems for Bridges: Experimental and Analytical Study of a System Consisting of Lubricated PTFE Sliding Bearings and Mild Steel Dampers," by P. Tsopelas and M.C. Constantinou, 7/22/94, (PB95-182184, A08, MF-A02).
- NCEER-94-0023 "Development of Reliability-Based Design Criteria for Buildings Under Seismic Load," by Y.K. Wen, H. Hwang and M. Shinozuka, 8/1/94, (PB95-211934, A08, MF-A02).
- NCEER-94-0024 "Experimental Verification of Acceleration Feedback Control Strategies for an Active Tendon System," by S.J. Dyke, B.F. Spencer, Jr., P. Quast, M.K. Sain, D.C. Kaspari, Jr. and T.T. Soong, 8/29/94, (PB95-212320, A05, MF-A01).
- NCEER-94-0025 "Seismic Retrofitting Manual for Highway Bridges," Edited by I.G. Buckle and I.F. Friedland, published by the Federal Highway Administration (PB95-212676, A15, MF-A03).
- NCEER-94-0026 "Proceedings from the Fifth U.S.-Japan Workshop on Earthquake Resistant Design of Lifeline Facilities and Countermeasures Against Soil Liquefaction," Edited by T.D. O'Rourke and M. Hamada, 11/7/94, (PB95-220802, A99, MF-E08).

- NCEER-95-0001 “Experimental and Analytical Investigation of Seismic Retrofit of Structures with Supplemental Damping: Part I - Fluid Viscous Damping Devices,” by A.M. Reinhorn, C. Li and M.C. Constantinou, 1/3/95, (PB95-266599, A09, MF-A02).
- NCEER-95-0002 “Experimental and Analytical Study of Low-Cycle Fatigue Behavior of Semi-Rigid Top-And-Seat Angle Connections,” by G. Pekcan, J.B. Mander and S.S. Chen, 1/5/95, (PB95-220042, A07, MF-A02).
- NCEER-95-0003 “NCEER-ATC Joint Study on Fragility of Buildings,” by T. Anagnos, C. Rojahn and A.S. Kiremidjian, 1/20/95, (PB95-220026, A06, MF-A02).
- NCEER-95-0004 “Nonlinear Control Algorithms for Peak Response Reduction,” by Z. Wu, T.T. Soong, V. Gattulli and R.C. Lin, 2/16/95, (PB95-220349, A05, MF-A01).
- NCEER-95-0005 “Pipeline Replacement Feasibility Study: A Methodology for Minimizing Seismic and Corrosion Risks to Underground Natural Gas Pipelines,” by R.T. Eguchi, H.A. Seligson and D.G. Honegger, 3/2/95, (PB95-252326, A06, MF-A02).
- NCEER-95-0006 “Evaluation of Seismic Performance of an 11-Story Frame Building During the 1994 Northridge Earthquake,” by F. Naeim, R. DiSulio, K. Benuska, A. Reinhorn and C. Li, to be published.
- NCEER-95-0007 “Prioritization of Bridges for Seismic Retrofitting,” by N. Basöz and A.S. Kiremidjian, 4/24/95, (PB95-252300, A08, MF-A02).
- NCEER-95-0008 “Method for Developing Motion Damage Relationships for Reinforced Concrete Frames,” by A. Singhal and A.S. Kiremidjian, 5/11/95, (PB95-266607, A06, MF-A02).
- NCEER-95-0009 “Experimental and Analytical Investigation of Seismic Retrofit of Structures with Supplemental Damping: Part II - Friction Devices,” by C. Li and A.M. Reinhorn, 7/6/95, (PB96-128087, A11, MF-A03).
- NCEER-95-0010 “Experimental Performance and Analytical Study of a Non-Ductile Reinforced Concrete Frame Structure Retrofitted with Elastomeric Spring Dampers,” by G. Pekcan, J.B. Mander and S.S. Chen, 7/14/95, (PB96-137161, A08, MF-A02).
- NCEER-95-0011 “Development and Experimental Study of Semi-Active Fluid Damping Devices for Seismic Protection of Structures,” by M.D. Symans and M.C. Constantinou, 8/3/95, (PB96-136940, A23, MF-A04).
- NCEER-95-0012 “Real-Time Structural Parameter Modification (RSPM): Development of Innervated Structures,” by Z. Liang, M. Tong and G.C. Lee, 4/11/95, (PB96-137153, A06, MF-A01).
- NCEER-95-0013 “Experimental and Analytical Investigation of Seismic Retrofit of Structures with Supplemental Damping: Part III - Viscous Damping Walls,” by A.M. Reinhorn and C. Li, 10/1/95, (PB96-176409, A11, MF-A03).
- NCEER-95-0014 “Seismic Fragility Analysis of Equipment and Structures in a Memphis Electric Substation,” by J-R. Huo and H.H.M. Hwang, 8/10/95, (PB96-128087, A09, MF-A02).
- NCEER-95-0015 “The Hanshin-Awaji Earthquake of January 17, 1995: Performance of Lifelines,” Edited by M. Shinozuka, 11/3/95, (PB96-176383, A15, MF-A03).
- NCEER-95-0016 “Highway Culvert Performance During Earthquakes,” by T.L. Youd and C.J. Beckman, available as NCEER-96-0015.
- NCEER-95-0017 “The Hanshin-Awaji Earthquake of January 17, 1995: Performance of Highway Bridges,” Edited by I.G. Buckle, 12/1/95, to be published.
- NCEER-95-0018 “Modeling of Masonry Infill Panels for Structural Analysis,” by A.M. Reinhorn, A. Madan, R.E. Valles, Y. Reichmann and J.B. Mander, 12/8/95, (PB97-110886, MF-A01, A06).
- NCEER-95-0019 “Optimal Polynomial Control for Linear and Nonlinear Structures,” by A.K. Agrawal and J.N. Yang, 12/11/95, (PB96-168737, A07, MF-A02).

- NCEER-95-0020 "Retrofit of Non-Ductile Reinforced Concrete Frames Using Friction Dampers," by R.S. Rao, P. Gergely and R.N. White, 12/22/95, (PB97-133508, A10, MF-A02).
- NCEER-95-0021 "Parametric Results for Seismic Response of Pile-Supported Bridge Bents," by G. Mylonakis, A. Nikolaou and G. Gazetas, 12/22/95, (PB97-100242, A12, MF-A03).
- NCEER-95-0022 "Kinematic Bending Moments in Seismically Stressed Piles," by A. Nikolaou, G. Mylonakis and G. Gazetas, 12/23/95, (PB97-113914, MF-A03, A13).
- NCEER-96-0001 "Dynamic Response of Unreinforced Masonry Buildings with Flexible Diaphragms," by A.C. Costley and D.P. Abrams, 10/10/96, (PB97-133573, MF-A03, A15).
- NCEER-96-0002 "State of the Art Review: Foundations and Retaining Structures," by I. Po Lam, to be published.
- NCEER-96-0003 "Ductility of Rectangular Reinforced Concrete Bridge Columns with Moderate Confinement," by N. Wehbe, M. Saiidi, D. Sanders and B. Douglas, 11/7/96, (PB97-133557, A06, MF-A02).
- NCEER-96-0004 "Proceedings of the Long-Span Bridge Seismic Research Workshop," edited by I.G. Buckle and I.M. Friedland, to be published.
- NCEER-96-0005 "Establish Representative Pier Types for Comprehensive Study: Eastern United States," by J. Kulicki and Z. Prucz, 5/28/96, (PB98-119217, A07, MF-A02).
- NCEER-96-0006 "Establish Representative Pier Types for Comprehensive Study: Western United States," by R. Imbsen, R.A. Schamber and T.A. Osterkamp, 5/28/96, (PB98-118607, A07, MF-A02).
- NCEER-96-0007 "Nonlinear Control Techniques for Dynamical Systems with Uncertain Parameters," by R.G. Ghanem and M.I. Bujakov, 5/27/96, (PB97-100259, A17, MF-A03).
- NCEER-96-0008 "Seismic Evaluation of a 30-Year Old Non-Ductile Highway Bridge Pier and Its Retrofit," by J.B. Mander, B. Mahmoodzadegan, S. Bhadra and S.S. Chen, 5/31/96, (PB97-110902, MF-A03, A10).
- NCEER-96-0009 "Seismic Performance of a Model Reinforced Concrete Bridge Pier Before and After Retrofit," by J.B. Mander, J.H. Kim and C.A. Ligozio, 5/31/96, (PB97-110910, MF-A02, A10).
- NCEER-96-0010 "IDARC2D Version 4.0: A Computer Program for the Inelastic Damage Analysis of Buildings," by R.E. Valles, A.M. Reinhorn, S.K. Kunnath, C. Li and A. Madan, 6/3/96, (PB97-100234, A17, MF-A03).
- NCEER-96-0011 "Estimation of the Economic Impact of Multiple Lifeline Disruption: Memphis Light, Gas and Water Division Case Study," by S.E. Chang, H.A. Seligson and R.T. Eguchi, 8/16/96, (PB97-133490, A11, MF-A03).
- NCEER-96-0012 "Proceedings from the Sixth Japan-U.S. Workshop on Earthquake Resistant Design of Lifeline Facilities and Countermeasures Against Soil Liquefaction, Edited by M. Hamada and T. O'Rourke, 9/11/96, (PB97-133581, A99, MF-A06).
- NCEER-96-0013 "Chemical Hazards, Mitigation and Preparedness in Areas of High Seismic Risk: A Methodology for Estimating the Risk of Post-Earthquake Hazardous Materials Release," by H.A. Seligson, R.T. Eguchi, K.J. Tierney and K. Richmond, 11/7/96, (PB97-133565, MF-A02, A08).
- NCEER-96-0014 "Response of Steel Bridge Bearings to Reversed Cyclic Loading," by J.B. Mander, D-K. Kim, S.S. Chen and G.J. Premus, 11/13/96, (PB97-140735, A12, MF-A03).
- NCEER-96-0015 "Highway Culvert Performance During Past Earthquakes," by T.L. Youd and C.J. Beckman, 11/25/96, (PB97-133532, A06, MF-A01).
- NCEER-97-0001 "Evaluation, Prevention and Mitigation of Pounding Effects in Building Structures," by R.E. Valles and A.M. Reinhorn, 2/20/97, (PB97-159552, A14, MF-A03).
- NCEER-97-0002 "Seismic Design Criteria for Bridges and Other Highway Structures," by C. Rojahn, R. Mayes, D.G. Anderson, J. Clark, J.H. Hom, R.V. Nutt and M.J. O'Rourke, 4/30/97, (PB97-194658, A06, MF-A03).

- NCEER-97-0003 "Proceedings of the U.S.-Italian Workshop on Seismic Evaluation and Retrofit," Edited by D.P. Abrams and G.M. Calvi, 3/19/97, (PB97-194666, A13, MF-A03).
- NCEER-97-0004 "Investigation of Seismic Response of Buildings with Linear and Nonlinear Fluid Viscous Dampers," by A.A. Seleemah and M.C. Constantinou, 5/21/97, (PB98-109002, A15, MF-A03).
- NCEER-97-0005 "Proceedings of the Workshop on Earthquake Engineering Frontiers in Transportation Facilities," edited by G.C. Lee and I.M. Friedland, 8/29/97, (PB98-128911, A25, MR-A04).
- NCEER-97-0006 "Cumulative Seismic Damage of Reinforced Concrete Bridge Piers," by S.K. Kunnath, A. El-Bahy, A. Taylor and W. Stone, 9/2/97, (PB98-108814, A11, MF-A03).
- NCEER-97-0007 "Structural Details to Accommodate Seismic Movements of Highway Bridges and Retaining Walls," by R.A. Imbsen, R.A. Schamber, E. Thorkildsen, A. Kartoum, B.T. Martin, T.N. Rosser and J.M. Kulicki, 9/3/97, (PB98-108996, A09, MF-A02).
- NCEER-97-0008 "A Method for Earthquake Motion-Damage Relationships with Application to Reinforced Concrete Frames," by A. Singhal and A.S. Kiremidjian, 9/10/97, (PB98-108988, A13, MF-A03).
- NCEER-97-0009 "Seismic Analysis and Design of Bridge Abutments Considering Sliding and Rotation," by K. Fishman and R. Richards, Jr., 9/15/97, (PB98-108897, A06, MF-A02).
- NCEER-97-0010 "Proceedings of the FHWA/NCEER Workshop on the National Representation of Seismic Ground Motion for New and Existing Highway Facilities," edited by I.M. Friedland, M.S. Power and R.L. Mayes, 9/22/97, (PB98-128903, A21, MF-A04).
- NCEER-97-0011 "Seismic Analysis for Design or Retrofit of Gravity Bridge Abutments," by K.L. Fishman, R. Richards, Jr. and R.C. Divito, 10/2/97, (PB98-128937, A08, MF-A02).
- NCEER-97-0012 "Evaluation of Simplified Methods of Analysis for Yielding Structures," by P. Tsopelas, M.C. Constantinou, C.A. Kircher and A.S. Whittaker, 10/31/97, (PB98-128929, A10, MF-A03).
- NCEER-97-0013 "Seismic Design of Bridge Columns Based on Control and Repairability of Damage," by C-T. Cheng and J.B. Mander, 12/8/97, (PB98-144249, A11, MF-A03).
- NCEER-97-0014 "Seismic Resistance of Bridge Piers Based on Damage Avoidance Design," by J.B. Mander and C-T. Cheng, 12/10/97, (PB98-144223, A09, MF-A02).
- NCEER-97-0015 "Seismic Response of Nominally Symmetric Systems with Strength Uncertainty," by S. Balopoulou and M. Grigoriu, 12/23/97, (PB98-153422, A11, MF-A03).
- NCEER-97-0016 "Evaluation of Seismic Retrofit Methods for Reinforced Concrete Bridge Columns," by T.J. Wipf, F.W. Klaiber and F.M. Russo, 12/28/97, (PB98-144215, A12, MF-A03).
- NCEER-97-0017 "Seismic Fragility of Existing Conventional Reinforced Concrete Highway Bridges," by C.L. Mullen and A.S. Cakmak, 12/30/97, (PB98-153406, A08, MF-A02).
- NCEER-97-0018 "Loss Assessment of Memphis Buildings," edited by D.P. Abrams and M. Shinozuka, 12/31/97, (PB98-144231, A13, MF-A03).
- NCEER-97-0019 "Seismic Evaluation of Frames with Infill Walls Using Quasi-static Experiments," by K.M. Mosalam, R.N. White and P. Gergely, 12/31/97, (PB98-153455, A07, MF-A02).
- NCEER-97-0020 "Seismic Evaluation of Frames with Infill Walls Using Pseudo-dynamic Experiments," by K.M. Mosalam, R.N. White and P. Gergely, 12/31/97, (PB98-153430, A07, MF-A02).
- NCEER-97-0021 "Computational Strategies for Frames with Infill Walls: Discrete and Smeared Crack Analyses and Seismic Fragility," by K.M. Mosalam, R.N. White and P. Gergely, 12/31/97, (PB98-153414, A10, MF-A02).

- NCEER-97-0022 "Proceedings of the NCEER Workshop on Evaluation of Liquefaction Resistance of Soils," edited by T.L. Youd and I.M. Idriss, 12/31/97, (PB98-155617, A15, MF-A03).
- MCEER-98-0001 "Extraction of Nonlinear Hysteretic Properties of Seismically Isolated Bridges from Quick-Release Field Tests," by Q. Chen, B.M. Douglas, E.M. Maragakis and I.G. Buckle, 5/26/98, (PB99-118838, A06, MF-A01).
- MCEER-98-0002 "Methodologies for Evaluating the Importance of Highway Bridges," by A. Thomas, S. Eshenaur and J. Kulicki, 5/29/98, (PB99-118846, A10, MF-A02).
- MCEER-98-0003 "Capacity Design of Bridge Piers and the Analysis of Overstrength," by J.B. Mander, A. Dutta and P. Goel, 6/1/98, (PB99-118853, A09, MF-A02).
- MCEER-98-0004 "Evaluation of Bridge Damage Data from the Loma Prieta and Northridge, California Earthquakes," by N. Basoz and A. Kiremidjian, 6/2/98, (PB99-118861, A15, MF-A03).
- MCEER-98-0005 "Screening Guide for Rapid Assessment of Liquefaction Hazard at Highway Bridge Sites," by T. L. Youd, 6/16/98, (PB99-118879, A06, not available on microfiche).
- MCEER-98-0006 "Structural Steel and Steel/Concrete Interface Details for Bridges," by P. Ritchie, N. Kauh and J. Kulicki, 7/13/98, (PB99-118945, A06, MF-A01).
- MCEER-98-0007 "Capacity Design and Fatigue Analysis of Confined Concrete Columns," by A. Dutta and J.B. Mander, 7/14/98, (PB99-118960, A14, MF-A03).
- MCEER-98-0008 "Proceedings of the Workshop on Performance Criteria for Telecommunication Services Under Earthquake Conditions," edited by A.J. Schiff, 7/15/98, (PB99-118952, A08, MF-A02).
- MCEER-98-0009 "Fatigue Analysis of Unconfined Concrete Columns," by J.B. Mander, A. Dutta and J.H. Kim, 9/12/98, (PB99-123655, A10, MF-A02).
- MCEER-98-0010 "Centrifuge Modeling of Cyclic Lateral Response of Pile-Cap Systems and Seat-Type Abutments in Dry Sands," by A.D. Gadre and R. Dobry, 10/2/98, (PB99-123606, A13, MF-A03).
- MCEER-98-0011 "IDARC-BRIDGE: A Computational Platform for Seismic Damage Assessment of Bridge Structures," by A.M. Reinhorn, V. Simeonov, G. Mylonakis and Y. Reichman, 10/2/98, (PB99-162919, A15, MF-A03).
- MCEER-98-0012 "Experimental Investigation of the Dynamic Response of Two Bridges Before and After Retrofitting with Elastomeric Bearings," by D.A. Wendichansky, S.S. Chen and J.B. Mander, 10/2/98, (PB99-162927, A15, MF-A03).
- MCEER-98-0013 "Design Procedures for Hinge Restrainers and Hinge Sear Width for Multiple-Frame Bridges," by R. Des Roches and G.L. Fenves, 11/3/98, (PB99-140477, A13, MF-A03).
- MCEER-98-0014 "Response Modification Factors for Seismically Isolated Bridges," by M.C. Constantinou and J.K. Quarshie, 11/3/98, (PB99-140485, A14, MF-A03).
- MCEER-98-0015 "Proceedings of the U.S.-Italy Workshop on Seismic Protective Systems for Bridges," edited by I.M. Friedland and M.C. Constantinou, 11/3/98, (PB2000-101711, A22, MF-A04).
- MCEER-98-0016 "Appropriate Seismic Reliability for Critical Equipment Systems: Recommendations Based on Regional Analysis of Financial and Life Loss," by K. Porter, C. Scawthorn, C. Taylor and N. Blais, 11/10/98, (PB99-157265, A08, MF-A02).
- MCEER-98-0017 "Proceedings of the U.S. Japan Joint Seminar on Civil Infrastructure Systems Research," edited by M. Shinozuka and A. Rose, 11/12/98, (PB99-156713, A16, MF-A03).
- MCEER-98-0018 "Modeling of Pile Footings and Drilled Shafts for Seismic Design," by I. PoLam, M. Kapuskar and D. Chaudhuri, 12/21/98, (PB99-157257, A09, MF-A02).

- MCEER-99-0001 "Seismic Evaluation of a Masonry Infilled Reinforced Concrete Frame by Pseudodynamic Testing," by S.G. Buonopane and R.N. White, 2/16/99, (PB99-162851, A09, MF-A02).
- MCEER-99-0002 "Response History Analysis of Structures with Seismic Isolation and Energy Dissipation Systems: Verification Examples for Program SAP2000," by J. Scheller and M.C. Constantinou, 2/22/99, (PB99-162869, A08, MF-A02).
- MCEER-99-0003 "Experimental Study on the Seismic Design and Retrofit of Bridge Columns Including Axial Load Effects," by A. Dutta, T. Kokorina and J.B. Mander, 2/22/99, (PB99-162877, A09, MF-A02).
- MCEER-99-0004 "Experimental Study of Bridge Elastomeric and Other Isolation and Energy Dissipation Systems with Emphasis on Uplift Prevention and High Velocity Near-source Seismic Excitation," by A. Kasalanati and M. C. Constantinou, 2/26/99, (PB99-162885, A12, MF-A03).
- MCEER-99-0005 "Truss Modeling of Reinforced Concrete Shear-flexure Behavior," by J.H. Kim and J.B. Mander, 3/8/99, (PB99-163693, A12, MF-A03).
- MCEER-99-0006 "Experimental Investigation and Computational Modeling of Seismic Response of a 1:4 Scale Model Steel Structure with a Load Balancing Supplemental Damping System," by G. Pekcan, J.B. Mander and S.S. Chen, 4/2/99, (PB99-162893, A11, MF-A03).
- MCEER-99-0007 "Effect of Vertical Ground Motions on the Structural Response of Highway Bridges," by M.R. Button, C.J. Cronin and R.L. Mayes, 4/10/99, (PB2000-101411, A10, MF-A03).
- MCEER-99-0008 "Seismic Reliability Assessment of Critical Facilities: A Handbook, Supporting Documentation, and Model Code Provisions," by G.S. Johnson, R.E. Sheppard, M.D. Quilici, S.J. Eder and C.R. Scawthorn, 4/12/99, (PB2000-101701, A18, MF-A04).
- MCEER-99-0009 "Impact Assessment of Selected MCEER Highway Project Research on the Seismic Design of Highway Structures," by C. Rojahn, R. Mayes, D.G. Anderson, J.H. Clark, D'Appolonia Engineering, S. Gloyd and R.V. Nutt, 4/14/99, (PB99-162901, A10, MF-A02).
- MCEER-99-0010 "Site Factors and Site Categories in Seismic Codes," by R. Dobry, R. Ramos and M.S. Power, 7/19/99, (PB2000-101705, A08, MF-A02).
- MCEER-99-0011 "Restrainer Design Procedures for Multi-Span Simply-Supported Bridges," by M.J. Randall, M. Saiidi, E. Maragakis and T. Isakovic, 7/20/99, (PB2000-101702, A10, MF-A02).
- MCEER-99-0012 "Property Modification Factors for Seismic Isolation Bearings," by M.C. Constantinou, P. Tsopelas, A. Kasalanati and E. Wolff, 7/20/99, (PB2000-103387, A11, MF-A03).
- MCEER-99-0013 "Critical Seismic Issues for Existing Steel Bridges," by P. Ritchie, N. Kauh and J. Kulicki, 7/20/99, (PB2000-101697, A09, MF-A02).
- MCEER-99-0014 "Nonstructural Damage Database," by A. Kao, T.T. Soong and A. Vender, 7/24/99, (PB2000-101407, A06, MF-A01).
- MCEER-99-0015 "Guide to Remedial Measures for Liquefaction Mitigation at Existing Highway Bridge Sites," by H.G. Cooke and J. K. Mitchell, 7/26/99, (PB2000-101703, A11, MF-A03).
- MCEER-99-0016 "Proceedings of the MCEER Workshop on Ground Motion Methodologies for the Eastern United States," edited by N. Abrahamson and A. Becker, 8/11/99, (PB2000-103385, A07, MF-A02).
- MCEER-99-0017 "Quindío, Colombia Earthquake of January 25, 1999: Reconnaissance Report," by A.P. Asfura and P.J. Flores, 10/4/99, (PB2000-106893, A06, MF-A01).
- MCEER-99-0018 "Hysteretic Models for Cyclic Behavior of Deteriorating Inelastic Structures," by M.V. Sivaselvan and A.M. Reinhorn, 11/5/99, (PB2000-103386, A08, MF-A02).

- MCEER-99-0019 "Proceedings of the 7<sup>th</sup> U.S.- Japan Workshop on Earthquake Resistant Design of Lifeline Facilities and Countermeasures Against Soil Liquefaction," edited by T.D. O'Rourke, J.P. Bardet and M. Hamada, 11/19/99, (PB2000-103354, A99, MF-A06).
- MCEER-99-0020 "Development of Measurement Capability for Micro-Vibration Evaluations with Application to Chip Fabrication Facilities," by G.C. Lee, Z. Liang, J.W. Song, J.D. Shen and W.C. Liu, 12/1/99, (PB2000-105993, A08, MF-A02).
- MCEER-99-0021 "Design and Retrofit Methodology for Building Structures with Supplemental Energy Dissipating Systems," by G. Pekcan, J.B. Mander and S.S. Chen, 12/31/99, (PB2000-105994, A11, MF-A03).
- MCEER-00-0001 "The Marmara, Turkey Earthquake of August 17, 1999: Reconnaissance Report," edited by C. Scawthorn; with major contributions by M. Bruneau, R. Eguchi, T. Holzer, G. Johnson, J. Mander, J. Mitchell, W. Mitchell, A. Papageorgiou, C. Scaethorn, and G. Webb, 3/23/00, (PB2000-106200, A11, MF-A03).
- MCEER-00-0002 "Proceedings of the MCEER Workshop for Seismic Hazard Mitigation of Health Care Facilities," edited by G.C. Lee, M. Ettouney, M. Grigoriu, J. Hauer and J. Nigg, 3/29/00, (PB2000-106892, A08, MF-A02).
- MCEER-00-0003 "The Chi-Chi, Taiwan Earthquake of September 21, 1999: Reconnaissance Report," edited by G.C. Lee and C.H. Loh, with major contributions by G.C. Lee, M. Bruneau, I.G. Buckle, S.E. Chang, P.J. Flores, T.D. O'Rourke, M. Shinozuka, T.T. Soong, C-H. Loh, K-C. Chang, Z-J. Chen, J-S. Hwang, M-L. Lin, G-Y. Liu, K-C. Tsai, G.C. Yao and C-L. Yen, 4/30/00, (PB2001-100980, A10, MF-A02).
- MCEER-00-0004 "Seismic Retrofit of End-Sway Frames of Steel Deck-Truss Bridges with a Supplemental Tendon System: Experimental and Analytical Investigation," by G. Pekcan, J.B. Mander and S.S. Chen, 7/1/00, (PB2001-100982, A10, MF-A02).
- MCEER-00-0005 "Sliding Fragility of Unrestrained Equipment in Critical Facilities," by W.H. Chong and T.T. Soong, 7/5/00, (PB2001-100983, A08, MF-A02).
- MCEER-00-0006 "Seismic Response of Reinforced Concrete Bridge Pier Walls in the Weak Direction," by N. Abo-Shadi, M. Saiidi and D. Sanders, 7/17/00, (PB2001-100981, A17, MF-A03).
- MCEER-00-0007 "Low-Cycle Fatigue Behavior of Longitudinal Reinforcement in Reinforced Concrete Bridge Columns," by J. Brown and S.K. Kunnath, 7/23/00, (PB2001-104392, A08, MF-A02).
- MCEER-00-0008 "Soil Structure Interaction of Bridges for Seismic Analysis," I. PoLam and H. Law, 9/25/00, (PB2001-105397, A08, MF-A02).
- MCEER-00-0009 "Proceedings of the First MCEER Workshop on Mitigation of Earthquake Disaster by Advanced Technologies (MEDAT-1), edited by M. Shinozuka, D.J. Inman and T.D. O'Rourke, 11/10/00, (PB2001-105399, A14, MF-A03).
- MCEER-00-0010 "Development and Evaluation of Simplified Procedures for Analysis and Design of Buildings with Passive Energy Dissipation Systems," by O.M. Ramirez, M.C. Constantinou, C.A. Kircher, A.S. Whittaker, M.W. Johnson, J.D. Gomez and C. Chrysostomou, 11/16/01, (PB2001-105523, A23, MF-A04).
- MCEER-00-0011 "Dynamic Soil-Foundation-Structure Interaction Analyses of Large Caissons," by C-Y. Chang, C-M. Mok, Z-L. Wang, R. Settgast, F. Waggoner, M.A. Ketchum, H.M. Gonnermann and C-C. Chin, 12/30/00, (PB2001-104373, A07, MF-A02).
- MCEER-00-0012 "Experimental Evaluation of Seismic Performance of Bridge Restrainers," by A.G. Vlassis, E.M. Maragakis and M. Saiid Saiidi, 12/30/00, (PB2001-104354, A09, MF-A02).
- MCEER-00-0013 "Effect of Spatial Variation of Ground Motion on Highway Structures," by M. Shinozuka, V. Saxena and G. Deodatis, 12/31/00, (PB2001-108755, A13, MF-A03).
- MCEER-00-0014 "A Risk-Based Methodology for Assessing the Seismic Performance of Highway Systems," by S.D. Werner, C.E. Taylor, J.E. Moore, II, J.S. Walton and S. Cho, 12/31/00, (PB2001-108756, A14, MF-A03).

- MCEER-01-0001 “Experimental Investigation of P-Delta Effects to Collapse During Earthquakes,” by D. Vian and M. Bruneau, 6/25/01, (PB2002-100534, A17, MF-A03).
- MCEER-01-0002 “Proceedings of the Second MCEER Workshop on Mitigation of Earthquake Disaster by Advanced Technologies (MEDAT-2),” edited by M. Bruneau and D.J. Inman, 7/23/01, (PB2002-100434, A16, MF-A03).
- MCEER-01-0003 “Sensitivity Analysis of Dynamic Systems Subjected to Seismic Loads,” by C. Roth and M. Grigoriu, 9/18/01, (PB2003-100884, A12, MF-A03).
- MCEER-01-0004 “Overcoming Obstacles to Implementing Earthquake Hazard Mitigation Policies: Stage 1 Report,” by D.J. Alesch and W.J. Petak, 12/17/01, (PB2002-107949, A07, MF-A02).
- MCEER-01-0005 “Updating Real-Time Earthquake Loss Estimates: Methods, Problems and Insights,” by C.E. Taylor, S.E. Chang and R.T. Eguchi, 12/17/01, (PB2002-107948, A05, MF-A01).
- MCEER-01-0006 “Experimental Investigation and Retrofit of Steel Pile Foundations and Pile Bents Under Cyclic Lateral Loadings,” by A. Shama, J. Mander, B. Blabac and S. Chen, 12/31/01, (PB2002-107950, A13, MF-A03).
- MCEER-02-0001 “Assessment of Performance of Bolu Viaduct in the 1999 Duzce Earthquake in Turkey” by P.C. Roussis, M.C. Constantinou, M. Erdik, E. Durukal and M. Dicleli, 5/8/02, (PB2003-100883, A08, MF-A02).
- MCEER-02-0002 “Seismic Behavior of Rail Counterweight Systems of Elevators in Buildings,” by M.P. Singh, Rildova and L.E. Suarez, 5/27/02. (PB2003-100882, A11, MF-A03).
- MCEER-02-0003 “Development of Analysis and Design Procedures for Spread Footings,” by G. Mylonakis, G. Gazetas, S. Nikolaou and A. Chauncey, 10/02/02, (PB2004-101636, A13, MF-A03, CD-A13).
- MCEER-02-0004 “Bare-Earth Algorithms for Use with SAR and LIDAR Digital Elevation Models,” by C.K. Huyck, R.T. Eguchi and B. Houshmand, 10/16/02, (PB2004-101637, A07, CD-A07).
- MCEER-02-0005 “Review of Energy Dissipation of Compression Members in Concentrically Braced Frames,” by K.Lee and M. Bruneau, 10/18/02, (PB2004-101638, A10, CD-A10).
- MCEER-03-0001 “Experimental Investigation of Light-Gauge Steel Plate Shear Walls for the Seismic Retrofit of Buildings” by J. Berman and M. Bruneau, 5/2/03, (PB2004-101622, A10, MF-A03, CD-A10).
- MCEER-03-0002 “Statistical Analysis of Fragility Curves,” by M. Shinozuka, M.Q. Feng, H. Kim, T. Uzawa and T. Ueda, 6/16/03, (PB2004-101849, A09, CD-A09).
- MCEER-03-0003 “Proceedings of the Eighth U.S.-Japan Workshop on Earthquake Resistant Design of Lifeline Facilities and Countermeasures Against Liquefaction,” edited by M. Hamada, J.P. Bardet and T.D. O’Rourke, 6/30/03, (PB2004-104386, A99, CD-A99).
- MCEER-03-0004 “Proceedings of the PRC-US Workshop on Seismic Analysis and Design of Special Bridges,” edited by L.C. Fan and G.C. Lee, 7/15/03, (PB2004-104387, A14, CD-A14).
- MCEER-03-0005 “Urban Disaster Recovery: A Framework and Simulation Model,” by S.B. Miles and S.E. Chang, 7/25/03, (PB2004-104388, A07, CD-A07).
- MCEER-03-0006 “Behavior of Underground Piping Joints Due to Static and Dynamic Loading,” by R.D. Meis, M. Maragakis and R. Siddharthan, 11/17/03, (PB2005-102194, A13, MF-A03, CD-A00).
- MCEER-03-0007 “Seismic Vulnerability of Timber Bridges and Timber Substructures,” by A.A. Shama, J.B. Mander, I.M. Friedland and D.R. Allicock, 12/15/03.
- MCEER-04-0001 “Experimental Study of Seismic Isolation Systems with Emphasis on Secondary System Response and Verification of Accuracy of Dynamic Response History Analysis Methods,” by E. Wolff and M. Constantinou, 1/16/04 (PB2005-102195, A99, MF-E08, CD-A00).

- MCEER-04-0002 “Tension, Compression and Cyclic Testing of Engineered Cementitious Composite Materials,” by K. Kesner and S.L. Billington, 3/1/04, (PB2005-102196, A08, CD-A08).
- MCEER-04-0003 “Cyclic Testing of Braces Laterally Restrained by Steel Studs to Enhance Performance During Earthquakes,” by O.C. Celik, J.W. Berman and M. Bruneau, 3/16/04, (PB2005-102197, A13, MF-A03, CD-A00).
- MCEER-04-0004 “Methodologies for Post Earthquake Building Damage Detection Using SAR and Optical Remote Sensing: Application to the August 17, 1999 Marmara, Turkey Earthquake,” by C.K. Huyck, B.J. Adams, S. Cho, R.T. Eguchi, B. Mansouri and B. Houshmand, 6/15/04, (PB2005-104888, A10, CD-A00).
- MCEER-04-0005 “Nonlinear Structural Analysis Towards Collapse Simulation: A Dynamical Systems Approach,” by M.V. Sivaselvan and A.M. Reinhorn, 6/16/04, (PB2005-104889, A11, MF-A03, CD-A00).
- MCEER-04-0006 “Proceedings of the Second PRC-US Workshop on Seismic Analysis and Design of Special Bridges,” edited by G.C. Lee and L.C. Fan, 6/25/04, (PB2005-104890, A16, CD-A00).
- MCEER-04-0007 “Seismic Vulnerability Evaluation of Axially Loaded Steel Built-up Laced Members,” by K. Lee and M. Bruneau, 6/30/04, (PB2005-104891, A16, CD-A00).
- MCEER-04-0008 “Evaluation of Accuracy of Simplified Methods of Analysis and Design of Buildings with Damping Systems for Near-Fault and for Soft-Soil Seismic Motions,” by E.A. Pavlou and M.C. Constantinou, 8/16/04, (PB2005-104892, A08, MF-A02, CD-A00).
- MCEER-04-0009 “Assessment of Geotechnical Issues in Acute Care Facilities in California,” by M. Lew, T.D. O’Rourke, R. Dobry and M. Koch, 9/15/04, (PB2005-104893, A08, CD-A00).
- MCEER-04-0010 “Scissor-Jack-Damper Energy Dissipation System,” by A.N. Sigaher-Boyle and M.C. Constantinou, 12/1/04 (PB2005-108221).
- MCEER-04-0011 “Seismic Retrofit of Bridge Steel Truss Piers Using a Controlled Rocking Approach,” by M. Pollino and M. Bruneau, 12/20/04.
- MCEER-05-0001 “Experimental and Analytical Studies of Structures Seismically Isolated with an Uplift-Restraint Isolation System,” by P.C. Roussis and M.C. Constantinou, 1/10/05 (PB2005-108222).
- MCEER-05-0002 “A Versatile Experimentation Model for Study of Structures Near Collapse Applied to Seismic Evaluation of Irregular Structures,” by D. Kusumastuti, A.M. Reinhorn and A. Rutenberg, 3/31/05 (PB2006-101523).
- MCEER-05-0003 “Proceedings of the Third PRC-US Workshop on Seismic Analysis and Design of Special Bridges,” edited by L.C. Fan and G.C. Lee, 4/20/05.
- MCEER-05-0004 “Approaches for the Seismic Retrofit of Braced Steel Bridge Piers and Proof-of-Concept Testing of an Eccentrically Braced Frame with Tubular Link,” by J.W. Berman and M. Bruneau, 4/21/05 (PB2006-101524).
- MCEER-05-0005 “Simulation of Strong Ground Motions for Seismic Fragility Evaluation of Nonstructural Components in Hospitals,” by A. Wanitkorkul and A. Filiatrault, 5/26/05.
- MCEER-05-0006 “Seismic Safety in California Hospitals: Assessing an Attempt to Accelerate the Replacement or Seismic Retrofit of Older Hospital Facilities,” by D.J. Alesch, L.A. Arendt and W.J. Petak, 6/6/05.
- MCEER-05-0007 “Development of Seismic Strengthening and Retrofit Strategies for Critical Facilities Using Engineered Cementitious Composite Materials,” by K. Kesner and S.L. Billington, 8/29/05.
- MCEER-05-0008 “Experimental and Analytical Studies of Base Isolation Systems for Seismic Protection of Power Transformers,” by N. Murota, M.Q. Feng and G-Y. Liu, 9/30/05.
- MCEER-05-0009 “3D-BASIS-ME-MB: Computer Program for Nonlinear Dynamic Analysis of Seismically Isolated Structures,” by P.C. Tsopelas, P.C. Roussis, M.C. Constantinou, R. Buchanan and A.M. Reinhorn, 10/3/05.

- MCEER-05-0010 “Steel Plate Shear Walls for Seismic Design and Retrofit of Building Structures,” by D. Vian and M. Bruneau, 12/15/05.
- MCEER-05-0011 “The Performance-Based Design Paradigm,” by M.J. Astrella and A. Whittaker, 12/15/05.
- MCEER-06-0001 “Seismic Fragility of Suspended Ceiling Systems,” H. Badillo-Almaraz, A.S. Whittaker, A.M. Reinhorn and G.P. Cimellaro, 2/4/06.
- MCEER-06-0002 “Multi-Dimensional Fragility of Structures,” by G.P. Cimellaro, A.M. Reinhorn and M. Bruneau, 3/1/06.
- MCEER-06-0003 “Built-Up Shear Links as Energy Dissipators for Seismic Protection of Bridges,” by P. Dusicka, A.M. Itani and I.G. Buckle, 3/15/06.



MULTIDISCIPLINARY CENTER FOR EARTHQUAKE ENGINEERING RESEARCH

*A National Center of Excellence in Advanced Technology Applications*

University at Buffalo, State University of New York

Red Jacket Quadrangle • Buffalo, New York 14261

Phone: (716) 645-3391 • Fax: (716) 645-3399

E-mail: [mceer@mceermail.buffalo.edu](mailto:mceer@mceermail.buffalo.edu) • WWW Site <http://mceer.buffalo.edu>



University at Buffalo *The State University of New York*

ISSN 1520-295X